



On the origin of masses at the LHC

Juan González Fraile

ADVERTIMENT. La consulta d'aquesta tesi queda condicionada a l'acceptació de les següents condicions d'ús: La difusió d'aquesta tesi per mitjà del servei TDX (www.tdx.cat) i a través del Dipòsit Digital de la UB (diposit.ub.edu) ha estat autoritzada pels titulars dels drets de propietat intel·lectual únicament per a usos privats emmarcats en activitats d'investigació i docència. No s'autoritza la seva reproducció amb finalitats de lucre ni la seva difusió i posada a disposició des d'un lloc aliè al servei TDX ni al Dipòsit Digital de la UB. No s'autoritza la presentació del seu contingut en una finestra o marc aliè a TDX o al Dipòsit Digital de la UB (framing). Aquesta reserva de drets afecta tant al resum de presentació de la tesi com als seus continguts. En la utilització o cita de parts de la tesi és obligat indicar el nom de la persona autora.

ADVERTENCIA. La consulta de esta tesis queda condicionada a la aceptación de las siguientes condiciones de uso: La difusión de esta tesis por medio del servicio TDR (www.tdx.cat) y a través del Repositorio Digital de la UB (diposit.ub.edu) ha sido autorizada por los titulares de los derechos de propiedad intelectual únicamente para usos privados enmarcados en actividades de investigación y docencia. No se autoriza su reproducción con finalidades de lucro ni su difusión y puesta a disposición desde un sitio ajeno al servicio TDR o al Repositorio Digital de la UB. No se autoriza la presentación de su contenido en una ventana o marco ajeno a TDR o al Repositorio Digital de la UB (framing). Esta reserva de derechos afecta tanto al resumen de presentación de la tesis como a sus contenidos. En la utilización o cita de partes de la tesis es obligado indicar el nombre de la persona autora.

WARNING. On having consulted this thesis you're accepting the following use conditions: Spreading this thesis by the TDX (www.tdx.cat) service and by the UB Digital Repository (diposit.ub.edu) has been authorized by the titular of the intellectual property rights only for private uses placed in investigation and teaching activities. Reproduction with lucrative aims is not authorized nor its spreading and availability from a site foreign to the TDX service or to the UB Digital Repository. Introducing its content in a window or frame foreign to the TDX service or to the UB Digital Repository is not authorized (framing). Those rights affect to the presentation summary of the thesis as well as to its contents. In the using or citation of parts of the thesis it's obliged to indicate the name of the author.

On the origin of masses at the LHC



Universitat de Barcelona



Institut de Ciències del Cosmos

Juan González Fraile

Departament d'Estructura i Constituents de la Matèria
Institut de Ciències del Cosmos
Universitat de Barcelona

PhD advisor and tutor:

Prof. Dr. María Concepción González García

Thesis submitted for the degree of *Philosophiæ Doctor (PhD) in Physics*
Tesi presentada per obtenir el grau de *Doctor en Física*
(Programa de Doctorat en Física)

June 2014

A mi familia

Contents

| | |
|---|-----------|
| Agradecimientos / Acknowledgements | v |
| List of publications | 1 |
| List of abbreviations | 3 |
| 1 Introduction: an amazing era | 5 |
| 2 Effective Lagrangian for the EWSB sector: the linear realization | 13 |
| 2.1 Lagrangian for an elementary Higgs | 14 |
| 2.1.1 Higgs interactions with gauge bosons | 16 |
| 2.1.2 Higgs interactions with fermions | 21 |
| 2.1.3 Phenomenology of dimension–six operators | 24 |
| 2.1.4 The right of choice | 28 |
| 2.2 Analysis framework | 31 |
| 2.2.1 Higgs data: signal strengths | 32 |
| 2.2.2 Triple gauge boson vertex data | 38 |
| 2.2.3 Including electroweak precision data | 39 |
| 2.3 Status after the 7 and 8 TeV LHC runs | 41 |
| 2.3.1 Bosonic dimension–six operator analysis | 41 |
| 2.3.2 Including fermionic operators | 47 |
| 2.4 Determining TGV’s from Higgs data | 51 |
| 2.4.1 Direct collider TGV measurements | 53 |
| 2.4.2 Bounds on TGV’s from Higgs data | 54 |
| 2.5 Conclusions | 57 |
| 3 Alternative Lagrangians | 59 |
| 3.1 Disentangling a dynamical Higgs | 60 |
| 3.1.1 Chiral effective Lagrangian | 62 |
| 3.1.2 A different phenomenology | 68 |
| 3.1.3 Status after the 7 and 8 TeV LHC runs | 75 |
| 3.2 Scrutinizing the WWZ vertex | 80 |
| 3.2.1 Lagrangian for TGV interactions | 81 |

| | | |
|----------|--|------------|
| 3.2.2 | Optimizing measurements: preliminary analysis | 84 |
| 3.2.3 | Dynamical Higgs and TGV's: updated analysis | 93 |
| 3.3 | Conclusions | 99 |
| 4 | New resonances in EW gauge boson pair production | 103 |
| 4.1 | Analysis framework | 105 |
| 4.2 | Determination of the spin | 107 |
| 4.2.1 | W' spin determination | 107 |
| 4.2.2 | Z' spin determination | 117 |
| 4.3 | Bounds on Z' decaying to W^+W^- | 125 |
| 4.3.1 | Selection of events and statistical analysis | 126 |
| 4.3.2 | Present bounds on Z' | 134 |
| 4.4 | Conclusions | 138 |
| 5 | New states in neutrino mass models | 141 |
| 5.1 | MLFV type-III see-saw model | 143 |
| 5.2 | Signatures | 153 |
| 5.3 | Analysis and results | 158 |
| 5.3.1 | Process $pp \rightarrow \ell\ell jj\cancel{E}_T$ | 158 |
| 5.3.2 | Process $pp \rightarrow \ell\ell jjjj$ | 166 |
| 5.3.3 | Accessing the unknown lepton parameters | 172 |
| 5.4 | Conclusions | 175 |
| 6 | Summary: an amazing outlook | 179 |
| | Resumen | 185 |
| | List of figures | 195 |
| | List of tables | 197 |
| | Bibliography | 199 |

Agradecimientos / Acknowledgements

Estas líneas cierran simbólicamente lo que han sido varios años de intenso trabajo, pero también de una intensa experiencia vital. Condensar aquí el sentimiento de enorme agradecimiento que siento por vosotros, compañeros de viaje, no es solo imposible dado el espacio moderadamente limitado, sino porque en muchos casos los sentimientos que afloran superan enormemente mi capacidad de expresión. Intentaré transmitir al menos una mínima parte de un sentir que espero no sorprenda a nadie.

Se me hace impensable imaginar estos años de trabajo y aprendizaje sin mi guía principal, Concha. Sin ti esto no hubiera salido adelante. Gracias, por todo lo que me has enseñado, por el trato que siempre me has dado, por tantas horas de dedicación y trabajo, sin perder nunca la paciencia con alguien que ahora se mira y ve lo ingenuo que era y sigue siendo. ¡Y gracias además por haberlo hecho siempre tan ameno! Si me llevo una mínima parte de tu buen hacer y decisión me doy por más que satisfecho. Y si difícil es expresar mi agradecimiento en términos científicos, expresarlo en todos los aspectos que trascienden la ciencia es impensable. Gracias por tu energía inacabable, tu optimismo inspirador, por tu ética infatigable, científica y personal, y por haber estado siempre, desde el primer día, disponible para todo. Y pese a que pueda parecer contradictorio con el mencionado optimismo, escribir estas líneas tiene para mi un punto muy grande de pena, porque suponen de algún modo el cierre de una etapa como estudiante tuyo, ¡muchísimas gracias!

Regarding first the scientific side, thanks to all of you that somehow have collaborated scientifically with me, I only have good words for you! Yendo primero a la vertiente más científica, gracias a todos los que de algún modo habéis colaborado científicamente conmigo, ¡solo tengo buenas palabras para vosotros! Thanks to you Oscar, for what I have learnt, for your optimism and always good character, and for sharing a fruitfull collaboration and every *grain of salt* along these years. Thanks a lot for being also an incredible host, you make me feel that travelling in science could be an amazing experience, *obrigado!*

AGRADECIMIENTOS/ACKNOWLEDGEMENTS

After thousands of emails, code versions, results, discussions, plots and etcetera have been exchanged, sometimes in a continuous and exhausting rush, I thank you Tyler, for being an excellent collaborator, and for never having a bad word to me. Thanks and best of the lucks for the future!

Thanks also to Sheng, Ilaria, Belén, Luca, Stefano, Cédric, Tom, Seung, Giuliano and Gilad, and to Juan, Tilman, Joerg and David, and the rest of colleagues that, regardless of the current results and publications, have shared at some point a collaboration with me.

Una parte importante del tiempo que cubre esta tesis lo he pasado entre estancias, congresos y escuelas, en los lugares mas variopintos y en cada uno de estos lugares siempre he encontrado con quien sonreír, conversar, compartir penas y glorias y por supuesto trabajar. El maravilloso São Paulo de Oscar fue la primera parada destacable, ¡y cuán destacable!, pero no fue la única. Además de la enorme experiencia que supuso la estancia en Berkeley, I am deeply indebted to Gilad, for accepting me as a visitor at CERN, desinterestedly, and for being always willing to work with me, and to support me. I really appreciate all the work done together and your always nice words. En el CERN también conocí al fantástico grupo del madrileño IFT, y además de los agradecimientos por haber sido unos magníficos colaboradores científicos, os agradezco vuestro trato siempre agradable. En especial, gracias Belén, porque además de todo esto, siempre has tenido una respuesta positiva ante cualquier cuestión. Finally, thanks a lot Tilman, for accepting me at Heidelberg, for your support, of any type, for being always willing to help, to talk and to work! I am really indebted to you for the days, past, present and future, in Heidelberg.

One of the best things of these years, and this intense research world, if not the best, is the people I have met. Una de las mejores cosas de estos años, y de este intenso mundo de la investigación, si no la mejor, es la gente que he conocido. Además de todos los arriba mencionados, no me gustaría dejar de nombrar a Miki, Rodrigo y David, por mantener además el contacto en la distancia.

Y volviendo a la que ha sido por muchos años mi casa, gracias a todos los que me han apoyado en la Universitat de Barcelona y más específicamente en el Departament d'Estructura i Constituents de la Matèria. Desde los primeros días de la licenciatura a los últimos pasos del doctorado, pasando por el máster. Por vuestra labor, por lo enseñado, por el apoyo logístico, pero sobretodo, por vuestro trato personal. Por mantener un despacho con solo palabras de ánimo y sonrisas, gracias a Arnau, Marc, Jaume, Alessandro, Clara y Vicente, y por compartir vicisitudes y procesos administrativos, a todos los compañeros del programa de doctorado, en especial, Xumeu y Alejandro.

Gracias también a todos los que me habéis ayudado con este manuscrito.

Y a Sergio y Lobato, tranquilos, viviréis más. Las risas, charlas y silencios en años de diarios almuerzos han hecho mella en mi, no sé cuán

AGRADECIMIENTOS/ACKNOWLEDGEMENTS

sanos han sido, pero los echaré de menos.

El desarrollo de esta tesis ha sido una labor extremadamente exigente, y sin lugar a dudas, hubiese sido imposible sin el apoyo de todos los que, perteneciendo o no al entorno estrictamente científico, me habéis apoyado y ayudado. A este círculo cercano, a los que dais sentido a todo esto, van dedicadas las últimas líneas. Primero os debo una disculpa. Uno de los mayores retos detrás de esta tesis ha sido encontrar un balance temporal equilibrado para que todo tuviese cabida. Siento si no lo he logrado, en mi defensa diré que uno de mis mayores esfuerzos, pasados, presentes y futuros, ha sido siempre optimizar este equilibrio, lo seguiré intentando. Gracias a mis amigos, por vuestro ánimo y apoyo, y por seguir manteniendo, después de mucho tiempo en algunos casos, con mayor o menor intensidad la llama de una amistad. A todos vosotros, a los que ya habéis sido mencionados arriba, y en especial también a Miguel, Rocky, Sergio, Hèctor, Ferran, McClane. Y así ya solo me queda agradecer a los que no he podido elegir, ¡y doy gracias por ello! Si no, mi decisión solo podría haber sido peor, nunca mejor. A mi familia.

A los que desde la distancia siempre me han mostrado su cariño y apoyo y a los que con su cercanía han endulzado esta tesis. A Montse y Juan, por el trato casi paternal que siempre he recibido.

A Carmen, Jaime, David y Adri. Por vuestros ánimos y apoyo inacabable, por vuestro interés, y por todo el tiempo que pasamos juntos. Porque se me haría imposible, e innecesario, imaginar un futuro sin vosotros, ¡gracias por ser una parte fundamental en mi vida!

Y a mis padres, Isabel y Juan, las razones son tantas que no sé si tiene sentido intentar escribir siquiera estas líneas. Esta tesis es vuestra, porque sin vosotros simplemente no habría tesis. Por criar, por educar, por proveer, por animar, por enseñar, por apoyar, por tener paciencia, simplemente por como sois, y por tantas y tantas cosas que no sé cuáles listar. Por amar.

Y por último gracias a ti Montse. En estas páginas hay más cosas tuyas de las que te puedas llegar a imaginar, esta tesis también es tuya. Por ser pieza fundamental, apoyo incesante, incansable consejera, optimista incorregible, ¡no cambies nunca compañera infatigable! Me permito la libertad, miraremos nuevas rutas, *amb l'esguard lent del copsador distret*.

¡Gracias a todos por haber conseguido que, sin importar el resultado, el camino haya merecido la pena!

Juan González Fraile

AGRADECIMIENTOS/ACKNOWLEDGEMENTS

This thesis has been supported by a FPU (Formación del Profesorado Universitario) grant by the Spanish Ministry of education with reference AP2009-2546.

The work has also received support at different stages from the projects: Spanish MICINN FPA2007-66665-C02-01, MICINN FPA2010-20807 and consolider-ingenio 2010 program CSD-2008-0037, and European Union grant FP7 ITN INVISIBLES (Marie Curie Actions PITN-GA-2011-289442).

The author also acknowledges support by Instituto de Física, Universidade de São Paulo, CERN TH–division and Institute für Theoretische Physik, Universität Heidelberg.

List of publications

The original contents of this thesis are based on the following publications:

1. O. J. P. Éboli, J. Gonzalez-Fraile and M. C. Gonzalez-Garcia, “Scrutinizing the $ZW+W^-$ vertex at the Large Hadron Collider at 7 TeV,” *Phys. Lett. B* **692**, 20 (2010) [arXiv:1006.3562 [hep-ph]].
2. O. J. P. Éboli, C. S. Fong, J. Gonzalez-Fraile and M. C. Gonzalez-Garcia, “Determination of the Spin of New Resonances in Electroweak Gauge Boson Pair Production at the LHC,” *Phys. Rev. D* **83**, 095014 (2011) [arXiv:1102.3429 [hep-ph]].
3. O. J. P. Éboli, J. Gonzalez-Fraile and M. C. Gonzalez-Garcia, “Neutrino Masses at LHC: Minimal Lepton Flavour Violation in Type-III See-saw,” *JHEP* **1112**, 009 (2011) [arXiv:1108.0661 [hep-ph]].
4. O. J. P. Éboli, J. Gonzalez-Fraile and M. C. Gonzalez-Garcia, “Present Bounds on New Neutral Vector Resonances from Electroweak Gauge Boson Pair Production at the LHC,” *Phys. Rev. D* **85**, 055019 (2012) [arXiv:1112.0316 [hep-ph]].
These results were updated with the larger data set presented in this dissertation in

J. Gonzalez-Fraile, “Update of the Present Bounds on New Neutral Vector Resonances from Electroweak Gauge Boson Pair Production at the LHC,” [arXiv:1205.5802 [hep-ph]].
5. T. Corbett, O. J. P. Éboli, J. Gonzalez-Fraile and M. C. Gonzalez-Garcia, “Constraining anomalous Higgs interactions,” *Phys. Rev. D* **86**, 075013 (2012) [arXiv:1207.1344 [hep-ph]].
6. T. Corbett, O. J. P. Éboli, J. Gonzalez-Fraile and M. C. Gonzalez-Garcia, “Robust Determination of the Higgs Couplings: Power to the Data,” *Phys. Rev. D* **87**, 015022 (2013) [arXiv:1211.4580 [hep-ph]].
7. T. Corbett, O. J. P. Éboli, J. Gonzalez-Fraile and M. C. Gonzalez-Garcia, “Determining Triple Gauge Boson Couplings from Higgs Data,” *Phys. Rev. Lett.* **111**, no. 1, 011801 (2013) [arXiv:1304.1151 [hep-ph]].

8. I. Brivio, T. Corbett, O. J. P. Éboli, M. B. Gavela, J. Gonzalez-Fraile, M. C. Gonzalez-Garcia, L. Merlo and S. Rigolin, “Disentangling a dynamical Higgs,” JHEP **1403**, 024 (2014) [arXiv:1311.1823 [hep-ph]].

The following publications have been developed in parallel to the content of this thesis, although they have not been included in this dissertation:

1. M. Baak, A. Blondel, A. Bodek, R. Caputo, T. Corbett, C. Degrande, O. J. P. Éboli and J. Erler, B. Feigl, A. Freitas, J. Gonzalez-Fraile, M. C. Gonzalez-Garcia *et al.*, “Study of Electroweak Interactions at the Energy Frontier,” [arXiv:1310.6708 [hep-ph]].
2. Cédric Delaunay, Thomas Flacke, J. Gonzalez-Fraile, Seung J. Lee, Giuliano Panico and Gilad Perez, “Light Non-degenerate Composite Partners at the LHC,” JHEP **1402**, 055 (2014) [arXiv:1311.2072 [hep-ph]].

List of abbreviations

| | |
|-------------|-------------------------------------|
| BSM | Beyond the standard model |
| CHM | Composite Higgs model |
| COM | Center-of-mass |
| EOM | Equations of motion |
| EW | Electroweak |
| EWPD | Electroweak precision data |
| EWPO | Electroweak precision observables |
| EWSB | Electroweak symmetry breaking |
| IO | Inverted ordering |
| LHC | Large Hadron Collider |
| MAOS | M_{T2} assisted on-shell |
| MLFV | Minimal lepton flavor violation |
| NLO | Next-to-leading order |
| NO | Normal ordering |
| NP | New physics |
| pNGB | Pseudo-Nambu-Golstone boson |
| QCD | Quantum chromodynamics |
| SM | Standard model |
| TGV | Triple gauge boson vertex |
| UV | Ultraviolet |
| VBF | Vector boson fusion |
| vev | Vacuum expectation value |
| VH | Associated production |
| WIMP | Weakly interacting massive particle |

Chapter 1

Introduction: an amazing era

On March 2010 the first 7 TeV collisions were recorded at the CERN Large Hadron Collider (LHC). This date marked the beginning of the LHC fascinating research program. Rapidly improving on its performance, the LHC has faced since then several challenges, before culminating to what is so far the main success of its operation. The Higgs discovery was announced on July the 4th, 2012 [1, 2], which was the closure of almost fifty years of research since its existence was postulated [3–8]. Its discovery is, hopefully, the first of the milestones associated to the LHC operation. The observation and study of the first state that seems directly related to electroweak symmetry breaking (EWSB) leave the first footprints of this new era in particle physics, that has a promising prospect for the future high energy LHC operation.

In parallel to the initial LHC runs, the content of this thesis was developed. Consequently, besides the pure scientific dissertation, that we start describing in the following, this thesis hopefully transmits to the reader part of the thrilling joy that the scientific events that took place during its completion caused on the author and his scientific collaborators. This way, we enthusiastically describe along the forthcoming Chapters the main role that the LHC data can play on our understanding of several of the open mysteries in particle physics. In this lifetime unique context, the LHC can guide us through a trip, back in time, to the origin of masses.

The standard model (SM) of particle physics is built relying on the invariance under gauge symmetries as one of its key pillars. Nevertheless, with the particles that were known before the Higgs discovery, no $SU(3)_C \times SU(2)_L \times U(1)_Y$ gauge invariant term (at least in its linear realization) could be constructed in order to generate a mass for the observed, and massive, gauge bosons and fermions. Without the Higgs boson, the theory remained non-renormalizable and, in addition, the energy growth of the longitudinal gauge boson scattering led to perturbative unitarity violation at the TeV scale. The origin of the masses of the particles, and the

mechanism responsible for the EWSB was, and still is, one of the main open questions in particle physics.

The SM Higgs boson was proposed as probably the simplest of the solutions to explain EWSB. In the SM, the addition of only one $SU(2)_L$ doublet, whose scalar potential develops a vacuum expectation value (vev) causing the spontaneous breaking of the electroweak (EW) gauge symmetry, is enough to generate the masses of the observed gauge bosons. Introducing in the theory the gauge invariant Yukawa terms can account, in addition, for the generation of the observed fermion masses, with the possible exception of the neutrinos, the lightest of the known fermions, whose peculiar mass origin we will also discuss in the following. The SM Higgs boson is able then to explain the pattern of the observed particle masses, while keeping at the same time the gauge invariance and the renormalizability of the theory. Furthermore, the SM Higgs boson cures the dangerous energy growth on the longitudinal gauge boson scattering. Thus, before the LHC operation, the Higgs boson was the only missing piece in the SM, with which it would be structurally complete.

A SM Higgs boson is, however, not the only possible explanation for the EWSB mechanism. And it is clearly not the most satisfactory theoretically, as it leads to the well-known “hierarchy problem” that we describe in the following. This limitation was the underlying motivation for the construction of alternative descriptions to explain EWSB. In these beyond the standard model (BSM) theories new resonances are usually introduced, and they often include particles that are similar to the scalar SM boson. Moreover, regardless of the mechanism considered (SM or not), either with or without a Higgs-like particle, given the energy growth of the longitudinal gauge boson scattering, some new phenomena was known to have to appear at the TeV scale. As a consequence, the expectations for a new physics (NP) observation at the LHC were really high, as the machine had the potential to directly access, for the first time, this scale.

Luckily, these expectations were early confirmed. On July 2012 a new state was observed, after only the first two years of recording LHC collisions, and with the experimental facility working at *only* half its designed center-of-mass (COM) energy. The Higgs boson¹ discovery announcement at CERN put an end to what it seemed an endless wait. At the same time, the Higgs boson discovery launched a new research program. After its observation, there is an obvious question that has to be answered regarding the origin of the masses and the discovered new state. Is this the—almost fifty years old—SM Higgs boson? Or is it one of the look-alikes in some BSM extension? Is it even related to EWSB? While its discovery has been a major event on the scientific community, we are still far from understanding the

¹In this dissertation we refer generically as the Higgs boson to the recently observed state, regardless of its nature, purely SM or not.

mechanism responsible for EWSB and how the origin of masses is described. These are some of the main questions that motivate this dissertation.

In this context, the study and measurement of the properties of the discovered particle: its spin, its parity or its couplings, is a necessary step to decipher whether the observed new state is the SM Higgs boson or, instead, one of the analogous partners in some of the alternative descriptions. The initial experimental studies [9, 10] indicate that the new particle is a scalar boson, with CP -even properties, as in the SM. Furthermore, considering its interactions to WW and ZZ pairs, and the first studies performed right after the discovery (such as, for instance, the analyses we present in the first Chapters of this thesis), it seems that the observed state is directly connected to EWSB. This means that we can now directly study the mechanism responsible for the origin of the masses of the observed particles through the analysis of the recently discovered state properties. With this purpose in mind, we devote the initial Chapters of this thesis to seek for an answer to the previously asked questions. We work towards understanding the nature of the observed state, in particular, we focus on the study of the Higgs couplings and the related gauge self-interactions.

In order to study the couplings of the observed state we look for ways of confronting all the existing available data with the different proposed mechanisms and theoretical descriptions. Instead of constraining ourselves to a specific SM completion, we aim to make a model-independent approach, where as many theories as possible can be included in the study, minimizing at the same time the number of theoretical assumptions required. In this thesis, a guiding role in the analyses relies on the available data, whereas we try to avoid, as much as we can, any theory prejudice. With this spirit, one of the most suitable approaches is that of effective Lagrangians [11–13].

The effective Lagrangian approach is a model-independent way to describe new physics that is expected to manifest directly at a scale Λ , which is higher than the scale at which the experiments are performed. By simply specifying the particle content and the symmetries respected at the low-energy theory, the Lagrangian can be extended with higher dimensional operators, that are suppressed by powers of the high energy scale, and that parametrize the effects of new physics at the low scale.

In this thesis we apply this effective Lagrangian framework to study the properties of the Higgs boson. More precisely, we study in Chapters 2 and 3 of the thesis the effective Lagrangian approach to the Higgs couplings. At present, with no guidance as of where the scale of NP could be laying, the effective Lagrangian may provide the only option on the route to understand the origin of EWSB, alternative to the direct search for the hypothesized new particles in EWSB extensions (an approach that we also study in the following). In particular the effective Lagrangian expansion may be especially important in cases where these new particles are elusive or where the scale of new physics is above the TeV scale but still leading to observable deviations

of the SM expectations, though not to observable new particles. Although within the present experimental accuracy it is too soon to interpret the results of the effective field approach in terms of high energy predictions, the correlations and coupling patterns that the approach introduces are useful to test and study the Higgs couplings in a motivated way, setting the roots for the future, when the precision will improve.

Once the philosophy of the approach is presented, we can apply it to the described open question: deciphering the nature of the observed new state. In Chapter 2 of the thesis we present the effective Lagrangian approach to the Higgs sector, assuming that the Higgs comes in an $SU(2)_L$ doublet, and thus that EWSB is linearly realized. Leaving the details for the corresponding Chapter, this is the case suitable for the SM and for the different BSM extensions where the Higgs is an elementary state, or where it behaves as coming in a doublet at the low energies, for instance in supersymmetry models. In the analysis we use all the available data in a leading guiding role through the study. We perform a bottom–up approach, where the different aspects of the analysis, as for instance the independent basis of higher dimensional operators used, are driven by the existing data on the EWSB sector, minimizing at the same time the theoretical bias. We use all the Higgs available data recently collected at the LHC during the initial 7 and 8 TeV runs, as well as the Tevatron analyses on Higgs physics. In addition, we use triple gauge boson vertex (TGV) measurements from both LHC and Tevatron, and from LEP searches as well. Finally we include also the information from low energy electroweak precision observables (EWPO). All these sources of data are analyzed to study the couplings of the observed Higgs boson. With them we build the proper statistical tools to perform a global fit based on the measurements and information that we have access to. The purpose of the analysis is to look for deviations that would be translated in the future on information regarding the ultraviolet (UV) completion of the SM. We will conclude that the current picture looks completely SM–like, with no observed significant deviation from the SM expectations on the couplings. Furthermore this bottom–up approach will serve us to propose and analyze interesting correlations that can be useful to further test the observed particle nature. These correlations involve data coming from different sectors: Higgs searches, and also TGV measurements. They both show a very interesting complementarity in order to constrain the higher dimensional operators and test the Higgs boson nature. We will show that the current reachable precision in these different experiments is comparable, what makes the correlation already testable.

In Chapter 3 we follow also the effective Lagrangian approach, but in contrast to the first analysis, in this Chapter we do not assume that the Higgs is part of an $SU(2)_L$ doublet. The main difference with Chapter 2 is that Chapter 3 makes use of a non–linear (*i.e.* chiral) realization of the gauge symmetry in the effective Lagrangian expansion. This is suitable

for the family of models where the Higgs is not an elementary state, but where it is a composite state of a theory that contains a strong interacting EWSB sector, as in composite Higgs models (CHM)'s. As a consequence, the nature of this second expansion is different from the first one, leading to relevant phenomenological possible signatures. We focus our analysis into the comparison of the phenomenology of both linear and non-linear expansions, and how both could be disentangled at the LHC. We will find that the interesting correlations between interactions measurable in different experimental searches, that we derive in Chapter 2, may disappear in this case. In addition, striking signals on TGV measurements may also allow for a disentanglement of the Higgs nature. Both approaches point to the importance of studying TGV interactions in order to have a complete access to the EWSB sector. With this motivation we describe in detail the historical parametrization that is usually used in the experimental TGV measurements. In the second part of Chapter 3 we study and optimize the realistic LHC capability to observe the different new interactions, deviating from the SM behavior, that could appear on these TGV measurements. This is the first of the collider *simulations* that we present in this thesis, and it already shows the importance of a proper optimization of the observables and cuts in order to increase the signal to background ratio in the studied LHC channels. We will conclude that the LHC has the potential to improve the current existing bounds on anomalous TGV interactions, and consequently our knowledge of the EWSB sector.

At the LHC the effective Lagrangian approach is not the only way to look for BSM signals associated to EWSB and the generation of masses. In the following we describe a complementary approach, that relies on the direct search for the new resonances that many of the EWSB extensions introduce.

Even if we found out that the observed particle was exactly as the SM Higgs boson, there would still be different open questions that we are not able to answer in the context of the SM. For instance, we are currently unable to explain the baryon asymmetry of the universe, the origin of the dark matter or the experimental observed neutrino mass and mixing pattern. Unfortunately, none of these questions give us a strong hint as of where NP may be laying. There are in addition important theoretical open questions associated to a full SM picture and the existence of a light Higgs boson. For instance, we do not know what is the origin of the Yukawa terms, or why we need so many of them. We can not explain yet what is the origin of the observed flavor pattern in the SM or simply why the SM relies on the $SU(3)_C \times SU(2)_L \times U(1)_Y$ gauge invariance. But the main open question is related to the fact that the SM is a complete weakly coupled theory up to extremely short distances. The SM minimality seems to come with a theoretical drawback, or at least an aspect of the theory that we are unable to fully understand within this SM minimality. In a dessert like

paradigm, where no high energy scale is present up to the Planck scale, the Higgs mass can receive arbitrary high energy contributions, whose renormalization implies that the EW scale is technically unnatural. This is the known naturalness or hierarchy problem. As we have commented before, the search for an answer to this question has been a motivation to build several of the most common SM extensions. The currently most accepted BSM plausible theories can be classified roughly on two families: supersymmetry extensions and CHM completions. Both types of theories, besides possible corrections to the SM particle couplings, such as the ones studied in the first two Chapters of the thesis, introduce several new resonances associated to new dynamics that lie close to the EW scale in order to tame the hierarchy problem. The observation of any of these new particles would be a major step towards deciphering the EWSB mechanism. This is consequently the main motivation behind Chapter 4 of the thesis.

The observation of new particles expected in BSM completions is possible if these new particles have masses inside the LHC reach. But analysis techniques have to be developed to cover in the most exhaustive way all the hypothesized possible new partners at the LHC². With this purpose in mind, in this thesis we focus on new vector resonances and we analyze and optimize the LHC potential to observe and study resonances that are generically related to the unitarization of the longitudinal weak boson scattering. This relation is established by looking for new vector resonances that decay to EW gauge boson pairs, either WW or WZ pairs. A few generic assumptions serve us to perform a realistic collider study, whose conclusions are useful for a large variety of resonances. This way, in a first analysis we study the use of different angular observables and asymmetries to determine the spin of an hypothetical new W' or Z' state. This is accomplished comparing their vectorial nature to a scalar, Higgs-like, hypothesis. After we estimate the LHC potential for the spin discrimination, that extends up to masses on the multi-TeV range, we proceed to derive which are the current LHC bounds on the existence of some of these resonances after the initial 7 TeV LHC run is considered. In particular, we make a realistic collider analysis that, with the help of the LHC experimental simulations and observed data, serves us to present the strongest bounds on the existence of neutral vector resonances decaying into W^+W^- . As we will detail, the LHC has a huge potential to discover and exclude this type of spin-1 resonances, improving

²From a low-energy point of view, the most severe UV sensitivity is due to the quantum Higgs process where a top-anti-top fermion pair with arbitrary high energy pushes the mass of the Higgs boson towards the high energy boundary of the theory. The most common of the new resonances that tame this naturalness problem are the denoted as top-partners. Their nomenclature is due to the fact that they usually have the same gauge quantum numbers than the SM top quark, as it is commonly required in order to cancel the dangerous SM top loop contributions to the Higgs mass. Their possible observation has been studied as well in a work not included in this thesis [14].

consequently our capability to understand EWSB.

Up to this point, we have only discussed the LHC potential to seek for an explanation regarding the open mystery hiding behind EWSB and the masses of the observed SM particles. Notwithstanding, the EWSB is not the only mystery related to generically the origin of the masses that remains open. Questions like the nature of dark matter or the observed matter–anti–matter asymmetry in the Universe, or the origin of the smallness of the neutrino masses are far from being understood. It is on this last point that we focus the final part of the thesis. In the SM, even after including the Higgs boson, the neutrinos are massless particles. There is no gauge invariant renormalizable mass term that can be built for the neutrinos as long as only their interacting part is included in the theory. Consequently, the observation of the neutrino masses and mixing in oscillation experiments is a clear experimental proof of physics BSM. If we consider in addition the impressive LHC potential, we are led to face an obvious question. Could we obtain information on the origin of the neutrino masses at the LHC? We devote Chapter 5 of this dissertation to study this possibility.

In order to answer the question, the first challenge we have to face is related to the construction of consistent TeV scale models that generate the observed neutrino masses and mixing. The difficulty comes from the fact that the smallness of the neutrino masses is usually related in the most simple models to extremely massive partners, clearly out of the LHC reach. Notwithstanding, we present in this thesis a consistent construction where the new heavy states associated to the generation of the neutrino masses can live within the LHC reach. The model presents additional interesting features as well. In the considered realization, the relation of the couplings of the new heavy states with the observed pattern of neutrino masses and mixing leads to a peculiar phenomenology. This interesting feature is translated at the end into highly predictable signatures at the LHC. With the purpose of studying these signatures we perform a realistic collider study, and indeed we will conclude that the observation of these neutrino partners at the LHC is not only possible for a sizable range of masses and couplings, but the observation could even help to understand and extend the structure of the observed neutrino mixing parameters. Thus we will conclude that the LHC can also shed light on the neutrino mass generation.

Summarizing, the purpose of this thesis is to study the LHC potential to search for answers regarding the mechanism responsible for EWSB and, in addition, the theory describing the origin of the neutrino masses. The thesis is organized following the structure of this Introduction. First, in Chapter 2 we present the effective Lagrangian approach to the Higgs couplings assuming a linear realization of the SM gauge symmetry. In Chapter 3 we present the study of alternative effective Lagrangians. These are the effective Lagrangian approach suitable for a non–linear realization of the SM gauge symmetry and, in addition, the analysis at the LHC of the historical

TGV parametrization. In Chapter 4 we study the existence of new vector resonances, associated to EWSB extensions, in EW pair production processes at the LHC. We present the analysis of their spin determination and we derive as well the current strongest bounds on neutral vector resonances after considering the LHC 7 TeV run. In Chapter 5 we study the potential that the LHC has to access a consistent TeV scale neutrino mass generation model. Finally we end the thesis dissertation presenting the conclusions and the future outlook.

As we hope to transmit along the whole dissertation, the LHC has a great potential to study the mechanism responsible for the EWSB and to search for possible signals related to the origin of the neutrino masses. The prospects are promising, and definitively, the LHC facility can drive us through this long route towards understanding what is hiding behind the origin of the observed particle masses.

Chapter 2

Effective Lagrangian for the EWSB sector: the linear realization

The discovery of the Higgs boson at the CERN LHC [1,2], has already been stored in the memory of the scientific community as— hopefully— the first of the golden days of the LHC era. Its major impact trespassing the usually too tight fences between the scientific community and the general media is justified by its crucial importance. After almost 50 years since the existence of the SM Higgs boson was proposed [3–8] and with the light scalar having evaded detection at both LEP and Tevatron colliders, the discovery of a particle that resembles the proposed state finally marks the starting point for the direct exploration of the EWSB sector. Now we have observed a new state that may play a key role in the breaking of the EW symmetry and thus on the generation of the masses of the existing particles. We are finally aware of the precise ($\sim \pm 2$ GeV) value of its mass and we also have a robust idea of in which experimental accessible channels the new state is already showing up. In summary, we have already experimental data to study the different properties of this new state in order to start understanding what is hiding behind EWSB. This Chapter is devoted to the study of some of the properties of this recently discovered state: its couplings.

The analysis of the characteristics of the new particle: its spin, its parity or its couplings, will serve us to access the mechanism responsible for EWSB. This will be useful to decipher whether the observed state is indeed the Higgs boson as predicted in the SM or the corresponding state in some BSM extension. This analysis is thus complementary to the searches for the direct observation of the hypothetical partners appearing in some of these extensions of the SM (whose study will be partially covered in Chapters 4 and 5). Indeed, the precise measurements of the couplings of the new observed state may help us to infer at which scale some of these new states

may appear. With this aim, in this Chapter we present a model independent approach to the couplings of the Higgs boson by means of an effective Lagrangian, where we follow a bottom–up approach in order to minimize the number of theoretical hypothesis in this study.

The Chapter, that is based on the published works [15–18], is structured as follows. First, in Section 2.1, we describe the features of the effective Lagrangian approach to the observed Higgs interactions. We present the most general set of operators that need to be considered because they involve triple couplings of the low energy scalar to the SM gauge bosons and fermions and can affect the present Higgs data. We argue how, using the equations of motion (EOM), the operators can be related, giving us the freedom of choice in the election of the final basis used in the analysis of the data. We describe a sensible choice of this basis, that follows a simple guideline relying on how easily some of the operators can be constrained by existing data from other well tested sectors of the theory. This reduces to eight the number of operators testable with an analysis of the existing Higgs data. In Section 2.2 we describe the details of the analysis and the data that we use to constrain their eight coefficients. In addition to the Tevatron and LHC Higgs searches, the data contains also precise measurements of TGV’s from LEP, Tevatron and LHC, and also electroweak precision data (EWPD) from LEP and other low energy experiments. In Section 2.3 we present the current results of this analysis, updated to include the full 7 and 8 TeV LHC Higgs data sets. Finally, in Section 2.4, we describe in detail one of the most interesting features of this approach: the complementarity between the Higgs data analysis and the study of TGV interactions at the colliders. We end summarizing the main conclusions and open discussions on the effective Lagrangian approach to the EWSB sector in Section 2.5.

2.1 Lagrangian for an elementary Higgs

Consistently with the present data we start assuming that, even if there is NP associated with the EWSB sector, the observed particle is an elementary state which belongs to a light EW doublet scalar, and consequently, that the $SU(2)_L \otimes U(1)_Y$ symmetry is linearly realized in the effective theory [19–32]. This implies that the new physics effects decouple when the scale of NP, Λ , goes to high values [33].

Thus we think of the SM as an effective low energy theory but we still retain the gauge group, the particle spectrum and the pattern of spontaneous symmetry breaking as valid ingredients to describe Nature at energies $E \ll \Lambda$. The SM predictions are, however, modified by small effects that are proportional to powers of E/Λ . In other words, the difference between the SM as a complete description of Nature and as a low energy effective theory is that in the latter case we must consider also non–renormalizable terms.

2.1. LAGRANGIAN FOR AN ELEMENTARY HIGGS

At low energies the Lagrangian of the theory can be described then by the expansion

$$\mathcal{L} = \mathcal{L}_0^{\text{SM}} + \sum_{m=1}^{\infty} \sum_n \frac{f_n^{(4+m)}}{\Lambda^m} \mathcal{O}_n^{(4+m)} . \quad (2.1)$$

where $\mathcal{L}_0^{\text{SM}}$ is the SM Lagrangian. The additional operators $\mathcal{O}_n^{(4+m)}$ have a dimension $d = 4 + m$, and the effects of NP are encoded on the coefficients accompanying them, $f_n^{(4+m)}$, that are suppressed by powers of the associated NP scale. They parametrize our ignorance of the NP effects in the low energy phenomenology. The imposed invariance under the SM local gauge group $SU(3)_c \otimes SU(2)_L \otimes U(1)_Y$ in the effective Lagrangian implicitly assumes that the breaking of $SU(2)_L \otimes U(1)_Y$ takes place at the weak scale and not at the high energy scale. In addition to the invariance under the SM local group, and regarding the particle content, we assume that there are no other light states present in the low energy spectrum besides the discovered Higgs boson and the SM gauge bosons and fermions.

With these assumptions the first of the higher dimensional ($d > 4$) operators appearing in the effective Lagrangian is a dimension–five total lepton number violating operator, the Weinberg operator [34]. This operator gives a Majorana mass to the neutrinos, but given their small mass the scale suppressing the operator is expected to be clearly above the TeV scale. Its effects are then most likely irrelevant for the phenomenology of the Higgs boson at the LHC, and thus, we ignore this operator for the current Chapter. Its effects will become relevant when studying the neutrino mass generation models, and we will address them in Chapter 5.

Neglecting the effects of the dimension–five total lepton number violating operator, the lowest order effective operators that can be built are of dimension–six. It is a well know result in the literature [35] that, of all dimension–six operators, 59 of them, up to flavor and Hermitian conjugation, are enough to generate the most general S –matrix elements consistent with baryon number conservation and the SM gauge symmetry. However, in the present Chapter the starting basis of operators is not this minimal set of 59 operators [35] for two reasons. First, besides the $SU(3)_c \otimes SU(2)_L \otimes U(1)_Y$ SM local symmetry, we assume the conservation of baryon and lepton numbers and the \mathcal{O}_n operators to be C and P even as well¹. Second, the fact that operators connected by the EOM lead to the same S –matrix elements [36–39], can be used to select the proper basis of operators for the final analysis if one does not start from a minimal set of operators, but instead from an extended one, where the EOM still need to be applied. Following

¹These extra assumptions have the aim of reducing the set of operators to be studied while the current precision of the LHC Higgs searches does not allow for a discrimination between operators respecting or violating some of these symmetries. However, when the precision reached increases some of these assumptions may be relaxed, allowing for instance for C and P violating operators to be included and studied.

this idea, instead of starting from the minimal basis in [35], we start with an extended (*i.e.* non-minimal) selection of dimension-six operators that is based in what has been referred in the literature as the HISZ basis [22, 25]. Before deciding the final independent basis of operators to be used in our analyses, let us discuss the several interactions that modify the Higgs couplings to gauge bosons and to fermions that the dimension-six operators in the HISZ basis lead to.

2.1.1 Higgs interactions with gauge bosons

In this Subsection we start describing the dimension-six operators that modify the Higgs interactions with the gauge bosons. In a first block we have eight C and P even operators modifying the Higgs interactions with the EW gauge bosons in addition to one operator containing interactions of the Higgs boson with the gluons [19, 20]:

$$\begin{aligned}
 \mathcal{O}_{\Phi,1} &= (D_\mu \Phi)^\dagger \Phi \Phi^\dagger (D^\mu \Phi) , \\
 \mathcal{O}_{\Phi,2} &= \frac{1}{2} \partial^\mu (\Phi^\dagger \Phi) \partial_\mu (\Phi^\dagger \Phi) , \\
 \mathcal{O}_{\Phi,4} &= (D_\mu \Phi)^\dagger (D^\mu \Phi) (\Phi^\dagger \Phi) , \\
 \mathcal{O}_B &= (D_\mu \Phi)^\dagger \hat{B}^{\mu\nu} (D_\nu \Phi) , \\
 \mathcal{O}_W &= (D_\mu \Phi)^\dagger \hat{W}^{\mu\nu} (D_\nu \Phi) , \\
 \mathcal{O}_{BB} &= \Phi^\dagger \hat{B}_{\mu\nu} \hat{B}^{\mu\nu} \Phi , \\
 \mathcal{O}_{WW} &= \Phi^\dagger \hat{W}_{\mu\nu} \hat{W}^{\mu\nu} \Phi , \\
 \mathcal{O}_{BW} &= \Phi^\dagger \hat{B}_{\mu\nu} \hat{W}^{\mu\nu} \Phi , \\
 \mathcal{O}_{GG} &= \Phi^\dagger \Phi G_{\mu\nu}^a G^{a\mu\nu} ,
 \end{aligned} \tag{2.2}$$

where we have denoted the Higgs doublet by Φ , and in our conventions its covariant derivative is $D_\mu \Phi = (\partial_\mu + i\frac{1}{2}g' B_\mu + ig\frac{\sigma_a}{2} W_\mu^a) \Phi$. The hatted field strengths are defined as $\hat{B}_{\mu\nu} = i\frac{g'}{2} B_{\mu\nu}$ and $\hat{W}_{\mu\nu} = i\frac{g}{2} \sigma_a W_{\mu\nu}^a$, and

$$\begin{aligned}
 B_{\mu\nu} &= \partial_\mu B_\nu - \partial_\nu B_\mu , \\
 W_{\mu\nu}^a &= \partial_\mu W_\nu^a - \partial_\nu W_\mu^a - g\epsilon^{abc} W_\mu^b W_\nu^c , \\
 G_{\mu\nu}^a &= \partial_\mu G_\nu^a - \partial_\nu G_\mu^a - g_S f^{abc} G_\mu^b G_\nu^c .
 \end{aligned} \tag{2.3}$$

g (g') [g_S] denotes the $SU(2)_L$ ($U(1)_Y$) [$SU(3)_C$] gauge coupling and the Pauli matrices are σ_a . In our conventions the EW gauge fields are

$$W_\mu^\pm = \frac{1}{\sqrt{2}} (W_\mu^1 \mp iW_\mu^2) , \quad Z_\mu^{SM} = \frac{1}{\sqrt{g^2 + g'^2}} (gW_\mu^3 - g'B_\mu) , \tag{2.4}$$

and

$$A_\mu^{SM} = \frac{1}{\sqrt{g^2 + g'^2}} (g'W_\mu^3 + gB_\mu) , \tag{2.5}$$

2.1. LAGRANGIAN FOR AN ELEMENTARY HIGGS

and G_μ^a are the gluon fields. In the unitary gauge the Higgs doublet is written as

$$\Phi = \frac{1}{\sqrt{2}} \begin{pmatrix} 0 \\ v + h(x) \end{pmatrix}, \quad (2.6)$$

where v is its vev and h is the Higgs boson field.

Once we have introduced the operators and the corresponding notation, a first mandatory step in order to study their contribution to the Higgs interactions is to account for their effects on the field, coupling and mass renormalizations. Let's start with the operators made of Higgs doublets and partial or covariant derivatives acting on them. In Eq. (2.2) we have three of such operators: $\mathcal{O}_{\Phi,1}$, $\mathcal{O}_{\Phi,2}$, and $\mathcal{O}_{\Phi,4}$. In addition there is a fourth operator respecting the symmetries which is not included in Eq. (2.2) because it is irrelevant for the present Higgs boson phenomenology:

$$\mathcal{O}_{\Phi,3} = \frac{1}{3} (\Phi^\dagger \Phi)^3. \quad (2.7)$$

It gives an additional contribution to the Higgs potential

$$\mu_0^2 (\Phi^\dagger \Phi) + \lambda_0 (\Phi^\dagger \Phi)^2 - \frac{f_{\Phi,3}}{3\Lambda^2} (\Phi^\dagger \Phi)^3, \quad (2.8)$$

and it leads to a shift of its minimum with respect to the SM

$$v^2 = -\frac{\mu_0^2}{\lambda_0} \left(1 + \frac{v^2}{4\Lambda^2} \frac{f_{\Phi,3}}{\lambda_0} \right) \equiv v_0^2 \left(1 + \frac{v^2}{4\Lambda^2} \frac{f_{\Phi,3}}{\lambda_0} \right), \quad (2.9)$$

where v_0 follows the SM relation $v_0^2 \equiv -\frac{\mu_0^2}{\lambda_0}$.

The three operators relevant for this study $\mathcal{O}_{\Phi,1}$, $\mathcal{O}_{\Phi,2}$, and $\mathcal{O}_{\Phi,4}$, contribute to the kinetic energy of the Higgs boson field h , *i.e.* the term $(\partial_\mu h \partial^\mu h)$. Hence, in order to bring the Higgs kinetic term to the canonical form, we have to introduce a finite wave function renormalization to the Higgs field

$$H = h \left[1 + \frac{v^2}{2\Lambda^2} (f_{\Phi,1} + 2f_{\Phi,2} + f_{\Phi,4}) \right]^{1/2}. \quad (2.10)$$

Furthermore, the operators $\mathcal{O}_{\Phi,1}$, $\mathcal{O}_{\Phi,2}$, $\mathcal{O}_{\Phi,3}$ and $\mathcal{O}_{\Phi,4}$ all alter the Higgs mass according to the expression

$$M_H^2 = 2\lambda_0 v^2 \left[1 - \frac{v^2}{2\Lambda^2} \left(f_{\Phi,1} + 2f_{\Phi,2} + f_{\Phi,4} + \frac{f_{\Phi,3}}{\lambda_0} \right) \right],$$

where we have expanded to linear order in the f_i coefficients.

We focus now on the operators that include the hatted gauge field strengths. The operators with only one hatted field strength, *i.e.* \mathcal{O}_B and \mathcal{O}_W , have no effect on the field, mass and coupling renormalizations. Whereas the effects of three of the operators with two hatted field strengths, \mathcal{O}_{BB} ,

\mathcal{O}_{GG} , and \mathcal{O}_{WW} on field renormalization are irrelevant at the end as they are completely eliminated after ineffective field and coupling constant redefinitions [25]:

$$W_{\mu\nu} = \left[1 + \frac{2M_W^2}{\Lambda^2} f_{WW}\right]^{1/2} W_{\mu\nu}^{SM}, \quad g = \left[1 + \frac{2M_W^2}{\Lambda^2} f_{WW}\right]^{-1/2} g^{SM}, \quad (2.11)$$

$$B_{\mu\nu} = \left[1 + \frac{2M_Z^2 s_\theta^2}{\Lambda^2} f_{BB}\right]^{1/2} B_{\mu\nu}^{SM}, \quad g' = \left[1 + \frac{2M_Z^2 s_\theta^2}{\Lambda^2} f_{BB}\right]^{-1/2} g'^{SM} \quad (2.12)$$

where $s_\theta \equiv g'/\sqrt{g^2 + g'^2}$ stands for the tree level sine of the SM weak mixing angle. In summary the effects of \mathcal{O}_B , \mathcal{O}_W , \mathcal{O}_{BB} , \mathcal{O}_{GG} , and \mathcal{O}_{WW} in the phenomenology of the Higgs boson arise from their direct contributions to interaction vertices, and not through field or coupling constant redefinitions. On the contrary \mathcal{O}_{BW} contributes at tree level to $Z\gamma$ mixing, and therefore to the definition of the mass eigenstates

$$Z_\mu = \left[1 - \frac{g^2 g'^2}{2(g^2 + g'^2)} \frac{v^2}{\Lambda^2} f_{BW}\right]^{-1/2} Z_\mu^{SM}, \quad (2.13)$$

$$A_\mu = \left[1 + \frac{g^2 g'^2}{2(g^2 + g'^2)} \frac{v^2}{\Lambda^2} f_{BW}\right]^{-1/2} A_\mu^{SM} - \left[\frac{g g' (g^2 - g'^2)}{4(g^2 + g'^2)} \frac{v^2}{\Lambda^2} f_{BW}\right] Z_\mu^{SM} \quad (2.14)$$

Operators $\mathcal{O}_{\Phi,1}$, $\mathcal{O}_{\Phi,4}$, and \mathcal{O}_{BW} have also an impact on the EW gauge boson masses. Expanding to linear order in the f_i coefficients they read

$$M_Z^2 = \frac{g^2 + g'^2}{4} v^2 \left[1 + \frac{v^2}{2\Lambda^2} \left(f_{\Phi,1} + f_{\Phi,4} - \frac{g^2 g'^2}{(g^2 + g'^2)} f_{BW}\right)\right] \quad (2.15)$$

$$M_W^2 = \frac{g^2}{4} v^2 \left[1 + \frac{v^2}{2\Lambda^2} f_{\Phi,4}\right]. \quad (2.16)$$

Notice that \mathcal{O}_{BW} and $\mathcal{O}_{\Phi,1}$ contribute to the Z mass but not to the W mass, therefore, violating the custodial $SU(2)$ symmetry. As we will see when we consider the effects of EWPD on the dimension–six operators, \mathcal{O}_{BW} and $\mathcal{O}_{\Phi,1}$ contribute at the tree level to S and T (or $\Delta\rho$) parameters respectively. We will use this contribution to constrain them.

In what follows we work in the commonly referred as Z -scheme. This means that besides the most precise measured value of the strong constant α_S , taken from the world average in [40], and the measured mass of the Higgs, assumed in this analysis to be 125 GeV, all the calculations use as inputs the most precise measured values of the Fermi constant (G_F), M_Z and the electromagnetic fine–structure constant (α_{em}), extracted from the muon decay rate, the Z line–shape at LEP I and the Thompson scattering [40]. Furthermore, when convenient, we also absorb part of the tree–level renormalization factors by using the measured value of M_W . In particular using

2.1. LAGRANGIAN FOR AN ELEMENTARY HIGGS

$\frac{G_F}{\sqrt{2}} = \frac{g^2}{8M_W^2}$ and Eqs. (2.15) and (2.16) we obtain the relations

$$v = \left(\sqrt{2}G_F\right)^{-1/2} \left(1 - \frac{v^2}{4\Lambda^2}f_{\Phi,4}\right), \quad (2.17)$$

$$M_Z^2 = \left(\sqrt{2}G_F\right)^{-1} \frac{g^2}{4c_\theta^2} \left(1 + \frac{v^2}{2\Lambda^2}f_{\Phi,1} - \frac{g^2g'^2}{2(g^2+g'^2)}\frac{v^2}{\Lambda^2}f_{BW}\right), \quad (2.18)$$

where we have denoted by $c_\theta \equiv g/\sqrt{g^2+g'^2}$ the tree level cosine of the SM weak mixing angle, and where in the second line it is understood that g (g') has to be expressed as a function of the input parameters.

After renormalization, the dimension–six effective operators in Eq. (2.2) give rise to Higgs interactions with SM gauge boson pairs that take the following form in the unitary gauge:

$$\begin{aligned} \mathcal{L}_{\text{eff}}^{\text{HVV}} &= g_{Hgg} HG_{\mu\nu}^a G^{a\mu\nu} + g_{H\gamma\gamma} HA_{\mu\nu}A^{\mu\nu} \\ &+ g_{HZ\gamma}^{(1)} A_{\mu\nu}Z^\mu\partial^\nu H + g_{HZ\gamma}^{(2)} HA_{\mu\nu}Z^{\mu\nu} \\ &+ g_{HZZ}^{(1)} Z_{\mu\nu}Z^\mu\partial^\nu H + g_{HZZ}^{(2)} HZ_{\mu\nu}Z^{\mu\nu} + g_{HZZ}^{(3)} HZ_\mu Z^\mu \\ &+ g_{HWW}^{(1)} (W_{\mu\nu}^+W^{-\mu}\partial^\nu H + \text{h.c.}) + g_{HWW}^{(2)} HW_{\mu\nu}^+W^{-\mu\nu} \\ &+ g_{HWW}^{(3)} HW_\mu^+W^{-\mu}, \end{aligned} \quad (2.19)$$

where in this case $V_{\mu\nu} = \partial_\mu V_\nu - \partial_\nu V_\mu$, with $V = A, Z, W$, and G . The effective couplings g_{Hgg} , $g_{H\gamma\gamma}$, $g_{HZ\gamma}^{(1,2)}$, $g_{HWW}^{(1,2,3)}$ and $g_{HZZ}^{(1,2,3)}$ are related to the coefficients of the operators appearing in Eq. (2.1) through

$$\begin{aligned} g_{Hgg} &= \frac{f_{GG}v}{\Lambda^2} \equiv -\frac{\alpha_s}{8\pi} \frac{f_g v}{\Lambda^2}, \\ g_{H\gamma\gamma} &= -\left(\frac{g^2 v s_\theta^2}{2\Lambda^2}\right) \frac{f_{BB} + f_{WW} - f_{BW}}{2}, \\ g_{HZ\gamma}^{(1)} &= \left(\frac{g^2 v}{2\Lambda^2}\right) \frac{s_\theta(f_W - f_B)}{2c_\theta}, \\ g_{HZ\gamma}^{(2)} &= \left(\frac{g^2 v}{2\Lambda^2}\right) \frac{s_\theta[2s_\theta^2 f_{BB} - 2c_\theta^2 f_{WW} + (c_\theta^2 - s_\theta^2)f_{BW}]}{2c_\theta}, \end{aligned}$$

$$\begin{aligned}
 g_{HZZ}^{(1)} &= \left(\frac{g^2 v}{2\Lambda^2} \right) \frac{c_\theta^2 f_W + s_\theta^2 f_B}{2c_\theta^2} , \\
 g_{HZZ}^{(2)} &= - \left(\frac{g^2 v}{2\Lambda^2} \right) \frac{s_\theta^4 f_{BB} + c_\theta^4 f_{WW} + c_\theta^2 s_\theta^2 f_{BW}}{2c_\theta^2} , \\
 g_{HZZ}^{(3)} &= \left(\frac{g^2 v}{4c_\theta^2} \right) \left[1 + \frac{v^2}{4\Lambda^2} \left(3f_{\Phi,1} + 3f_{\Phi,4} - 2f_{\Phi,2} - \frac{2g^2 g'^2}{(g^2 + g'^2)} f_{BW} \right) \right] \\
 &= M_Z^2 (\sqrt{2} G_F)^{1/2} \left[1 + \frac{v^2}{4\Lambda^2} (f_{\Phi,1} + 2f_{\Phi,4} - 2f_{\Phi,2}) \right] , \\
 g_{HWW}^{(1)} &= \left(\frac{g^2 v}{2\Lambda^2} \right) \frac{f_W}{2} , \\
 g_{HWW}^{(2)} &= - \left(\frac{g^2 v}{2\Lambda^2} \right) f_{WW} , \\
 g_{HWW}^{(3)} &= \left(\frac{g^2 v}{2} \right) \left[1 + \frac{v^2}{4\Lambda^2} (3f_{\Phi,4} - f_{\Phi,1} - 2f_{\Phi,2}) \right] , \\
 &= 2M_W^2 (\sqrt{2} G_F)^{1/2} \left[1 + \frac{v^2}{4\Lambda^2} (2f_{\Phi,4} - f_{\Phi,1} - 2f_{\Phi,2}) \right] ,
 \end{aligned} \tag{2.20}$$

where, as previously, we have expanded to linear order in the f_i coefficients. Also, for convenience, we have rescaled the coefficient of the gluonic operator, f_{GG} , by a loop factor $-\alpha_s/(8\pi)$. This way an anomalous gluonic coupling of order $f_g \sim \mathcal{O}(1-10)$ gives a contribution comparable to the SM top loop, which is the main loop contributing to the coupling of the Higgs boson to gluons in the SM. For the rest of dimension–six operators, the ones involving EW gauge bosons, we have decided to keep the same normalization commonly used in all the pre–LHC studies for an easier comparison with the existing literature. Notice that the general expressions above reproduce in the different cases considered those of [23, 26–31, 41].

Before moving to introduce the dimension–six operators involving Higgs interactions with the fermions, for the sake of completeness we list here some additional dimension–six operators that involve only bosons. These are not relevant for the Higgs phenomenology analysis, but some of them will be discussed at the end of this Chapter and in the next one. The first operator is made of Higgs doublets and covariant derivatives acting on them:

$$\mathcal{O}_{\square\Phi} = (D_\mu D^\mu \Phi)^\dagger (D_\nu D^\nu \Phi) . \tag{2.21}$$

As it was already discussed in [19, 35], this operator is usually removed by the use of EOM in exchange of some of the operators listed in Eq. (2.2), plus some of the fermionic operators we will list in the following Subsection. Thus this operator is redundant and irrelevant for the analysis of the present Chapter. It would only become relevant if we decided to avoid to use the EOM, as we will see in the next Chapter.

2.1. LAGRANGIAN FOR AN ELEMENTARY HIGGS

We can finally list in addition a set of five operators made only of EW and strong gauge fields. Thus they do not contribute to the Higgs interactions, but for the sake of presenting all the dimension–six operators we discuss in this thesis on the same Section, we present them here. The set is [22, 25]:

$$\begin{aligned}\mathcal{O}_{WWW} &= i\epsilon_{ijk}\hat{W}_\mu^{i\nu}\hat{W}_\nu^{j\rho}\hat{W}_\rho^{k\mu}, & \mathcal{O}_{GGG} &= if_{abc}G_\mu^{a\nu}G_\nu^{b\rho}G_\rho^{c\mu}, \\ \mathcal{O}_{DW} &= \left(D^\mu\hat{W}_{\mu\nu}\right)^i\left(D_\rho\hat{W}^{\rho\nu}\right)^i, & \mathcal{O}_{DB} &= \left(\partial^\mu\hat{B}_{\mu\nu}\right)\left(\partial_\rho\hat{B}^{\rho\nu}\right), \\ \mathcal{O}_{DG} &= (D^\mu G_{\mu\nu})^a(D_\rho G^{\rho\nu})^a,\end{aligned}\quad (2.22)$$

where $(D^\mu W_{\mu\nu})^i = \partial^\mu W_{\mu\nu}^i - g\epsilon^{ijk}W^{\mu j}W_{\mu\nu}^k$ and where in \mathcal{O}_{DG} , D^μ denotes the covariant derivative acting on a field transforming in the adjoint of $SU(3)_C$, $(D^\mu G_{\mu\nu})^a = \partial^\mu G_{\mu\nu}^a - g_s f^{abc}G^{\mu b}G_{\mu\nu}^c$. It is worth to note that this set is not minimal, and usually the operators \mathcal{O}_{DW} , \mathcal{O}_{DB} and \mathcal{O}_{DG} are traded using EOM by \mathcal{O}_{WWW} and \mathcal{O}_{GGG} , plus fermionic operators. The operator \mathcal{O}_{WWW} will be discussed at the end of this Chapter when describing the complementarity between Higgs searches and TGV collider analyses. Moreover this set will be recovered as well when comparing the linear and non–linear basis in the next Chapter.

2.1.2 Higgs interactions with fermions

The list of dimension–six operators in [35] contributing to the Higgs interactions with fermion pairs reads:

$$\begin{aligned}\mathcal{O}_{e\Phi,ij} &= (\Phi^\dagger\Phi)(\bar{L}_i\Phi e_{R_j}), & \mathcal{O}_{\Phi L,ij}^{(1)} &= \Phi^\dagger(i\overleftrightarrow{D}_\mu\Phi)(\bar{L}_i\gamma^\mu L_j), \\ \mathcal{O}_{u\Phi,ij} &= (\Phi^\dagger\Phi)(\bar{Q}_i\tilde{\Phi}u_{R_j}), & \mathcal{O}_{\Phi Q,ij}^{(1)} &= \Phi^\dagger(i\overleftrightarrow{D}_\mu\Phi)(\bar{Q}_i\gamma^\mu Q_j), \\ \mathcal{O}_{d\Phi,ij} &= (\Phi^\dagger\Phi)(\bar{Q}_i\Phi d_{R_j}), & \mathcal{O}_{\Phi e,ij}^{(1)} &= \Phi^\dagger(i\overleftrightarrow{D}_\mu\Phi)(\bar{e}_{R_i}\gamma^\mu e_{R_j}), \\ & & \mathcal{O}_{\Phi u,ij}^{(1)} &= \Phi^\dagger(i\overleftrightarrow{D}_\mu\Phi)(\bar{u}_{R_i}\gamma^\mu u_{R_j}), \\ & & \mathcal{O}_{\Phi d,ij}^{(1)} &= \Phi^\dagger(i\overleftrightarrow{D}_\mu\Phi)(\bar{d}_{R_i}\gamma^\mu d_{R_j}), \\ & & \mathcal{O}_{\Phi ud,ij}^{(1)} &= \tilde{\Phi}^\dagger(i\overleftrightarrow{D}_\mu\Phi)(\bar{u}_{R_i}\gamma^\mu d_{R_j}), \\ & & \mathcal{O}_{\Phi L,ij}^{(3)} &= \Phi^\dagger(i\overleftrightarrow{D}_\mu^a\Phi)(\bar{L}_i\gamma^\mu\sigma_a L_j), \\ & & \mathcal{O}_{\Phi Q,ij}^{(3)} &= \Phi^\dagger(i\overleftrightarrow{D}_\mu^a\Phi)(\bar{Q}_i\gamma^\mu\sigma_a Q_j),\end{aligned}\quad (2.23)$$

where we define the doublet $\tilde{\Phi} = i\sigma_2\Phi^*$, and the operators $\Phi^\dagger\overleftrightarrow{D}_\mu\Phi = \Phi^\dagger D_\mu\Phi - (D_\mu\Phi)^\dagger\Phi$ and $\Phi^\dagger\overleftrightarrow{D}_\mu^a\Phi = \Phi^\dagger\sigma^a D_\mu\Phi - (D_\mu\Phi)^\dagger\sigma^a\Phi$. The conventions for the fermion fields are L for the lepton doublet, Q for the quark doublet and f_R for the $SU(2)_L$ singlet fermions. In Eq. (2.23) i, j are family indices. Notice that, unlike the Higgs–gauge boson operators of the previous Subsection, not all Higgs–fermion operators listed above are Hermitian. In particular the Hermitian conjugation of the right column operators in Eq. (2.23) (except for $\mathcal{O}_{\Phi ud,ij}^{(1)}$) is equivalent to a transposition of the family

indices in each of the fermionic currents, while it is not explicitly listed for the rest.

The dimension–six operators in Eq. (2.23) have been classified according to the number of Higgs fields that they contain. In the first column, the operators are denoted by $\mathcal{O}_{f\Phi,ij}$ and they are made of three Higgs doublets. After spontaneous symmetry breaking these operators lead to modifications of the SM Higgs Yukawa couplings as we will see below. The second column, $\mathcal{O}_{\Phi f,ij}^{(1)}$, contains operators with two Higgs doublets and one covariant derivative acting on them. Consequently, they contribute to the Higgs couplings to fermion pairs, but also modify the neutral current weak interactions of the corresponding fermions, with the exception of $\mathcal{O}_{\Phi ud,ij}^{(1)}$ that also changes the charged weak interactions. $\mathcal{O}_{\Phi f,ij}^{(3)}$, besides contributing to the Higgs couplings to fermion pairs, also lead to modifications of the fermionic neutral and charged current interactions.

As in the previous Subsection, a first step to study the contribution of these operators to the Higgs interactions is to account for their contribution to renormalization, in this case to the fermion masses and mixing. In particular the operators in the first column of Eq. (2.23), $\mathcal{O}_{f\Phi,ij}$, renormalize the fermion masses and mixing, and they modify the Yukawa interactions as well. While in the SM these interactions take the form

$$\mathcal{L}_{Yuk} = -y_{ij}^e \bar{L}_i \Phi e_{Rj} - y_{ij}^d \bar{Q}_i \Phi d_{Rj} - y_{ij}^u \bar{Q}_i \tilde{\Phi} u_{Rj} + \text{h.c.} , \quad (2.24)$$

the dimension–six modifications to the Yukawa interactions are

$$\mathcal{L}_{eff}^{Hqq} = \frac{f_{d\Phi,ij}}{\Lambda^2} \mathcal{O}_{d\Phi,ij} + \frac{f_{u\Phi,ij}}{\Lambda^2} \mathcal{O}_{u\Phi,ij} + \frac{f_{e\Phi,ij}}{\Lambda^2} \mathcal{O}_{e\Phi,ij} + \text{h.c.} , \quad (2.25)$$

where a sum over the three families $i, j = 1, 2, 3$ is understood in both equations. After spontaneous symmetry breaking and prior to the finite Higgs wave function renormalization in Eq. (2.10), we can conveniently decompose Eqs. (2.24) and (2.25) in two pieces, \mathcal{L}_0 and \mathcal{L}_1 , given by

$$\begin{aligned} \mathcal{L}_0 = & \frac{1}{\sqrt{2}} \bar{d}_{L_i} \left(-y_{ij}^d + \frac{v^2}{2\Lambda^2} f_{d\Phi,ij} \right) d_{R_j} (v + h) \\ & + \frac{1}{\sqrt{2}} \bar{u}_{L_i} \left(-y_{ij}^u + \frac{v^2}{2\Lambda^2} f_{u\Phi,ij} \right) u_{R_j} (v + h) \\ & + \frac{1}{\sqrt{2}} \bar{e}_{L_i} \left(-y_{ij}^e + \frac{v^2}{2\Lambda^2} f_{e\Phi,ij} \right) e_{R_j} (v + h) + \text{h.c.} , \end{aligned} \quad (2.26)$$

and

$$\mathcal{L}_1 = \frac{1}{\sqrt{2}} \frac{v^2}{\Lambda^2} \left(f_{d\Phi,ij} \bar{d}_{L_i} d_{R_j} h + f_{u\Phi,ij} \bar{u}_{L_i} u_{R_j} h + f_{e\Phi,ij} \bar{e}_{L_i} e_{R_j} h + \text{h.c.} \right) , \quad (2.27)$$

2.1. LAGRANGIAN FOR AN ELEMENTARY HIGGS

where again a sum over the three generations is understood. With this decomposition one can easily identify \mathcal{L}_0 as being proportional to the mass term of the fermions and then in the mass basis it leads to the SM-like Higgs–fermion interactions with renormalized fermion masses and quark weak mixing². On the other hand, generically, the new interactions contained in \mathcal{L}_1 are not necessarily flavor diagonal in the mass basis unless $f_{f\Phi} \propto y^f$, where here $f_{f\Phi}$ and y^f are the 3×3 matrices in generation space whose components are $f_{f\Phi,ij}$ and y_{ij}^f with $f = u, \text{ or } d \text{ or } e$.

After the renormalization of the fermion masses and mixing and after considering also the renormalization of the Higgs wave function in Eq. (2.10) the $H\bar{f}f$ couplings in the fermion mass basis can be written as

$$\mathcal{L}^{Hff} = g_{Hij}^f \bar{f}_{L_i}^{\prime} f_{R_j}^{\prime} H + \text{h.c.} \quad , \quad (2.28)$$

with the definition

$$g_{Hij}^f = -\frac{m_i^f}{v} \delta_{ij} \left[1 - \frac{v^2}{4\Lambda^2} (f_{\Phi,1} + 2f_{\Phi,2} + f_{\Phi,4}) \right] + \frac{v^2}{\sqrt{2}\Lambda^2} f_{f\Phi,ij}^{\prime} \quad . \quad (2.29)$$

Here we have denoted the physical masses and fermions (*i.e.* the eigenvalues and eigenstates of the v terms in Eq. (2.26)) by m_i^f and $f_{L(R)i}^{\prime}$, and $f_{f\Phi,ij}^{\prime}$ are the coefficients of the corresponding operators in this mass basis. For the rest of the Chapter and for the sake of simplicity we will denote these coefficients and fermion fields without the prime.

For the sake of completeness we present here an extra set of operators containing Higgs interactions with fermions, but with at least an additional gauge boson in the vertex [35]:

$$\begin{aligned} \mathcal{O}_{eW,ij} &= (\bar{L}_i \sigma^{\mu\nu} e_{R_j}) \sigma^a \Phi W_{\mu\nu}^a, & \mathcal{O}_{eB,ij} &= (\bar{L}_i \sigma^{\mu\nu} e_{R_j}) \Phi B_{\mu\nu}, \\ \mathcal{O}_{uW,ij} &= (\bar{Q}_i \sigma^{\mu\nu} u_{R_j}) \sigma^a \tilde{\Phi} W_{\mu\nu}^a, & \mathcal{O}_{uB,ij} &= (\bar{Q}_i \sigma^{\mu\nu} u_{R_j}) \tilde{\Phi} B_{\mu\nu}, \\ \mathcal{O}_{dW,ij} &= (\bar{Q}_i \sigma^{\mu\nu} d_{R_j}) \sigma^a \Phi W_{\mu\nu}^a, & \mathcal{O}_{dB,ij} &= (\bar{Q}_i \sigma^{\mu\nu} d_{R_j}) \Phi B_{\mu\nu}, \\ \mathcal{O}_{uG,ij} &= (\bar{Q}_i \sigma^{\mu\nu} T^A u_{R_j}) \tilde{\Phi} G_{\mu\nu}^A, & \mathcal{O}_{dG,ij} &= (\bar{Q}_i \sigma^{\mu\nu} T^A d_{R_j}) \Phi G_{\mu\nu}^A, \end{aligned} \quad (2.30)$$

the notation follows that in Eq. (2.23), with T^A referring to the $SU(3)_c$ generators and $\sigma^{\mu\nu} = \frac{i}{2}(\gamma^\mu \gamma^\nu - \gamma^\nu \gamma^\mu)$, where γ^μ are the Dirac matrices and where Hermitian conjugation has not been explicitly listed. These dimension–six operators are usually referred as dipole–operators and most of them are strongly constrained by dipole moment measurements. Their effect is negligible for the current Higgs data.

²In the present Chapter we are not adding right-handed neutrinos to the fermion basis nor allowing for the total lepton number violating dimension–five operator, thus the couplings to the charged leptons can be chosen to be generation diagonal in the mass basis as in the SM.

2.1.3 Phenomenology of dimension–six operators

As we will argue in the following Subsection, one of the most sensible choices of the basis of dimension–six operators can be made guided by their contribution to the existing data. Thus before describing the choice of the final basis for the analysis of the Higgs data, we summarize here the contributions of the dimension–six operators to Higgs observables as well as to other well tested sectors of the SM, in particular to the EWPD and gauge boson self couplings.

In what respects the Higgs observables, from Eq. (2.19) we see that

- \mathcal{O}_{GG} gives a tree level correction to the coupling of the Higgs boson with gluons. Its contribution to gluon fusion is especially important, as gluon fusion, which in the SM is a loop process, constitutes the main production mode for the SM Higgs boson at the LHC.
- Operators $\mathcal{O}_{\Phi,1}$, $\mathcal{O}_{\Phi,2}$, and $\mathcal{O}_{\Phi,4}$ mainly contribute to Higgs physics via the renormalization of the Higgs wave function, Eq (2.10). Through this renormalization the three operators give a shift to all the SM Higgs vertices, not only with the EW gauge bosons, but also with the fermion pairs.
- The dimension–six operators containing gauge field strengths present a much richer phenomenology. All \mathcal{O}_B , \mathcal{O}_W , \mathcal{O}_{BB} , \mathcal{O}_{BW} and \mathcal{O}_{WW} contribute to the interactions of the Higgs state to W^+W^- and ZZ pairs, and what is more interesting, with a different kinematic structure than that of the SM, as can be seen in Eq. (2.19). Furthermore, they also contribute, at the tree level, to Higgs interactions that are generated in loop processes in the SM. For instance the five operators affect at the tree level the decay of the Higgs boson to $Z\gamma$, which comes from a top and a W loop in the SM. Given its low rate, this process has not been observed at the LHC yet, but we will see in the next Section how the exclusion bounds that have been placed on the decay are sufficiently strong to have a mild effect on the tree level contribution of the dimension–six operators.
- In addition, \mathcal{O}_{BB} , \mathcal{O}_{BW} and \mathcal{O}_{WW} contribute at the tree level to the diphoton decay of the Higgs boson. The fact that this process, a loop decay in the SM, is currently the decay mode measured with the highest precision has important consequences on these dimension–six operators as we will see in Sec. 2.3.
- The fermionic operators are also relevant for Higgs physics considering that the LHC is already measuring two Higgs decays to fermions: to $b\bar{b}$ and to $\tau\bar{\tau}$ pairs. In addition there is the loop contribution of the top quark to gluon fusion production and to Higgs to $\gamma\gamma$ and $Z\gamma$ decays.

2.1. LAGRANGIAN FOR AN ELEMENTARY HIGGS

Next we focus on the effect of the dimension–six operators in TGV’s. Triple gauge boson vertices have been measured with $\mathcal{O}(10\%)$ precision at LEP II and Tevatron, and currently studied also at LHC [40, 42–51]. They should be considered when discussing the choice of basis, as operators \mathcal{O}_B , \mathcal{O}_W , \mathcal{O}_{BW} , and $\mathcal{O}_{\Phi,1}$ modify the $\gamma W^+ W^-$ and $Z W^+ W^-$ vertices.

The most general form of these vertices compatible with Lorentz invariance and relevant for a collider analysis was introduced in [52], and it has been the parametrization commonly used by the experimental collaborations at LEP, Tevatron and LHC in order to measure these triple vertices. For C and P even couplings and for at least one of the gauge bosons on–shell, the parametrization reads:

$$\begin{aligned} \mathcal{L}_{WWV} = & -ig_{WWV} \left\{ g_1^V \left(W_{\mu\nu}^+ W^{-\mu} V^\nu - W_\mu^+ V_\nu W^{-\mu\nu} \right) + \kappa_V W_\mu^+ W_\nu^- V^{\mu\nu} \right. \\ & \left. + \frac{\lambda_V}{m_W^2} W_{\mu\nu}^+ W^{-\nu\rho} V_\rho^\mu \right\}, \end{aligned} \quad (2.31)$$

where $g_{WW\gamma} = e = gs_\theta$ and $g_{WWZ} = gc_\theta$. In general these vertices involve the six dimensionless couplings g_1^V , κ_V , and λ_V ($V = \gamma$ or Z). Notwithstanding, electromagnetic gauge invariance requires that $g_1^\gamma = 1$, while the five remaining couplings are related to the dimension–six operators \mathcal{O}_B , \mathcal{O}_W , \mathcal{O}_{BW} , and $\mathcal{O}_{\Phi,1}$ [22]:

$$\begin{aligned} \Delta g_1^Z &= g_1^Z - 1 = \frac{g^2 v^2}{8c_\theta^2 \Lambda^2} \left(f_W + 2 \frac{s_\theta^2}{c_\theta^2 - s_\theta^2} f_{BW} \right) - \frac{1}{4(c_\theta^2 - s_\theta^2)} f_{\Phi,1} \frac{v^2}{\Lambda^2}, \\ \Delta \kappa_\gamma &= \kappa_\gamma - 1 = \frac{g^2 v^2}{8\Lambda^2} \left(f_W + f_B - 2f_{BW} \right), \\ \Delta \kappa_Z &= \kappa_Z - 1 = \frac{g^2 v^2}{8c_\theta^2 \Lambda^2} \left(c_\theta^2 f_W - s_\theta^2 f_B + \frac{4s_\theta^2 c_\theta^2}{c_\theta^2 - s_\theta^2} f_{BW} \right) - \frac{1}{4(c_\theta^2 - s_\theta^2)} f_{\Phi,1} \frac{v^2}{\Lambda^2}, \end{aligned} \quad (2.32)$$

with no contribution from \mathcal{O}_B , \mathcal{O}_W , \mathcal{O}_{BW} , and $\mathcal{O}_{\Phi,1}$ to λ_γ and λ_Z . As we will see in the following Sections, the only contribution from dimension–six operators to those comes from \mathcal{O}_{WWW} :

$$\lambda_\gamma = \lambda_Z = \frac{3g^2 M_W^2}{2\Lambda^2} f_{WWW}. \quad (2.33)$$

Finally we move to electroweak precision observables (EWPO) which can be summarized in the determination of the Z and W couplings to fermions as well as the oblique parameters S , T , and U . They are in agreement with the SM at the per mil to per cent level [53]. These results impose severe constraints on the operators which modify these observables: $\mathcal{O}_{\Phi f,ij}^{(1)}$, $\mathcal{O}_{\Phi f,ij}^{(3)}$, \mathcal{O}_{BW} and $\mathcal{O}_{\Phi,1}$. In particular \mathcal{O}_{BW} and $\mathcal{O}_{\Phi,1}$ give a tree

level correction to the gauge boson self-energies which contribute to the combinations S and T [21, 22, 52, 54]:

$$\alpha_{\text{em}}\Delta S = e^2 \frac{v^2}{\Lambda^2} f_{BW} \quad \text{and} \quad \alpha_{\text{em}}\Delta T = \frac{1}{2} \frac{v^2}{\Lambda^2} f_{\Phi,1} \quad , \quad (2.34)$$

while $\mathcal{O}_{\Phi f,ij}^{(1)}$ and $\mathcal{O}_{\Phi f,ij}^{(3)}$ give tree level corrections to the Wff' and Zff vertices. As a consequence of these contributions, it may seem that we can directly constrain all these dimension-six operators. Nonetheless, in order to take full advantage of these EWPO we must be sure that there is no combination of the anomalous operators whose contribution at the tree level to EWPO cancels out, *i.e.* we must avoid the existence of what has been referred in the literature as *blind* directions [21, 55]. This is a point that needs to be addressed before making the final choice of the basis. Thus, for illustration we analyze the dependence on the dimension-six couplings of a subset of the EWPO that contains the W mass (M_W), the W leptonic width ($\Gamma_{\ell\ell}^W$), the Z width into charged leptons ($\Gamma_{\ell\ell}$), the leptonic Z left-right asymmetry (A_ℓ) as well as the invisible Z width (Γ_{inv})³. In general we can write the departures of the observables ($\Delta\text{Obs} \equiv \frac{\text{Obs} - \text{Obs}_{\text{SM}}}{\text{Obs}_{\text{SM}}}$) from the SM predictions as [56]

$$\begin{pmatrix} \Delta\Gamma_{\ell\ell} \\ \Delta\Gamma_{\text{inv}} \\ \Delta A_\ell \\ \Delta M_W \\ \Delta\Gamma_{\ell\nu}^W \end{pmatrix} = M \begin{pmatrix} f_{\Phi e}^{(1)} \\ f_{\Phi L}^{(1)} \\ f_{\Phi L}^{(3)} \\ f_{\Phi,1} \\ -\frac{gg'}{4} f_{BW} \end{pmatrix} \frac{v^2}{\Lambda^2} \quad , \quad (2.35)$$

where $f_{\Phi L}^{(1)}$ ($f_{\Phi e}^{(1)}$) stands for the coefficient of the dimension-six operator $\mathcal{O}_{\Phi L,ij}^{(1)}$ ($\mathcal{O}_{\Phi e,ij}^{(1)}$) assuming flavor universality, and $f_{\Phi L}^{(3)}$ is the corresponding one for $\mathcal{O}_{\Phi L,ij}^{(3)}$ under the same assumption. The matrix M is given by

$$\begin{pmatrix} -\frac{4s_\theta^2}{1-4s_\theta^2+8s_\theta^4} & \frac{2-4s_\theta^2}{1-4s_\theta^2+8s_\theta^4} & \frac{4s_\theta^2(4s_\theta^2-1)}{(c_\theta^2-s_\theta^2)(1-4s_\theta^2+8s_\theta^4)} & -\frac{1-2s_\theta^2-4s_\theta^4}{2(c_\theta^2-s_\theta^2)(1-4s_\theta^2+8s_\theta^4)} & \frac{4c_\theta s_\theta(4s_\theta^2-1)}{(c_\theta^2-s_\theta^2)(1-4s_\theta^2+8s_\theta^4)} \\ 0 & -2 & 0 & -\frac{1}{2} & 0 \\ \frac{2s_\theta^2(s_\theta^2-1/2)^2}{-s_\theta^8+(s_\theta^2-1/2)^4} & -\frac{2s_\theta^4(s_\theta^2-1/2)}{-s_\theta^8+(s_\theta^2-1/2)^4} & -\frac{s_\theta^4}{-s_\theta^8+(s_\theta^2-1/2)^4} & -\frac{c_\theta^2 s_\theta^4}{2(-s_\theta^8+(s_\theta^2-1/2)^4)} & -\frac{c_\theta s_\theta^3}{-s_\theta^8+(s_\theta^2-1/2)^4} \\ 0 & 0 & -\frac{s_\theta^2}{c_\theta^2-s_\theta^2} & -\frac{c_\theta^2}{4(c_\theta^2-s_\theta^2)} & -\frac{c_\theta s_\theta}{c_\theta^2-s_\theta^2} \\ 0 & 0 & -\frac{3s_\theta^2}{c_\theta^2-s_\theta^2} & -\frac{3c_\theta^2}{4(c_\theta^2-s_\theta^2)} & -\frac{3c_\theta s_\theta}{c_\theta^2-s_\theta^2} \end{pmatrix} .$$

It can be verified that the matrix M exhibits two zero eigenvalues, which indicates that two combinations of dimension-six coupling constants can not

³Here, for the sake of simplicity we assume lepton flavor universality.

2.1. LAGRANGIAN FOR AN ELEMENTARY HIGGS

be determined; there are two blind directions. Let us note that in general there are two blind directions even when we consider all LEP observables as well as the quark dimension–six operators. In the current example, the blind directions are

$$f_{\Phi,1} = -4f_{\Phi L}^{(1)} = -2f_{\Phi e}^{(1)} = g'^2 f_{BW} \quad \text{and} \quad f_{\Phi L}^{(3)} = \frac{g^2}{4} f_{BW} . \quad (2.36)$$

This means that, in spite of what it seemed a priori, actually there are two combinations of operators which do not contribute to these precisely measured observables. These are any two linear combinations of

$$\mathcal{O}_{\text{lep blind},1} = g'^2 (\mathcal{O}_{\Phi,1} - \frac{1}{4} \sum_i \mathcal{O}_{\Phi L,ii}^{(1)} - \frac{1}{2} \sum_i \mathcal{O}_{\Phi e,ii}^{(1)}) + \mathcal{O}_{BW} , \quad (2.37)$$

$$\mathcal{O}_{\text{lep blind},2} = \mathcal{O}_{BW} + \sum_i \mathcal{O}_{\Phi L,ii}^{(3)} \frac{g^2}{4} . \quad (2.38)$$

There is a deep relation between operators that do not lead to any tree level contribution to the EWPO and blind directions. In fact, if the elimination using the EOM of one of the operators that do not contribute at the tree level to EWPO leads to a combination of operators that contributes instead, then this combination defines a blind direction. The reason is that it has been proven that operators connected by the EOM lead to the same S –matrix elements [36–39], and therefore this new combination of operators generates the same S –matrix element than the original operator, that, as we have said, has no impact on the EWPO [21]. Let us illustrate this with a concrete example. The bosonic operator $\mathcal{O}_{\Phi,2}$ does not contribute to the EWPO at the tree level since it modifies only the Higgs couplings, therefore, it is a blind operator. Using the EOM, that we show explicitly in Eqs. (2.40)–(2.42), we can write that

$$3g^2 \mathcal{O}_{\Phi,2} = \left[2\mathcal{O}_{BW} + 4\mathcal{O}_W + 2\mathcal{O}_{WW} + \frac{g^2}{2} \sum_i (\mathcal{O}_{\Phi L,ii}^{(3)} + \mathcal{O}_{\Phi Q,ii}^{(3)}) + g^2 \left(\sum_{ij} (y_{ij}^e (\mathcal{O}_{e\Phi,ij})^\dagger + y_{ij}^u \mathcal{O}_{u\Phi,ij} + y_{ij}^d (\mathcal{O}_{d\Phi,ij})^\dagger + \text{h.c.}) - \frac{\partial V(h)}{\partial h} \right) \right] .$$

Hence the right hand side of the last equation defines a blind direction in the EWPO. In fact, only the operators \mathcal{O}_{BW} and $\sum_i \mathcal{O}_{\Phi L,ii}^{(3)}$ in the right hand side of Eq. (2.39) contribute to the above leptonic observables, therefore the effect of $\mathcal{O}_{\Phi,2}$ is equivalent to, for these observables,

$$\frac{2}{3g^2} \left(\mathcal{O}_{BW} + \frac{g^2}{4} \sum_i \mathcal{O}_{\Phi L,ii}^{(3)} \right) , \quad (2.39)$$

that corresponds exactly to the blind direction in Eq. (2.38).

After describing the main contributions of the different dimension–six operators to the phenomenology of the Higgs boson, to TGV’s and to EWPO we proceed to describe our choice of the basis.

2.1.4 The right of choice

In the effective Lagrangian framework not all operators at a given order are independent, as they can be related by the use of the classical EOM of the SM fields. As we have said, the invariance of the physical observables under the associated operator redefinitions is guaranteed as operators connected by the EOM lead to the same S –matrix elements [36–39]. This equivalence gives us the freedom to choose the basis of dimension–six operators to be analyzed depending on the approach that we take. In general terms, we can distinguish two different approaches depending on the assumptions that we make on the high energy theory completing the SM. On the one hand, in a top–bottom approach, one starts from the full theory and integrates out heavy degrees of freedom to match the coefficients of the higher dimension operators at low energies. Thus, in this case, it is convenient not to choose a minimal set of operators in order to guarantee that all the operators generated by the underlying theory can be easily identified [57]. On the other hand, in a bottom–up approach, one uses the effective Lagrangian to obtain bounds on generic extensions of the SM. Here the details of the high energy theory remain unknown. Hence, in this approach one must choose instead a minimum operator basis to avoid parameter combinations that can not be probed.

This generic overview can also be applied to the study of the Higgs couplings. In our case at hand, we have to take into account the SM EOM which imply that not all the operators in Eqs. (2.2) and (2.23) are independent. In particular the EOM for the Higgs field and the EW gauge bosons lead to three relations between the operators:

$$2\mathcal{O}_{\Phi,2} + 2\mathcal{O}_{\Phi,4} = \sum_{ij} \left(y_{ij}^e \mathcal{O}_{e\Phi,ij}^\dagger + y_{ij}^u \mathcal{O}_{u\Phi,ij} + y_{ij}^d \mathcal{O}_{d\Phi,ij}^\dagger + \text{h.c.} \right) - \frac{\partial V(h)}{\partial h}, \quad (2.40)$$

$$2\mathcal{O}_B + \mathcal{O}_{BW} + \mathcal{O}_{BB} + g'^2 \left(\mathcal{O}_{\Phi,1} - \frac{1}{2} \mathcal{O}_{\Phi,2} \right) = -\frac{g'^2}{12} \sum_i \left(-3\mathcal{O}_{\Phi L,ii}^{(1)} + \mathcal{O}_{\Phi Q,ii}^{(1)} - 6\mathcal{O}_{\Phi e,ii}^{(1)} + 4\mathcal{O}_{\Phi u,ii}^{(1)} - 2\mathcal{O}_{\Phi d,ii}^{(1)} \right), \quad (2.41)$$

2.1. LAGRANGIAN FOR AN ELEMENTARY HIGGS

$$2\mathcal{O}_W + \mathcal{O}_{BW} + \mathcal{O}_{WW} + g^2 \left(\mathcal{O}_{\Phi,4} - \frac{1}{2} \mathcal{O}_{\Phi,2} \right) = -\frac{g^2}{4} \sum_i \left(\mathcal{O}_{\Phi L,ii}^{(3)} + \mathcal{O}_{\Phi Q,ii}^{(3)} \right) . \quad (2.42)$$

Hence, these equations allow for the elimination of three of the operators listed in Eqs. (2.2) and (2.23). At this point we are faced with the decision of which operators to leave in the basis to be used in the analysis of the Higgs data; the two different approaches can be followed in doing so. Again, in a top–bottom approach in which some *a priori* knowledge is assumed about the BSM theory one can use this theoretical prejudice to choose the basis. For example if the UV completion of the SM is a given gauge theory, it is possible to predict whether a given operator is generated at tree level or at loop level [58]. One may then be tempted to keep the tree level ones in the basis, as larger coefficients are expected [41]. However, in the absence of such illumination it is impossible to know if the low energy theory would contain any tree level generated operator; for instance see [54] for a model whose low energy theory contains only loop induced operators. Furthermore, caution should be used when translating the bounds on the effective operators into the scale of the new physics, since after the use of EOM coefficients of operators generated at loop level can, in fact, originate from tree level operators eliminated using the EOM and vice-versa [57]. Actually, all choices of basis suffer from this problem!⁴

In this thesis we follow the bottom–up approach. Our purpose is to constrain generically any extension of the SM without relying on any specific theory. Thus we choose a minimum set of operators in order to parametrize all possible contributions to the Higgs interactions avoiding the addition of redundant operators and extra theoretical assumptions. In principle, given the proof of the equivalence of the S –matrix elements the determination of physical observables like production cross sections or decay branching ratios would be independent of the choice of basis. Nevertheless, independent does not mean equivalent in real life. For this reason in this thesis we advocate that in the absence of theoretical prejudices it turns out to be beneficial to use a basis chosen by the data: “Power to the Data”. With this we mean that the sensible (and certainly technically convenient) choice is to leave in the basis to be used to study Higgs results those operators which are more directly related to the existing data, in particular to the bulk of precision EW measurements which have helped us to establish the SM.

⁴In addition, in the cases like the current Higgs analyses where the experimental data has a much higher sensitivity to dimension–six operators which are understood to be generated at the loop level in this class of theories– compensating then the assumed suppression of the coefficients of these operators with respect to the rest– a rigorous and consistent analysis should also take into account the contributions of the tree level generated dimension–eight operators.

Thus using the relations in Eqs. (2.40)–(2.42), that allow for the elimination of three of the dimension–six operators we have presented, our purpose is to choose a basis that takes full advantage of the Higgs data, TGV searches and EWPO. This means that we want to keep all the operators contributing to TGV’s and at least one operator per each new Lorentz structure in Eq. (2.19). And as we have described in the previous Subsection, in order to take advantage of the EW precision measurements we should avoid the existence of blind directions in the parameter space. This can be achieved using the EOM to eliminate some of the operators that contribute at tree level to the EWPO in such a way that the new form of the matrix M in Eq. (2.35), relating the observables and the dimension–six operators contributing to them, does not have vanishing determinant. We accomplish this by eliminating two combinations of $\mathcal{O}_{\Phi L,ii}^{(1)}$ and $\mathcal{O}_{\Phi L,ii}^{(3)}$ using Eqs. (2.41)–(2.42). Furthermore we use Eq. (2.40) to remove $\mathcal{O}_{\Phi,4}$. This way our choice for the operator basis allows us to take full advantage of the EWPO, as well as, of data on TGV’s, while keeping in the basis all the different kinematic structures that appear in Eq. (2.19).

With this choice, the dimension–six operators considered for the Higgs analyses are

$$\left\{ \mathcal{O}_{GG}, \mathcal{O}_{BB}, \mathcal{O}_{WW}, \mathcal{O}_{BW}, \mathcal{O}_B, \mathcal{O}_W, \mathcal{O}_{\Phi,2}, \mathcal{O}_{\Phi,1}, \mathcal{O}_{f\Phi}, \mathcal{O}_{\Phi f}^{(1)}, \mathcal{O}_{\Phi f}^{(3)} \right\}, \quad (2.43)$$

except for $\mathcal{O}_{\Phi,L}^{(1)}$ and $\mathcal{O}_{\Phi,L}^{(3)}$, that are removed using EOM as we have described. The dimension–six operators in Eq. (2.43) constitute the basis of operators relevant for the Higgs phenomenology to be analyzed using the existing experimental data.

Before starting the proper analysis of the Higgs couplings at the LHC, we reduce the number of dimension–six parameters relevant for the analysis. First we use the available pre–LHC experimental information in order to reduce the number of relevant parameters. Second, some of the dimension–six operators whose coefficients are not strongly constrained may still be irrelevant for Higgs physics at the LHC given the current accessible experimental channels. This can be summarized in the following three points:

- Taking into account the bulk of precision data on Z and W fermionic currents and oblique corrections that we have discussed in the previous Subsection, the coefficients of all operators that modify these couplings are so constrained that they will have no impact in the Higgs physics. This means that, in addition to the operators that we have removed from the final basis using the EOM, we do not consider the operators $\mathcal{O}_{\Phi f}^{(1)}$, $\mathcal{O}_{\Phi f}^{(3)}$, \mathcal{O}_{BW} and $\mathcal{O}_{\Phi,1}$ in our analyses.
- Additional bounds on low energy flavor–changing interactions impose strong bounds on off–diagonal Yukawa couplings [59–65]. There could

2.2. ANALYSIS FRAMEWORK

still be sizable flavor changing effects in $\bar{\tau}e$ and $\bar{\tau}\mu$ [62–64] which would be, however, not relevant to the present analyses. Consequently we also discard from our basis the flavor changing $\mathcal{O}_{f\Phi,i\neq j}$.

- Flavor diagonal $\mathcal{O}_{f\Phi,ii}$ from first and second generations affect the present Higgs data only via their contribution to the Higgs–gluon–gluon and Higgs– γ – γ vertices at one loop. The loop form factors are very suppressed for light fermions and correspondingly their effect is totally negligible in the analysis. Consequently, we keep only the fermionic operators $\mathcal{O}_{e\Phi,33}$, $\mathcal{O}_{u\Phi,33}$ and $\mathcal{O}_{d\Phi,33}$.

Summarizing, after using EOM, considering the constraints from EWPO and removing the operators that are simply irrelevant given the current existing Higgs data, the final effective Lagrangian that we use in our analyses is

$$\begin{aligned} \mathcal{L}_{eff} = & -\frac{\alpha_s v}{8\pi} \frac{f_g}{\Lambda^2} \mathcal{O}_{GG} + \frac{f_{\Phi,2}}{\Lambda^2} \mathcal{O}_{\Phi,2} + \frac{f_{BB}}{\Lambda^2} \mathcal{O}_{BB} + \frac{f_{WW}}{\Lambda^2} \mathcal{O}_{WW} + \frac{f_B}{\Lambda^2} \mathcal{O}_B + \frac{f_W}{\Lambda^2} \mathcal{O}_W \\ & + \frac{f_\tau}{\Lambda^2} \mathcal{O}_{e\Phi,33} + \frac{f_{\text{bot}}}{\Lambda^2} \mathcal{O}_{d\Phi,33} + \frac{f_{\text{top}}}{\Lambda^2} \mathcal{O}_{u\Phi,33} . \end{aligned} \quad (2.44)$$

Notice that with this choice of basis all of the dimension–six operators considered contribute to the Higgs–gauge boson and Higgs–fermion couplings at tree level. Before moving to the description of the analysis framework there is a final remark regarding the top Yukawa–like dimension–six operator $\mathcal{O}_{u\Phi,33}$ to be considered. The tree level information on $h\bar{t}t$ from associate production has still very large errors. Thus, quantitatively the effects of the parameter f_{top} enter mainly via its contribution to the one–loop Higgs couplings to photon pairs and gluon pairs. These contributions can be absorbed in the redefinition of the rest of parameters contributing to these vertices, f_g and $f_{WW} + f_{BB}$, and therefore, we set $f_{\text{top}} \equiv 0$. In the future, when a larger luminosity is accumulated, it will be necessary to introduce f_{top} as one of the parameters in the fit.

2.2 Analysis framework

In this Section we describe the statistical analysis that we perform to study the Higgs couplings. We present the statistical discriminant built to analyze the Higgs interactions, and we list the data included in the analysis. In order to obtain the present constraints on the coefficients of the operators in Eq. (2.44) we start performing a chi–square test based on the available data on the signal strength (μ) from Tevatron and LHC (at both 7 TeV and 8 TeV), from the searches for the Higgs channels presented in Tables 2.1, 2.2 and 2.3. The details of this first part of the analysis are treated in Subsection 2.2.1. In addition, we further combine in the chi–square the data

coming from the most precise determination of triple EW gauge boson couplings, as well as, the one-loop constraints coming from EWPO on the basis of dimension-six operators considered. The details of the combinations of these additional data sets are described in Subsections 2.2.2 and 2.2.3.

2.2.1 Higgs data: signal strengths

In order to analyze the Higgs data coming from both LHC and Tevatron experimental analyses we build a chi-square function based on the signal strengths of the different available channels. The signal strength is defined as the measured cross section divided by the expected cross section in the SM. For this first part of the analysis, and given the accessible public data, we assume that the correlations between the different channels are negligible, except for the theoretical uncertainties which are treated with the pull method [81, 82] in order to account for their correlations. The chi-square can be schematically written as

$$\chi^2 = \min_{\xi_{\text{pull}}} \sum_j \frac{(\mu_j - \mu_j^{\text{exp}})^2}{\sigma_j^2} + \sum_{\text{pull}} \left(\frac{\xi_{\text{pull}}}{\sigma_{\text{pull}}} \right)^2, \quad (2.45)$$

where j stand for the different experimental channels considered. We present the different Tevatron and LHC at 7 TeV and 8 TeV data points in Tables 2.1, 2.2 and 2.3. In Eq. (2.45) we denote the theoretically expected signal as μ_j , the observed best fit values as μ_j^{exp} and the corresponding errors as σ_j . As we can see from these Tables the errors are not symmetric in some of the channels, showing a deviation from a Gaussian behavior as expected from the still low statistics. In our calculations we make the errors in each channel symmetric by taking

$$\sigma_j = \sqrt{\frac{(\sigma_j^+)^2 + (\sigma_j^-)^2}{2}}. \quad (2.46)$$

Concerning the theoretical uncertainties, the largest ones are associated with the gluon fusion production subprocess and to account for them we introduce two pull factors, one for the Tevatron uncertainty (ξ_g^T), and one to account for both the LHC at 7 and 8 TeV uncertainties (ξ_g^L). We consider that the errors associated with these pulls are $\sigma_g^T = 0.43$ and $\sigma_g^L = 0.15$ [83]. We introduce as well two pull factors to account for the theoretical uncertainties associated with vector boson fusion (VBF) cross sections, one for Tevatron (ξ_{VBF}^T) with associated error $\sigma_{VBF}^T = 0.035$, and one for LHC at both 7 and 8 TeV (ξ_{VBF}^L) with associated error $\sigma_{VBF}^L = 0.03$ [83]. Finally theoretical uncertainties from associated production (VH) cross sections are included with two more pulls, one for Tevatron (ξ_{VH}^T) with associated error $\sigma_{VH}^T = 0.075$, and one for LHC at both 7 and 8 TeV (ξ_{VH}^L) with associated error

2.2. ANALYSIS FRAMEWORK

$\sigma_{VH}^L = 0.05$ [83]. These pulls modify the signal strength predictions as we describe in the following.

In order to predict the expected signal strengths in the presence of the dimension–six operators we need to include their effect in both the production channels, as well as, in the decay branching ratios. From the expressions in the previous Section it is straight forward to include them in these observables at tree level. Concerning the higher order corrections we assume that the corresponding “ K -factors” (defined as the ratios of the higher order predictions divided by the predictions at the leading order) are the same for the SM than for the new operator contributions. In this approximation we then write:

$$\sigma_Y^{\text{ano}} = \frac{\sigma_Y^{\text{ano}}}{\sigma_Y^{\text{SM}}}\Bigg|_{\text{tree}} \sigma_Y^{\text{SM}}\Big|_{\text{soa}} \quad , \quad (2.47)$$

$$\Gamma^{\text{ano}}(h \rightarrow X) = \frac{\Gamma^{\text{ano}}(h \rightarrow X)}{\Gamma^{\text{SM}}(h \rightarrow X)}\Bigg|_{\text{tree}} \Gamma^{\text{SM}}(h \rightarrow X)\Big|_{\text{soa}} \quad , \quad (2.48)$$

with the superscript *ano* (*SM*) standing for the value of the observable considering both the anomalous and SM interactions (only the pure SM contributions without dimension–six operators) and we label as *soa* the value for the state–of–the–art SM calculations, $\sigma_Y^{\text{SM}}\Big|_{\text{soa}}$ and $\Gamma^{\text{SM}}(h \rightarrow X)\Big|_{\text{soa}}$, presented in [83]. The subscript *Y* refers to the different production modes: gluon fusion (*gg*), vector boson fusion (*VBF*), associated production (*VH*) and top–associated production (*t \bar{t} H*), while *X* refers to the final state in the given decay mode. As we have explained in the previous Section, one of the assumptions in our effective Lagrangian approach is that there are not undiscovered light states present at the low energies that couple to the Higgs boson. This means that we do not include in our analyses an eventual invisible decay of the Higgs particle [84,85]. Thus, the total width is obtained by summing over the decays into only the SM particles. In order to evaluate the relevant tree level cross sections we use the package MadGraph5 [86] with the anomalous Higgs interactions introduced using the package FeynRules [87]. We further cross check our results using two alternative packages, COMPHEP [88,89] and VBFNLO [90].

With all these considerations, for any final state *X* listed in Tables 2.1, 2.2 and 2.3 we can write the theoretical signal strength as

$$\mu_X = \frac{\epsilon_{gg}^X \sigma_{gg}^{\text{*ano}} + \epsilon_{VBF}^X \sigma_{VBF}^{\text{*ano}} + \epsilon_{WH}^X \sigma_{WH}^{\text{*ano}} + \epsilon_{ZH}^X \sigma_{ZH}^{\text{*ano}} + \epsilon_{t\bar{t}H}^X \sigma_{t\bar{t}H}^{\text{*ano}}}{\epsilon_{gg}^X \sigma_{gg}^{\text{SM}} + \epsilon_{VBF}^X \sigma_{VBF}^{\text{SM}} + \epsilon_{WH}^X \sigma_{WH}^{\text{SM}} + \epsilon_{ZH}^X \sigma_{ZH}^{\text{SM}} + \epsilon_{t\bar{t}H}^X \sigma_{t\bar{t}H}^{\text{SM}}} \otimes \frac{\text{Br}^{\text{ano}}[h \rightarrow X]}{\text{Br}^{\text{SM}}[h \rightarrow X]} \quad , \quad (2.49)$$

where

$$\sigma_Y^{\text{*ano}} = \sigma_Y^{\text{ano}}(1 + \xi_Y) \quad , \quad (2.50)$$

with *Y* (*X*) standing again for the production mode (final state). Thus ξ_g , ξ_{VBF} and ξ_{VH} are the pulls associated with the gluon fusion, vector boson fusion and associated production cross section uncertainties (see Eq. (2.45)).

| Channel | $\mu^{\text{exp}} \begin{smallmatrix} +\sigma^+ \\ -\sigma^- \end{smallmatrix}$ | Experiment |
|--|---|--------------------------|
| $p\bar{p} \rightarrow W^+W^-$ | $0.94^{+0.85}_{-0.83}$ | CDF & DØ [66] |
| $p\bar{p} \rightarrow \tau\bar{\tau}$ | $1.68^{+2.28}_{-1.68}$ | CDF & DØ [66] |
| $p\bar{p} \rightarrow b\bar{b}$ | $1.59^{+0.69}_{-0.72}$ | CDF & DØ [66] |
| $p\bar{p} \rightarrow \gamma\gamma$ | $5.97^{+3.39}_{-3.12}$ | CDF & DØ [66] |
| $pp \rightarrow \tau\bar{\tau}$ | $0.7^{+0.7}_{-0.7}$ | ATLAS @ 7 and 8 TeV [67] |
| $pp \rightarrow b\bar{b}$ | $-2.1^{+1.4}_{-1.4}$ | ATLAS @ 7 TeV [68] |
| $pp \rightarrow b\bar{b}$ | $0.6^{+0.7}_{-0.7}$ | ATLAS @ 8 TeV [68] |
| $pp \rightarrow ZZ^* \rightarrow \ell^+\ell^-\ell^+\ell^-$ | $1.7^{+0.5}_{-0.4}$ | ATLAS @ 7 and 8 TeV [69] |
| $pp \rightarrow WW^* \rightarrow \ell^+\nu\ell^-\bar{\nu}$ | $0.0^{+0.6}_{-0.6}$ | ATLAS @ 7 TeV [70] |
| $pp \rightarrow WW^* \rightarrow \ell^+\nu\ell^-\bar{\nu}$ | $1.26^{+0.35}_{-0.35}$ | ATLAS @ 8 TeV [70] |
| $pp \rightarrow Z\gamma \rightarrow \ell^+\ell^-\gamma$ | $4.7^{+6.89}_{-6.89}$ | ATLAS @ 7 and 8 TeV [71] |
| $pp \rightarrow \tau\bar{\tau}$ | $1.1^{+0.4}_{-0.4}$ | CMS @ 7 and 8 TeV [72] |
| $pp \rightarrow b\bar{b}$ | $1.0^{+0.49}_{-0.49}$ | CMS @ 7 and 8 TeV [73] |
| $pp \rightarrow b\bar{b}$ VBF | $0.7^{+1.4}_{-1.4}$ | CMS @ 8 TeV [74] |
| $pp \rightarrow ZZ^* \rightarrow \ell^+\ell^-\ell^+\ell^-$ | $0.91^{+0.30}_{-0.24}$ | CMS @ 7 and 8 TeV [75] |
| $pp \rightarrow WW^* \rightarrow \ell^+\nu\ell^-\bar{\nu}$ | $0.91^{+0.44}_{-0.44}$ | CMS @ 7 TeV [76] |
| $pp \rightarrow WW^* \rightarrow \ell^+\nu\ell^-\bar{\nu}$ | $0.71^{+0.22}_{-0.22}$ | CMS @ 8 TeV [76] |
| $pp \rightarrow Z\gamma \rightarrow \ell^+\ell^-\gamma$ | $-0.5^{+4.87}_{-4.87}$ | CMS @ 7 and 8 TeV [77] |

Table 2.1: Results included in the analysis for the Higgs decay modes listed, except for the $\gamma\gamma$ channels.

| Channel | $\mu^{\text{exp}} \begin{smallmatrix} +\sigma^+ \\ -\sigma^- \end{smallmatrix}$ | |
|-------------------------------------|---|-------------------------|
| | 7 TeV | 8 TeV |
| Unconverted central, low p_{T_t} | $0.52^{+1.45}_{-1.40}$ | $0.89^{+0.74}_{-0.71}$ |
| Unconverted central, high p_{T_t} | $0.23^{+1.98}_{-1.98}$ | $0.95^{+1.08}_{-0.92}$ |
| Unconverted rest, low p_{T_t} | $2.56^{+1.69}_{-1.69}$ | $2.52^{+0.92}_{-0.77}$ |
| Unconverted rest, high p_{T_t} | $10.47^{+3.66}_{-3.72}$ | $2.71^{+1.35}_{-1.14}$ |
| Converted central, low p_{T_t} | $6.10^{+2.62}_{-2.62}$ | $1.39^{+1.05}_{-0.95}$ |
| Converted central, high p_{T_t} | $-4.36^{+1.80}_{-1.80}$ | $2.0^{+1.54}_{-1.26}$ |
| Converted rest, low p_{T_t} | $2.73^{+1.98}_{-1.98}$ | $2.22^{+1.17}_{-0.99}$ |
| Converted rest, high p_{T_t} | $-1.57^{+2.91}_{-2.91}$ | $1.29^{+1.32}_{-1.26}$ |
| Converted transition | $0.41^{+3.55}_{-3.66}$ | $2.83^{+1.69}_{-1.60}$ |
| 2-jets / 2-jets high mass tight | $2.73^{+1.92}_{-1.86}$ | $1.63^{+0.83}_{-0.68}$ |
| 2-jets high mass loose | — | $2.77^{+1.79}_{-1.39}$ |
| 2-jets low mass | — | $0.338^{+1.72}_{-1.48}$ |
| E_T^{miss} significance | — | $2.99^{+2.74}_{-2.15}$ |
| One Lepton | — | $2.71^{+2.00}_{-1.66}$ |

Table 2.2: $H \rightarrow \gamma\gamma$ results from ATLAS [78, 79] included in the analysis.

2.2. ANALYSIS FRAMEWORK

| Channel | $\mu^{\text{exp}} \begin{smallmatrix} +\sigma^+ \\ -\sigma^- \end{smallmatrix}$ | |
|--|---|---|
| | 7 TeV | 8 TeV |
| $pp \rightarrow \gamma\gamma$ Untagged 3 | $1.48^{+1.65}_{-1.60}$ | $-0.364^{+0.85}_{-0.82}$ |
| $pp \rightarrow \gamma\gamma$ Untagged 2 | $0.024^{+1.24}_{-1.24}$ | $0.291^{+0.49}_{-0.46}$ |
| $pp \rightarrow \gamma\gamma$ Untagged 1 | $0.194^{+0.99}_{-0.95}$ | $0.024^{+0.703}_{-0.655}$ |
| $pp \rightarrow \gamma\gamma$ Untagged 0 | $3.83^{+2.01}_{-1.67}$ | $2.16^{+0.95}_{-0.75}$ |
| $pp \rightarrow \gamma\gamma jj$ | $4.19^{+2.30}_{-1.77}$ | loose $0.80^{+1.09}_{-0.99}$ tight $0.291^{+0.679}_{-0.606}$ |
| $pp \rightarrow \gamma\gamma$ MET | — | $1.89^{+2.62}_{-2.28}$ |
| $pp \rightarrow \gamma\gamma$ Electron | — | $-0.655^{+2.76}_{-1.96}$ |
| $pp \rightarrow \gamma\gamma$ Muon | — | $0.412^{+1.79}_{-1.38}$ |

Table 2.3: $H \rightarrow \gamma\gamma$ results from CMS [80] included in the analysis.

The weight of the different production channels to each final state X are encoded in the parameters ϵ_Y^X with $Y = VBF, gg, WH, ZH$ and $t\bar{t}H$. The experimental analyses are usually separated into different subcategories, each of them with cuts tailored to enhance and/or suppress different production modes. This benefits the chi-square analysis, giving a richer variety of efficiency combinations.

The search for Higgs decaying into $b\bar{b}$ pairs takes place through Higgs production in association with a W or a Z , so in this case

$$\epsilon_{gg}^{b\bar{b}} = \epsilon_{VBF}^{b\bar{b}} = \epsilon_{t\bar{t}H}^{b\bar{b}} = 0, \quad \epsilon_{WH}^{b\bar{b}} = \epsilon_{ZH}^{b\bar{b}} = 1, \quad (2.51)$$

except for the recent CMS analysis [74], where the main production mode is assumed to be VBF

$$\epsilon_{gg}^{b\bar{b}} = \epsilon_{WH}^{b\bar{b}} = \epsilon_{ZH}^{b\bar{b}} = \epsilon_{t\bar{t}H}^{b\bar{b}} = 0, \quad \epsilon_{VBF}^{b\bar{b}} = 1. \quad (2.52)$$

The ATLAS and CMS analyses of the 7 and 8 TeV data sets separate the $\gamma\gamma$ signal into different categories and the contribution of each production mechanism to a given category is presented in Table 6 of ATLAS [78], Table 1 of ATLAS [79] and Table 2 of CMS [80]. We summarize them in Tables 2.4 and 2.5.

With the exception of the above processes, all other channels $X = WW^*, ZZ^*, \tau\tau$, and $Z\gamma$ are treated as inclusive,

$$\epsilon_{gg}^X = \epsilon_{VBF}^X = \epsilon_{t\bar{t}H}^X = \epsilon_{WH}^X = \epsilon_{ZH}^X = 1. \quad (2.53)$$

For some of the final states considered the available LHC 8 TeV data has been presented combined with the 7 TeV results. Given the limited available information on errors and correlations, we construct the expected theoretical signal strength as an average of the expected signal strengths for

| Channel | $\epsilon_{gg}^{\gamma\gamma}$ | $\epsilon_{VBF}^{\gamma\gamma}$ | $\epsilon_{WH}^{\gamma\gamma}$ | $\epsilon_{ZH}^{\gamma\gamma}$ | $\epsilon_{t\bar{t}H}^{\gamma\gamma}$ |
|---|--------------------------------|---------------------------------|--------------------------------|--------------------------------|---------------------------------------|
| Unconverted central, low p_{T_t} | 1.06 | 0.579 | 0.550 | 0.555 | 0.355 |
| | 1.07 | 0.572 | 0.448 | 0.452 | 0.343 |
| Unconverted central, high p_{T_t} | 0.760 | 2.27 | 3.03 | 3.16 | 4.26 |
| | 0.906 | 1.80 | 1.31 | 1.41 | 2.40 |
| Unconverted rest, low p_{T_t} | 1.06 | 0.564 | 0.612 | 0.610 | 0.355 |
| | 1.06 | 0.572 | 0.512 | 0.566 | 0.171 |
| Unconverted rest, high p_{T_t} | 0.748 | 2.33 | 3.30 | 3.38 | 3.19 |
| | 0.892 | 1.90 | 1.50 | 1.58 | 1.88 |
| Converted central, low p_{T_t} | 1.06 | 0.578 | 0.581 | 0.555 | 0.357 |
| | 1.07 | 0.572 | 0.416 | 0.509 | 0.343 |
| Converted central, high p_{T_t} | 0.761 | 2.21 | 3.06 | 3.16 | 4.43 |
| | 0.901 | 1.80 | 1.38 | 1.53 | 2.57 |
| Converted rest, low p_{T_t} | 1.06 | 0.549 | 0.612 | 0.610 | 0.355 |
| | 1.06 | 0.586 | 0.512 | 0.566 | 0.171 |
| Converted rest, high p_{T_t} | 0.747 | 2.31 | 3.36 | 3.27 | 3.19 |
| | 0.887 | 1.86 | 1.66 | 1.70 | 1.88 |
| Converted transition | 1.02 | 0.752 | 1.01 | 0.943 | 0.532 |
| | 1.04 | 0.787 | 0.704 | 0.735 | 0.343 |
| 2-jets / 2-jets high mass tight | 0.257 | 11.1 | 0.122 | 0.111 | 0.177 |
| | 0.272 | 10.9 | 0.032 | 0.056 | 0.0 |
| 2-jets high mass loose (only 8 TeV) | 0.514 | 7.74 | 0.160 | 0.170 | 0.171 |
| 2-jets low mass (only 8 TeV) | 0.550 | 0.429 | 9.51 | 9.73 | 3.25 |
| E_T^{miss} significance (only 8 TeV) | 0.047 | 0.072 | 11.4 | 26.9 | 20.7 |
| One lepton (only 8 TeV) | 0.025 | 0.086 | 20.2 | 8.71 | 31.9 |

Table 2.4: Weight of each production mechanism for the different $\gamma\gamma$ categories in the ATLAS analyses of the 7 TeV data (upper values) and 8 TeV (lower values). For the 8 TeV analysis three new exclusive categories enriched in vector boson associated production were added with the 2-jets low mass (one lepton) [E_T^{miss} significance] category being built to select hadronic (leptonic) [invisible] decays of the associated vector boson.

the COM energies of 7 and 8 TeV. We weight the contributions by the total number of events expected at each energy in the framework of the SM, *i.e.* given a final state X we evaluate

$$\mu_X^{\text{comb}} = \frac{\mu_X^{7\text{TeV}} \sigma_X^{SM,7\text{TeV}} \mathcal{L}_{7\text{TeV}} + \mu_X^{8\text{TeV}} \sigma_X^{SM,8\text{TeV}} \mathcal{L}_{8\text{TeV}}}{\sigma_X^{SM,7\text{TeV}} \mathcal{L}_{7\text{TeV}} + \sigma_X^{SM,8\text{TeV}} \mathcal{L}_{8\text{TeV}}}, \quad (2.54)$$

where $\mathcal{L}_{7(8)\text{TeV}}$ stands for the integrated luminosity accumulated at 7 (8) TeV in the channel being analyzed. We indicate in Table 2.1 that the data has been combined by “@ 7 and 8 TeV”.

The results that we present in this thesis, based on the experimental

2.2. ANALYSIS FRAMEWORK

| Channel | $\epsilon_{gg}^{\gamma\gamma}$ | $\epsilon_{VBF}^{\gamma\gamma}$ | $\epsilon_{VH}^{\gamma\gamma}$ | $\epsilon_{t\bar{t}H}^{\gamma\gamma}$ |
|---|--------------------------------|---------------------------------|--------------------------------|---------------------------------------|
| $pp \rightarrow \gamma\gamma$ Untagged 3 | 1.04 | 0.637 | 0.808 | 0.355 |
| | 1.06 | 0.558 | 0.675 | 0.343 |
| $pp \rightarrow \gamma\gamma$ Untagged 2 | 1.04 | 0.637 | 0.769 | 0.532 |
| | 1.05 | 0.629 | 0.715 | 0.685 |
| $pp \rightarrow \gamma\gamma$ Untagged 1 | 1.00 | 0.897 | 1.10 | 0.887 |
| | 0.954 | 1.20 | 1.45 | 1.71 |
| $pp \rightarrow \gamma\gamma$ Untagged 0 | 0.702 | 2.43 | 3.69 | 5.50 |
| | 0.833 | 1.66 | 2.66 | 4.45 |
| $pp \rightarrow \gamma\gamma jj$ (7 TeV) | 0.306 | 10.5 | 0.118 | 0 |
| $pp \rightarrow \gamma\gamma jj$ loose (8 TeV) | 0.535 | 7.31 | 0.348 | 0.856 |
| $pp \rightarrow \gamma\gamma jj$ tight (8 TeV) | 0.236 | 11.3 | 0.061 | 0.171 |
| $pp \rightarrow \gamma\gamma, \mu$ -tag (8 TeV) | 0.0 | 0.029 | 16.2 | 35.6 |
| $pp \rightarrow \gamma\gamma, e$ -tag (8 TeV) | 0.013 | 0.057 | 16.1 | 33.7 |
| $pp \rightarrow \gamma\gamma, E_T^{\text{miss}}$ -tag (8 TeV) | 0.241 | 0.358 | 13.2 | 20.2 |

Table 2.5: Weight of each production mechanism for the different $\gamma\gamma$ categories in the CMS analyses of the 7 TeV data (upper values) and 8 TeV (lower values). $\epsilon_{VH}^{\gamma\gamma} = \epsilon_{ZH}^{\gamma\gamma} = \epsilon_{WH}^{\gamma\gamma}$ in this case. For the $pp \rightarrow \gamma\gamma jj$ category the 8 TeV data was divided in two independent subsamples labeled as “loose” and “tight” according to the requirement on the minimum transverse momentum of the softer jet and the minimum dijet invariant mass. For the 8 TeV analysis three new exclusive categories were added enriched in vector boson associated production: μ -tag, e-tag and E_T^{miss} -tag.

analyses in Tables 2.1, 2.2 and 2.3, rely on almost the full 7 and 8 TeV LHC data sets. These correspond to around $\sim 5 \text{ fb}^{-1}$ from each 7 TeV Higgs analysis in addition to almost the complete 8 TeV data sets, that for each of the different Higgs channels amount to $\sim 20 \text{ fb}^{-1}$ more. Altogether, the complete LHC data sets contain almost $\sim 25 \text{ fb}^{-1}$ of data per Higgs channel, which added to the Tevatron analyses, form a set of 56 data points whose overall precision already allows to perform a consistent study of the Higgs boson interactions. So aside of hypothetical improvements on some experimental analyses, the results that we present here form a robust picture of the status of our knowledge of Higgs couplings that will hold until the LHC starts its operation at 13 TeV.

Before proceeding to present the results a final remark is in order. In our analysis we implicitly assume that the detection efficiencies with respect to the cuts in each of the experimental analyses, ϵ_V^X in Eq. (2.49), are the same for the contributions from the dimension–six operators than the ones for the SM Higgs boson Lagrangian. This is an important approximation in the analysis as it means that the effects associated to the new kinematic structures generated by the anomalous operators, see Eq. (2.19)

(which generically can lead to differences in the kinematic distributions of the final states compared to the SM ones) are neglected for the efficiencies. A full simulation of the Higgs couplings taking into account all the new Lorentz structures introduced by the dimension–six operators in the different vertices and the corresponding kinematic distributions might increase the current sensitivity on the anomalous couplings and it could also allow for breaking degeneracies between the operators. Especially between the ones that only lead to an overall shift of the strength of the SM vertices and the ones that introduce new Lorentz structures (see [91–93] for related work). Nevertheless, at present, there is not enough information outside of the experimental collaborations to perform such analysis including all the different kinematic information.

2.2.2 Triple gauge boson vertex data

As we have pointed out in the previous Section, a very interesting source of data to study the dimension–six operators originates from the contribution of some of them to $\gamma W^+ W^-$ and $Z W^+ W^-$ TGV’s. Motivated by these contributions, we combine in this Subsection the results of Higgs data from Tevatron and LHC that we have described in the previous Subsection with those from the most precise determination of TGV’s.

From the final basis of dimension–six operators in Eq. (2.44), both \mathcal{O}_W and \mathcal{O}_B contribute to the TGV’s, as can be seen in Eqs. (2.31) and (2.32), while the contributions from \mathcal{O}_{BW} and $\mathcal{O}_{\Phi,1}$ are negligible after imposing the constraints on the corresponding coefficients on their tree level contribution to the S and T parameters (see Eqs. (2.34) and (2.63)). Focusing on the three parameters that receive contributions from \mathcal{O}_W and \mathcal{O}_B we have

$$\Delta g_1^Z = \frac{g^2 v^2}{8c^2 \Lambda^2} f_W, \quad \Delta \kappa_\gamma = \frac{g^2 v^2}{8\Lambda^2} (f_W + f_B), \quad \Delta \kappa_Z = -\frac{s_\theta^2}{c_\theta^2} \Delta \kappa_\gamma + \Delta g_1^Z. \quad (2.55)$$

Thus it is clear that only two of the three anomalous TGV’s are independent in this framework. As a consequence, for consistency with our multi-parameter analysis, we need to include the results of the experimental collider measurements of TGV’s under these relations. From all the references that we have listed [40, 42–51], it suffices now to consider only the results from LEP analysis [42], as they are still the most precise ones. The LEP analysis was performed in terms of g_1^Z , κ_Z and κ_γ as determined by the relations in Eq. (2.55) (assuming $\lambda_\gamma = \lambda_Z = 0$ as well). The precise measurements of TGV’s they obtained are

$$\begin{aligned} \kappa_\gamma^{\text{exp}} &= 0.984_{-0.049}^{+0.049}, \\ g_1^{Z,\text{exp}} &= 1.004_{-0.025}^{+0.024}, \end{aligned} \quad (2.56)$$

with a correlation factor $\rho = 0.11$. Thus, in order to combine the TGV data with the Higgs data from the previous Subsection we can add to the χ^2 in

2.2. ANALYSIS FRAMEWORK

Eq. (2.45) an extra piece χ_{TGV}^2 with the schematic form

$$\chi_{\text{TGV}}^2 = \left(\delta g_1^Z, \delta \kappa_\gamma \right) C_{\text{TGV}}^{-1} \left(\delta g_1^Z, \delta \kappa_\gamma \right)^T, \quad (2.57)$$

where

$$\left(\delta g_1^Z, \delta \kappa_\gamma \right) \equiv \left(\frac{g_1^Z - g_1^{Z,\text{exp}}}{\sigma_{g_1^Z}}, \frac{\kappa_\gamma - \kappa_\gamma^{\text{exp}}}{\sigma_{\kappa_\gamma}} \right). \quad (2.58)$$

There g_1^Z and κ_γ contain the contributions of the dimension–six operators \mathcal{O}_W and \mathcal{O}_B as shown in Eq. (2.55), $g_1^{Z,\text{exp}}$ and $\kappa_\gamma^{\text{exp}}$ are the measured values shown in Eq. (2.56), with the corresponding errors $\sigma_{g_1^Z}$ and σ_{κ_γ} obtained from the same Eq. (2.56) symmetrizing as in Eq. (2.46). They are assumed to be Gaussian behaved. Finally the correlation matrix C_{TGV} has the trivial form

$$C_{\text{TGV}} = \begin{pmatrix} 1 & \rho \\ \rho & 1 \end{pmatrix}. \quad (2.59)$$

In the following Section we will show the results of the analyses of the Higgs data with and without combining it with TGV data.

2.2.3 Including electroweak precision data

Finally in this Subsection we describe how we estimate in our analysis the constraints from EWPO besides what is described in Secs. 2.1.3 and 2.1.4. We remind the reader that the two operators that contribute at the tree level to EWPO, \mathcal{O}_{BW} and $\mathcal{O}_{\Phi,1}$, have already been neglected for the present analysis given the strong constraints from EWPO. Here we describe the additional constraints on the dimension–six operators still remaining in the final basis of Eq. (2.44). These operators contribute to EWPO only at higher order in perturbation theory (at one loop) and therefore these contributions are subject to the usual problems with interpretation of non–tree level effects from non–renormalizable operators.

Here, in order to estimate the possible size of these effects we account for the constraints from EWPD on the higher–order corrections from dimension–six operators in terms of their contribution to the S , T and U parameters as presented for example in [54]. We do not consider additional effects associated with the possible energy dependence of those corrections and we retain only the $\log(\mu)$ terms which can be interpreted as the running of the corresponding coefficients between the renormalization scale μ (here taken to be the NP scale Λ) and the EW scale. The contributions from \mathcal{O}_B , \mathcal{O}_W ,

\mathcal{O}_{BB} , \mathcal{O}_{WW} and $\mathcal{O}_{\Phi,2}$ read

$$\begin{aligned} \alpha_{\text{em}}\Delta S &= \frac{1}{6} \frac{e^2}{16\pi^2} \left\{ 3(f_W + f_B) \frac{M_H^2}{\Lambda^2} \log\left(\frac{\Lambda^2}{M_H^2}\right) + \right. \\ &\quad + 2\left[(5c_\theta^2 - 2)f_W - (5c_\theta^2 - 3)f_B\right] \frac{M_Z^2}{\Lambda^2} \log\left(\frac{\Lambda^2}{M_H^2}\right) \\ &\quad - \left[(22c_\theta^2 - 1)f_W - (30c_\theta^2 + 1)f_B\right] \frac{M_Z^2}{\Lambda^2} \log\left(\frac{\Lambda^2}{M_Z^2}\right) \\ &\quad \left. - 24(c_\theta^2 f_{WW} + s_\theta^2 f_{BB}) \frac{M_Z^2}{\Lambda^2} \log\left(\frac{\Lambda^2}{M_H^2}\right) + 2f_{\Phi,2} \frac{v^2}{\Lambda^2} \log\left(\frac{\Lambda^2}{M_H^2}\right) \right\}, \end{aligned} \quad (2.60)$$

$$\begin{aligned} \alpha_{\text{em}}\Delta T &= \frac{3}{4c_\theta^2} \frac{e^2}{16\pi^2} \left\{ f_B \frac{M_H^2}{\Lambda^2} \log\left(\frac{\Lambda^2}{M_H^2}\right) \right. \\ &\quad + (c_\theta^2 f_W + f_B) \frac{M_Z^2}{\Lambda^2} \log\left(\frac{\Lambda^2}{M_H^2}\right) \\ &\quad \left. + \left[2c_\theta^2 f_W + (3c_\theta^2 - 1)f_B\right] \frac{M_Z^2}{\Lambda^2} \log\left(\frac{\Lambda^2}{M_Z^2}\right) - f_{\Phi,2} \frac{v^2}{\Lambda^2} \log\left(\frac{\Lambda^2}{M_H^2}\right) \right\}, \end{aligned} \quad (2.61)$$

$$\begin{aligned} \alpha_{\text{em}}\Delta U &= -\frac{1}{3} \frac{e^2 s_\theta^2}{16\pi^2} \left\{ (-4f_W + 5f_B) \frac{M_Z^2}{\Lambda^2} \log\left(\frac{\Lambda^2}{M_H^2}\right) \right. \\ &\quad \left. + (2f_W - 5f_B) \frac{M_Z^2}{\Lambda^2} \log\left(\frac{\Lambda^2}{M_Z^2}\right) \right\}. \end{aligned} \quad (2.62)$$

At present the most precise determination of S , T and U from a global fit yields the following values and correlation matrix:

$$\Delta S^{\text{exp}} = 0.00 \pm 0.10, \quad \Delta T^{\text{exp}} = 0.02 \pm 0.11, \quad \Delta U^{\text{exp}} = 0.03 \pm 0.09, \quad (2.63)$$

$$C_{\text{EWPO}} = \begin{pmatrix} 1 & 0.89 & -0.55 \\ 0.89 & 1 & -0.8 \\ -0.55 & -0.8 & 1 \end{pmatrix}. \quad (2.64)$$

Thus, we can combine this data with the Higgs and TGV data by adding an extra piece to the Higgs χ^2 in Eq. (2.45) and the TGV χ_{TGV}^2 in Eq. (2.57) of a similar form:

$$\chi_{\text{EWPO}}^2 = (\delta S, \delta T, \delta U) C_{\text{EWPO}}^{-1} (\delta S, \delta T, \delta U)^T, \quad (2.65)$$

where here

$$(\delta S, \delta T, \delta U) \equiv \left(\frac{\Delta S - \Delta S^{\text{exp}}}{\sigma_{\Delta S}}, \frac{\Delta T - \Delta T^{\text{exp}}}{\sigma_{\Delta T}}, \frac{\Delta U - \Delta U^{\text{exp}}}{\sigma_{\Delta U}} \right). \quad (2.66)$$

2.3. STATUS AFTER THE 7 AND 8 TEV LHC RUNS

with ΔS , ΔT and ΔU given in Eqs. (2.60)–(2.62), and where ΔS^{exp} , ΔT^{exp} and ΔU^{exp} , and the corresponding uncertainties are the quantities in Eq. (2.63).

In the following Section we will study the effects of each set of data on the determination of the dimension–six operators. We will present the results corresponding to the analysis including only Higgs data, *i.e.* using only χ^2 in Eq. (2.45), combining Higgs and TGV data, *i.e.* $\chi^2 + \chi_{\text{TGV}}^2$, and finally combining the three sets of data, *i.e.* $\chi^2 + \chi_{\text{TGV}}^2 + \chi_{\text{EWPO}}^2$.

Notice that, as long as only tree level effects are considered, *i.e.* for the analysis of Higgs and/or TGV data, the derived results apply to the combinations f_i/Λ^2 . However when including the bounds on the loop induced effects on EWPO the constraints depend separately on Λ since it appears in the logarithms (because we take the NP scale to be the renormalization scale).

2.3 Status after the 7 and 8 TeV LHC runs

We present here the updated status of the analysis of the Higgs couplings using all the current existing data. The purpose of the Section is to look for deviations and/or establish generic exclusion bounds on NP by means of the bottom–up effective Lagrangian approach. With this aim we describe here the constraints obtained in each of the dimension–six operators of our basis. We focus the discussion on describing the set of data where the strongest constraints come from. The data–driven approach allows us to easily identify the operators and experimental channels with a more promising outlook for the future 13 TeV LHC run. Furthermore, an important corollary of this approach will be developed as a complete new Section of the present Chapter.

2.3.1 Bosonic dimension–six operator analysis

We start the presentation of the results focusing on the scenario where the Higgs–fermion interactions are set to the corresponding SM values. In other words, we set $f_{\text{bot}} = f_{\tau} = 0$, and we fit the available data using the coefficients of the remaining six bosonic operators in Eq. (2.44), *i.e.* $\{f_g, f_{WW}, f_{BB}, f_W, f_B, f_{\Phi,2}\}$ are the free independent parameters. Results corresponding to different subsets of these bosonic operators can be found in [15].

Higgs collider data analysis

As a first step we study the constraints derived from the analysis of the Higgs collider data from ATLAS, CMS and Tevatron, that amount to a total of 56 observables, using the χ^2 in Eq. (2.45). We find the minimum of the chi–square to lay at $\chi_{\text{min}}^2 = 66.8$ for the combined analysis, whereas the

SM lies very close, at $\chi_{SM}^2 = 68.1$. This means that the SM is inside the 3% CL region of the six dimensional parameter space spanning the bosonic operators.

The results of this analysis are shown in Figure 2.1. The first column of the Figure displays the chi-square (indeed $\Delta\chi^2$) dependence upon the six bosonic anomalous coefficients after marginalizing over the five undisplayed ones. In other words, for each of the values of the dimension-six coefficient shown on a given panel, each of the undisplayed parameters are set to the values minimizing the corresponding $\Delta\chi^2$. In the different panels the solid red curve corresponds to the analysis of the combined Higgs collider data, whereas the dashed purple line is obtained using Higgs collider and TGV data and finally the dotted blue line corresponds to the analysis of Higgs collider, TGV, as well as EWPD (using $\Lambda = 10$ TeV in the evaluation of the logarithms in Eqs. (2.60)-(2.62)).

Focusing on the first column we can see that the $\Delta\chi^2$ behavior as a function of f_g exhibits two degenerate minima in all cases. This is due to the interference between the SM and the anomalous contributions in the gluon fusion production process and in the Higgs gluonic decay. There, both the SM and the anomalous contributions possess exactly the same momentum dependence. The high precision obtained on f_g is caused because f_g enters at tree level in gluon fusion while this is a loop process in the SM. Around the secondary minimum the anomalous contribution to the scattering amplitude is approximately twice the one of SM loop but with the opposite sign. This way the gluon fusion production and the gluonic Higgs decay have almost the same value than in the SM after squaring the corresponding amplitudes. The gluon fusion Higgs production cross section is too depleted for f_g values between the minima, giving rise to the intermediate barrier that can be observed. Far from the two minima the $\Delta\chi^2$ dependence on f_g is not completely symmetric between the two minima because of the effect of $f_{\Phi,2}$ in gluon fusion production.

Looking still at the first column of Fig. 2.1 we note that the current data in all the three cases is powerful enough to lead to bounded ranges of the different dimension-six parameters up to confidence levels well above the 99% CL. Both f_{WW} and f_{BB} receive the strongest constraints from the diphoton decay of the Higgs boson. The reason is that this decay channel is currently the one measured with the highest precision, to which the f_{WW} and f_{BB} tree level corrections, see Eqs. (2.19) and (2.20), can easily compete with the SM loop contributions. The other SM decay to EW bosons coming from a loop process in the SM, the Higgs decay to $Z\gamma$, has almost no effect on f_{WW} and f_{BB} given the fact that currently the exclusion bounds on this channel are still $O(1) - O(10)$ times above the SM expectation. Nevertheless, this is already enough to help closing the confidence level regions for the highest values of both f_W and f_B , that contribute to $Z\gamma$ but not to the diphoton decay, as seen in Eqs. (2.19) and (2.20). Currently the constraints

2.3. STATUS AFTER THE 7 AND 8 TEV LHC RUNS

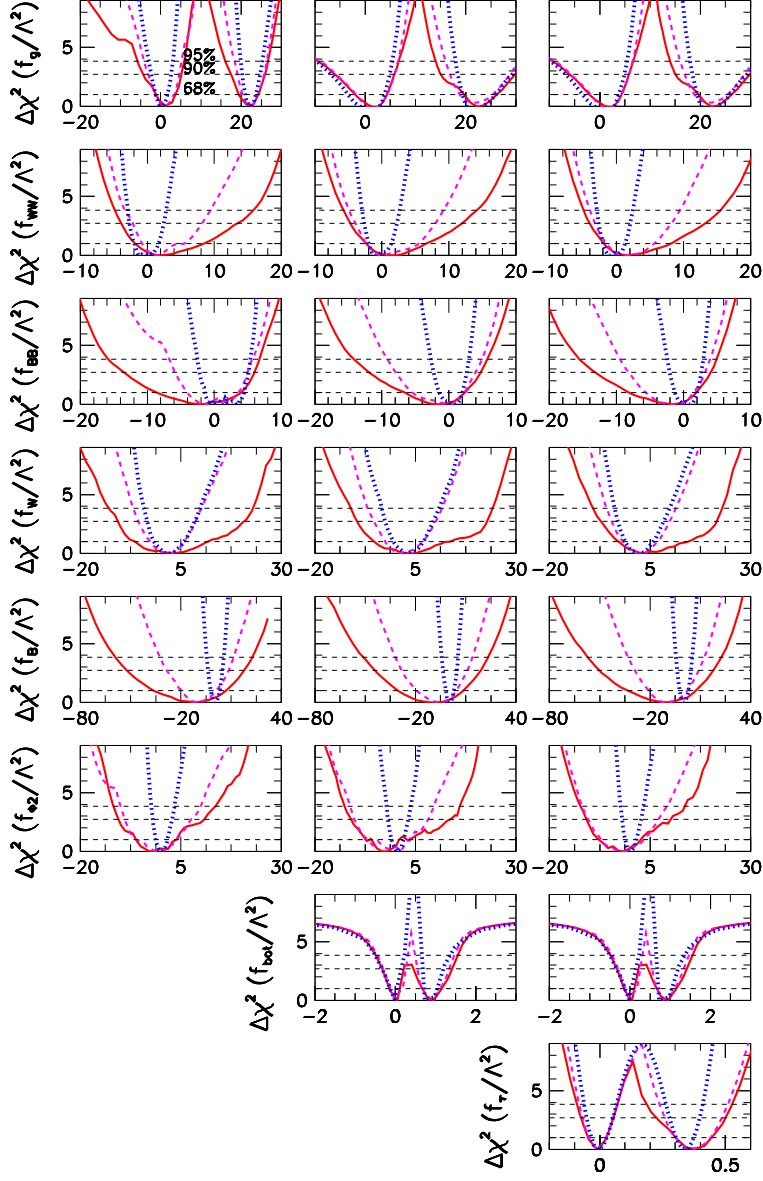


Figure 2.1: $\Delta\chi^2$ dependence on the fit parameters when we consider all Higgs collider data (red solid line), Higgs collider plus TGV data (dashed purple line), and Higgs collider plus TGV and EWP (dotted blue line). The rows depict the $\Delta\chi^2$ dependence with respect to the fit parameter shown in the left of the row, with the anomalous couplings f/Λ^2 given in TeV^{-2} , while the rest of undisplayed parameters are marginalized. In the first column we use f_g , f_{WW} , f_{BB} , f_W , f_B , and $f_{\Phi,2}$ as fit parameters with $f_{\text{bot}} = f_\tau = 0$. In the second column the fitting parameters are f_g , $f_{WW} = -f_{BB}$, f_W , f_B , $f_{\Phi,2}$, and f_{bot} with $f_\tau = 0$. In the panels of the right column we fit the data in terms of f_g , $f_{WW} = -f_{BB}$, f_W , f_B , $f_{\Phi,2}$, f_{bot} , and f_τ .

from the Higgs collider analysis on f_W are stronger than the ones on f_B because of the larger contributions of f_W to the different hW^+W^- and hZZ vertices: f_B only contributes to hZZ with a strength suppressed by the weak mixing angle compared to f_W . Finally the contribution of $f_{\Phi,2}$ as a shift of all the SM vertices leads to high confidence level closed regions as well, with an overall level of precision similar to the one of the rest of the bosonic dimension–six operators.

Adding TGV data

We now move to describe the effects of combining the Higgs collider and TGV data sets (dashed purple curves in Fig. 2.1) on this bosonic set of dimension–six operators. As we showed in Eq. (2.32), f_B and f_W are the only two fit parameters that modify the TGV’s at tree level, and therefore, they are the ones that show the largest impact of the TGV data, as can be seen in the corresponding panels of Fig. 2.1.

From these two parameters, f_W is the most constrained by the inclusion of the TGV data since it is the only dimension–six parameter that modifies the most precisely determined TGV: g_1^Z . Nevertheless, the common contribution of f_B and f_W , together with the other weak dimension–six operators, *i.e.* f_{BB} , f_{WW} and $f_{\Phi,2}$, to the different vertices involving the Higgs boson and the weak gauge bosons as well as the $Z\gamma$ vertex propagates the effects of the TGV data set to these other parameters. It is also worth noting that the level of precision of the TGV data set on f_B and f_W is very similar to the one from the Higgs collider data. This will be further exploited in the following Section, that is devoted to the interesting complementarity of the TGV data set effects with respect to the Higgs collider analyses.

Adding EWPO

Finally, the inclusion of EWPO in the fit (blue dotted lines in Fig. 2.1) significantly reduces the errors on f_B , $f_{\Phi,2}$, f_{BB} , and f_{WW} , as could be expected by looking at Eqs. (2.60)–(2.62). We remark once more that the logarithms on these equations are evaluated setting the high energy scale to $\Lambda = 10$ TeV. As mentioned above the quantitative interpretation of these one loop effects is debatable. We include them here for illustration of the possible size, but we will not include them in the final combined results given in Table 2.6 nor in the remaining figures of the present Section.

Resulting bounds

The best fit values and 90% CL allowed ranges for the couplings and observables in the combined analysis of Higgs collider and TGV data can be found in the first two columns of Table 2.6. The inclusion of the TGV data

2.3. STATUS AFTER THE 7 AND 8 TEV LHC RUNS

has almost no quantitative impact on the values of neither χ^2_{\min} nor the SM CL.

| | Fit with $f_{\text{bot}} = f_\tau = 0$ | | Fit including f_{bot} and f_τ | |
|--|--|-----------------------------|---|-----------------------------------|
| | Best fit | 90% CL allowed range | Best fit | 90% CL allowed range |
| f_g/Λ^2 (TeV ⁻²) | 1.1, 22 | $[-3.3, 5.1] \cup [19, 26]$ | 2.1, 21 | $[-5.3, 5.8] \cup [17, 22]$ |
| f_{WW}/Λ^2 (TeV ⁻²) | 1.5 | $[-3.2, 8.2]$ | 0.65 | $[-4.2, 7.7]$ |
| f_{BB}/Λ^2 (TeV ⁻²) | -1.6 | $[-7.5, 5.3]$ | -0.65 | $[-7.7, 4.2]$ |
| f_W/Λ^2 (TeV ⁻²) | 2.1 | $[-5.6, 9.6]$ | 1.7 | $[-5.4, 9.8]$ |
| f_B/Λ^2 (TeV ⁻²) | -10 | $[-29, 8.9]$ | -7.9 | $[-28, 11]$ |
| $f_{\phi,2}/\Lambda^2$ (TeV ⁻²) | -1.0 | $[-10, 8.5]$ | -1.3 | $[-9.8, 7.5]$ |
| f_{bot}/Λ^2 (TeV ⁻²) | — | — | 0.01, 0.84 | $[-0.28, 0.24] \cup [0.55, 1.3]$ |
| f_τ/Λ^2 (TeV ⁻²) | — | — | -0.01, 0.37 | $[-0.07, 0.05] \cup [0.26, 0.49]$ |
| $BR_{\gamma\gamma}^{\text{ano}}/BR_{\gamma\gamma}^{\text{SM}}$ | 1.2 | $[0.78, 1.7]$ | 1.2 | $[0.55, 1.9]$ |
| $BR_{WW}^{\text{ano}}/BR_{WW}^{\text{SM}}$ | 1.0 | $[0.89, 1.1]$ | 1.2 | $[0.51, 1.9]$ |
| $BR_{ZZ}^{\text{ano}}/BR_{ZZ}^{\text{SM}}$ | 1.2 | $[0.84, 1.5]$ | 1.4 | $[0.6, 2.2]$ |
| $BR_{bb}^{\text{ano}}/BR_{bb}^{\text{SM}}$ | 1.0 | $[0.92, 1.1]$ | 0.89 | $[0.46, 1.3]$ |
| $BR_{\tau\tau}^{\text{ano}}/BR_{\tau\tau}^{\text{SM}}$ | 1.0 | $[0.92, 1.1]$ | 1.1 | $[0.42, 2.6]$ |
| $\sigma_{gg}^{\text{ano}}/\sigma_{gg}^{\text{SM}}$ | 0.88 | $[0.59, 1.3]$ | 0.73 | $[0.38, 2.0]$ |
| $\sigma_{VBF}^{\text{ano}}/\sigma_{VBF}^{\text{SM}}$ | 1.1 | $[0.52, 1.9]$ | 1.1 | $[0.58, 1.8]$ |
| $\sigma_{VH}^{\text{ano}}/\sigma_{VH}^{\text{SM}}$ | 0.82 | $[0.43, 1.4]$ | 0.96 | $[0.47, 1.5]$ |

Table 2.6: Best fit values and 90% CL allowed ranges for the combination of all available Tevatron and LHC Higgs data as well as TGV data.

The $\Delta\chi^2$ dependence on each of the dimension–six operators of Fig. 2.1 can be easily translated into $\Delta\chi^2$ as a function of the physical observables by projecting the 6–dimensional space into the corresponding combinations entering in each observable. In Fig. 2.2 we show the results of this translation. There we can see the $\Delta\chi^2$ dependence on the different production cross sections and Higgs decay branching ratios when combining all the Higgs collider plus TGV measurements. In Fig. 2.2 the top panels correspond to the analysis of only the bosonic operators in Eq. (2.44), setting the Higgs fermionic interactions to the SM values. As we can see from the two top panels, all the SM predictions are within the 68% CL allowed ranges using the Higgs collider and TGV data. Notice that with the current available data the Higgs branching ratios are known with a precision around 20% while the production cross sections are known with an uncertainty of 30%.

When looking at the f_{WW} and f_{BB} panels in Fig. 2.1 we observe what seems like a mirror symmetric behavior. This is further illustrated in Figure 2.3 where we depict the 95% and 99% CL allowed regions of the plane $f_{WW} \times f_{BB}$, after marginalizing over the undisplayed variables. The Figure corresponds to the case where we consider only the Higgs collider data. Actually, as we can see, there is a strong anti–correlation between f_{WW} and f_{BB} . The origin lies on the diphoton decay of the Higgs boson: f_{WW} and f_{BB} give the dominant contributions to the Higgs branching ratio into two photons which is proportional to $f_{WW} + f_{BB}$, see Eqs. (2.19) and (2.20). The 95% CL allowed region is then formed by two narrow islands: one with

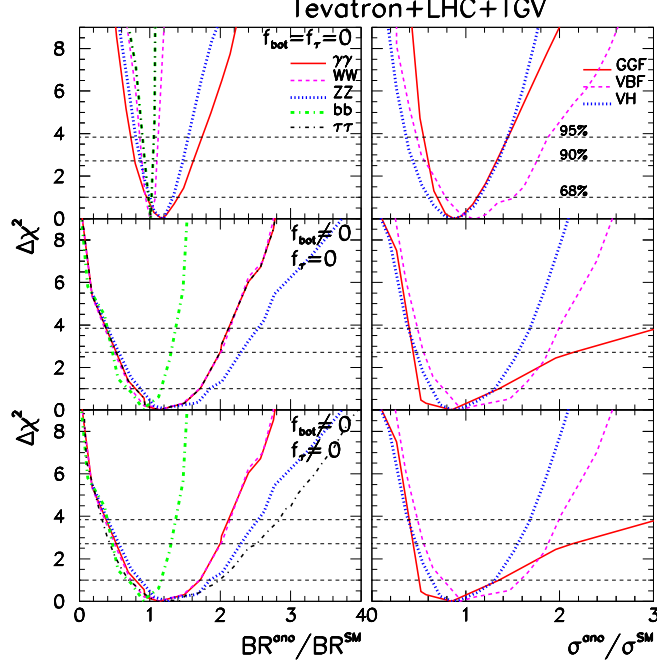


Figure 2.2: $\Delta\chi^2$ dependence on the Higgs branching ratios (left panels) and production cross sections (right panels) when we consider all Higgs collider and TGV data. In the upper panels we use f_g , f_{WW} , f_{BB} , f_W , f_B , and $f_{\Phi,2}$ as fitting parameters with $f_{\text{bot}} = f_\tau = 0$, while in the middle panels the fitting parameters are f_g , $f_{WW} = -f_{BB}$, f_W , f_B , $f_{\Phi,2}$, and f_{bot} with $f_\tau = 0$. In the lower row we parametrize the data in terms of f_g , $f_{WW} = -f_{BB}$, f_W , f_B , $f_{\Phi,2}$, f_{bot} , and f_τ . The dependence of $\Delta\chi^2$ on the branching ratios to the fermions not considered in a given analysis arises from the effect of the other parameters in the total decay width.

small departures from the SM contribution and a second one around the anomalous couplings values such that their contribution to the Higgs decay amplitude to photons is twice the SM one but with the opposite sign. This gives, after squaring, the same branching ratio to photons. This degeneracy of the minima is not exact, since the f_{WW} and f_{BB} couplings not only contribute to Higgs decay into photons, but also to its decay into WW^* and ZZ^* , as well as in Vh and VBF production mechanisms, lifting as a consequence the degeneracy of the local minima. Notice also that after the marginalization over f_{BB} (f_{WW}), the one-dimensional $\Delta\chi^2$ curve for f_{WW} (f_{BB}) shown in the second (third) row of the first column in Fig. 2.1 has only one minima and the anti-correlation is translated in these two curves being close to mirror symmetric.

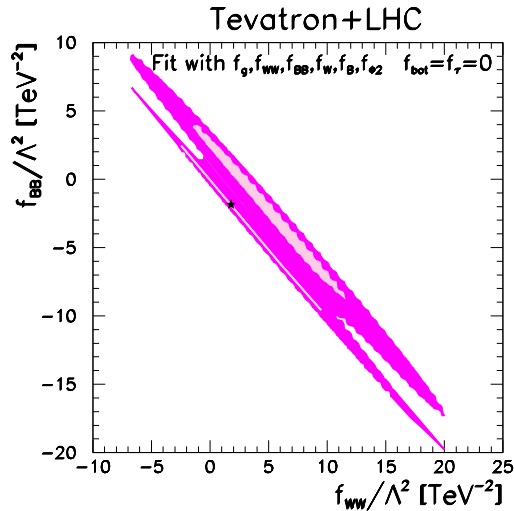


Figure 2.3: We display the 95% and 99% CL allowed regions in the plane $f_{WW} \times f_{BB}$ when we fit the Higgs collider data varying f_g , f_{WW} , f_{BB} , f_W , f_B , and $f_{\Phi,2}$. The star stands for the global minima and we marginalized over the undisplayed parameters.

Interesting correlations can also be observed in Figure 2.4 which contains the 68%, 90%, 95%, and 99% CL 2-dimensional projection in the plane $f_g \times f_{\Phi,2}$ after marginalizing over the four undisplayed parameters. The results are shown for the combination of Higgs collider and TGV data sets. As we can see, this Figure exhibits two isolated islands that originate from the interference between the anomalous and the SM contributions to the Higgs coupling to two gluons. Within each island there is an anti-correlation between f_g and $f_{\Phi,2}$, that stems from the fact that the anomalous contribution to the Higgs gluon fusion production is proportional to $F_{gg}^{SM} f_{\Phi,2} + 2f_g$ where $F_{gg}^{SM} \simeq 0.7$ is the SM loop contribution to the Hgg vertex.

The allowed ranges of observables also show interesting correlations as seen in Fig. 2.5. The left panel displays the correlations between the Higgs branching ratio into photons and its gluon fusion production cross section in the scenario with $f_{\text{bot}} = f_\tau = 0$. The Figure corresponds to the analysis of Higgs collider data in combination to the TGV data. Clearly, the two quantities shown in Fig. 2.5 are anti-correlated, since their product is the major source of Higgs events decaying into two photons.

2.3.2 Including fermionic operators

We now move to the effects of including the fermionic operators in the analysis of the different sets of data. We first increase the operator set in the

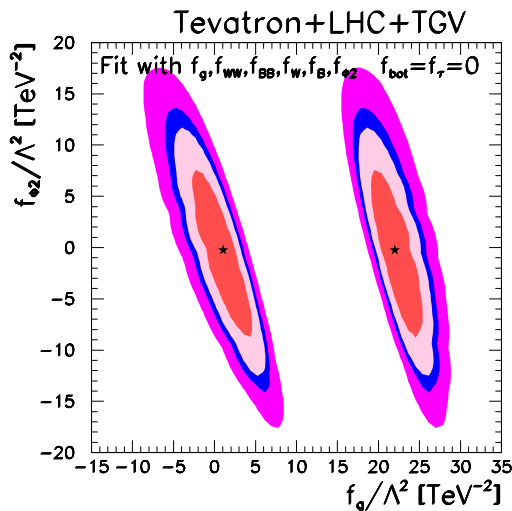


Figure 2.4: We present the 68%, 90%, 95%, and 99% CL allowed regions in the plane $f_g \times f_{\phi,2}$ when we fit the Higgs collider and TGV data varying f_g , f_{WW} , f_{BB} , f_W , f_B , and $f_{\phi,2}$. The stars stand for the global minima and we marginalized over the undisplayed parameters.

previous Subsection by adding the anomalous bottom Yukawa-like coupling f_{bot} . In this case to simplify the numerical analyses we make use of the strong correlation observed in Fig. 2.3 between f_{WW} and f_{BB} by imposing that $f_{WW} = -f_{BB}$. We have checked that this assumption has no effect on the rest of parameters and observables of the analysis but considerably speeds up the numerics. Therefore, our free dimension-six coefficients are $\{f_g, f_W, f_B, f_{WW} = -f_{BB}, f_{\phi,2}, f_{\text{bot}}\}$, where we are still keeping $f_\tau = 0$.

The results for this set of dimension-six operators are presented in the middle panels of Fig. 2.1. First we see that the $\Delta\chi^2$ dependence of f_{bot} presents two degenerate minima, one corresponding to a small correction to the SM Yukawa coupling, and one leading to a larger positive correction which flips the sign of the $Hb\bar{b}$ coupling and as a consequence of the decay amplitude. After squaring the corresponding amplitudes we obtain the same decay width for both minima. Comparing with the first column in the Figure, we see that the allowed range for f_g becomes much larger. This behavior originates from the fact that at large f_{bot} the Higgs branching ratio into the b -quark pairs approaches 1, so that in order to fit the data for any channel $X \neq b\bar{b}$, a production mode must be enhanced to compensate the dilution of the $H \rightarrow X$ branching ratios. This is accomplished by enhancing the gluon fusion cross section, which is the only production mode that is currently not directly measured in any of the Higgs to $b\bar{b}$ decay channels.

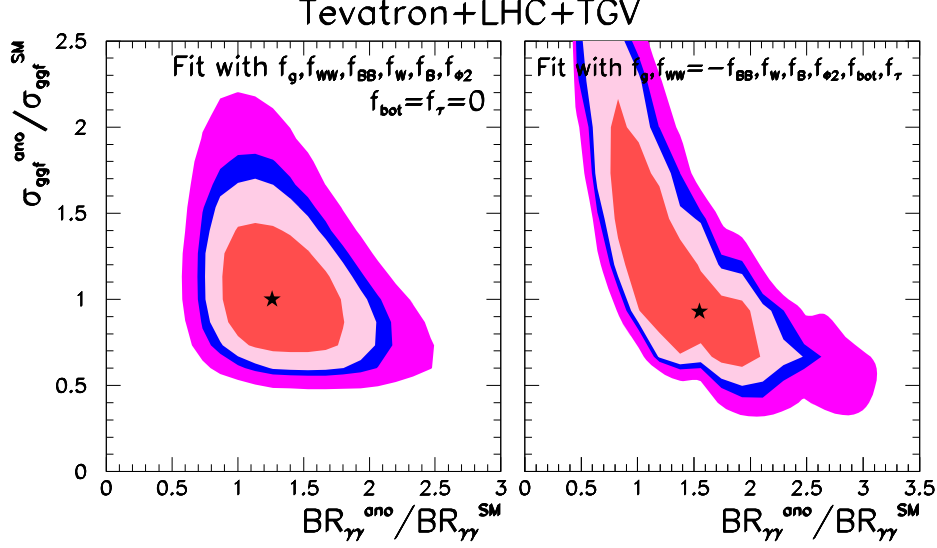


Figure 2.5: In the left (right) panel we present the 68%, 90%, 95%, and 99% CL allowed regions in the plane $\sigma_{gg}^{ano}/\sigma_{gg}^{SM} \times \text{Br}(h \rightarrow \gamma\gamma)^{ano}/\text{Br}(h \rightarrow \gamma\gamma)^{SM}$ when we fit the Higgs collider and TGV data varying f_g , f_{WW} , f_{BB} , f_W , f_B , and $f_{\Phi,2}$ (f_g , $f_{WW} = -f_{BB}$, f_W , f_B , $f_{\Phi,2}$, and f_{bot}). The stars stand for the global minima and we marginalized over the undisplayed parameters.

This can be more clearly seen in Fig. 2.6. This Figure depicts the strong correlation between the allowed values of $f_{bot} \times f_g$ when combining Higgs collider and TGV data. This correlation has an impact which is transferred to the determination of the gluon fusion production cross section and the Higgs branching ratio into photon pairs, as illustrated in the right panel of Fig. 2.5. This panel now shows that in this case the gluon fusion production cross section can be much larger than the SM cross section, but only as long as the Higgs branching ratio into photons is well below the SM value in order to fit the observed rate of $\gamma\gamma$ events. This corresponds to the case with f_{bot} and f_g going far from their corresponding minima.

On the other hand, allowing for $f_{bot} \neq 0$ has a small impact on the parameters affecting the Higgs couplings to EW gauge bosons f_W , f_B , f_{WW} , f_{BB} , and $f_{\Phi,2}$, as seen comparing the corresponding left and central panels of Fig. 2.1, even prior to the inclusion of TGV constraints on f_W and f_B . Hence the same comments than in the previous Section apply here.

We look further at the effects coming from the inclusion of f_{bot} to the set of dimension–six operators, now studying the chi–square dependence on the physical observables. These effects can be seen by comparing the upper and central lines in Fig. 2.2 which contain the chi–square dependence on Higgs

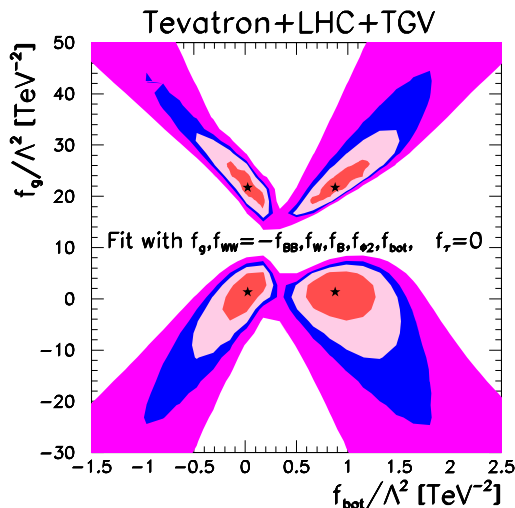


Figure 2.6: We present the 68%, 90%, 95%, and 99% CL allowed regions in the plane $f_{\text{bot}} \times f_g$ when we fit the Higgs collider and TGV data varying f_g , f_W , f_B , $f_{WW} = -f_{BB}$, $f_{\Phi,2}$, and f_{bot} . The stars stand for the global minima and we have marginalized over the undisplayed parameters.

branching ratios (left) and production cross sections (right) for the analysis with $f_{\text{bot}} = 0$ (upper) and $f_{\text{bot}} \neq 0$ (central). We can immediately see that the bounds on branching ratios and cross sections get loosened, with the VBF and VH production cross sections being the least affected quantities, while the gluon fusion cross section is the one becoming less constrained. The reason for this deterioration of the constraints is due to the strong correlation between f_g and f_{bot} we have just mentioned.

As a conclusion, the impact of f_{bot} on the fit is mainly due to the absence of data on the direct process $pp \rightarrow h \rightarrow b\bar{b}$, because of to the huge SM backgrounds when looking for the gluon fusion production mode. A possible way to mitigate the lack of information in this channel is to have smaller statistical errors in the processes taking place via VBF or VH associated production. Nevertheless, this will require a larger data sample than the one presently available.

In order to close the results Section we move finally to study the more general case including also the τ Yukawa-like dimension-six operator, *i.e.* $f_\tau \neq 0$. For the sake of simplicity we keep the number of free parameters equal to seven and we choose them to be $\{f_g, f_W, f_B, f_{WW} = -f_{BB}, f_{\Phi,2}, f_{\text{bot}}, f_\tau\}$. Here we use, once more, the strong correlation between f_{WW} and f_{BB} to reduce the number of free parameters to a treatable level, without any effect on the relevant parameters and observables of the analysis as we have

2.4. DETERMINING TGV'S FROM HIGGS DATA

checked. We present in the right panels of Fig. 2.1 the chi-square as a function of the free parameters in this general case, and in the lower panels of Fig. 2.2 the corresponding chi-square dependence on the decay branching ratios and production cross sections. The results show that the inclusion of f_τ in the analysis does not introduce any further strong correlation. The reason is that the data on $pp \rightarrow h \rightarrow \tau\bar{\tau}$ cuts off any strong correlation between f_τ and f_g . The determination of the parameters is not affected very much with respect to the previous case with $f_{\text{bot}} \neq 0$ and $f_\tau = 0$. Concerning the observables, only the $\tau\bar{\tau}$ Higgs branching ratio is affected.

The corresponding best fit values and allowed 90% CL ranges for the parameters and observables are given in the right two columns of Table 2.6. There we combine the collider Higgs and TGV data sets. We see that at the best fit point the present global analysis favors a $BR_{\tau\tau}^{\text{ano}}/BR_{\tau\tau}^{\text{SM}}$ slightly bigger than 1 (1.1), which leads to two possible values of f_τ . One that leads to a small positive correction to the negative SM Yukawa coupling, and one that gives a larger positive correction that flips the sign of the $H\tau\bar{\tau}$ coupling, but leading to the same absolute decay width after squaring the decay amplitudes. This is the origin of the two minima observed in the lowest panel in the right column of Fig. 2.1. Furthermore, the inclusion of the fermion couplings has no impact on the values of $\chi_{\text{min},(SM)}^2$, and it still holds that the SM is in overall agreement with the Higgs and TGV results at better than 9% CL.

The lack of any deviation from the SM behavior, after the dilution of the promising initial Higgs diphoton enhancement [15], is one of the main conclusions of the current status of the Higgs coupling studies. The very well tested SM is proving to be a valid theory also for the Higgs sector, given the measurements done so far. Besides theoretical open questions, the SM is standing robustly against the challenge of the LHC, without showing a sign of its hypothetical weakness. This is forcing us to wait for the improved 13 TeV high energy analyses in order to keep looking for NP signals in the EWSB sector. Furthermore this is making us to further struggle ourselves for new strategies to try to decipher and understand the EWSB mechanism. Following this spirit we devote the final Section of this Chapter to a possible strategy to further test the EWSB sector taking advantage of the very interesting complementarity between Higgs collider searches and TGV direct measurements.

2.4 Determining TGV's from Higgs data

In this Chapter we have described how, within the effective Lagrangian approach based on the linear realization of the $SU(2)_L \times U(1)_Y$ symmetry, some of the relevant dimension-six operators contribute at the same time to Higgs couplings and to TGV interactions. In the previous Sections we have

taken advantage of this feature with the aim of using TGV data in order to further constrain the dimension–six operators. In the present Section instead, we exploit this double contribution in, qualitatively, the opposite direction. We show that the Higgs collider data we have presented, from both Tevatron and LHC experiments, give rise by itself to strong bounds on TGV’s that are complementary to the bounds derived from the direct TGV measurements at the different colliders. Furthermore, we present here the combination of constraints coming from the direct measurements of TGV’s and from the TGV determinations using Higgs data. This combination of bounds corresponds at the end to the strongest constraints on TGV’s that we are aware of in this framework.

From all the operators in the final dimension–six basis relevant for the Higgs analysis, that we have presented in Eq. (2.44), both \mathcal{O}_W and \mathcal{O}_B contribute at the same time to Higgs couplings and TGV interactions. Modifications of the couplings of the Higgs state to the EW gauge bosons are thus related to TGV’s in a model independent way due to gauge invariance and the assumption of a linearly realized gauge symmetry. For the present study we use again the classical parametrization of the TGV interactions [52], that we have introduced in Eq. (2.31) for the C and P even subset of couplings. The contribution from \mathcal{O}_W and \mathcal{O}_B to the corresponding parameters Δg_1^Z , $\Delta\kappa_\gamma$ and $\Delta\kappa_Z$ is given in Eq. (2.55). In addition \mathcal{O}_{WWW} in Eq. (2.22) gives an independent modification to $\lambda_\gamma = \lambda_Z$ shown in Eq. (2.33).

Equations (2.55) and (2.33) imply that only three of the five relevant TGV interactions are independent in the framework of the dimension–six operators. These three can be chosen to be $\Delta\kappa_\gamma$, λ_γ , and Δg_1^Z , while λ_Z and $\Delta\kappa_Z$ remain to be determined by the relations

$$\lambda_Z = \lambda_\gamma \quad \text{and} \quad \Delta\kappa_Z = -\frac{s_\theta^2}{c_\theta^2} \Delta\kappa_\gamma + \Delta g_1^Z . \quad (2.67)$$

As we have commented, the parametrization in Eq. (2.31) has been established as the common Lagrangian to study TGV’s in the several collider analyses. In these studies, the experimental collaborations analyze the production of EW gauge bosons to measure the different parameters in Eq. (2.31). In most of these experimental analyses one or at most two couplings at the time are allowed to deviate from the SM predictions, while the others are fixed to their SM values. Several of these searches, performed by LEP collaborations, followed by Tevatron experiments and recently by LHC searches, were done in the constrained framework determined by the relations in Eq. (2.67) which is usually denoted as the “LEP” scenario. We review here these different experimental searches that will be compared and combined to the TGV bounds derived from our analysis of the Higgs data.

2.4.1 Direct collider TGV measurements

We start describing the relevant LEP analyses and afterwards we present the measurements from Tevatron and LHC studies.

LEP

As we have commented when applying TGV measurements to further constrain the Higgs interactions in the previous Sections, LEP searches are still the source of the most precise measurements of the different TGV interactions in Eq. (2.31). The different LEP experiments, OPAL, ALEPH and L3, were sensitive to anomalous TGV's through the W^+W^- pair production and the single γ and W productions. These different processes yield information on both WWZ and $WW\gamma$ vertices, as seen from the combination of the analyses that was presented in [42]. At LEP, the analyses based the precision of the measurements on the sensitivity of the different angular distributions to the anomalous TGV's. Although the total event rates and differential cross sections were also combined in addition to the angular distributions. We depict in Fig. 2.7 the bounds obtained in [42] from the combined analysis of the LEP collaborations in the LEP scenario. This corresponds to the region delimited by the blue line, which is the 95% CL allowed region (2 d.o.f.) on the plane $\Delta\kappa_\gamma \times \Delta g_1^Z$, for $\lambda_\gamma = \lambda_Z = 0$.

Tevatron

Tevatron experiments have also set relevant bounds on TGV's from the combination of different EW gauge boson production processes. In particular, Tevatron collaborations have studied WW , WZ and $W\gamma$ pair productions in $p\bar{p}$ collisions. Notice that at Tevatron, with a COM energy clearly above the W -pair production threshold, the use of total event rates and energy distributions is possible. In the most recent results presented in [43], $D\emptyset$ combined the different data sets containing from 0.7 to 8.6 fb^{-1} of integrated luminosity. In addition, CDF has also presented results from WZ production [44] with an integrated luminosity of 7.1 fb^{-1} , and from W^+W^- [45] with 3.6 fb^{-1} of data. However the CDF bounds were not presented in the LEP scenario, and as the expected precision obtainable would be below the rest of combined bounds we safely omit them for the rest of the Section. Conversely we show in Fig. 2.7 the bounds obtained from the $D\emptyset$ combined analysis in [43] for the LEP scenario. The green line delimits the 95% CL allowed region on the plane $\Delta\kappa_\gamma \times \Delta g_1^Z$, where the bounds were derived assuming $\lambda_\gamma = \lambda_Z = 0$. We also note here that the $D\emptyset$ results were obtained assuming a form factor for the anomalous TGV's of the form: $\frac{1}{(1+\frac{\hat{s}}{\Lambda'^2})^2}$ with $\Lambda' = 2 \text{ TeV}$ and \hat{s} being the collision energy of the event. As we will describe in the next Chapter when studying in detail all the anomalous TGV

interactions from the parametrization in [52], it is well known that the introduction of anomalous couplings can spoil delicate cancellations in scattering amplitudes. This may lead, eventually, to unitarity violation above a certain scale Λ' . A common established way to cure this problem in the literature is to introduce an energy dependent form factor that directly dumps the anomalous scattering amplitude growth at high energy. Given the COM energy at the Tevatron collider collisions and considering the level of precision reached by the $D\bar{\theta}$ combination in [43], the introduction of this form factor has only a very minor effect in our study. We note that all the other TGV measurements reviewed in this Section and presented in Fig. 2.7 were always obtained without including form factors.

LHC

As it was expected before the LHC started its operation [94], after the initial LHC runs the experiments are starting to provide direct bounds on TGV interactions. ATLAS has studied TGV's in W^+W^- [46], WZ [47] and $W\gamma$ and $Z\gamma$ fully leptonic channels [48], using the full 7 TeV data set, which amounts to an integrated luminosity of 4.6 fb^{-1} per channel. In addition CMS has also constrained the anomalous TGV interactions using the 7 TeV set of data. CMS has studied TGV's on the leptonic channels in WW [49] with 4.92 fb^{-1} , on $W\gamma$ and $Z\gamma$ channels [50] with 5.0 fb^{-1} of integrated luminosity, and finally on WW and WZ productions with two jets in the final state [51] and 5.0 fb^{-1} of data. From all these LHC searches we present in Fig. 2.7 the most sensitive results done for the LEP scenario. These correspond to the WW and WZ analyses from ATLAS [46, 47], whose 95% CL allowed regions on the plane $\Delta\kappa_\gamma \times \Delta g_1^Z$ are delimited by the solid and dash black curves respectively. As in the LEP and Tevatron combinations, these bounds were derived assuming in addition $\lambda_\gamma = \lambda_Z = 0$. We note here that from these two ATLAS searches, the limits on the WWZ TGV's from the WZ channel [47] were obtained by a two parameter analysis and shown in terms of $\Delta\kappa_Z$ and Δg_1^Z only. Hence, in Fig. 2.7 we expressed these bounds in terms of $\Delta\kappa_\gamma$ and Δg_1^Z after using Eq. (2.67) for the needed translation. The results on $W\gamma$ searches from both ATLAS and CMS [48, 50] are only sensitive to $WW\gamma$, *i.e.* to $\Delta\kappa_\gamma$ and λ_γ , leading thus to horizontal bands in Fig. 2.7. These limits are weaker than the bounds shown from WW and WZ productions. All the LHC bounds presented in Fig. 2.7 were obtained without the use of form factors.

2.4.2 Bounds on TGV's from Higgs data

We present here the bounds on TGV's that we can obtain from the analysis of the Higgs data in the framework of the effective Lagrangian approach that we have presented in the previous Sections. There, the analysis of

2.4. DETERMINING TGV'S FROM HIGGS DATA

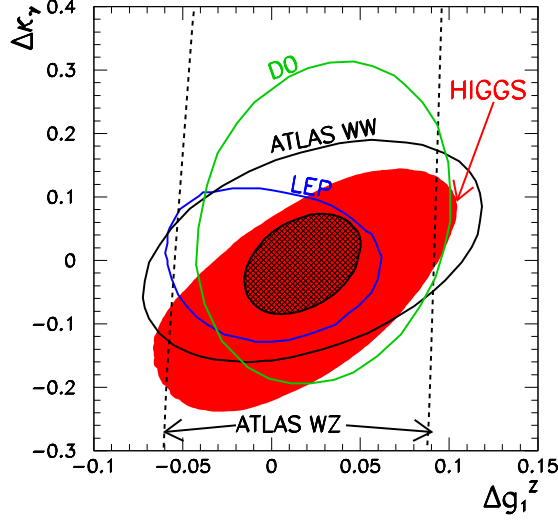


Figure 2.7: The 95% C.L. allowed regions (2 d.o.f.) on the plane $\Delta\kappa_\gamma \otimes \Delta g_1^Z$ from the analysis of the Higgs data from LHC and Tevatron (filled red region) together with the relevant bounds from different TGV studies from collider experiments as labeled in the panel, see text for details. We also show the estimated constraints obtainable by combining all these bounds (hatched region).

the latest Higgs data from the LHC and Tevatron collaborations has been performed to constrain the relevant dimension–six operators in Eq. (2.44): $f_g, f_{WW}, f_{BB}, f_{\Phi,2}, f_W, f_B, f_{\text{bot}}$, and f_τ . Nevertheless, as we have observed in Sec. 2.3.2, the inclusion of the fermionic operators, f_{bot} and f_τ , has a negligible effect on the constraints on f_W and f_B . Therefore, for simplicity we show here the results corresponding to the analysis done when the fermionic interactions are set to the SM values, spanning then the six dimensional space in Sec. 2.3.1: $f_g, f_{WW}, f_{BB}, f_{\Phi,2}, f_W$, and f_B . While the results of the corresponding analysis using all the available Higgs data have been presented and described in Sec. 2.3.1, Eq. (2.55) now allows us to translate the constraints on f_W and f_B from this analysis to bounds on $\Delta\kappa_\gamma, \Delta\kappa_Z$ and Δg_1^Z of which only two are independent. We show the results of the fitting to the Higgs data only as the red solid region in Fig. 2.7. There we plot the 95% CL allowed region in the plane $\Delta\kappa_\gamma \otimes \Delta g_1^Z$ after marginalizing over the other four parameters on the Higgs analysis, f_g, f_{WW}, f_{BB} and $f_{\Phi,2}$. To be more precise, we define

$$\Delta\chi^2(\Delta\kappa_\gamma, \Delta g_1^Z) = \min_{f_g, f_{WW}, f_{BB}, f_{\Phi,2}} \Delta\chi^2(f_g, f_{WW}, f_{BB}, f_{\Phi,2}, f_B, f_W) , \quad (2.68)$$

where $\Delta\chi^2$ is defined using only Higgs data as in Eq. (2.45). This means that we do not make any additional assumption about the coefficients of the six operators which contribute to the Higgs analysis when considering only bosonic dimension–six operators. We note as well that the bounds obtained from the Higgs data are independent of the value of $\lambda_\gamma = \lambda_Z$, and thus they can be directly compared to the experimental TGV measurements that we have described in the previous Subsection. We define the two-dimensional 95% CL allowed region plotted in Fig. 2.7 from the condition $\Delta\chi^2(\Delta\kappa_\gamma, \Delta g_1^Z) \leq 5.99$.

We can observe in Fig. 2.7 that the present Higgs physics bounds on the $\Delta\kappa_\gamma \otimes \Delta g_1^Z$ plane exhibit a non-negligible correlation. This is originated from the correlation imposed on the high values of f_W and f_B from their tree level contribution to $Z\gamma$ data, as can be observed in Eqs. (2.19) and (2.20). We already noted in the previous Sections that the current LHC precision on the $Z\gamma$ decay of the Higgs boson is still low, reaching only exclusion bounds of $O(1) - O(10)$. Nonetheless, the precision is enough to have a mild effect on the tree level contributions of f_W and f_B . These fit parameters only have to compete there, besides f_{WW} and f_{BB} coefficients which can be more strongly constrained from diphoton measurements, with the SM loop process. Fig. 2.7 shows that the present constraints on $\Delta\kappa_\gamma \otimes \Delta g_1^Z$ from the analysis of Higgs data exhibit a correlation which is different from the correlation in the bounds from direct TGV studies at the colliders. This illustrates the complementarity of the bounds on NP effects originating from the analysis of Higgs signals and from direct studies of the gauge–boson couplings.

The 90% CL 1 d.o.f. allowed ranges after consistently marginalizing over the other TGV parameters are:

$$\begin{aligned}
 -0.047 \leq \Delta g_1^Z \leq 0.089, \quad -0.19 \leq \Delta\kappa_\gamma \leq 0.099, \quad (2.69) \\
 \text{which imply} \quad -0.019 \leq \Delta\kappa_Z \leq 0.083.
 \end{aligned}$$

Thus the strength of the bounds derived from the analysis of the Higgs data are at the same precision level than the bounds derived from the direct TGV experimental measurements.

In order to estimate the potential of the described complementarity we combine our bounds derived from Higgs data with those from the TGV analysis from LEP, Tevatron and LHC, all of them shown in Fig. 2.7. In order to perform this combination we reconstruct approximate Gaussian functions $\chi_i^2(\Delta\kappa_\gamma, \Delta g_1^Z)$ which reproduce each of the 95% CL regions for the TGV analyses in the Figure. Thus, $i = \text{LEP, D}\emptyset, \text{ATLAS WW and ATLAS WZ}$, and we obtain the best fit point and two–dimensional covariance matrix which better reproduce the corresponding curve from the condition $\chi_i^2 = 5.99$. We write then

$$\chi_{\text{comb}}^2 = \chi^2(\Delta\kappa_\gamma, \Delta g_1^Z) + \sum_i \chi_i^2(\Delta\kappa_\gamma, \Delta g_1^Z), \quad (2.70)$$

2.5. CONCLUSIONS

where $\chi^2(\Delta\kappa_\gamma, \Delta g_1^Z)$ is based on the $\Delta\chi^2$ definition from Eq. (2.68) that was based in turn on the definition from Eq. (2.45). The combined 95% CL region in Fig. 2.7 (hatched region) is obtained with the condition $\Delta\chi_{\text{comb}}^2 \leq 5.99$. As we can observe, the combined region corresponds to the strongest 95% CL bounds that we are aware of in the LEP scenario. After consistently marginalizing, the combined 90% CL 1 d.o.f. allowed ranges read

$$\begin{aligned}
 -0.005 \leq \Delta g_1^Z \leq 0.040, & \quad -0.058 \leq \Delta\kappa_\gamma \leq 0.047 \quad , & (2.71) \\
 \text{which imply} & \quad -0.004 \leq \Delta\kappa_Z \leq 0.040 \quad .
 \end{aligned}$$

2.5 Conclusions

After the discovery of the Higgs boson the 7 and 8 TeV LHC runs have accumulated enough data to allow us to present a robust picture of the Higgs interactions and start accessing in consequence the theory responsible for EWSB. In this Chapter we have presented a bottom–up effective Lagrangian approach to the Higgs couplings, based on the published works [15–17].

One of the first conclusions we have obtained is related to the interesting features of the data–driven approach when choosing the final basis of dimension–six operators to be analyzed. If we start from all the dimension–six operators that can be built respecting the SM gauge symmetries and its corresponding particle content, EOM are useful to select the preferred basis. On this step we can minimize the number of theoretical assumptions with a choice guided by the existing data, which leads us to the operators in Eq. (2.44). In addition, a data–driven approach allows us for a more clear determination of the operator coefficients using all the available sets of data, that include, besides Higgs production analyses at LHC and Tevatron, the precise measurements of gauge boson interactions with fermions, which have been used for long to establish the SM, and the measurements of TGV interactions at the different colliders. A very interesting corollary of this data–driven choice is the correlation between couplings of the Higgs boson and TGV interactions.

After describing the details of the analysis based on the signal strengths, we have presented the updated results of the Higgs coupling study once all the Tevatron and LHC at 7 and 8 TeV data sets have been considered, describing also how both TGV and EWPD can be used to further constrain the Higgs couplings. It is especially interesting to observe that the TGV constraints on dimension–six operators are at a similar precision level than the constraints coming from Higgs data, a feature that directly drives us to the next point.

To further study the EWSB sector we have exploited the correlation between Higgs interactions and TGV analyses to test the linearly realized setup. We have concluded that the determination of TGV’s from Higgs

coupling analyses is complementary to the direct TGV measurements at the colliders (LEP, Tevatron and LHC), as both type of determinations present distinctive correlations, but with a similar constraining power. We have combined both types of measurements to give the strongest available constraints on anomalous TGV's in the linear framework.

This Chapter leads to a very promising outlook. First of all, to search for deviations from the pattern of Higgs interactions and TGV measurements as dictated by the linear realization of the SM gauge symmetry is a very interesting way to look for NP related to the EWSB sector and to understand the observed Higgs nature. This motivation directly leads to the studies presented in the following Chapter, consequently we leave the deeper discussion for the corresponding Sections. In addition, there are other promising improvements on the analyses of the present Chapter that are worth addressing in here.

Obvious improvements will be derived from the completion of the sets of data included in the analyses. First of all, although the Higgs analyses we have presented are based on almost the full 7 and 8 TeV LHC data sets, TGV studies are still relying on only the 7 TeV LHC set. Thus, the combination of Higgs production searches and direct 8 TeV TGV measurements will be a direct further test of the EWSB sector. Additionally, we can start looking at the promising high energy LHC run. There, we will have the potential to increase the precision on the determination of all the already measured couplings of the Higgs: to $\gamma\gamma$, to WW and ZZ pairs and especially to the fermionic $b\bar{b}$ and $\tau\bar{\tau}$ pairs [95]. Furthermore, it is also expected that the measurement of $Z\gamma$ decays, $ht\bar{t}$ associated production and even muonic decays may be possible. This will increase the number of studied couplings, and in consequence our knowledge of EWSB. The $Z\gamma$ decay will have the power to constrain the tree level contribution of the dimension–six operators contributing in there, which is especially important for \mathcal{O}_W and \mathcal{O}_B , since they are the two operators contributing at the same time to TGV interactions. The importance of directly measuring $ht\bar{t}$ associated production is out of any doubt, given the key role of the top quark in the hierarchy problem in the SM.

On the other hand, there are promising features of the dimension–six operators that should be exploited to further access the EWSB sector. We refer in particular to the distinctive new kinematic structures that they include in the Higgs interaction to weak gauge bosons, see Eq. (2.19). The study of these kinematic features not only will increase our power to constrain dimension–six operators, but it will also serve to break degeneracies between operators that simply shift the SM couplings and operators which affect the Lorentz structure of the interactions. Nevertheless, we note here that in order to access the kinematic distinctive signals of the dimension–six operators a direct interaction with the experimental collaborations is desirable.

Chapter 3

Alternative Lagrangians

The effective Lagrangian expansion used in Chapter 2 is not the only possible model independent Lagrangian that can be used to parametrize low energy effects associated with the mechanism behind EWSB. In this Chapter we present some alternatives.

In the first part, Sec. 3.1, we present an alternative expansion in terms of a non-linear (or chiral) effective Lagrangian. While the linear realization is appropriate for models where the Higgs boson is an elementary particle or in theories where at the low energies the Higgs boson behaves generically as a doublet of $SU(2)_L$, the chiral expansion is suitable for theories where the observed state is a composite field, a “dynamical” Higgs boson. This is the case for instance in theories where it is a pseudo-Nambu-Goldstone boson (pNGB) of a new global symmetry at the high energy scale. We discuss in this initial part of the Chapter how this non-linear expansion qualitatively contains less symmetry constraints and thus more independent invariant operators can be built in comparison to the linear case. The construction of the non-linear Lagrangian is not part of this thesis, but it was developed instead in [96] of which we select in Sec. 3.1.1 the relevant list of operators (though we use the notation and classification in [97], the published work on which Sec. 3.1 is based). In Sec. 3.1.2 we describe and quantify some differentiating signatures between the linear and the non-linear expansions and we present in addition the status of the analysis of a set of chiral operators after considering all available Higgs data from the 7 and 8 TeV LHC initial runs, as well as from Tevatron, in addition to the low-energy, TGV and LEP data. One of the conclusions we find is the importance of the TGV interaction measurements in order to disentangle a dynamical Higgs boson. This, in agreement with the conclusions of Chapter 2, stresses how the study of TGV interactions is an interesting way of accessing the EWSB mechanism.

Motivated by this, we devote the second part of this Chapter, Sec. 3.2, to the general established Lagrangian parametrization of TGV interactions [52].

This Lagrangian provides a useful parametrization to cover all possible relevant TGV interactions which are Lorentz invariant, regardless of their origin and the rest of symmetries that they respect. After its introduction in Sec. 3.2.1 we present in Sec. 3.2.2 a prospect analysis of the WWZ vertex at the LHC, published in [94] and previous to the LHC operation. It serves us to understand the main phenomenological implications of the anomalous TGV interactions, especially their distinctive high energy behavior. We analyze which cuts help to optimize their observation and we study two possible asymmetries that can be used to assess the special CP behavior of some of these anomalous TGV's. Next, in Sec. 3.2.3 (based on the published works [94,97] and also on ongoing work [98]), we update this analysis after the 7 and 8 TeV LHC runs have been completed, taking advantage now of the realistic LHC experimental TGV measurements that have been performed during the last two years. We focus on the anomalous TGV's with special CP properties, which are the ones related to the possible distinction between a dynamical Higgs boson and an elementary one. We close the present Chapter presenting the main conclusions in Chapter 3.3.

3.1 Disentangling a dynamical Higgs

In dynamical Higgs scenarios the Higgs state is a composite field, usually a pNGB of a global symmetry which is exact at a high energy scale Λ_s . This often corresponds to the scale at which new resonances would live, whereas the pNGB nature of the Higgs boson explains its light mass. The main motivation for such models is the fact that in this case the mass of the observed Higgs particle is protected by the global symmetry, taming to some extent the EW hierarchy problem. Concrete examples of this type of theories are the usually called CHM's, [99–108] for different strong groups and symmetry breaking patterns, generically “little Higgs” models [109] (see [110] for a review) and some higher dimensional scenarios can also be considered in the category of constructions in which the Higgs is a Goldstone boson. The non-linear expansion can accommodate dilaton-like scalar frameworks [111–117] as well, where the dilaton participates in EWSB.

In the previous Chapter we have observed that in the linear realization the Higgs boson is assumed to belong to an $SU(2)_L$ doublet, and thus the leading order operators extending the renormalizable SM are dimension-six operators suppressed by Λ^2 . In dynamical Higgs scenarios instead, the Goldstone boson parenthood of the Higgs boson makes a non-linear or chiral realization suitable [118]: a derivative expansion as corresponds to the Goldstone boson dynamics assumed for the recently discovered particle. The Lagrangian that we present in the following has generically its origin in the historical simplest formulations of “Technicolor” theories [119–121]. There, EWSB was described starting from a Higgsless model that included, on the

3.1. DISENTANGLING A DYNAMICAL HIGGS

other hand, the longitudinal degrees of freedom of the EW gauge bosons explicitly in the construction as propagating modes. Inspired by the chiral Lagrangian describing the pion interactions in quantum chromodynamics (QCD), the suitable effective Lagrangian expansion started from a non-renormalizable theory (non-decoupling scenario), and it was based on a derivative expansion. In the simplest case of Technicolor theories the three SM would-be-Goldstone bosons had a characteristic scale $f = v$. In the present Chapter the expansion is modified and adapted to include a light Higgs boson in the low energy theory, and in particular the characteristic scales involved are also different. Qualitatively the symmetry breaking can be explained in a two-steps process. On a first one the global symmetry at the high energy scale Λ_s , in a setup that has to contain an explicit symmetry violating source to allow for a non-zero mass of the pNGB Higgs, is spontaneously broken as in Technicolor theories to a subgroup containing the SM gauge group. This way, the characteristic scale f of the Goldstone bosons arising from this spontaneous breaking is different from both the EW scale v (defined by the EW gauge boson mass, *e.g.* the W mass $M_W = gv/2$), and the EWSB scale $\langle h \rangle$. At this scale $\langle h \rangle$, the Higgs develops generically a potential, which is usually linked to loops of fermions and bosons, and finally the $SU(2)_L \otimes U(1)_Y$ group is broken into $U(1)_{\text{em}}$, hence the usual EWSB process happens in this second step. The involved scales respect usually the relation $\Lambda_s < 4\pi f$, while a model dependent function g usually links the three scales, $v = g(f, \langle h \rangle)$. In this context it is very useful to introduce a parameter measuring the “degree of non-linearity” of the Higgs dynamics [96]:

$$\xi \equiv (v/f)^2, \quad (3.1)$$

which is appropriate to compare both linear and non-linear expansions.

The concrete non-linear description that we use here is based on the work in [96], where a complete effective Lagrangian basis for pure gauge and gauge-Higgs operators up to four derivatives was presented. However, the first attempts to formulate a non-linear effective Lagrangian in the presence of a “non-standard/singlet light Higgs boson” go back to the 90’s [122, 123], and later works [124, 125]. More recently, [126] introduced a relevant set of operators, while [127] added the pure Higgs operator in [128], as well as fermionic couplings, to propose a complete basis for all SM fields up to four derivatives, trading some of the operators in [96] by fermionic ones. However we rely in this Chapter on the conventions in [96, 97].

The particle content of the chiral Lagrangian includes all the SM fermions and gauge bosons and the Higgs field h . The longitudinal degrees of freedom of the EW gauge bosons are explicitly included in the description in terms of a dimensionless unitary matrix transforming as a bi-doublet of the global symmetry:

$$\mathbf{U}(x) = e^{i\sigma_a \pi^a(x)/v}, \quad \mathbf{U}(x) \rightarrow L \mathbf{U}(x) R^\dagger, \quad (3.2)$$

where here the scale associated with the eaten GB's (π^a) is v , and not f , in order to provide canonically normalized kinetic terms. L, R denote $SU(2)_{L,R}$ global transformations, and as usual σ_a are the Pauli matrices. Because of EWSB, the $SU(2)_{L,R}$ symmetries are broken down to the diagonal $SU(2)_C$ group, which in turn is explicitly broken by the gauged $U(1)_Y$ and by the heterogeneity of the fermion masses. The effective linear and chiral Lagrangians with a light Higgs particle h are intrinsically different, in particular from the point of view of the transformation properties under the $SU(2)_L$ symmetry. In addition in the case of the non-linear expansion, the insertions of the Higgs particle, a SM singlet, are weighted down as h/f , instead of coming as Φ/Λ as in the linear case.

Altogether, less symmetry constraints means more possible invariant operators [129–131] at a given order, and in summary two points can be emphasized:

- In the non-linear realization, the chiral symmetry breaking interactions of h are now generic/arbitrary functions $\mathcal{F}(h)$ (instead of coming always in $(v+h)$ powers as in the linear case).
- A relative reshuffling of the order at which couplings appear in each expansion takes place [96, 132, 133]. As a consequence, a higher number of independent (uncorrelated) couplings are present in the leading corrections of a non-linear Lagrangian.

Both effects increase the relative freedom of the purely phenomenological Lorentz and $U(1)_{\text{em}}$ couplings required at a given order of the expansion in the non-linear case compared to the linear expansion. Decorrelations resulting from the above arguments lead to distinctive discriminating signals. The point is that if higher orders in both expansions are considered, all possible Lorentz and $U(1)_{\text{em}}$ couplings will appear in both towers (as it is easily seen in the unitary gauge, as we illustrate in the following with several examples), but not necessarily at the same leading or subleading order. This means that leading interactions and (de)correlations in one expansion may be subleading in the other and vice versa. We describe in this Section examples of both cases.

We proceed now to present the basis of CP -even bosonic operators for the general non-linear effective Lagrangian and we analyze in detail its complete and independent set of pure gauge and gauge-Higgs operators.

3.1.1 Chiral effective Lagrangian

Here we list the different operators of the effective Lagrangian for a light dynamical Higgs [96]. We present only the CP -even operators, under the assumption, as in the linear case, that the Higgs state is a CP -even state. Furthermore, we restrict the list to bosonic operators, except for the Yukawa-like fermionic ones, and we only consider operators up to four derivatives.

3.1. DISENTANGLING A DYNAMICAL HIGGS

Furthermore, as it can be already inferred from the different degeneracies we have found on the analysis of the linear expansion, *e.g.* the degeneracies on the gluonic or on the fermionic operators, so far the data does not have a clear preference for any of the two possible signs of the Higgs interaction to fermions. This means that both Yukawa interactions, with the SM sign or with a flipped sign, are still allowed by the data. To account for this unresolved ambiguity, in the analyses of this Section we study both possible alternatives. Therefore, instead of directly using the definition in Eq. (2.1), we slightly modify this expression to

$$\mathcal{L} = \mathcal{L}_0 + \mathcal{L}_{\text{eff}} \quad , \quad (3.3)$$

where \mathcal{L}_0 is the SM Lagrangian, except for the cases when we flip the sign of the Yukawa interactions. This way \mathcal{L}_0 is written as:

$$\begin{aligned} \mathcal{L}_0 = & \frac{1}{2}(\partial_\mu h)(\partial^\mu h) - \frac{1}{4}W_{\mu\nu}^a W^{a\mu\nu} - \frac{1}{4}B_{\mu\nu}B^{\mu\nu} - \frac{1}{4}G_{\mu\nu}^a G^{a\mu\nu} - V(h) \\ & - \frac{(v+h)^2}{4}\text{Tr}[\mathbf{V}_\mu\mathbf{V}^\mu] + i\bar{Q}\not{D}Q + i\bar{L}\not{D}L \\ & - \frac{v+s_Y h}{\sqrt{2}}(\bar{Q}_L\mathbf{U}\mathbf{Y}_Q Q_R + \text{h.c.}) - \frac{v+s_Y h}{\sqrt{2}}(\bar{L}_L\mathbf{U}\mathbf{Y}_L L_R + \text{h.c.}) \quad , \end{aligned} \quad (3.4)$$

where $\mathbf{V}_\mu \equiv (\mathbf{D}_\mu \mathbf{U}) \mathbf{U}^\dagger$ ($\mathbf{T} \equiv \mathbf{U}\sigma_3\mathbf{U}^\dagger$) is the vector (scalar) chiral field transforming in the adjoint of $SU(2)_L$. The covariant derivative reads

$$\mathbf{D}_\mu \mathbf{U}(x) \equiv \partial_\mu \mathbf{U}(x) + \frac{i}{2}gW_\mu^a(x)\sigma_a \mathbf{U}(x) - \frac{ig'}{2}B_\mu(x)\mathbf{U}(x)\sigma_3 \quad . \quad (3.5)$$

The first line in Eq. (3.4) describes the Higgs and gauge boson kinetic terms, and the effective scalar potential $V(h)$, accounting for the breaking of the EW symmetry (it does not need to be specified for the present study). The second line describes the W and Z masses and their interactions with the Higgs, as well as the kinetic terms for the GB's and the fermions. Finally, the third line corresponds to the Yukawa-like interactions written in the fermionic mass eigenstate basis (the CKM mixing is implicitly encoded in Q_L). There $s_Y \equiv \pm$ controls the sign of the Higgs-fermion couplings, as we have stated we study here both possible signs. Furthermore, a compact notation for the right-handed fields has been adopted by using doublets, Q_R and L_R . This way \mathbf{Y}_Q and \mathbf{Y}_L are two 6×6 block-diagonal matrices containing the usual Yukawa couplings:

$$\mathbf{Y}_Q \equiv \mathbf{diag}(Y_U, Y_D) \quad , \quad \text{and} \quad \mathbf{Y}_L \equiv \mathbf{diag}(Y_\nu, Y_L) \quad . \quad (3.6)$$

In the case of the non-linear Lagrangian, and following [96], the ordering of operators does not exactly match a division in terms of the number of derivatives. Instead, this division is data-driven, while being consistent

with a derivative expansion up to four derivatives. For instance, the usual custodial breaking term $\text{Tr}(\mathbf{T}\mathbf{V}_\mu)\text{Tr}(\mathbf{T}\mathbf{V}^\mu)$ is a two derivative operator and should be listed at the leading order in the chiral expansion. Nevertheless, as it is not present in the SM at tree level, it belongs to \mathcal{L}_{eff} by definition. Furthermore, the data strongly constrains its coefficient so that it can be always considered a subleading operator [134]. Finally, we write \mathcal{L}_{eff} considering terms up to four derivatives [96] and with only bosonic (*i.e.* pure gauge, pure Higgs and gauge–Higgs operators) and Yukawa–like operators:

$$\begin{aligned} \mathcal{L}_{\text{eff}} = & \xi [c_B \mathcal{P}_B(h) + c_W \mathcal{P}_W(h) + c_G \mathcal{P}_G(h) + c_C \mathcal{P}_C(h) + c_T \mathcal{P}_T(h) \\ & + c_H \mathcal{P}_H(h) + c_{\square H} \mathcal{P}_{\square H}(h)] + \xi \sum_{i=1}^{10} c_i \mathcal{P}_i(h) + \xi^2 \sum_{i=11}^{25} c_i \mathcal{P}_i(h) \\ & + \xi^4 c_{26} \mathcal{P}_{26}(h) + \sum_i \xi^{n_i} c_{HH}^i \mathcal{P}_{HH}^i(h) \ , \end{aligned} \quad (3.7)$$

where c_i are the model dependent constant coefficients accompanying the operators. The last term accounts for all possible pure Higgs operators weighted by ξ^{n_i} with $n_i \geq 2$. We further discuss in the following the role of the parameter ξ in the non–linear effective Lagrangian. The set of pure–gauge and gauge–Higgs operators is defined by [96, 97]:

Weighted by ξ :

$$\begin{aligned} \mathcal{P}_C(h) &= -\frac{v^2}{4} \text{Tr}(\mathbf{V}^\mu \mathbf{V}_\mu) \mathcal{F}_C(h) & \mathcal{P}_4(h) &= ig' B_{\mu\nu} \text{Tr}(\mathbf{T}\mathbf{V}^\mu) \partial^\nu \mathcal{F}_4(h) \\ \mathcal{P}_T(h) &= \frac{v^2}{4} \text{Tr}(\mathbf{T}\mathbf{V}_\mu) \text{Tr}(\mathbf{T}\mathbf{V}^\mu) \mathcal{F}_T(h) & \mathcal{P}_5(h) &= ig \text{Tr}(W_{\mu\nu} \mathbf{V}^\mu) \partial^\nu \mathcal{F}_5(h) \\ \mathcal{P}_B(h) &= -\frac{g'^2}{4} B_{\mu\nu} B^{\mu\nu} \mathcal{F}_B(h) & \mathcal{P}_6(h) &= (\text{Tr}(\mathbf{V}_\mu \mathbf{V}^\mu))^2 \mathcal{F}_6(h) \\ \mathcal{P}_W(h) &= -\frac{g^2}{4} W_{\mu\nu}^a W^{a\mu\nu} \mathcal{F}_W(h) & \mathcal{P}_7(h) &= \text{Tr}(\mathbf{V}_\mu \mathbf{V}^\mu) \partial_\nu \partial^\nu \mathcal{F}_7(h) \\ \mathcal{P}_G(h) &= -\frac{g_s^2}{4} G_{\mu\nu}^a G^{a\mu\nu} \mathcal{F}_G(h) & \mathcal{P}_8(h) &= \text{Tr}(\mathbf{V}_\mu \mathbf{V}_\nu) \partial^\mu \mathcal{F}_8(h) \partial^\nu \mathcal{F}'_8(h) \\ \mathcal{P}_1(h) &= gg' B_{\mu\nu} \text{Tr}(\mathbf{T}W^{\mu\nu}) \mathcal{F}_1(h) & \mathcal{P}_9(h) &= \text{Tr}((\mathcal{D}_\mu \mathbf{V}^\mu)^2) \mathcal{F}_9(h) \\ \mathcal{P}_2(h) &= ig' B_{\mu\nu} \text{Tr}(\mathbf{T}[\mathbf{V}^\mu, \mathbf{V}^\nu]) \mathcal{F}_2(h) & \mathcal{P}_{10}(h) &= \text{Tr}(\mathbf{V}_\nu \mathcal{D}_\mu \mathbf{V}^\mu) \partial^\nu \mathcal{F}_{10}(h) \\ \mathcal{P}_3(h) &= ig \text{Tr}(W_{\mu\nu} [\mathbf{V}^\mu, \mathbf{V}^\nu]) \mathcal{F}_3(h) \ , \end{aligned} \quad (3.8)$$

Weighted by ξ^2 :

$$\begin{aligned}
 \mathcal{P}_{11}(h) &= (\text{Tr}(\mathbf{V}_\mu \mathbf{V}_\nu))^2 \mathcal{F}_{11}(h) & \mathcal{P}_{19}(h) &= \text{Tr}(\mathbf{T} \mathcal{D}_\mu \mathbf{V}^\mu) \text{Tr}(\mathbf{T} \mathbf{V}_\nu) \partial^\nu \mathcal{F}_{19}(h) \\
 \mathcal{P}_{12}(h) &= g^2 (\text{Tr}(\mathbf{T} W_{\mu\nu}))^2 \mathcal{F}_{12}(h) & \mathcal{P}_{20}(h) &= \text{Tr}(\mathbf{V}_\mu \mathbf{V}^\mu) \partial_\nu \mathcal{F}_{20}(h) \partial^\nu \mathcal{F}'_{20}(h) \\
 \mathcal{P}_{13}(h) &= ig \text{Tr}(\mathbf{T} W_{\mu\nu}) \text{Tr}(\mathbf{T} [\mathbf{V}^\mu, \mathbf{V}^\nu]) \mathcal{F}_{13}(h) & \mathcal{P}_{21}(h) &= (\text{Tr}(\mathbf{T} \mathbf{V}_\mu))^2 \partial_\nu \mathcal{F}_{21}(h) \partial^\nu \mathcal{F}'_{21}(h) \\
 \mathcal{P}_{14}(h) &= g \varepsilon^{\mu\nu\rho\lambda} \text{Tr}(\mathbf{T} \mathbf{V}_\mu) \text{Tr}(\mathbf{V}_\nu W_{\rho\lambda}) \mathcal{F}_{14}(h) & \mathcal{P}_{22}(h) &= \text{Tr}(\mathbf{T} \mathbf{V}_\mu) \text{Tr}(\mathbf{T} \mathbf{V}_\nu) \partial^\mu \mathcal{F}_{22}(h) \partial^\nu \mathcal{F}'_{22}(h) \\
 \mathcal{P}_{15}(h) &= \text{Tr}(\mathbf{T} \mathcal{D}_\mu \mathbf{V}^\mu) \text{Tr}(\mathbf{T} \mathcal{D}_\nu \mathbf{V}^\nu) \mathcal{F}_{15}(h) & \mathcal{P}_{23}(h) &= \text{Tr}(\mathbf{V}_\mu \mathbf{V}^\mu) (\text{Tr}(\mathbf{T} \mathbf{V}_\nu))^2 \mathcal{F}_{23}(h) \\
 \mathcal{P}_{16}(h) &= \text{Tr}([\mathbf{T}, \mathbf{V}_\nu] \mathcal{D}_\mu \mathbf{V}^\mu) \text{Tr}(\mathbf{T} \mathbf{V}^\nu) \mathcal{F}_{16}(h) & \mathcal{P}_{24}(h) &= \text{Tr}(\mathbf{V}_\mu \mathbf{V}_\nu) \text{Tr}(\mathbf{T} \mathbf{V}^\mu) \text{Tr}(\mathbf{T} \mathbf{V}^\nu) \mathcal{F}_{24}(h) \\
 \mathcal{P}_{17}(h) &= ig \text{Tr}(\mathbf{T} W_{\mu\nu}) \text{Tr}(\mathbf{T} \mathbf{V}^\mu) \partial^\nu \mathcal{F}_{17}(h) & \mathcal{P}_{25}(h) &= (\text{Tr}(\mathbf{T} \mathbf{V}_\mu))^2 \partial_\nu \partial^\nu \mathcal{F}_{25}(h) \\
 \mathcal{P}_{18}(h) &= \text{Tr}(\mathbf{T} [\mathbf{V}_\mu, \mathbf{V}_\nu]) \text{Tr}(\mathbf{T} \mathbf{V}^\mu) \partial^\nu \mathcal{F}_{18}(h) \quad , & &
 \end{aligned} \tag{3.9}$$

Weighted by ξ^4 :

$$\mathcal{P}_{26}(h) = (\text{Tr}(\mathbf{T} \mathbf{V}_\mu) \text{Tr}(\mathbf{T} \mathbf{V}_\nu))^2 \mathcal{F}_{26}(h) . \tag{3.10}$$

In Eqs. (3.8) and (3.9), \mathcal{D}_μ denotes the covariant derivative on a field transforming in the adjoint representation of $SU(2)_L$, *i.e.*

$$\mathcal{D}_\mu \mathbf{V}_\nu \equiv \partial_\mu \mathbf{V}_\nu + ig \left[W_\mu^a \frac{\sigma_a}{2}, \mathbf{V}_\nu \right] . \tag{3.11}$$

Finally, the pure Higgs operators are:

Weighted by ξ : this set includes two operators, one with two derivatives and one with four,

$$\mathcal{P}_H(h) = \frac{1}{2} (\partial_\mu h) (\partial^\mu h) \mathcal{F}_H(h) , \quad \mathcal{P}_{\square H} = \frac{1}{v^2} (\partial_\mu \partial^\mu h)^2 \mathcal{F}_{\square H}(h) . \tag{3.12}$$

In spite of not containing gauge interactions, they are considered here as they affect the renormalization of the SM parameters, and the propagator of the h field, respectively, as it happened with operators $\mathcal{O}_{\phi,1}$, $\mathcal{O}_{\phi,2}$ and $\mathcal{O}_{\phi,4}$ in the linear expansion.

Weighted by $\xi^{\geq 2}$: this class consists of all possible pure Higgs operators with four derivatives weighted by $\xi^{\geq 2}$, $\mathcal{P}_{HH}^i(h)$. An example of ξ^2 -weighted operator would be [111, 128]

$$\mathcal{P}_{DH}(h) = \frac{1}{v^4} ((\partial_\mu h) (\partial^\mu h))^2 \mathcal{F}_{DH}(h) . \tag{3.13}$$

However, we do not list all of them here as they are not relevant for the present study.

ξ -weight and $\mathcal{F}(h)$

We stress here that the ξ -weight does not reflect an expansion in terms of ξ , it is only introduced to facilitate the comparison and relation of the non-linear operators with respect to the linear expansion. The ξ -weight of a given chiral operator is independent of the linear basis used in the comparison, however this comparison needs to be done with a complete linear basis. In the present case we compare the non-linear expansion with the linear basis we have presented in Chapter 2. A “sibling” of a chiral operator $\mathcal{P}_i(h)$ is defined as the operator of the linear expansion whose pure gauge interactions coincide with those described by $\mathcal{P}_i(h)$. The canonical dimension d of the sibling is related to the power of ξ^n as $d = 4 + 2n$, and consequently ξ^n acts as an indicator of at which order in the linear expansion it is necessary and sufficient to go to account for the same gauge interactions of the given chiral operator. In the cases where the chiral operator corresponds to a combination of linear operators with different canonical dimensions, the power of ξ stands for the lowest dimension of such operators where it is sufficient to go to lead to the same phenomenological gauge interactions. In brief, the lowest dimensional siblings of the operators in Eqs. (3.8) and (3.12) have $d = 6$; those in Eqs. (3.9) have $d = 8$, and that of Eq. (3.10) has $d = 12$. In this context ξ is not a physical quantity *per se* in the framework of the effective Lagrangian. Indeed the ξ weights could be reabsorbed in a redefinition of the coefficients c_i and be altogether forgotten; nevertheless, they allow for a fast connection with the analyses performed in the linear expansion, as illustrated later on.

Looking now at the different operators included in the definition of \mathcal{L}_{eff} we can directly see that the Higgs boson is introduced through model dependent functions, $\mathcal{F}(h)$, instead of being introduced in powers of $(v + h)$ as in the linear case. Each of these functions can be defined by $\mathcal{F}(h) \equiv g_0(h, v) + \xi g_1(h, v) + \xi^2 g_2(h, v) + \dots$, where $g_i(h, v)$ are model dependent functions of h and of v (once $\langle h \rangle$ is expressed in terms of ξ and v). In the present work we assume that the $\mathcal{F}(h)$ functions are completely general polynomials of v and h , not including derivatives of h .

Relation with the Linear basis

Finally, we end this Subsection highlighting the usefulness of the ξ -weighting and the relation between the higher dimensional operators appearing in the chiral and linear expansions. As we have stated, an obvious difference between both expansions comes from the Higgs dependence, that is (linear vs. non-linear)

$$\Phi = \frac{1}{\sqrt{2}} \begin{pmatrix} 0 \\ v + h(x) \end{pmatrix} \quad \text{vs.} \quad \mathcal{F}(h). \quad (3.14)$$

3.1. DISENTANGLING A DYNAMICAL HIGGS

Another difference comes from all the ξ^n operators, with $n \geq 2$. Some of the interactions that these operators generate appear in leading operators in the chiral expansion and may be sizable if ξ is also sizable. However the corresponding linear operators containing the same couplings are subleading, of dimension–eight or higher in the linear expansion. We analyze in detail in the following Section one of such operators and the possibility of a measurement at the LHC. The same type of leading–subleading distinction can be observed in the opposite direction. In particular, all the pure gauge operators in Eq. (2.22) are leading operators in the linear expansion. However, as they contain six derivatives they are not inside the leading ones in the chiral case. In other words they are not siblings of any chiral operator up to four derivatives. This means that the interactions and Lorentz structures that they generate are subleading non–linear effects. Concrete phenomenology examples of both cases are described in the next Subsection.

A distinctive striking feature is related to the number of independent couplings that both expansions span, or in other words, it is related to (de)correlations between the different couplings even in the limit where both expansions should converge ($\xi \rightarrow 0$). This can be best illustrated truncating the non–linear expansion at order ξ and comparing the result with the $d = 6$ linear basis that contributes to gauge–Higgs couplings. The linear basis in this case contains ten independent couplings, the ones in Eqs. (2.2) and (2.21), whereas the chiral one depends on seventeen. A more precise illustration follows when taking momentarily $\mathcal{F}_i(h) = (1 + h/v)^2$, in all $\mathcal{P}_i(h)$ under discussion, which in addition leads to:

$$\begin{aligned}
 \mathcal{O}_{BB} &= \frac{v^2}{2} \mathcal{P}_B(h), & \mathcal{O}_{WW} &= \frac{v^2}{2} \mathcal{P}_W(h), \\
 \mathcal{O}_{GG} &= -\frac{2v^2}{g_s^2} \mathcal{P}_G(h), & \mathcal{O}_{BW} &= \frac{v^2}{8} \mathcal{P}_1(h), \\
 \mathcal{O}_B &= \frac{v^2}{16} \mathcal{P}_2(h) + \frac{v^2}{8} \mathcal{P}_4(h), & \mathcal{O}_W &= \frac{v^2}{8} \mathcal{P}_3(h) - \frac{v^2}{4} \mathcal{P}_5(h), \\
 \mathcal{O}_{\Phi,1} &= \frac{v^2}{2} \mathcal{P}_H(h) - \frac{v^2}{4} \mathcal{F}(h) \mathcal{P}_T(h), & \mathcal{O}_{\Phi,2} &= v^2 \mathcal{P}_H(h), \\
 \mathcal{O}_{\Phi,4} &= \frac{v^2}{2} \mathcal{P}_H(h) + \frac{v^2}{2} \mathcal{F}(h) \mathcal{P}_C(h), & &
 \end{aligned} \tag{3.15}$$

$$\mathcal{O}_{\square\Phi} = \frac{v^2}{2} \mathcal{P}_{\square H}(h) + \frac{v^2}{8} \mathcal{P}_6(h) + \frac{v^2}{4} \mathcal{P}_7(h) - v^2 \mathcal{P}_8(h) - \frac{v^2}{4} \mathcal{P}_9(h) - \frac{v^2}{2} \mathcal{P}_{10}(h).$$

These relations show that five chiral operators, $\mathcal{P}_B(h)$, $\mathcal{P}_W(h)$, $\mathcal{P}_G(h)$, $\mathcal{P}_1(h)$ and $\mathcal{P}_H(h)$ are in a one–to–one correspondence with the linear operators \mathcal{O}_{BB} , \mathcal{O}_{WW} , \mathcal{O}_{GG} , \mathcal{O}_{BW} and $\mathcal{O}_{\Phi,2}$, respectively, whereas the operator $\mathcal{P}_T(h)$ ($\mathcal{P}_C(h)$) corresponds to a combination of the linear operators $\mathcal{O}_{\Phi,1}$ and $\mathcal{O}_{\Phi,2}$ ($\mathcal{O}_{\Phi,4}$ and $\mathcal{O}_{\Phi,2}$). In contrast, it follows from Eq. (3.15) above that:

- Only a specific combination of the non-linear operators $\mathcal{P}_2(h)$ and $\mathcal{P}_4(h)$ corresponds to the linear operator \mathcal{O}_B .
- Similarly, only a specific combination of the non-linear operators $\mathcal{P}_3(h)$ and $\mathcal{P}_5(h)$ corresponds to the linear operator \mathcal{O}_W .
- And finally only a specific combination of the non-linear operators $\mathcal{P}_{\square H}(h)$, $\mathcal{P}_6(h)$, $\mathcal{P}_7(h)$, $\mathcal{P}_8(h)$, $\mathcal{P}_9(h)$ and $\mathcal{P}_{10}(h)$ corresponds to the linear operator $\mathcal{O}_{\square\Phi}$.

It is necessary to go to the next order in the linear basis, $d = 8$, to identify the operators which break these correlations. For instance it can be checked that, for the first two correlations, the linear $d = 8$ operators

$$\left((D_\mu \Phi)^\dagger \Phi \right) \hat{B}^{\mu\nu} \left(\Phi^\dagger D_\nu \Phi \right) \quad \text{and} \quad \left((D_\mu \Phi)^\dagger \Phi \right) \hat{W}^{\mu\nu} \left(\Phi^\dagger D_\nu \Phi \right) \quad (3.16)$$

correspond separately to $\mathcal{P}_4(h)$ and $\mathcal{P}_5(h)$, respectively. These different numbers of independent couplings are translated into distinctive signatures that we proceed to describe.

3.1.2 A different phenomenology

In this Subsection we study the phenomenology of the non-linear effective Lagrangian operators and the discriminating signatures with respect to the linear ones. This includes testable effects in trilinear and quartic interaction vertices. For the sake of brevity we focus here on trilinear interactions, though in Ref. [97] the quartic gauge boson interactions were also discussed.

Trilinear interactions

As in Chapter 2, the first step previous to showing the contributions of the operators to the pure gauge and Higgs-gauge interactions is to fix the renormalization procedure. As before, we work on the Z -scheme, with α_s , G_F , M_Z , α_{em} and M_H as input parameters¹. In the following expressions it is then understood that when an alternative parameter is written, for instance g , g' , v , e or the mixing angle, they have to be expressed in terms of the input parameters.

Regarding the $\mathcal{F}_i(h)$ functions, for concreteness we assume the parametrization

$$\mathcal{F}_i(h) \equiv 1 + 2\tilde{a}_i \frac{h}{v} + \tilde{b}_i \frac{h^2}{v^2} + \dots \quad , \quad (3.17)$$

where the dots stand for higher powers of h/v , that will not be considered in what follows. To further simplify the notation, a_i and b_i will indicate

¹In the case of the non-linear analysis, with no fermionic operators included besides the Yukawa interactions, we can forget about the fermion masses for the present analysis.

3.1. DISENTANGLING A DYNAMICAL HIGGS

below the products $a_i \equiv c_i \tilde{a}_i$ and $b_i \equiv c_i \tilde{b}_i$, respectively, where c_i are the global operator coefficients appearing in Eq. (3.7). Below $s_{2\theta}$ and $c_{2\theta}$ stand for $\sin 2\theta_W$ and $\cos 2\theta_W$ of the weak mixing angle, respectively.

Working in the unitary gauge one can easily show that $\mathcal{P}_B(h)$, $\mathcal{P}_W(h)$, $\mathcal{P}_G(h)$, $\mathcal{P}_H(h)$, $\mathcal{P}_1(h)$ and $\mathcal{P}_{12}(h)$ introduce corrections to the SM kinetic terms, and in consequence field redefinitions are necessary to obtain canonical kinetic terms. As it was the case with \mathcal{O}_{WW} , \mathcal{O}_{BB} and \mathcal{O}_{GG} in the linear expansion, $\mathcal{P}_B(h)$, $\mathcal{P}_W(h)$ and $\mathcal{P}_G(h)$ can be considered innocuous operators with respect to \mathcal{L}_0 , as the impact on the latter is totally eliminated by ineffectual field and coupling constant redefinitions in similarity to Eqs. (2.11) and (2.12). On the other hand, the effects of $\mathcal{P}_H(h)$, $\mathcal{P}_1(h)$ and $\mathcal{P}_{12}(h)$ are similar to the ones of $\mathcal{O}_{\Phi,1}$, $\mathcal{O}_{\Phi,2}$ and $\mathcal{O}_{\Phi,4}$ in the linear expansion. After these considerations, and with canonical kinetic terms, we can identify the contributions of \mathcal{L}_{eff} to the input parameters:

$$\begin{aligned} \frac{\delta\alpha_{\text{em}}}{\alpha_{\text{em}}} &\simeq 4e^2 c_1 \xi + 4e^2 c_{12} \xi^2, & \frac{\delta G_F}{G_F} &\simeq 0, \\ \frac{\delta M_Z}{M_Z} &\simeq -c_T \xi - 2e^2 c_1 \xi + 2e^2 \frac{c_\theta^2}{s_\theta^2} c_{12} \xi^2, & \frac{\delta M_H}{M_H} &\simeq 0, \end{aligned} \quad (3.18)$$

where we keep only terms linear in the coefficients c_i . Regarding the W mass, and consistent with Eqs. (2.15), (2.16) and (3.15), the prediction for M_W departs from the SM expectation by

$$\begin{aligned} \frac{\Delta M_W^2}{M_W^2} &= \frac{4e^2}{c_{2\theta}} c_1 \xi + \frac{2c_\theta^2}{c_{2\theta}} c_T \xi - \frac{4e^2}{s_\theta^2} c_{12} \xi^2 \\ &= \frac{e^2}{2c_{2\theta}} f_{BW} \frac{v^2}{\Lambda^2} - \frac{c_\theta^2}{2c_{2\theta}} f_{\Phi,1} \frac{v^2}{\Lambda^2}, \end{aligned} \quad (3.19)$$

where the second line shows for comparison the corresponding expression in the linear expansion at order $d = 6$. Additionally, as it could be expected after presenting Eqs. (2.34) and (3.15), $\mathcal{P}_1(h)$ and $\mathcal{P}_T(h)$ generate tree level contributions to the oblique parameters S and T , which read

$$\alpha_{\text{em}} \Delta S = -8e^2 c_1 \xi \quad \text{and} \quad \alpha_{\text{em}} \Delta T = 2c_T \xi. \quad (3.20)$$

Hence, as we have done for the linear case, the use of EWPO is also useful here in order to strongly constrain these tree level contributing operators. We leave the numerical analysis of the constraints for the following Subsection.

In the case of the effective operators described in the non-linear Lagrangian, Eqs. (3.8)–(3.10) and (3.12), there are also important contributions to TGV's. In order to cover all the possible chiral contributions to TGV's, we have to consider the different terms in Eq. (2.31) (which come

from [52]) and add as well the pieces

$$\begin{aligned}
 & -ig_{WWV} \left\{ -ig_5^V \epsilon^{\mu\nu\rho\sigma} (W_\mu^+ \partial_\rho W_\nu^- - W_\nu^- \partial_\rho W_\mu^+) V_\sigma \right. \\
 & \quad \left. + g_6^V (\partial_\mu W^{+\mu} W^{-\nu} - \partial_\mu W^{-\mu} W^{+\nu}) V_\nu \right\}, \quad (3.21)
 \end{aligned}$$

where again $V \equiv \{\gamma, Z\}$, $g_{WW\gamma} \equiv e = gs_\theta$, $g_{WWZ} = gc_\theta$, and where $W_{\mu\nu}^\pm$ and $V_{\mu\nu}$ stand exclusively for the kinetic part of the gauge field strengths. Electromagnetic gauge invariance requires $g_5^\gamma = 0$ and in the SM $g_5^Z = g_6^\gamma = g_6^Z = 0$ in addition. A few comments are in order regarding these TGV interactions, the first one concerns the coupling g_5^V , that is already present in [52]. This is a C and P violating term that respects instead CP invariance. However even if we had considered C and P violating, but CP invariant, operators in the linear case, this anomalous TGV interaction would have received contributions only from operators at dimension eight or higher in the linear expansion. Thus, its coupling receives a contribution from leading operators in the non-linear derivative expansion, whereas it is subleading in the linear one. We exploit further this feature as a discriminating signal at the end of this Subsection and in Sec. 3.2. Furthermore, we have also introduced the terms g_6^V with respect to Eq. (2.31). These interactions are associated to operators that contain the contraction $\mathcal{D}_\mu \mathbf{V}^\mu$, while its $\partial_\mu \mathbf{V}^\mu$ part vanishes only for on-shell gauge bosons, in all generality $\mathcal{D}_\mu \mathbf{V}^\mu$ insertions could be disregarded in the present context when fermion masses are neglected. Thus, these g_6^V anomalous TGV's are irrelevant for the LHC analyses presented here. Table 3.1 shows the departures from the SM TGV values due to the effective couplings in Eq. (3.7); it illustrates the ξ and ξ^2 -weighted chiral operator contributions. For the sake of comparison, the corresponding expressions in terms of the coefficients of $d = 6$ operators in the linear expansion are shown as well, see also Eq. (2.32). We note that the coefficient λ_V (associated with a linear $d = 6$ operator, see Eq. (2.33)) is omitted here as this coupling does not receive contributions from the non-linear effective chiral Lagrangian expanded up to four derivatives. We further discuss this feature by the end of the present Subsection.

We move now to interactions involving also the Higgs boson together with the gauge fields, to which we refer as HVV couplings. These vertices can be parametrized as in Eq. (2.19), adding the following extra pieces to cover all possible non-linear contributions

$$\begin{aligned}
 \mathcal{L}_{\text{eff}}^{\text{HVV},2} \equiv & g_{HZZ}^{(4)} Z_\mu Z^\mu \square H + g_{HZZ}^{(5)} \partial_\mu Z^\mu Z_\nu \partial^\nu H + g_{HZZ}^{(6)} \partial_\mu Z^\mu \partial_\nu Z^\nu H \\
 & + g_{HWW}^{(4)} W_\mu^+ W^{-\mu} \square H + g_{HWW}^{(5)} (\partial_\mu W^{+\mu} W_\nu^- \partial^\nu H + \text{h.c.}) \\
 & + g_{HWW}^{(6)} \partial_\mu W^{+\mu} \partial_\nu W^{-\nu} H. \quad (3.22)
 \end{aligned}$$

3.1. DISENTANGLING A DYNAMICAL HIGGS

| | Coeff. $\times e^2/s_\theta^2$ | Chiral | | Linear $\times v^2/\Lambda^2$ |
|-----------------------|-----------------------------------|---|----------------------|--|
| | | $\times \xi$ | $\times \xi^2$ | |
| $\Delta\kappa_\gamma$ | 1 | $-2c_1 + 2c_2 + c_3$ | $-4c_{12} + 2c_{13}$ | $\frac{1}{8}(f_W + f_B - 2f_{BW})$ |
| Δg_6^γ | 1 | $-c_9$ | – | – |
| Δg_1^Z | $\frac{1}{c_\theta^2}$ | $\frac{s_\theta^2}{4e^2 c_{2\theta}} c_T + \frac{2s_\theta^2}{c_{2\theta}} c_1 + c_3$ | – | $\frac{1}{8}f_W + \frac{s_\theta^2}{4c_{2\theta}}f_{BW} - \frac{s_\theta^2}{16e^2 c_{2\theta}}f_{\Phi,1}$ |
| $\Delta\kappa_Z$ | 1 | $\frac{s_\theta^2}{e^2 c_{2\theta}} c_T + \frac{4s_\theta^2}{c_{2\theta}} c_1 - \frac{2s_\theta^2}{c_\theta^2} c_2 + c_3$ | $-4c_{12} + 2c_{13}$ | $\frac{1}{8}f_W - \frac{s_\theta^2}{8c_\theta^2}f_B + \frac{s_\theta^2}{2c_{2\theta}}f_{BW} - \frac{s_\theta^2}{4e^2 c_{2\theta}}f_{\Phi,1}$ |
| Δg_5^Z | $\frac{1}{c_\theta^2}$ | – | c_{14} | – |
| Δg_6^Z | $\frac{1}{c_\theta^2}$ | $s_\theta^2 c_9$ | $-c_{16}$ | – |

Table 3.1: Effective couplings parametrizing the VW^+W^- vertices defined in Eqs. (2.31) and (3.21). The coefficients in the second column are common to both the chiral and the linear expansions. In the third and fourth columns we show the specific contributions from the operators in the chiral Lagrangian. For comparison, the last column exhibits the corresponding contributions from the linear $d = 6$ operators.

Separating the contributions into SM values plus corrections we have

$$g_i^{(j)} \simeq g_i^{(j)SM} + \Delta g_i^{(j)}. \quad (3.23)$$

where we remind the reader that

$$g_{HZZ}^{(3)SM} = \frac{M_Z^2}{v} \quad \text{and} \quad g_{HWW}^{(3)SM} = \frac{2M_Z^2 c_\theta^2}{v}, \quad (3.24)$$

while the tree level SM value for all other couplings in Eqs. (2.19) and (3.22) vanish. Nevertheless, as in the linear analysis, the SM loop induced values for g_{Hgg} , $g_{H\gamma\gamma}$ and $g_{HZ\gamma}^{(2)}$ are also taken into account in the numerical analysis. Table 3.2 shows the expressions for the corrections Δg_{Hgg} , $\Delta g_{H\gamma\gamma}$, $\Delta g_{HZ\gamma}^{(1,2)}$, $\Delta g_{HWW}^{(1,2,3,4,5,6)}$, and $\Delta g_{HZZ}^{(1,2,3,4,5,6)}$, induced at tree level by the effective non-linear couplings under discussion. In writing Eq. (3.22) we have introduced the coefficients $\Delta g_{HVV}^{(4,5,6)}$: $\Delta g_{HVV}^{(4)}$ become redundant for on-shell H , while $\Delta g_{HVV}^{(5,6)}$ vanish for on-shell W_μ and Z_μ or for massless fermions. As a consequence their effects are of no relevance for the numerical LHC analyses, but we include them here for a complete exposition of the chiral contributions. Notice also that the leading chiral corrections include operators weighted by ξ powers up to ξ^2 . For the sake of comparison, the corresponding expressions in terms of the coefficients of the linear $d = 6$ operators in Eq. (3.15) are also shown again in the last column of the Table. They can be also recovered from Eq. (2.20)². As it happened in the linear

²Notice that the coefficient of $\Delta g_{HWW}^{(3)}$ can be defined also in terms of the measured value of M_W as M_W^2/e^2 . In this case the entries in columns 3–5 of Table 3.2 read $-4c_H + 4(2a_C - c_C)$, $-32\frac{e^2}{s_\theta^2}$, and $-2f_{\Phi,1} + 4f_{\Phi,4} - 4f_{\Phi,2}$ respectively in agreement with Eq. (2.20).

case with $\mathcal{O}_{\Phi,2}$ and $\mathcal{O}_{\Phi,4}$, notice that the bosonic operators $\mathcal{P}_H(h)$ and $\mathcal{P}_C(h)$ induce universal shifts to the SM-like couplings of the Higgs to weak gauge bosons. Similarly $\mathcal{P}_H(h)$ induces universal shifts to the Yukawa couplings to fermions.

| | Coeff. $\times e^2/4v$ | Chiral | | Linear $\times v^2/\Lambda^2$ |
|-----------------------------|----------------------------------|--|---|---|
| | | $\times \xi$ | $\times \xi^2$ | |
| Δg_{Hgg} | $\frac{g^2}{c_\theta^2}$ | $-2a_G$ | – | $-4f_{GG}$ |
| $\Delta g_{H\gamma\gamma}$ | 1 | $-2(a_B + a_W) + 8a_1$ | $8a_{12}$ | $-(f_{BB} + f_{WW}) + f_{BW}$ |
| $\Delta g_{HZ\gamma}^{(1)}$ | $\frac{1}{s_{2\theta}}$ | $-8(a_5 + 2a_4)$ | $-16a_{17}$ | $2(f_W - f_B)$ |
| $\Delta g_{HZ\gamma}^{(2)}$ | $\frac{c_\theta}{s_\theta}$ | $4\frac{s_\theta^2}{c_\theta^2}a_B - 4a_W + 8\frac{c_{2\theta}^2}{c_\theta^2}a_1$ | $16a_{12}$ | $2\frac{s_\theta^2}{c_\theta^2}f_{BB} - 2f_{WW} + \frac{c_{2\theta}^2}{c_\theta^2}f_{BW}$ |
| $\Delta g_{HZZ}^{(1)}$ | $\frac{1}{c_\theta}$ | $-4\frac{c_\theta^2}{s_\theta^2}a_5 + 8a_4$ | $-8\frac{c_\theta^2}{s_\theta^2}a_{17}$ | $\frac{c_\theta^2}{s_\theta^2}f_W + f_B$ |
| $\Delta g_{HZZ}^{(2)}$ | $-\frac{c_\theta^2}{s_\theta^2}$ | $2\frac{s_\theta^4}{c_\theta^4}a_B + 2a_W + 8\frac{s_\theta^2}{c_\theta^2}a_1$ | $-8a_{12}$ | $\frac{s_\theta^4}{c_\theta^4}f_{BB} + f_{WW} + \frac{s_\theta^2}{c_\theta^2}f_{BW}$ |
| $\Delta g_{HZZ}^{(3)}$ | $\frac{m_Z^2}{e^2}$ | $-2c_H + 2(2a_C - c_C) - 8(a_T - c_T)$ | – | $f_{\Phi,1} + 2f_{\Phi,4} - 2f_{\Phi,2}$ |
| $\Delta g_{HZZ}^{(4)}$ | $-\frac{1}{s_{2\theta}}$ | $16a_7$ | $32a_{25}$ | – |
| $\Delta g_{HZZ}^{(5)}$ | $-\frac{1}{s_{2\theta}}$ | $16a_{10}$ | $32a_{19}$ | – |
| $\Delta g_{HZZ}^{(6)}$ | $-\frac{1}{s_{2\theta}}$ | $16a_9$ | $32a_{15}$ | – |
| $\Delta g_{HWW}^{(1)}$ | $\frac{1}{s_\theta^2}$ | $-4a_5$ | – | f_W |
| $\Delta g_{HWW}^{(2)}$ | $\frac{1}{s_\theta^2}$ | $-4a_W$ | – | $-2f_{WW}$ |
| $\Delta g_{HWW}^{(3)}$ | $\frac{m_Z^2 c_\theta^2}{e^2}$ | $-4c_H + 4(2a_C - c_C) + \frac{32e^2}{c_{2\theta}^2}c_1 + \frac{16c_\theta^2}{c_{2\theta}^2}c_T$ | $-\frac{32e^2}{s_\theta^2}c_{12}$ | $-\frac{2(3c_\theta^2 - s_\theta^2)}{c_{2\theta}}f_{\Phi,1} + 4f_{\Phi,4} - 4f_{\Phi,2} + \frac{4e^2}{c_{2\theta}}f_{BW}$ |
| $\Delta g_{HWW}^{(4)}$ | $-\frac{1}{s_\theta^2}$ | $8a_7$ | – | – |
| $\Delta g_{HWW}^{(5)}$ | $-\frac{1}{s_\theta^2}$ | $4a_{10}$ | – | – |
| $\Delta g_{HWW}^{(6)}$ | $-\frac{1}{s_\theta^2}$ | $8a_9$ | – | – |

Table 3.2: The trilinear Higgs–gauge bosons couplings defined in Eqs. (2.19) and (3.22). The coefficients in the second column are common to both the chiral and linear expansions. The contributions from the operators weighted by ξ and $\xi^{\geq 2}$ are listed in the third and fourth columns, respectively. For comparison, we show in the last column the corresponding expressions for the linear expansion at order $d = 6$.

Discriminating signals

The first discriminating signature between the linear and the non-linear expansion that we describe corresponds to one of the anomalous TGV's in Eq. (2.31). As we have commented, all the linear dimension–six operators in Eq. (2.22) contain six derivatives in the non-linear derivative expansion, consequently they are subleading with respect to the ones with four derivatives. This means that while some of the dimension–six linear operators, for instance \mathcal{O}_{WWW} , contribute at the tree level to the anomalous TGV λ_V ,

3.1. DISENTANGLING A DYNAMICAL HIGGS

as we already explicitly showed in Eq. (2.33), this coupling can not receive contributions from any of the non-linear operators up to dimension four in the derivative expansion. Consequently the strength of the contributions to λ_V in the non-linear case are expected to be suppressed with respect to the rest of leading contributions. In the linear case the strength of the λ_V contributions could have the same size than all the other leading order operators instead. Therefore, a measurement of an anomalous TGV signal compatible with the nature of λ_V , which is the anomalous TGV with the most striking high energy signature as we will see in the following, would point to a linear nature of the Higgs boson.

Another promising distinctive signature follows the same spirit, but in the opposite direction. As we have commented in the previous Subsection, for large ξ all chiral operators weighted by ξ^n with $n \geq 2$, Eqs. (3.9) and (3.10), are equally relevant to the ξ -weighted ones in Eqs. (3.8) and (3.12). However their siblings require operators of dimension $d \geq 8$ in the linear expansion. A case of special interest is $\mathcal{P}_{14}(h)$, as some of the couplings encoded in this operator are absent in the SM Lagrangian. This fact provides a viable strategy to test the nature of the physical Higgs. Here, we show the example of the anomalous $Z - W - W$ and $\gamma - Z - W - W$ vertices, assuming for simplicity that the $\mathcal{F}_{14}(h)$ function admits a polynomial expansion in h/v . The operator $\mathcal{P}_{14}(h)$ contains the couplings

$$\varepsilon^{\mu\nu\rho\lambda}\partial_\mu W_\nu^+ W_\rho^- Z_\lambda \mathcal{F}_{14}(h), \quad \varepsilon^{\mu\nu\rho\lambda} Z_\mu A_\nu W_\rho^- W_\lambda^+ \mathcal{F}_{14}(h), \quad (3.25)$$

which correspond to an anomalous $Z - W - W$ TGV and to an anomalous $\gamma - Z - W - W$ quartic vertex, respectively. These couplings are not present neither in the SM nor in the $d = 6$ linear Lagrangians. The anomalous TGV corresponds to g_5^Z in the parametrization [52] in Eq. (3.21). A signal of this type of C and P violating, but CP invariant, interactions at colliders, with a strength comparable to that expected for the couplings in the $d = 6$ linear Lagrangian, would be a clear hint of strong dynamics in the EWSB sector. Consequently this promising TGV distinctive signal is studied in detail in the collider analysis in Sec. 3.2.

These two preceding discriminating signals come directly from the different intrinsic nature of the two expansions. Additional differences are found when considering only the ξ -weighed operators.

The parameter ξ is a free parameter in the effective chiral approach, nevertheless, in concrete composite Higgs models EW corrections imply $\xi \lesssim 0.2 - 0.4$ [135] (more constraining bounds $\xi \lesssim 0.1 - 0.2$ had been advocated in older analyses [136–138]). Therefore it is interesting, for the sake of comparison between the two expansions, to consider the truncation of the chiral \mathcal{L}_{eff} which keeps only the terms weighted by ξ and disregard those weighted by higher ξ powers. Hence, we analyze now only those operators in Eqs. (3.8) and (3.12). We refer to this truncation as $\mathcal{L}_{\text{eff}}^\xi$ and define

$\mathcal{L}_{\text{chiral}}^\xi \equiv \mathcal{L}_0 + \mathcal{L}_{\text{eff}}^\xi$. This way all operators in $\mathcal{L}_{\text{eff}}^\xi$ have by definition lowest dimensional linear siblings of $d = 6$. We compare $\mathcal{L}_{\text{chiral}}^\xi$ with the $d = 6$ linear expansion in the previous Chapter. For low enough values of ξ , that is, when the new physics scale $\Lambda_s \gg v$, $\mathcal{L}_{\text{chiral}}^\xi$ is expected to collapse into the $d = 6$ linear Lagrangian³ if it should account correctly for EWSB via an $SU(2)_L$ doublet scalar, but the non-linear Lagrangian encodes more general scenarios (for instance that for a SM singlet) as well.

The comparison of the effects in the non-linear versus the linear expansion is illuminating when done in the context of the maximal set of independent (and thus non-redundant) operators in the gauge boson-Higgs sector for each expansion: comparing complete bases of those characteristics. The number of independent bosonic operators that induce leading deviations in gauge-Higgs couplings turns out to be different for both expansions: ten $d = 6$ operators in the linear expansion (Eqs (2.2) and (2.21)), for seventeen ξ -weighted operators in the chiral one as we have already pointed out, see Eqs. (3.8) and (3.12). For illustration, further details are given here on one example pointed out in the previous Subsection: $\mathcal{P}_2(h)$ and $\mathcal{P}_4(h)$ versus the $d = 6$ operator \mathcal{O}_B . From Eq. (3.15) it followed that only the combination $\mathcal{P}_2(h) + 2\mathcal{P}_4(h)$ has a $d = 6$ linear equivalent (with $\mathcal{F}_i(h)$ substituted by $(1 + h/v)^2$). In the unitary gauge $\mathcal{P}_2(h)$ and $\mathcal{P}_4(h)$ read:

$$\mathcal{P}_2(h) = 2ieg^2 A_{\mu\nu} W^{-\mu} W^{+\nu} \mathcal{F}_2(h) - 2 \frac{ie^2 g}{\cos \theta_W} Z_{\mu\nu} W^{-\mu} W^{+\nu} \mathcal{F}_2(h), \quad (3.26)$$

$$\mathcal{P}_4(h) = -\frac{eg}{\cos \theta_W} A_{\mu\nu} Z^\mu \partial^\nu \mathcal{F}_4(h) + \frac{e^2}{\cos^2 \theta_W} Z_{\mu\nu} Z^\mu \partial^\nu \mathcal{F}_4(h), \quad (3.27)$$

with their coefficients c_2 and c_4 taking arbitrary (model dependent) values. In contrast, their $d = 6$ sibling \mathcal{O}_B results in the combination:

$$\begin{aligned} \mathcal{O}_B = & \frac{ieg^2}{8} A_{\mu\nu} W^{-\mu} W^{+\nu} (v + h)^2 - \frac{ie^2 g}{8 \cos \theta_W} Z_{\mu\nu} W^{-\mu} W^{+\nu} (v + h)^2 \\ & - \frac{eg}{4 \cos \theta_W} A_{\mu\nu} Z^\mu \partial^\nu h (v + h) + \frac{e^2}{4 \cos^2 \theta_W} Z_{\mu\nu} Z^\mu \partial^\nu h (v + h). \end{aligned} \quad (3.28)$$

In consequence, the following interactions encoded in \mathcal{O}_B — and for the precise Lorentz structures shown above— get decorrelated in a general non-linear analysis:

- $\gamma - W - W$ from $\gamma - Z - h$ and $Z - Z - h$, and $Z - W - W$ from $\gamma - Z - h$ and $Z - Z - h$; these are examples of interactions involving different number of external Higgs legs.
- $\gamma - W - W - h$ from $\gamma - Z - h$ and $Z - Z - h$, and $Z - W - W - h$ from $\gamma - Z - h$ and $Z - Z - h$, which are interactions involving the same number of external Higgs legs.

³ After including the dimension-six operators in Eq. (2.22) as well.

3.1. DISENTANGLING A DYNAMICAL HIGGS

In brief, such decorrelations are expected among the leading SM deviations in a generic non-linear expansion but they require us to consider $d = 8$ operators in scenarios with linearly realized EWSB. This statement is a physical effect, which means that it holds irrespective of the linear basis used. The study of the (de)correlations described represents an interesting method to investigate the nature of the light Higgs. The argument developed above focuses on just one operator, for illustration, but a parallel analysis on (de)correlations also applies to the interactions described by $\mathcal{P}_3(h)$ and $\mathcal{P}_5(h)$ versus those in the $d = 6$ linear operator \mathcal{O}_W . Obviously, in order to firmly establish the pattern of deviations expected, all possible operators at a given order of an expansion should be considered together, and this is done in Sec. 3.1.3.

Notice that the decorrelation in the point above is exactly the promising correlation that we have studied in detail in Chapter 2 in the context of the linear effective Lagrangian approach. There we have observed that the contributions of \mathcal{O}_W and \mathcal{O}_B to both HVV and TGV interactions at the same time lead to a promising way of further testing the EWSB mechanism and the linear nature of the Higgs boson. Here we see that this correlation may be broken in the case of a dynamical Higgs, a decorrelation that could point as a consequence to strong dynamics in the EWSB sector. The observation of this (de)correlation becomes very interesting because it involves HVV and TGV interactions, two couplings that are currently measured in different experiments and channels as we have already described. Additional (de)correlations when one considers chiral operators weighted by higher powers of ξ^n can be found in [97].

3.1.3 Status after the 7 and 8 TeV LHC runs

For this part of the analysis we focus on the bounds that can be derived on the ξ -weighted non-linear operators. As in the linear case, we start constraining the operators that contribute at the tree level to the S , T and U parameters. As we have described in the previous Chapter, the most precise determination of S , T and U comes from a global fit to EWPD, yielding the values and correlation matrix in Sec. 2.2.3, Eqs. (2.63) and (2.64). Using this information and the tree level contributions of the operators $\mathcal{P}_1(h)$ and $\mathcal{P}_T(h)$ to these observables, see Eq. (3.20), we can build a χ^2 as in Eq. (2.65). The corresponding 95% CL allowed ranges for the $\mathcal{P}_1(h)$ and $\mathcal{P}_T(h)$ coefficients that we obtain are

$$-4.7 \times 10^{-3} \leq \xi c_1 \leq 4 \times 10^{-3} \quad \text{and} \quad -2 \times 10^{-3} \leq \xi c_T \leq 1.7 \times 10^{-3} . \quad (3.29)$$

These constraints render the contribution of $\mathcal{P}_1(h)$ and $\mathcal{P}_T(h)$ to the gauge-boson self-couplings and to the present Higgs data too small to give any observable effect. Consequently we do not include them in the following

discussion, what is analogous to the treatment of $\mathcal{O}_{\Phi,1}$ and \mathcal{O}_{BW} in the previous Chapter.

We move now to study the effects of TGV data on the non-linear operators. Recovering the LEP data in Eq. (2.56) with the correlation factor $\rho = 0.11$, we can construct a χ^2 as in Eq. (2.57). If we consider the ξ -weighted TGV contributions, the impact of $\mathcal{P}_2(h)$ and $\mathcal{P}_3(h)$ on the coefficients $\Delta\kappa_\gamma$, Δg_1^Z and $\Delta\kappa_Z$ has been described in Table 3.1, and is compatible with the framework of the LEP analysis [42] in Eq. (2.67), which we remind the reader is still the TGV measurement leading to the strongest constraints. We present in Table 3.3 the derived 90% CL allowed ranges on the coefficients c_2 and c_3 from the analysis of this described TGV data.

| | 90% CL allowed range | |
|-------------------------|---|--|
| | Set A | Set B |
| $a_G\xi(\cdot 10^{-3})$ | $s_Y = +1: [-1.8, 2.1] \cup [6.5, 10]$ $s_Y = -1: [-9.9, -6.5] \cup [-2.1, 1.8]$ | $s_Y = +1: [-0.78, 2.4] \cup [6.5, 12]$ $s_Y = -1: [-12, -6.5] \cup [-2.3, 0.75]$ |
| $a_4\xi$ | [-0.47, 0.14] | |
| $a_5\xi$ | [-0.33, 0.17] | |
| $a_W\xi$ | [-0.12, 0.51] | |
| $a_B\xi$ | [-0.50, 0.21] | |
| $c_H\xi$ | [-0.66, 0.66] | [-1.1, 0.49] |
| $c_2\xi$ | [-0.12, 0.076] | |
| $c_3\xi$ | [-0.064, 0.079] | |

Table 3.3: 90% CL allowed ranges of the coefficients of the operators contributing to Higgs data (a_G , a_4 , a_5 , a_W , a_B , and c_H) and to TGV's (c_2 and c_3). For the coefficients a_4 , a_5 , a_W , and a_B , for which the range is almost the same for the analysis with both sets and both values of s_Y , we show the inclusive range of the four analysis. For c_H the allowed range is the same for both signs of s_Y .

Finally, let us focus on the constraints on ξ -weighted operators that can be derived from the analysis of the Higgs data coming from Tevatron and LHC. From the list of ξ -weighted operators, there are seven bosonic operators in this category⁴

$$\mathcal{P}_G(h), \mathcal{P}_4(h), \mathcal{P}_5(h), \mathcal{P}_B(h), \mathcal{P}_W(h), \mathcal{P}_H(h), \mathcal{P}_C(h). \quad (3.30)$$

For the present analysis we consider sets of *only* six of them simultaneously,

⁴In the present Higgs data analysis, the Higgs state is on-shell and in this case $\Delta g_{HVV}^{(4)}$ can be recasted as a M_H^2 correction to $\Delta g_{HVV}^{(3)}$. Thus the contribution from a_7 , *i.e.* the coefficient of $\mathcal{P}_7(h)$ to the Higgs observables, can be reabsorbed in a redefinition of $2a_C - c_C$. For possible future $\mathcal{P}_7(h)$ off-shell effects see [139].

3.1. DISENTANGLING A DYNAMICAL HIGGS

in two different frameworks, leaving out a different coupling in each set. In the first set, **A**, we neglect $\mathcal{P}_C(h)$ and in the second one, **B**, we link its contribution to that of $\mathcal{P}_H(h)$, so the 6 parameters in each set read:

$$\text{Set A : } \quad a_G, a_4, a_5, a_B, a_W, c_H, 2a_C - c_C = 0, \quad (3.31)$$

$$\text{Set B : } \quad a_G, a_4, a_5, a_B, a_W, c_H = 2a_C - c_C. \quad (3.32)$$

For both sets we explore the sensitivity of the results to the sign of the Higgs–fermion couplings by performing analyses with both values of the discrete parameter $s_\gamma = \pm$.

As mentioned before, $\mathcal{P}_H(h)$ and $\mathcal{P}_C(h)$ induce a universal shift of the SM–like HVV couplings involving EW gauge bosons, while $\mathcal{P}_H(h)$ also induces a universal shift of the Yukawa Higgs–fermion couplings. Thus, the two sets above correspond to the case in which the shift to the SM–like HVV couplings involving EW bosons and to the Yukawa Higgs–fermion couplings are the same (**set A**), or in the case where the shift of the Yukawa Higgs–fermion couplings is totally unrelated to the modification of the HVV couplings involving EW bosons (**set B**). In both sets we keep all other five operators which induce modifications of the HVV couplings with different Lorentz structures than those of the SM, as well as the tree level contributions to the SM loop induced vertices $h\gamma\gamma$, $h\gamma Z$ and hgg . Our choice allows us to stay close to the spirit of this Section, existing data confronting directly the gauge and gauge–Higgs sector, while performing a powerful six–dimensional exploration of possible correlations.

In order to obtain the present constraints on the coefficients of the bosonic operators listed in Eqs. (3.31) and (3.32) we perform a chi–square test using the available data on the signal strengths. All the technical details of this analysis follow the fit we have performed in the case of the linear expansion. Therefore, the details regarding the statistical tools used, the treatment of uncertainties, calculations, data included etc can be found in Section 2.2.1.

The results of the analysis are presented in Fig. 3.1. There we display the chi–square ($\Delta\chi^2$ indeed) dependence from the analysis of the Higgs data on the six bosonic couplings for the two sets **A** and **B** of operators, and for the two values of the discrete parameter $s_\gamma = \pm$. As in the linear case, for the illustration of the results, in each panel $\Delta\chi^2$ is shown after marginalizing over the other five parameters not shown. The first thing we notice is the lack of any substantial difference between both sets, **A** and **B**, in the determination of the five common parameters with only slight differences in a_G , that we explain below. Actually, the quality of the fit is equally good for both sets, that have very close values for the χ^2 in the minima ($|\chi_{\min,A}^2 - \chi_{\min,B}^2| < 0.5$). We remind the reader, that as in the linear case, when considering only Higgs data (56 observables), the SM lays at $\chi_{SM}^2 = 68.1$, within the 4% CL region in the current six dimensional parameter space of either set.

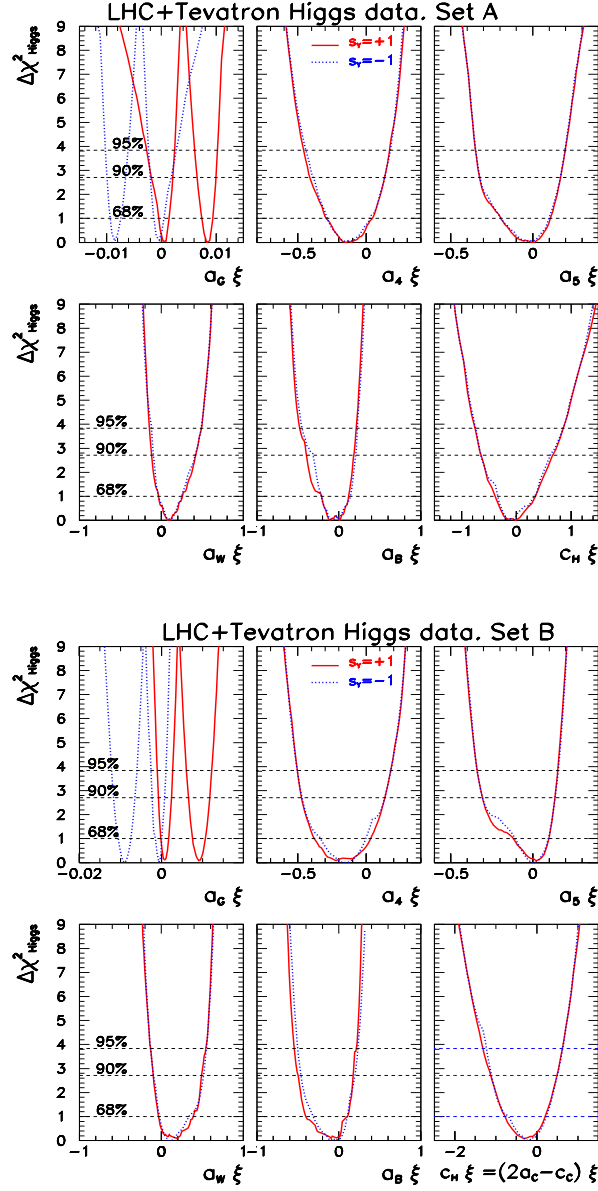


Figure 3.1: $\Delta\chi^2$ dependence on the coefficients of the bosonic operators in Eq. (3.30) from the analysis of all Higgs collider (ATLAS, CMS and Tevatron) data. The six upper (lower) panels corresponds to analysis with set **A** (**B**), see text for details. In each panel the red solid (blue dotted) line stands for the analysis with the discrete parameter $s_Y = +(-)$. We have marginalized over the five undisplayed variables in each panel.

3.1. DISENTANGLING A DYNAMICAL HIGGS

Furthermore, in Fig. 3.1, for each set, the two curves of $\Delta\chi^2$ for $s_Y = \pm$ are defined with respect to the same χ_{\min}^2 , corresponding to the minimum value of the two signs. However, as seen in the Figure, the difference is inappreciable. In other words, we find that in both six-parameter analyses the quality of the description of the data is equally good for both signs of the Higgs-fermion couplings; for either set $|\chi_{\min,+}^2 - \chi_{\min,-}^2|$ is compatible with zero within numerical accuracy. This is consistent with the several degeneracies we have described in the case of the linear analysis of the previous Chapter. In contrast, if all the anomalous couplings are set to zero the quality of the fit is dramatically different for both signs, with $\chi_-^2 - \chi_+^2 \sim 26$. This arises from the different sign of the interference between the W - and top-loop contributions to $H\gamma\gamma$, which is negative for the SM value $s_Y = +$, but positive for $s_Y = -$ which increases $BR_-(h \rightarrow \gamma\gamma)/BR_{SM}(h \rightarrow \gamma\gamma) \sim 2.5$, a value strongly disfavored by data after the complete 7 and 8 TeV data sets have been analyzed. However, once the effect of the 6 bosonic operators is included, in particular that of $\mathcal{P}_B(h)$ and $\mathcal{P}_W(h)$, which give a tree level contribution to the $H\gamma\gamma$ vertex, we find that both signs of the Higgs-fermion couplings are equally probable.

In the Figure we also see that, in all cases, $\Delta\chi^2$ as a function of a_G exhibits two degenerate minima, as it happened with f_g in the linear case. As in there, the degeneracy is due to the interference between the SM and the anomalous contribution. For the values in the middle of the two minima the gluon fusion Higgs production cross section is too depleted. Obviously the allowed values of a_G around both minima are different for $s_Y = +$ and $s_Y = -$, as a consequence of the different relative sign of the a_G and the top-loop contributions to the Hgg vertex. In the convention chosen for the chiral Lagrangian, the relative sign of both contributions is negative (positive) for $s_Y = +$, ($s_Y = -$), so that the non-zero minimum occurs for a_G around 0.01 (-0.01). The precise value of the a_G coupling at the minima is slightly different for the analysis with set **A** and **B**, due to the effect of the coefficient c_H near the minima, which shifts the contribution of the top-loop by a slightly different quantity in both analysis.

In the present case, as it happened with \mathcal{O}_{WW} and \mathcal{O}_{BB} in the linear analyses, Fig. 3.1 also shows that in all the non-linear sets the curves for a_B and a_W are almost “mirror symmetric”. The reason behind this strongly correlated behavior is analogous to the one described in Chapter 2: a_B and a_W give the dominant contributions to the Higgs branching ratio into two photons, which is proportional to $a_B + a_W$. In Table 3.3 we list the corresponding 90% CL allowed ranges for the six coefficients and for the different variants of the analysis. With the expected uncertainties attainable in the Higgs signal strengths in CMS and ATLAS at 14 TeV with an integrated luminosity of 300 fb^{-1} [140, 141], we estimate that the sensitivity to those couplings can improve by a factor $\mathcal{O}(3 - 5)$ with a similar analysis.

Decorrelating TGV and Higgs data

Following the structure of the study of the linear effective Lagrangian approach, we close the non-linear analysis of the ξ -weighted operators focusing on the interplay between HVV and TGV measurements and the discussed (de)correlations in the different expansions. In the linear case we have observed that both sets of interactions are connected and correlated thanks to the operators \mathcal{O}_B and \mathcal{O}_W . In the notation of this Chapter, the linear expansion would correspond to $2c_2 = a_4$ and $2c_3 = -a_5$, which establishes the interesting complementarity in the experimental searches for the signals in TGV and HVV couplings in the linear expansion. As a consequence, the analysis of the data from the two sectors is essential to further test the linear realization, especially after we have observed that currently the constraints from both types of measurements lead to comparable but complementary bounds, as seen in Fig. 2.7 and the related discussion in Chapter 2. In contrast, we stress that in the context of ξ -weighted operators in the chiral expansion, the results from the TGV analysis and those from the HVV analysis apply to two independent sets of operators as discussed in the previous Subsection. Therefore, in the event of an anomalous observation in either of these two sectors, the presence of this (de)correlation would allow for a direct test of the nature of the Higgs boson. This is best illustrated in Fig. 3.2. There the results of the combined analysis of the TGV and HVV data, in the chiral expansion, are projected into combinations of the coefficients of the operators $\mathcal{P}_2(h)$, $\mathcal{P}_3(h)$, $\mathcal{P}_4(h)$ and $\mathcal{P}_5(h)$:

$$\begin{aligned}\Sigma_B &\equiv 4(2c_2 + a_4), & \Sigma_W &\equiv 2(2c_3 - a_5), \\ \Delta_B &\equiv 4(2c_2 - a_4), & \Delta_W &\equiv 2(2c_3 + a_5),\end{aligned}\tag{3.33}$$

defined such that at order $d = 6$ of the linear regime $\Sigma_B = f_B$, $\Sigma_W = f_W$, while $\Delta_B = \Delta_W = 0$. The use of these variables helps us to study this (de)correlation in order to access the intrinsic Higgs nature. In the left panel of Fig. 3.2, the $(0, 0)$ coordinate corresponds to the SM point, while in the right panel it corresponds to the linear regime (at order $d = 6$). If future data pointed to a departure from $(0, 0)$ in the variables of the left panel it would indicate BSM physics irrespective of the linear or non-linear character of the underlying dynamics. Such a departure in the right panel would be consistent with a non-linear realization of EWSB instead. For concreteness the Figures are shown for the $s_Y = +$ analysis with set **A**, but very similar results hold for the other variants of the analysis.

3.2 Scrutinizing the WWZ vertex

The study of the linear effective Lagrangian presented in Chapter 2 and the comparison with the chiral effective expansion presented in the first part

3.2. SCRUTINIZING THE WWZ VERTEX

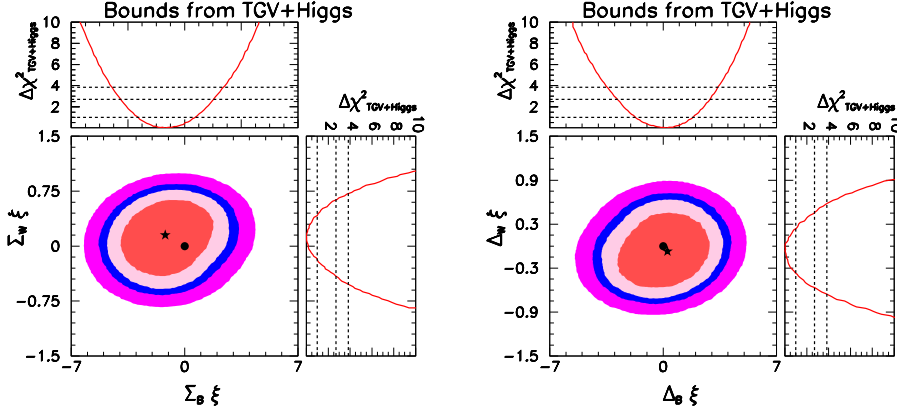


Figure 3.2: **Left:** A BSM sensor irrespective of the type of expansion: constraints from TGV and Higgs data on the combinations $\Sigma_B = 4(2c_2 + a_4)$ and $\Sigma_W = 2(2c_3 - a_5)$, which converge to f_B and f_W in the linear $d = 6$ limit. The dot at $(0, 0)$ signals the SM expectation. **Right:** A non-linear versus linear discriminator: constraints on the combinations $\Delta_B = 4(2c_2 - a_4)$ and $\Delta_W = 2(2c_3 + a_5)$, which would take zero values in the linear (order $d = 6$) limit (as well as in the SM), indicated by the dot at $(0, 0)$. For both Figures the lower left panels show the 2-dimensional allowed regions at 68%, 90%, 95%, and 99% CL after the marginalization with respect to the other six parameters ($a_G, a_W, a_B, c_H, \Delta_B$, and Δ_W) and ($a_G, a_W, a_B, c_H, \Sigma_B$, and Σ_W) respectively. The stars correspond to the best fit points of the analysis. The upper left and lower right panels give the corresponding 1-dimensional projections over each of the two combinations, after marginalizing over the undisplayed parameters.

of the present Chapter, both point to a common conclusion: the study of TGV interactions can seed interesting information to understand the EWSB sector. With this motivation we focus this Section in understanding, improving and quantifying the capability of the LHC to perform measurements of anomalous TGV interactions, in particular on the WWZ vertex.

3.2.1 Lagrangian for TGV interactions

The most general form of the WWZ vertex compatible with Lorentz invariance and with at least one W boson on-shell, is given by the effective Lagrangian in [52]. We have partially presented the terms in this Lagrangian

in Eqs. (2.31) and (3.21), and its complete form can be written as:

$$\begin{aligned}
 \mathcal{L}_{\text{eff}}^{WWZ} = & g_{WWZ} \left(-ig_1^Z \left(W_{\mu\nu}^\dagger W^\mu Z^\nu - W_\mu^\dagger W^{\mu\nu} Z_\nu \right) - i\kappa_Z W_\mu^\dagger W_\nu Z^{\mu\nu} \right. \\
 & -i\frac{\lambda_Z}{M_W^2} W_{\rho\mu}^\dagger W_\nu^\mu Z^{\nu\rho} - g_5^Z \epsilon^{\mu\nu\rho\sigma} (W_\mu^\dagger \partial_\rho W_\nu - \partial_\rho W_\mu^\dagger W_\nu) Z_\sigma \quad (3.34) \\
 & \left. +g_4^Z W_\mu^\dagger W_\nu (\partial^\mu Z^\nu + \partial^\nu Z^\mu) - i\tilde{\kappa}_Z W_\mu^\dagger W_\nu \tilde{Z}^{\mu\nu} - i\frac{\tilde{\lambda}_Z}{M_W^2} W_{\sigma\mu}^\dagger W_\nu^\mu \tilde{Z}^{\nu\sigma} \right)
 \end{aligned}$$

where $V^{\mu\nu} = \partial^\mu V^\nu - \partial^\nu V^\mu$, $\tilde{Z}^{\mu\nu} = \frac{1}{2}\epsilon^{\mu\nu\rho\sigma} Z_{\rho\sigma}$ and $g_{WWZ} = g_{C\theta}$. Within this parametrization the couplings g_1^Z , κ_Z and λ_Z are both C and P conserving, while $\tilde{\kappa}_Z$ and $\tilde{\lambda}_Z$ are P odd and violate CP and g_4^Z violates C and CP . Finally g_5^Z violates C and P , but it is the CP conserving term we have discussed in the previous Section. Recovering once more for completeness the values in the SM, we see that in there $g_1^Z = \kappa_Z = 1$ and $\lambda_Z = g_4^Z = g_5^Z = \tilde{\kappa}_Z = \tilde{\lambda}_Z = 0$. The vertices in Eq. (3.34) exhaust all the possible Lorentz structures for the WWZ vertex and for on-shell bosons (or for negligible fermion masses), the relevant case at the LHC. The Lagrangian in Eq. (3.34) has been established as the common Lorentz invariant parametrization to measure the TGV interactions and to experimentally search for possible non-SM deviations in the WWZ vertex. The couplings in Eq. (3.34) are not ordered in terms of any hierarchy, but as we have already seen for the CP -even structures, they can be easily linked to the different complete effective Lagrangian descriptions. This way, in addition to g_1^Z and κ_Z , that are already present in the SM, we find that after imposing the $SU(2)_L \times U(1)_Y$ gauge symmetry, g_1^Z , κ_Z , λ_Z , $\tilde{\kappa}_Z$ and $\tilde{\lambda}_Z$ are generated by leading operators in the linear expansion, while g_1^Z , κ_Z , g_5^Z , $\tilde{\kappa}_Z$ and g_4^Z can be generated by leading chiral operators. The model independent parametrization is extremely useful since it covers all possible new structures that can be present on the WWZ vertex regardless of the approach we are considering, thus allowing a comparison between them.

The Lagrangian in Eq. (3.34) has been used for long by the several experimental collaborations, from LEP to the LHC, with the invaluable impact of the Tevatron measurements. So far all the measurements are consistent with the SM expectations, we present in Table 3.4 a combination of some of the direct searches as performed by the Particle Data Group [40]. At LEP, see for instance [42, 145–149], the analyses of WW pair production and W single production were performed in the different W decay modes: hadronic, leptonic and semileptonic channels, and for the different collider energies, ranging from 183 to 209 GeV. The analyses were done by the different LEP collaborations; ALEPH, DELPHI, L3 and OPAL. There, the studies were usually based on the observations of the W production angular distributions and the distributions of the W decay products, as well as on

3.2. SCRUTINIZING THE WWZ VERTEX

| couplings | PDG bounds | Indirect limits | Unit. WW | Unit. WZ |
|---------------------|----------------------------|--------------------|------------|------------|
| Δg_1^Z | $-0.016_{-0.019}^{+0.022}$ | $[-0.051, 0.0092]$ | 2.7 | 0.22 |
| $\Delta \kappa_Z$ | $-0.076_{-0.056}^{+0.059}$ | $[-0.050, 0.0039]$ | 0.22 | 3.5 |
| λ_Z | $-0.088_{-0.057}^{+0.060}$ | $[-0.061, 0.10]$ | 0.15 | 0.14 |
| g_5^Z | -0.07 ± 0.09 | $[-0.085, 0.049]$ | 2.7 | 1.7 |
| g_4^Z | -0.30 ± 0.17 | — | 2.7 | 0.22 |
| $\tilde{\kappa}_Z$ | $-0.12_{-0.04}^{+0.06}$ | — | 2.7 | 3.5 |
| $\tilde{\lambda}_Z$ | -0.09 ± 0.07 | — | 0.15 | 0.14 |

Table 3.4: Compilation of available limits on the anomalous TGV interactions. The second column contains a compilation of the direct searches performed by the Particle Data Group [40]. The indirect bounds are presented in the third column [54, 142–144], where the entries not evaluated in the literature are marked as —. The fourth and fifth columns contain the bounds derived from the processes $qq \rightarrow W^+W^-$ and $W^\pm Z$ [150], imposing that unitarity is satisfied for energies below 2 TeV, see text for details.

the WW cross section determination. It is interesting to note that the strongest bounds on some of the different anomalous TGV’s still come from LEP studies. In particular the ones more relevant for this thesis: the g_1^Z , κ_Z and λ_Z strongest bounds in the framework of Eq. (2.67) come from [42], while the unique direct bounds on g_5^Z come from LEP [145–147], and the same happens with g_4^Z , $\tilde{\kappa}_Z$ and $\tilde{\lambda}_Z$ [147–149]. In contrast, at both Tevatron (see for instance [43–45]), and at the LHC (see some of the initial 7 TeV searches [46–51]), the higher collision energies, clearly above the WW and WZ thresholds, make the use of kinematic variables related to the energy of the event more suitable for the measurement of TGV’s in gauge boson pair production processes. In Table 3.4, besides the compilation of direct bounds from PDG of the second column [40], we can also observe in the third column the existing indirect bounds from EWPD and the study of the one-loop contributions of some of the anomalous TGV’s to Z physics, see for instance [54, 142–144]. The last two columns contain the bounds derived from the processes $qq \rightarrow W^+W^-$ and $W^\pm Z$ [150], imposing that unitarity is satisfied for energies below 2 TeV, we will further discuss unitarity at the end of Sec. 3.2.2.

With the existing bounds presented we proceed to study the anomalous TGV interactions at the LHC. There, as we have commented, the anomalous couplings will be eventually subject to a more scrutiny via the production of EW gauge boson pairs, for instance $W\gamma$, WZ and WW . Preliminary studies showed that at 14 TeV and with $30 - 100 \text{ fb}^{-1}$ of integrated luminosity the LHC could probe these couplings [151]. Now we proceed to study all the possible WWZ TGV’s in Eq. (3.34) at the LHC, trying to understand

their most characteristic signals and how they can be used to optimize the experimental searches.

3.2.2 Optimizing measurements: preliminary analysis

We study here the potential of the LHC to probe deviations from the SM predictions for the WWZ interaction, through the processes

$$pp \rightarrow W^+W^- \rightarrow \ell^+\ell'^-\cancel{E}_T \text{ and} \quad (3.35)$$

$$pp \rightarrow W^\pm Z \rightarrow \ell'^\pm\ell^+\ell^-\cancel{E}_T, \quad (3.36)$$

where $\ell^{(\prime)}$ = e or μ , and \cancel{E}_T stands for the missing transverse energy in the event, that accounts for the presence of the elusive neutrinos. For both processes the cross sections take the form

$$\sigma = \sigma_{\text{SM}} + \sum_i \sigma_{\text{int}}^i g_{\text{ano}}^i + \sum_{i,j \geq i} \sigma_{\text{ano}}^{ij} g_{\text{ano}}^i g_{\text{ano}}^j, \quad (3.37)$$

where σ_{SM} , σ_{int}^i , and σ_{ano}^{ij} are, respectively, the SM contribution, the interference between the SM and the anomalous contributions, and the pure anomalous contributions. If no CP -odd asymmetry is built, the interference terms σ_{int}^i for the CP violating couplings are irrelevant. Furthermore, as it is usually assumed in the experimental searches, for the time being we only consider one anomalous TGV departing from its corresponding SM value at a time. This is justified since our purpose in this preliminary analysis is to optimize and estimate the reachable sensitivity to anomalous TGV interactions at the LHC, while in the second part we will focus only on g_5^Z , g_4^Z , $\tilde{\kappa}_Z$ and $\tilde{\lambda}_Z$ TGV's. Nevertheless, we remain the reader that this assumption prevents the reinterpretation in terms of effective Lagrangians. Thus we believe that when the experimental analyses perform measurements of g_1^Z , κ_V and λ_V , multi-dimensional setups in the framework of Eq. (2.67) should be followed. See the related discussions in Section 2.4 of the previous Chapter.

One of the focus of this initial analysis is to compare the LHC sensitivity to TGV's between the two processes considered. In addition, we want to decipher which variables and cuts are the most adequate to analyze the different TGV's. With these purposes in mind, we perform a simulation, which includes the relevant sources of background events as well as a realistic selection of kinematic cuts in order to increase the signal to background ratio in the processes. Regarding the SM background contributions to $pp \rightarrow \ell^+\ell'^-\cancel{E}_T$, they include as the main source the EW processes leading to this final state, especially the irreducible background from SM WW production, but also ZZ production with one of the Z 's decaying into charged leptons and the other into neutrinos. In addition, $t\bar{t}$ production with the top quarks decaying semi-leptonically is also a dangerous source of background events if no jet veto is imposed, as we will see. In the case of WZ production and

3.2. SCRUTINIZING THE WWZ VERTEX

the $pp \rightarrow \ell^\pm \ell'^+ \ell'^- \cancel{E}_T$ channel, the main SM background comes from the EW production of WZ pairs, but ZZ production with the subsequent decay of the Z 's into leptons, when one charged lepton escapes detection, is also a source of background events. Finally, additional background comes from $t\bar{t}$ production if the semi-leptonic decay of a b gives rise to an isolated charged lepton. However, this is at the end a minor source of events.

Before we start the description of the kinematic analysis, we briefly present the simulation tools that we have used. The signal and background events are simulated at the parton level with full tree level matrix elements generated with the package MadGraph4 [152] conveniently modified to include the anomalous TGV's. We employ CTEQ6L parton distribution functions [153] throughout the thesis. For this preliminary study, that was done previous to the LHC operation, we simulate experimental resolutions in a simplified way by smearing the energies (but not directions) of all final state charged leptons with a Gaussian error $\Delta(E)/E = 0.02/\sqrt{E}$. We include in addition in our analysis a 90% lepton detection efficiency. For this Section we focus on the initial 7 TeV LHC run.

Selection of events

We begin now the description of the selection of events for the two processes considered. First we start imposing a set of common acceptance cuts aiming to detect the final state leptons, as well as a minimum transverse energy requirement. These cuts are applied to both processes in Eqs. (3.35) and (3.36):

$$p_T^\ell \geq 10 \text{ GeV} \quad , \quad |\eta_\ell| < 2.5 \quad , \quad \Delta R_{\ell\ell} \geq 0.4 \quad , \quad \cancel{E}_T \geq 10 \text{ GeV} \quad , \quad (3.38)$$

where z is the collision axis, $p_T \equiv \sqrt{p_x^2 + p_y^2}$ is the transverse momentum, the pseudorapidity is defined as $\eta \equiv \frac{1}{2} \ln \frac{|\vec{p}| + p_z}{|\vec{p}| - p_z}$ and finally $\Delta R \equiv \sqrt{\Delta\eta^2 + \Delta\phi^2}$, with ϕ being the azimuthal angle with respect to the beam axis.

For the $pp \rightarrow \ell^+ \ell^- \cancel{E}_T$ case, with the two leptons being of the same flavor, we require the lepton pair invariant mass ($M_{\ell\ell}$) to be outside of a range compatible with Z production in order to increase the signal to background ratio, *i.e.*

$$|M_{\ell\ell} - M_Z| > 10 \text{ GeV} \quad . \quad (3.39)$$

After these cuts the top pair production can still be a potentially large background due to its massive production via strong interactions at the LHC. To further suppress $t\bar{t}$ related events we impose a jet veto to the $pp \rightarrow \ell^+ \ell^- \cancel{E}_T$ case. We do not consider events with a jet if it accomplishes

$$p_T^j > 20 \text{ GeV} \quad \text{and} \quad |\eta_j| < 3 \quad . \quad (3.40)$$

This veto is introduced to moderate the activity of QCD processes that could ruin the sensitivity of $pp \rightarrow \ell^+ \ell^- \cancel{E}_T$ to measure TGV's. The cut

also guarantees that the next-to-leading order (NLO) QCD corrections, which are a potentially dangerous background, do not alter significantly this preliminary study of TGV's.

For $pp \rightarrow \ell'^{\pm}\ell^+\ell^-E_T$, we impose a requirement on $M_{\ell\ell}$ that goes on the opposite direction than the cut in Eq. (3.39). In the case with only a pair of same flavor opposite sign leptons (this is, $\ell' \neq \ell$) we demand that the invariant mass of the equal flavor lepton pair is compatible with the Z mass, *i.e.*

$$|M_{\ell\ell} - M_Z| < 10 \text{ GeV} . \quad (3.41)$$

In addition, the presence of only one neutrino in the final state of this channel permits a reconstruction of its momentum by imposing the transverse momentum conservation and requiring that the invariant mass of the third lepton and the neutrino matches the W mass

$$M_{\ell\nu} = M_W . \quad (3.42)$$

From this equation we obtain

$$p_L^\nu = \frac{1}{2p_T^{\ell'^2}} \left\{ [M_W^2 + 2(\vec{p}_T^{\ell'} \cdot \vec{\cancel{p}}_T)] p_L^{\ell'} \pm \sqrt{[M_W^2 + 2(\vec{p}_T^{\ell'} \cdot \vec{\cancel{p}}_T)]^2 |\vec{p}^{\ell'}|^2 - 4(p_T^{\ell'} E^{\ell'} \cancel{E}_T)^2} \right\} , \quad (3.43)$$

where $\vec{\cancel{p}}_T$ is the missing transverse momentum vector and $p^{\ell'}$ is the four-momentum of the same-charge lepton not associated to the Z . As we can see this procedure exhibits a twofold ambiguity on the neutrino longitudinal momentum determination. We use this reconstruction in our analysis to keep only events that possess a solution to the neutrino momentum. If the three leptons have the same flavor the possible combinatorics in the final state increase. In this case we impose that one opposite charge lepton pair satisfies the $M_{\ell\ell}$ cut in Eq. (3.41), and that the third lepton and the missing transverse momentum then reconstruct a W as in Eqs. (3.42) and (3.43). With the purpose of further reducing the background events and removing also combinatoric ambiguities, we require as well that the invariant mass of the third lepton and the lepton of opposite charge used to reconstruct the Z is not compatible with a Z . Thus these last two leptons have to comply with Eq. (3.39) instead. As we have said, in the case of the $pp \rightarrow \ell'^{\pm}\ell^+\ell^-E_T$ channel, $t\bar{t}$ is also a possible source of background events. Nevertheless, in this case, and after all the described cuts have been applied, *i.e.* Eqs. (3.38), (3.41)–(3.42) (plus (3.39) for $\ell' = \ell$), top pair background is already highly suppressed since it requires that one of the isolated leptons originates from a b quark semi-leptonic decay. Actually, after applying a jet veto as in Eq. (3.40) the effect of $t\bar{t}$ events is considered negligible for the preliminary analysis of the present Section.

3.2. SCRUTINIZING THE WWZ VERTEX

After applying this series of cuts the background event expectations have been considerably reduced to a level that allows for the measurement of the anomalous TGV signals. In Table 3.5 we show the cross sections for the SM backgrounds and for the anomalous contributions to the processes $pp \rightarrow \ell^+ \ell'^- \cancel{E}_T$ after the cuts in Eqs. (3.38)–(3.40), and $pp \rightarrow \ell'^{\pm} \ell^+ \ell^- \cancel{E}_T$ after the cuts in Eqs. (3.38) and (3.40)–(3.42) (plus Eq. (3.39) for $\ell' = \ell$.) Although it is not stated in the Table, the jet veto is crucial to tame the dangerous $t\bar{t}$ background to an acceptable level for the $pp \rightarrow \ell^+ \ell'^- \cancel{E}_T$ process. Indeed the $t\bar{t}$ cross section before the veto in Eq. (3.40) is ~ 3.9 pb for 7 TeV of COM energy.

| σ_{SM} (fb) | | σ_{ano} (fb) | | | | σ_{ano} (fb) | | |
|---|------------|----------------------------|-------------------|-------------|---------|----------------------------------|--------------------|---------------------|
| | | σ_{int} (fb) | | | | $\Delta\sigma_{\text{ano}}$ (fb) | | |
| $pp \rightarrow \ell^+ \ell'^- \cancel{E}_T$ | | | | | | | | |
| $l^+ \nu_l l'^- \nu_{l'}$ | $t\bar{t}$ | Δg_1^Z | $\Delta \kappa_Z$ | λ_Z | g_5^Z | g_4^Z | $\tilde{\kappa}_Z$ | $\tilde{\lambda}_Z$ |
| 824. | 11.1 | 254. | 2540. | 5750. | 163. | 219. | 412. | 6030. |
| | | -55.7 | -166. | -22.1 | 15.1 | 68.8 | -89.2 | 152. |
| $pp \rightarrow \ell'^{\pm} \ell^+ \ell^- \cancel{E}_T$ | | | | | | | | |
| $\ell^+ \ell^- \ell'^{\pm} \nu$ | ZZ | Δg_1^Z | $\Delta \kappa_Z$ | λ_Z | g_5^Z | g_4^Z | $\tilde{\kappa}_Z$ | $\tilde{\lambda}_Z$ |
| 63.0 | 2.32 | 1280. | 65.4 | 2290. | 391. | 1020. | 77.6 | 2390. |
| | | -106. | -21.3 | -24.3 | -7.2 | -20.2 | -2.2 | -10.0 |

Table 3.5: Cross sections for the process $pp \rightarrow \ell^+ \ell'^- \cancel{E}_T$ after the cuts in Eqs. (3.38)–(3.40) are applied, and $pp \rightarrow \ell'^{\pm} \ell^+ \ell^- \cancel{E}_T$ after the cuts in Eqs. (3.38) and (3.40)–(3.42) (plus Eq. (3.39) for $\ell' = \ell$) are imposed. ZZ denotes the SM process $pp \rightarrow \ell^+ \ell^- \ell'^{\pm} [\ell'^{\mp}]$ with $[\ell'^{\pm}]$ stating a charged lepton that escapes detection. In all cases the results include the charge lepton detection efficiency of 90%. In the case of CP violating couplings we provide the result for $\Delta\sigma_{\text{ano}}$, see Eq. (3.47).

Kinematic distributions and TGV measurements

In this Subsection we present the distributions of the cross sections with respect to different kinematic variables. The purpose of this exercise is to analyze which of the considered distributions has a higher sensitivity to anomalous TGV interactions, and additionally to optimize this sensitivity as a function of a cut in the corresponding variables. The distributions that we consider aim to trace the enhancement that anomalous TGV's typically cause on the higher values of variables related to the total energy of the event.

In the case of the $pp \rightarrow \ell^+ \ell'^- \cancel{E}_T$ channel, we consider three different variables. The p_T of the lepton with the highest transverse momentum in

the event (*hardest* lepton), $p_{T\ell}^{\max}$, the invariant mass of the pair of leptons, $M_{\ell\ell}$, and finally the transverse mass defined as

$$M_T^{WW} = \left[\left(\sqrt{(p_T^{\ell\ell})^2 + M_{\ell\ell}^2} + \sqrt{p_T^2 + M_{\ell\ell}^2} \right)^2 - (\vec{p}_T^{\ell\ell} + \vec{p}_T)^2 \right]^{1/2}, \quad (3.44)$$

where $\vec{p}_T^{\ell\ell}$ is the transverse momentum of the pair $\ell^+\ell^-$. The normalized spectra of the SM and the anomalous contributions for the three kinematic variables are displayed in the upper panels of Fig. 3.3.

For the $pp \rightarrow \ell'^{\pm}\ell^+\ell^-E_T$ process we also consider three variables. As in the other channel, the transverse mass of the hardest lepton, $p_{T\ell}^{\max}$, is studied. Furthermore, we define p_{TZ} as the transverse momentum of the opposite sign equal flavor lepton pair verifying Eq. (3.41). Finally, as we impose that the events permit a reconstruction of the neutrino momentum, we evaluate the total $\ell\ell\nu$ invariant mass, which we label M_{WZ}^{rec} . This variable takes however two possible values for each event, as it is expected from the twofold ambiguity when reconstructing the longitudinal component of the neutrino momentum, see Eq. (3.43). Consequently, we use the distribution of this variable after each of the two solutions have been added with a weight 1/2. The behavior of the SM background and some of the anomalous TGV cross sections with respect to these three variables can be seen in the lower panels of Fig. 3.3.

All the distributions in Fig. 3.3 have been normalized for an easier illustration of the high energy behavior of the several contributions plotted. In the different panels of Fig. 3.3, the SM background is represented as the dotted black line, while the most relevant pure anomalous contributions are shown in each case. $\Delta\kappa_Z$ (black solid), λ_Z and $\tilde{\lambda}_Z$ that are indistinguishable (blue solid), g_4^Z (red solid) and $\tilde{\kappa}_Z$ (magenta solid) are shown for the $pp \rightarrow \ell^+\ell'^-E_T$ channel, while Δg_1^Z (black solid), λ_Z and $\tilde{\lambda}_Z$ (blue solid), g_4^Z (red solid) and $\tilde{\kappa}_Z$ (magenta solid) are the ones shown for $pp \rightarrow \ell'^{\pm}\ell^+\ell^-E_T$. Figure 3.3 illustrates the well known fact that the anomalous contributions enhance the cross sections at higher collision energies (eventually leading to perturbative unitarity violation), and that this behavior can be well traced by either $p_{T\ell}^{\max}$, $M_{\ell\ell}$, M_{WW}^T , p_{TZ} or M_{WZ}^{rec} .

Once the different distributions have been presented, illustrating the enhancement that anomalous TGV distributions show on the different considered variables, we proceed to optimize the searches benefiting of this energetic behavior. In order to extract the attainable sensitivity on anomalous TGV's, we analyze for each kinematic variable shown in Fig. 3.3 the cut that maximizes the sensitivity to deviations on TGV's. In this preliminary analysis of the LHC capability at 7 TeV we do not attempt to make a fit to the distributions given the low statistics we are considering. We use instead, as unique statistical variable, the total number of observed events above a certain minimum cut for each of the variables, where this is the cut

3.2. SCRUTINIZING THE WWZ VERTEX

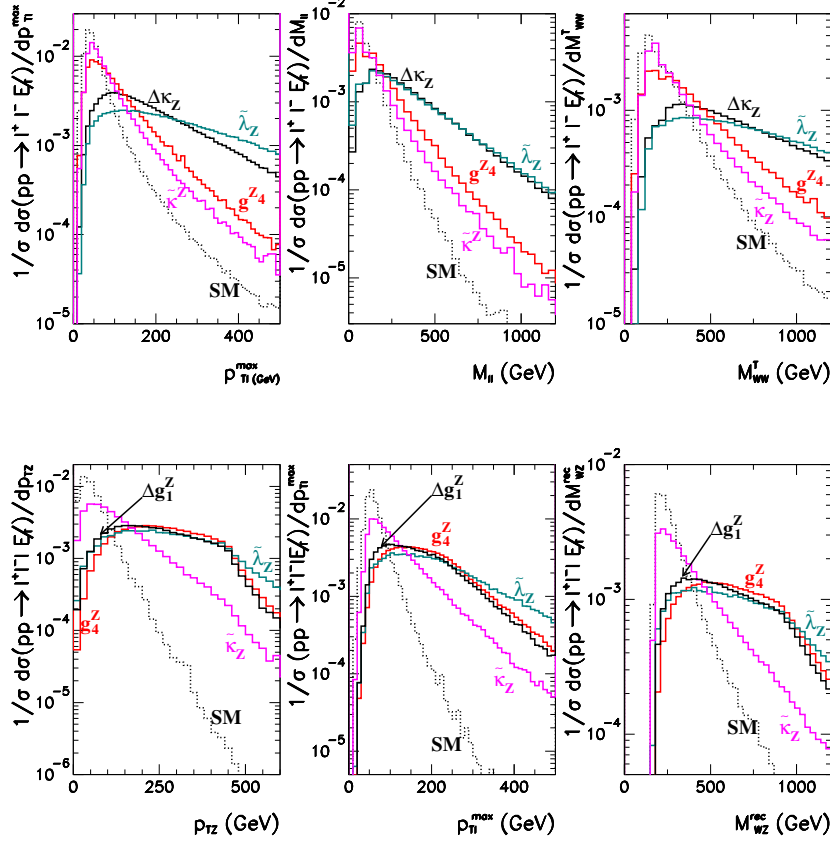


Figure 3.3: Normalized spectra for some relevant kinematic variables for the SM and some of the anomalous TGV's for $pp \rightarrow \ell^+ \ell'^- \cancel{E}_T$ (upper panels) and $pp \rightarrow \ell'^{\pm} \ell^+ \ell^- \cancel{E}_T$ (lower panels). The upper panels show the distribution in transverse momentum of the hardest lepton (left panel), dilepton invariant mass (central panel) and reconstructed WW transverse invariant mass (right panel) as in Eq. (3.44). The lower panels show the transverse momentum of the Z (left panel), the hardest lepton transverse momentum (central panel), and the reconstructed WZ invariant mass (right panel).

that we want to optimize. For all the different cases we assume that the total number of observed events is the one expected in the SM at 7 TeV and an integrated luminosity of 1 fb^{-1} . Finally the corresponding statistical uncertainties are obtained using Poisson or Gaussian statistics depending on whether the expected number of SM events is smaller or larger than 20. We perform our analysis of the channels $pp \rightarrow \ell^+ \ell'^- \cancel{E}_T$ and $pp \rightarrow \ell'^{\pm} \ell^+ \ell^- \cancel{E}_T$ independently.

The corresponding attainable 2σ bounds are listed in Table 3.6. After the

statistical analysis we find that for the channel $pp \rightarrow \ell^+ \ell'^- \cancel{E}_T$ the maximum sensitivity for any of the anomalous TGV's is obtained when one imposes a minimum cut on the transverse momentum of the hardest lepton with the optimum cut ranging between 50–200 GeV, depending on the anomalous coupling considered. Our results show that this channel at 7 TeV and with only 1 fb^{-1} can already tighten the present direct bounds on $\Delta\kappa_Z$, λ_Z , g_4^Z , and $\tilde{\lambda}_Z$.

| | W^+W^- 2σ limits | | $W^\pm Z$ 2σ limits | |
|---------------------|---------------------------|---------------------------|----------------------------|---------------------------|
| | No form factor | $\Lambda = 3 \text{ TeV}$ | No form factor | $\Lambda = 3 \text{ TeV}$ |
| Δg_1^Z | [-0.33 , 0.56] | [-0.35 , 0.59] | [-0.055 , 0.094] | [-0.061 , 0.11] |
| $\Delta\kappa_Z$ | [-0.088 , 0.11] | [-0.10 , 0.14] | [-0.27 , 0.55] | [-0.29 , 0.61] |
| λ_Z | [-0.055 , 0.056] | [-0.074 , 0.075] | [-0.051 , 0.054] | [-0.060 , 0.064] |
| g_5^Z | [-0.53 , 0.51] | [-0.56 , 0.55] | [-0.18 , 0.19] | [-0.19 , 0.20] |
| g_4^Z | [-0.48 , 0.48] | [-0.51 , 0.51] | [-0.080 , 0.080] | [-0.091 , 0.091] |
| $\tilde{\kappa}_Z$ | [-0.38 , 0.38] | [-0.39 , 0.39] | [-0.40 , 0.40] | [-0.42 , 0.42] |
| $\tilde{\lambda}_Z$ | [-0.055 , 0.055] | [-0.074 , 0.074] | [-0.053 , 0.053] | [-0.062 , 0.062] |

Table 3.6: Attainable 2σ bounds on anomalous TGV's at the LHC at 7 TeV with 1 fb^{-1} .

For the bounds coming from the analysis of $pp \rightarrow \ell'^\pm \ell^+ \ell^- \cancel{E}_T$, similar to the $pp \rightarrow \ell^+ \ell'^- \cancel{E}_T$ case, we find that a minimum cut in either of the transverse momentum variables (that of the Z or the hardest lepton p_T) leads to the best sensitivity. The use of these variables is also preferred, since they do not require the reconstruction of the neutrino momentum, reducing the uncertainties associated to the calibration of the electromagnetic calorimeters. The corresponding attainable 2σ bounds are also listed in Table 3.6, which shows that the channel can improve the present direct constraints on the couplings Δg_1^Z , λ_Z , g_4^Z and $\tilde{\lambda}_Z$.

From the observation of the attainable bounds in Table 3.6 we can conclude that while both processes have a very similar sensitivity to measure λ_Z , $\tilde{\lambda}_Z$ and $\tilde{\kappa}_Z$, $pp \rightarrow \ell^+ \ell'^- \cancel{E}_T$ is more sensitive to $\Delta\kappa_Z$, whereas $pp \rightarrow \ell'^\pm \ell^+ \ell^- \cancel{E}_T$ can reach a greater precision on Δg_1^Z , g_5^Z and g_4^Z . This fact will be of relevance for disentangling the hypothetical nature of the Higgs boson through the study of g_5^Z and g_4^Z as we describe in the following Subsection.

CP -odd anomalous TGV's

Up to this point we have applied the same type of analysis to both CP conserving and to CP violating couplings. In other words, if a deviation from the SM TGV was observed, it would not be possible to distinguish

3.2. SCRUTINIZING THE WWZ VERTEX

which is the CP nature of the operators on the Lagrangian in [52] causing the departure within the presented analysis framework. In this case, in order to infer the CP nature of the anomalous TGV some discriminating observable should be built and studied. Different studies on the literature [154–156] have addressed the CP -odd nature of the anomalous TGV's constructing some CP -odd or \hat{T} -odd observable. For instance $pp \rightarrow WZ$ was studied in [155] where a \hat{T} -odd observable was built to study CP violating effects at the LHC. There, it was shown that building an asymmetric observable based on the sign of the cross-product $p_q \cdot (p_Z \times p_{\ell'})$ could be a direct probe of CP violation. However, this cross-product involves p_q , the four-momentum of the incoming quark, and its determination is not possible in a pp machine like the LHC. Consequently, an alternative cross-product correlated to the desired one has to be built to bypass this complication. For instance, one can define [155]

$$\Xi_{\pm}^z \equiv \text{sign}(p_Z^z) \text{sign}(p_{\ell'} \times p_Z)^z, \quad (3.45)$$

as a substitute to the unmeasurable cross-product involving p_q , where z is the collision axis. For the $pp \rightarrow \ell^+ \ell'^- \cancel{E}_T$ channel we can build [156]

$$\Xi_{\pm} \equiv \text{sign}(\vec{p}_{\ell^+} - \vec{p}_{\ell'^-})^z \text{sign}(\vec{p}_{\ell^+} \times \vec{p}_{\ell'^-})^z. \quad (3.46)$$

The CP violating couplings give a non-vanishing contribution to the sign-weighted cross sections, defined as

$$g_{\text{ano}}^i \Delta\sigma_{\text{ano}}^i \equiv \int d\sigma \Xi_{\pm}. \quad (3.47)$$

On the other hand, the SM background and the CP -even anomalous TGV's all have a symmetric distribution of the events with respect to the sign definitions in Eqs. (3.45) and (3.46), thus they give a null contribution to the sign-weighted cross section besides statistical fluctuations. These different behaviors can be used to discriminate a CP -odd signal. We present in Table 3.5 the values of the corresponding sign-weighted cross sections. The resulting number of sign-weighted events has to be compared with the statistical fluctuations of the SM expectations. After performing such analysis we find that given the existing bounds on $\tilde{\kappa}_Z$, $\tilde{\lambda}^Z$ and g_4^Z , the study of these sign-weighted asymmetries at the 7 TeV LHC run is not precise enough to provide concluding information on the CP properties of the anomalous couplings. Nevertheless, we will observe in the following Subsection that for the higher energy runs, and with a higher luminosity accumulated, the use of such asymmetries has the potential to decipher the CP nature of a hypothetical observed TGV deviation from the SM expectations.

Unitarity

The introduction of anomalous couplings can spoil delicate cancellations in different scattering amplitudes, leading to their growth with energy and,

eventually, to unitarity violation above a certain scale Λ' . As we have described in Section 2.4, a way to control this problem that is used in the literature relies on the introduction of an energy dependent form factor that tames the anomalous scattering amplitude behavior at high energy, such as

$$\frac{1}{\left(1 + \frac{\hat{s}}{\Lambda'^2}\right)^2} , \quad (3.48)$$

where $\sqrt{\hat{s}}$ is the COM energy of the WW or the WZ pair, which roughly corresponds to the energy of the event if no NLO radiation is considered. A priori, the introduction of such form factors makes the sensitivity dependent on the assumptions on Λ' and the shape of the form factor considered. Nonetheless, here we advocate that the need to introduce a form factor at the 7 TeV run of LHC is marginal because the COM energy for the contributing sub-processes in Eqs. (3.35) and (3.36) are $\lesssim 2$ TeV, and the unitarity bounds on the anomalous TGV's stemming from these processes are much weaker than the ones that we obtain from the study we have presented; see the fourth and fifth columns of Table 3.4 in comparison to the bounds we have derived in Table 3.6. In principle one may worry about the corresponding unitarity violation in longitudinal VV ($V = W^\pm$ or Z) scattering, which can lead to stronger bounds on the TGV's since they can lead to a scattering amplitude which grows as \hat{s}^2 . However, the actual energy behavior of the scattering amplitude in longitudinal gauge boson scattering depends strongly on the assumptions about the quartic gauge boson couplings, see for instance [157–160]. In particular, if there is a mechanism relating the quartic and triple anomalous contributions the VV scattering unitarity bounds turn out to be similar to the ones in reference [150]. This indicates that some questions like unitarity violation can be better discussed in more complete approaches, like the effective Lagrangian approaches previously presented. In these cases the contribution of higher dimensional operators to all the different vertices, including TGV's and quartic vertices as well, are completely determined. Altogether we find that within the bounds that we derive, unitarity is held up to $\sqrt{\hat{s}} \simeq 3$ TeV. As a final consistency check we derive the bounds obtained if a form factor as in Eq. (3.48) was included with $\Lambda = 3$ TeV. We show in Table 3.6 the changes in the 2σ sensitivity. As it can be observed, the effects on the 2σ expectations after the inclusion of the form factor are marginal.

This preliminary analysis still leaves some room for improvement. For instance, we have considered only one kinematic distribution to extract the bounds, leaving out the possibility of optimizing the analysis for joint distributions or a binned maximum likelihood fit. In the next Subsection we partially improve on this direction by studying the impact that performing a binned maximum likelihood fit to one of the distributions has on the extracted bounds. Furthermore, our calculations have been carried out at

3.2. SCRUTINIZING THE WWZ VERTEX

the parton level with the lowest order perturbation theory. A full Monte Carlo analysis taking into account detector simulation, as well as, NLO QCD [161–163] and EW [164] corrections would be preferable. Although QCD NLO corrections are potentially dangerous due to changes in p_T distributions, the jet veto cut in Eq. (3.40) is enough to guarantee that the attainable limits are not significantly altered [161–163]. In the following Subsection we partially improve on this issue, by accounting in a simplified way for higher order corrections and detection efficiencies making use of one of the already existing LHC experimental searches.

3.2.3 Dynamical Higgs and TGV's: updated analysis

In this Subsection we present an updated analysis of the LHC capability to measure anomalous TGV signals originated by g_5^Z , g_4^Z , $\tilde{\kappa}_Z$ and $\tilde{\lambda}_Z$. The motivation to focus on these four anomalous TGV's is twofold. First, the strongest existing limits on them come still from LEP studies, as neither Tevatron nor LHC have focused their attention on them. Here we show that the LHC has the potential to greatly improve these bounds. Second, g_5^Z , g_4^Z and $\tilde{\lambda}_Z$ could be used as discriminating signals to decipher the nature of the Higgs boson. The case of g_5^Z has already been discussed in detail in the previous Section: leading operators in the chiral expansion can generate its signals, while only dimension–eight operators contribute to it on the linear expansion. The case of g_4^Z is completely analogous to g_5^Z , but in the context of CP –odd operators. The CP –odd study has been developed in a parallel work which is still in progress [98]. There we also observe that as we have stated in the CP –even case for λ_Z , in the CP –odd expansion, signals of $\tilde{\lambda}_Z$ would also point to a linear realization of the EWSB, as this anomalous TGV receives contributions from leading operators in the linear expansion, while it can only receive contributions from subleading chiral operators in the non–linear one.

In Sec. 3.2.2 we have concluded that while both $pp \rightarrow \ell^+ \ell'^- \cancel{E}_T$ and $pp \rightarrow \ell'^{\pm} \ell^+ \ell^- \cancel{E}_T$ processes are equally sensitive to $\tilde{\lambda}_Z$ and $\tilde{\kappa}_Z$, $pp \rightarrow \ell'^{\pm} \ell^+ \ell^- \cancel{E}_T$ is clearly more sensitive to g_5^Z and g_4^Z . Consequently we focus this updated study on the $pp \rightarrow \ell'^{\pm} \ell^+ \ell^- \cancel{E}_T$ channel. In the present analysis for the simulation of the signal we implement the anomalous TGV contributions via the package FeynRules [87] which is interfaced to MadGraph5 [86] for event generation. We then introduce detection efficiencies by tuning our homemade simulation tools to the public efficiencies quoted in the ATLAS search [47], as we describe in the following lines. Both our analysis and the ATLAS search [47] are based on the same selection procedure, therefore we can compare the response of our simulated signals to the different cuts with respect to the quoted one by ATLAS, tuning then the response of our tools to the proper detection efficiencies. We further crosscheck our results using an alternative FeynRules [87] and MadGraph5 [86] implementation

interfaced in addition in this case to PYTHIA [165] for parton shower and hadronization, and finally to PGS 4 [166] for the detector simulation. We apply the same procedure to the main background source, the irreducible EW WZ production. The rest of minor background sources are extracted from the ones presented in the ATLAS search [47] for the sake of a more realistic determination. They are properly rescaled for the 8 and 14 TeV studies, while the details on the estimation of these background sources can be found in [47]. This way, besides the main sources described in the previous Subsection, we can also account for the minor $Z + \gamma$ production and both W^\pm and Z minor productions in association with extra jets.

The selection of events is mainly based on the ATLAS search [47] which we briefly summarize here for completeness. The selection starts with the acceptance cuts for the final state leptons. Three leptons are required in the final state, where only muons and electrons are considered with

$$\begin{aligned} p_T^\ell &> 15 \text{ GeV} , \quad |\eta^\mu| < 2.5 , \\ |\eta^e| &< 1.37 \quad \text{or} \quad 1.52 < |\eta^e| < 2.47 . \end{aligned} \quad (3.49)$$

For isolation purposes the scalar sum of transverse momentum within $\Delta R = 0.3$ of the muon (electron) track, excluding it itself, is required to be below 15% (13%) of the lepton p_T . In the cases with both muons and electrons on the final state $\Delta R_{e\mu} > 0.1$ is imposed as a further isolation requirement. In order to reduce the number of background events from processes where there is no pair of leptons coming from the decay of a Z boson, as we did in the preliminary analysis, we impose that at least two of the leptons with the same flavor and opposite charge have an invariant mass within 10 GeV of the Z boson. The third lepton is required to accomplish a higher minimum p_T cut, these requirements are

$$\begin{aligned} M_{\ell\ell} &\in (M_Z - 10, M_Z + 10) \text{ GeV} , \\ p_T^{\ell'} &> 20 \text{ GeV} . \end{aligned} \quad (3.50)$$

In order to reduce most of the $Z + \text{jets}$ and diboson backgrounds, as in the preliminary analysis, we impose minimum transverse momentum requirements

$$\cancel{E}_T > 25 \text{ GeV} \quad \text{and} \quad M_T^W > 20 \text{ GeV} , \quad (3.51)$$

where here the transverse mass is defined as $M_T^W = \sqrt{2p_T^{\ell'}\cancel{E}_T(1 - \cos(\Delta\phi))}$, with $p_T^{\ell'}$ being the transverse momentum of the third lepton and $\Delta\phi$ the azimuthal angle between the missing transverse momentum and the p_T of the third lepton. Finally, with the aim of increasing the tagging efficiency we require an extra minimum p_T threshold for at least one of the selected leptons

$$p_T^{e(\mu)} > 25 \text{ (20) GeV} . \quad (3.52)$$

3.2. SCRUTINIZING THE WWZ VERTEX

Up to this point the selection procedure described exactly matches the one in the ATLAS search [47]. This can be used in our benefit in order to tune our simulation tools to the realistic detection efficiencies quoted in there. We first correct our signal and EW SM WZ production processes introducing a global K -factor to account in a simplified way for the higher order corrections. The K -factor is inferred from the comparison between our leading order predictions and the state of the art NLO calculations used in the ATLAS search [47], this leads to $K \sim 1.7$. After this correction, we compare the efficiencies of our prediction for SM EW WZ production when applying each of the described cuts with respect to the efficiencies quoted in Table 1 of [47]. We observe an overall agreement with respect to the cut flow quoted there, except for the detection and tagging cuts. To correct them, we apply final correction factors per flavor channel (eee , $ee\mu$, $e\mu\mu$ and $\mu\mu\mu$). These factors would be consistent with applying a detection efficiency for the leptons of roughly $\epsilon^{e(\mu)} = 0.8(0.95)$. After we have applied the selection procedure and these correction factors, we present in Table 3.7 the different cross section values relevant for the analysis. We quote in there the values at the different COM energies considered in the analysis: 7, 8 and 14 TeV.

| \sqrt{s} | σ_{SM} (fb) | σ_{bck} (fb) | $\sigma_{\text{ano}}^{g_z^i}$ (fb) | $\sigma_{\text{ano}}^{g_z^i}$ (fb) | $\sigma_{\text{ano}}^{\tilde{\kappa}_z}$ (fb) | $\sigma_{\text{ano}}^{\tilde{\lambda}_z}$ (fb) |
|------------|---------------------------|----------------------------|------------------------------------|------------------------------------|---|--|
| 7 TeV | 48.6 | 14.3 | 304 | 846 | 56.0 | 1914 |
| 8 TeV | 56.2 | 16.8 | 363 | 1117 | 67.7 | 2556 |
| 14 TeV | 97.9 | 29.0 | 707 | 3034 | 134 | 7471 |

Table 3.7: Values of the cross section predictions for the process $pp \rightarrow \ell'^{\pm}\ell^+\ell^-\cancel{E}_T$ after applying all the cuts from Eqs. (3.49)–(3.52) and the correction factors described in the text. Here σ_{SM} is the SM contribution from the EW WZ production, σ_{ano}^i are the pure anomalous contributions and σ_{bck} corresponds to all the background sources except for the EW SM WZ production.

Following the conclusions in Sec. 3.2.2, in order to quantify the reachable sensitivity on the determination of the anomalous TGV interactions, we take advantage of the enhancement they cause on the higher values of variables related to the total energy in the event. For the present analysis we choose p_T^Z , as it can be directly reconstructed from the measured lepton momentum with good precision without the need of reconstructing the neutrino momentum. In the left (right) panel of Fig. 3.4 we show the number of expected events with respect to the transverse momentum of the Z candidate for the 7 (14) TeV run, assuming an integrated luminosity of $\mathcal{L} = 4.64$ (300) fb^{-1} . The black histograms correspond to the sum of all the background sources for the $pp \rightarrow \ell'^{\pm}\ell^+\ell^-\cancel{E}_T$ channel, except for SM $pp \rightarrow W^{\pm}Z$ EW process, the red histograms correspond to the sum of all the backgrounds including now also the SM EW $pp \rightarrow W^{\pm}Z$ production. Finally for illustration the

dashed distributions correspond to the addition of an anomalous signal with $g_5^Z = 0.2$ ($g_5^Z = 0.1$). In the Figure the last bin contains all the events with $p_T^Z > 180$ GeV.

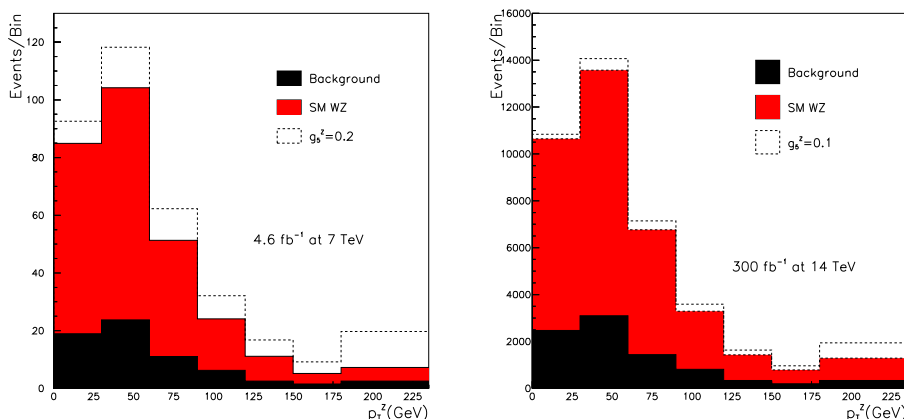


Figure 3.4: In the left (right) panel we show the distribution of events with respect to p_T^Z for the 7 (14) TeV run assuming $\mathcal{L} = 4.64$ (300) fb^{-1} of integrated luminosity. The black histograms contain all background sources for the $pp \rightarrow \ell'^{\pm} \ell^+ \ell^- \cancel{E}_T$ channel, except for the SM WZ production, the red histograms represent the sum of all the backgrounds, and finally the dashed distributions correspond to the addition of the contribution of an anomalous TGV with a value $g_5^Z = 0.2$ ($g_5^Z = 0.1$). The last bin contains all the events with $p_T^Z > 180$ GeV.

TGV measurement

We present here two statistical analyses: the first one is, as in Sec. 3.2.2, an event counting analysis assuming that the total number of observed events with

$$p_T^Z > 90 \text{ GeV}. \quad (3.53)$$

corresponds to the SM expectations. This final cut follows the optimization presented in the previous Subsection. We then determine what values of the anomalous TGV's are inside the 95% CL region. In this case this corresponds to search for the values with $N^{\text{ano}} > 1.96\sqrt{N^{\text{SM}}}$. Here $N^{\text{ano}} = (\sigma_{\text{int}}^i g_{\text{ano}}^i + \sigma_{\text{ano}}^i g_{\text{ano}}^{i,2}) \times \mathcal{L} \times \epsilon$, and $N^{\text{SM}} = (\sigma_{\text{SM}}) \times \mathcal{L} \times \epsilon$, where \mathcal{L} is the luminosity considered, while ϵ refers generically to the tuning factors that we have described. Finally the superscript i accounts for the anomalous TGV under consideration.

On a second analysis we take advantage of the presented p_T^Z distribution in Fig. 3.4 in order to strengthen the attainable bounds by means of a binned

3.2. SCRUTINIZING THE WWZ VERTEX

maximum likelihood fit. We build a binned χ^2 based on the contents of this distribution while assuming that the observed events correspond to the SM expectations. In this case χ^2 has the form

$$\chi^2 = 2 \sum_j [N_{\text{ano}}^j + N_{SM}^j \log \frac{N_{SM}^j}{N_{SM}^j + N_{\text{ano}}^j}] , \quad (3.54)$$

where the sum runs over the bins (j) of the p_T^Z distribution. We use the binning in Fig. 3.4 and as in the previous case we determine the values of g_5^Z , g_4^Z , $\tilde{\kappa}_Z$ and $\tilde{\lambda}_Z$ compatible at 95% CL with the assumed observed events, that correspond to the values for which $\sqrt{\chi^2} < 1.96$.

The results of both analyses are presented in Table 3.8. They are shown for two different data frameworks. We show first the present expectations after the hypothetical combination of the 7 TeV and 8 TeV existing sets of data. We assume $\mathcal{L} = 4.64 \text{ fb}^{-1}$ for the 7 TeV run and $\mathcal{L} = 19.6 \text{ fb}^{-1}$ for the 8 TeV one. Then we combine these existing sets with a hypothetical 14 TeV run containing $\mathcal{L} = 300 \text{ fb}^{-1}$ of data.

| Data set | 95% CL range | |
|---------------------|----------------------------------|-----------------|
| | $p_T^Z > 90 \text{ GeV}$ -count. | p_T^Z -binned |
| g_5^Z | | |
| 7+8 TeV | (-0.091, 0.083) | (-0.080, 0.072) |
| 7+8+14 TeV | (-0.040, 0.032) | (-0.033, 0.028) |
| g_4^Z | | |
| 7+8 TeV | (-0.037, 0.037) | (-0.027, 0.027) |
| 7+8+14 TeV | (-0.014, 0.014) | (-0.010, 0.010) |
| $\tilde{\kappa}_Z$ | | |
| 7+8 TeV | (-0.19, 0.19) | (-0.17, 0.17) |
| 7+8+14 TeV | (-0.079, 0.079) | (-0.067, 0.067) |
| $\tilde{\lambda}_Z$ | | |
| 7+8 TeV | (-0.025, 0.025) | (-0.018, 0.018) |
| 7+8+14 TeV | (-0.009, 0.009) | (-0.006, 0.006) |

Table 3.8: Expected sensitivity on g_5^Z , g_4^Z , $\tilde{\kappa}_Z$ and $\tilde{\lambda}_Z$ at the LHC. We assume $\mathcal{L} = 4.64 \text{ fb}^{-1}$ for the 7 TeV run, $\mathcal{L} = 19.6 \text{ fb}^{-1}$ for the 8 TeV one and $\mathcal{L} = 300 \text{ fb}^{-1}$ for the future 14 TeV expectations, see the text for the details on the statistical procedures.

Focusing first on the expectations for the observation of g_5^Z , we note that the attainable precision on g_5^Z at the LHC after combining the 7 and 8 TeV runs is already better than the present direct bounds stemming from LEP, this precision is also approaching the present indirect limits, as seen in Table 3.4. If a 14 TeV run with an integrated luminosity of 300 fb^{-1} is

included, the LHC precision on g_5^Z may approach the per cent level, clearly improving the present direct and indirect exclusion limits.

CP-odd anomalous TGV interactions

We see from the results in Table 3.4 that the present 7 and 8 TeV data sets could clearly improve the existing sensitivity on g_4^Z as well. Furthermore, the precision reachable in the future 14 TeV run will fast approach the per cent level. The reachable sensitivity on $\tilde{\kappa}_Z$ is not as precise as the one for g_4^Z , given its weaker effect on the events, a feature that can be already seen by looking at the behavior of this anomalous TGV in Fig. 3.3. Nevertheless, the future 14 TeV run has the potential to improve the direct bounds that LEP was able to derive and settle then the strongest direct available limits on $\tilde{\kappa}_Z$. On the contrary the effects of $\tilde{\lambda}_Z$ are the most striking ones as seen in Fig. 3.3. The existing 7 and 8 TeV data sets could set the strongest direct bounds on $\tilde{\lambda}_Z$, and the addition of the future 14 TeV run would bring the reachable precision well below the per cent level. As we have discussed, the observation of this anomalous TGV would present a great opportunity to disentangle a linear realized SM gauge symmetry from a non-linear EWSB sector.

In Sec. 3.2.2 we have concluded that the use of asymmetries to characterize the *CP* violating nature of the couplings would not lead to improvement in the initial 1fb^{-1} of the 7 TeV run. However, we show here that for the 14 TeV run and with the higher statistics the study of the *CP* nature of a hypothetical deviation on TGV measurements will have the potential to give us additional information. In the present case we use the sign definition

$$\Xi_{\pm}^{\ell} \equiv \text{sign}(p_{\ell'}^z) \text{sign}(p_{\ell'} \times p_Z)^z, \quad (3.55)$$

because we checked that the sensitivity reachable is slightly better than the one of the correlated definition in Eq. (3.45). Considering the sign-weighted cross section definition in Eq. (3.47) we note again that, while the *CP*-odd anomalous TGV's give a measurable contribution to this sign-weighted cross section, the SM background presents a symmetric distribution of the events. In Table 3.9 we quote on the first line the values of $\Delta\sigma_{\text{ano}}^i$ for the three *CP*-odd anomalous TGV's at the LHC at 14 TeV. The non-vanishing sign-weighted cross section for the *CP*-odd TGV's could allow in the future 14 TeV run to set relevant bounds when comparing with the SM background statistical fluctuations. To quantify this power we show on the second line of Table 3.9 the smaller value of the given *CP*-odd TGV that would allow for a 5σ non-zero observation of the sign-weighted cross section when comparing to the SM fluctuations. Comparing with Table 3.8 we find that, as expected, the use of the sign-weighted cross section yields a smaller sensitivity to the value of the anomalous coupling than the use of either total event rates or the kinematic distributions. However the reach is high enough to allow for a

3.3. CONCLUSIONS

promising determination of the CP properties in the event of a hypothetical anomalous TGV observation for a sizable range of TGV values.

| | g_4^Z | $\tilde{\kappa}_z$ | $\tilde{\lambda}_z$ |
|------------------------------------|---------|--------------------|---------------------|
| $\Delta\sigma_{\text{ano}}^i$ (fb) | -59 | -9.7 | -137 |
| $ g_{5\sigma}^i $ | 0.05 | 0.34 | 0.02 |

Table 3.9: Values of the sign-weighted cross section as defined in Eq. (3.47) at 14 TeV for g_4^Z , $\tilde{\kappa}_Z$ and $\tilde{\lambda}_Z$. On the second line we present the minimum value for each anomalous coupling that allows for a 5σ observation of the sign-weighted cross section after 300 fb^{-1} of integrated luminosity are collected in the 14 TeV run, see text for details.

3.3 Conclusions

Understanding the nature of the Higgs boson is a priority in order to decipher the mechanism behind EWSB. After we have presented in Chapter 2 the study of the EWSB sector through a linear effective Lagrangian expansion, we have moved in this Chapter to study alternative effective Lagrangian descriptions with the purpose of understanding the virtues of alternative frameworks and to point out possible discriminating signals between them. We have first studied in Sec. 3.1 a non-linear (chiral) effective Lagrangian for Higgs interactions following the published work [97]. This framework is suitable for the family of models where the Higgs is a composite bound state of some strong dynamics, although the approach can accommodate a large range of possibilities, from composite Higgs models to exotic singlet alternatives. The focus has been placed on the study of phenomenological signatures, especially regarding possible differences with respect to the correlated pattern of some couplings in the linear effective Lagrangian approach.

We have first described in Sec. 3.1.1 how the chiral expansion is intrinsically different from the linear one due to the transformation properties under $SU(2)_L$. In the non-linear expansion the Higgs is not part of a doublet of $SU(2)_L$, but comes instead in generic model dependent functions, $F(h)$. This has two direct consequences: first, less symmetry impositions means more possible independent couplings, and at the end more independent couplings are translated into decorrelations of interactions that are instead correlated in the linear case. Second, the chiral Lagrangian follows a derivative expansion as corresponds to the Goldstone parenthood of the Higgs boson. This implies a reshuffling of the order at which interactions appear between the two expansions.

These conclusions can be translated directly into two general phenomenological consequences which have been studied in Sec. 3.1.2. The first one

is related to the fact that the reshuffling of the order at which interactions appear could allow for disentangling the nature of the Higgs boson. For instance the TGV coupling λ_V can receive contributions from a dimension–six operator in the linear expansion, whereas it can not receive any contribution from leading operators in the non–linear one. Thus its observation would point to a linear nature of the EWSB. Conversely the anomalous TGV g_5^Z can receive contributions from leading chiral operators if ξ is sizable, while it is not present neither in the SM nor in any of the leading operators in the linear expansion in which appears only in dimension–eight operators. A positive observation of g_5^Z would be then a hint for a dynamical Higgs.

The second phenomenological consequence is related to (de)correlations between the couplings in the two approaches. Less symmetry in the chiral expansion means more possible invariant operators at a given order, and the result is that the non–linear realization for a light dynamical Higgs particle is expected to exhibit a larger number of independent couplings than in the linear case. This implies that, even keeping only operators weighted by ξ , the expected deviations from the SM predictions in the Higgs couplings to gauge bosons and that of TGV’s are independent in the chiral expansion, unlike what we have observed in the linear case.

We present in Sec. 3.1.3 the first six–parameter analysis in the context of the non–linear expansion, focusing on the ξ –weighted pure gauge and gauge–Higgs effective couplings. We have derived the current bounds on the coefficients of the operators from the analysis of EWPO, TGV and Higgs data, and they are summarized in Table 3.3 and Fig. 3.1. We have also quantified the degree of correlation between Higgs couplings to gauge bosons and TGV’s. A deviation from such correlation will point to strong dynamics on the EWSB sector, and with this purpose we have introduced the discriminators in Fig. 3.2.

We have devoted the second part of the Chapter, Sec. 3.2– based on the published [94, 97] and ongoing works [98]– to analyze the Lorentz invariant parametrization of TGV’s, that has been used for long as the common framework to measure these triple vertices. We have shown in Sec. 3.2.2 that the use of variables that trace the energy of the event collision increases the sensitivity to the anomalous TGV’s. The variables we have studied are $p_{T\ell}^{\max}$, $M_{\ell\ell}$, and M_T^{WW} for the $pp \rightarrow \ell^+\ell^-\cancel{E}_T$ channel, and $p_{T\ell}^{\max}$, p_{TZ} and M_{WZ}^{rec} for $pp \rightarrow \ell^{\pm}\ell^+\ell^-\cancel{E}_T$. We have seen that a minimum cut around 50–200 GeV on any of the transverse momentum variables optimize the sensitivity to the different anomalous TGV interactions. The combination of the two processes in the initial LHC run can improve the presently available direct limits on the WWZ anomalous couplings Δg_1^Z , $\Delta\kappa_Z$, λ_Z , g_4^Z , and $\tilde{\lambda}_Z$, see Table 3.6.

After the first LHC experimental measurements of TGV’s have been performed, we can extract from them useful information in order to improve the study of TGV’s. We can obtain realistic background determinations,

3.3. CONCLUSIONS

improved detection efficiencies or higher order corrections, as well as a more realistic selection of cuts. Consequently in Sec. 3.2.3 we have updated the analysis of the $pp \rightarrow \ell'^{\pm} \ell^+ \ell^- \cancel{E}_T$ channel, focusing on g_5^Z , g_4^Z , $\tilde{\kappa}_Z$ and $\tilde{\lambda}_Z$, the anomalous TGV's that have received less attention from both Tevatron and LHC. The combination of 7 and 8 TeV existing data sets has the potential to improve the present bounds on g_5^Z , g_4^Z and $\tilde{\lambda}_Z$, that are still obtained from LEP searches. Further combining a hypothetical 300 fb^{-1} set of 14 TeV data will clearly improve the present bounds on these four anomalous TGV's, with important consequences given the relation of g_5^Z , g_4^Z and $\tilde{\lambda}_Z$ with discriminating signals of the Higgs nature. These results are presented in Table 3.8. Finally we have also estimated the effect that the use of CP asymmetries could have on assessing the nature of a possible TGV deviation. With 300 fb^{-1} of 14 TeV data a sign-weighted cross section would have the sensitivity to probe CP -odd couplings at a promising level.

In summary, so far we have shown how effective Lagrangians can be used to understand the collected data, the Higgs boson and the EWSB process. Their study is arguably a safe route to BSM, while its coverage may have a broader scope than the search for new states, which is instead a more direct way to access the EWSB sector. Therefore, both approaches are complementary and after we have devoted half of the thesis to the analysis of effective Lagrangian descriptions we now move to the study of the direct search for new particles.

Chapter 4

New resonances in EW gauge boson pair production

In the SM, a unique light scalar doublet is responsible for EWSB. The SM Higgs boson is able to cut off the dangerous energy growth of the longitudinal gauge boson scattering and, together with the Yukawa terms, it can account for the mass of the SM particles. The SM thus remains as the most minimal scenario for EWSB. In the present context, the discovery of the scalar state and the existing measurements of its properties all point to a SM Higgs boson, as we have seen in Chapters 2 and 3. Furthermore, no other new particle has been detected at the LHC, and thus these results combined seem so far a great success of the SM. However, the same SM minimality leaves us with the unsatisfactory open questions we have discussed in the Introduction, such as the hierarchy problem and why the additive corrections to the Higgs boson seem to imply that the EW scale is technically unnatural. Many theories were built in order to answer these questions while successfully describing EWSB. Including (or not) a light Higgs boson, all these theories come at the end with different new states associated to the EWSB sector. Hence, the search for these extra resonances is an alternative way of directly studying the mechanism responsible for EWSB. We focus the present Chapter on this interesting alternative to the effective Lagrangian studies previously presented.

In particular we focus on the study of spin-1 resonances. These resonances are usually linked to the fact that the analysis of partial wave unitarity of longitudinal weak gauge boson scattering, for instance $W_L^+ W_L^- \rightarrow W_L^+ W_L^-$, indicated that there had to be a contribution from the EWSB sector at the TeV scale [167], well within the LHC reach. In many extensions of the SM these resonances were expected to have spin-1, for instance in the context of the now ruled out Higgsless models. There, an infinite tower of vector resonances, Kaluza–Klein excitations, is responsible for the restoration of unitarity without the presence of a Higgs boson, see for in-

stance different extra-dimensional scenarios [168–174]. Such scenarios could be viewed as the holographic version of strongly coupled theories [175–177]. Vector resonances are also common in models where EWSB is associated to a new strongly interacting sector [119, 120, 178, 179]. Many of these theories have already been ruled out after the Higgs discovery, which may turn out to be the only EWSB contribution at the TeV scale. However, related completions including both spin-1 resonances and a light Higgs particle are still alive. For instance, strongly interacting theories, such as the CHM’s we have quoted in the previous Chapter, are still plausible explanations to account for the EWSB. In these theories, modifications of the Higgs couplings to the SM fields from strong dynamics may be present (see Chapter 3), being particularly relevant for the EW gauge boson scattering and the delicate cancellations that have to be present to restore unitarity. There, other vector composite bound resonances are expected to be generated, analogous to the ρ mesons in QCD, to extend unitarity up to the high energy scale of the strong dynamics, Λ_S . In this context, the closer the properties of the discovered scalar are to the SM Higgs boson ones, the higher the mass of these vector resonances are expected [180].

As it is the common feature of many of the EWSB scenarios above mentioned, we assume that these new vector resonances, both neutral (Z') and charged (W'), couple to W^+W^- and $W^\pm Z$ pairs respectively. Their properties, such as mass, width, and relevant couplings to SM particles, are model dependent, and we treat them as free parameters in our analyses. This way we try to keep the analyses as model independent as possible. In this respect, the most pure *model independent* channel for detection of such spin-1 resonances would be their production via VBF-like processes or its production in association with an EW gauge boson, as there only the coupling with the SM gauge bosons is involved. Unfortunately, for a Z' these signals are unobservable in a clean purely leptonic channel at LHC, even with increased luminosity [181–183]. A W' could be observed in the VBF $W^\pm Z \rightarrow W^\pm Z$ elastic scattering [181, 182] but such VBF processes could be used to determine the spin of the W' resonance at LHC only for relatively light resonances and with the assumption of increased luminosity [182]. Alternatively, the new spin-1 states can also be directly produced in pp collisions assuming they couple to light quarks. In this case, in order to establish that such new vector bosons are indeed associated with EWSB, one should analyze processes in which the new spin-1 particles decay into EW gauge boson, as in [184]. These are the channels that we exploit in the present Chapter.

The Chapter is structured as follows. In Sec. 4.1 we describe in detail the framework of the analyses. We explain which are the assumptions that we make, as well as which are the free parameters in the studies. In Sec. 4.2 we study the determination of the spin of new resonances in EW gauge boson pair production at the 14 TeV LHC. This Section is based on the published work [185]. We first introduce the channels that we study, and

we describe the realistic set of cuts that we apply. After estimating the region of the parameter space where a 5σ discovery would be possible at the LHC, we present the angular variables and asymmetries useful for the spin analysis. We estimate the LHC potential to determine the spin of a new vector resonance comparing with the case of a scalar particle. The results are presented as a function of the relevant parameters of the approach, as well as of the collected luminosity at 14 TeV. Next, in Sec. 4.3, we estimate which are the bounds on the existence of Z' resonances related to EWSB after the 7 TeV LHC run. This Section is based on the published work [186] and the corresponding update in [187]. Finally we present in Sec. 4.4 the conclusions of the Chapter.

4.1 Analysis framework

In this Chapter we study the production of new vector resonances through the channels

$$\begin{aligned} pp &\rightarrow Z' \rightarrow W^+W^- \rightarrow \ell^+\ell^{(\prime)-}\cancel{E}_T \ , \\ pp &\rightarrow W' \rightarrow W^\pm Z \rightarrow \ell^+\ell^-\ell^{(\prime)\pm}\cancel{E}_T \ . \end{aligned} \quad (4.1)$$

In order to study these processes we need to know the couplings of the new resonances to light quarks and to EW gauge bosons. Furthermore we should also know the mass and the total decay width of the vector resonances. We consider that these couplings, masses and widths are free parameters of the study, so that we do not have to restrict ourselves to any specific model. However, for the sake of concreteness, we do have to assume what is the Lorentz structure of the couplings of the new Z' and W' resonances to the light quarks and to the gauge bosons. Inspired by models where the new spin-1 states interact with the light quarks and the gauge bosons via their mixing with the SM vector states, or by extra-dimension models where the new resonances are Kaluza-Klein replicas of the SM gauge bosons, we assume here that the Z' and W' couplings exhibit the same Lorentz structure than those of the SM, but with arbitrary strength. Finally, we veto the Z' coupling to ZZ pairs as it usually happens in this class of models.

In order to normalize the couplings of Z' and W' to WW and WZ pairs respectively, we introduce normalization values related to the saturation of unitarity. For the Z' case, the partial wave amplitude for the process $W^+W^- \rightarrow W^+W^-$ would be saturated by the exchange of a Z' provided its coupling to EW gauge bosons satisfies [181]

$$g_{Z'WW}_{\max} = g_{ZWW} \frac{M_Z}{\sqrt{3}M_{Z'}} \ , \quad (4.2)$$

where, as usual, $g_{ZWW} = gc_\theta$. Analogously, for the W' case, a charged vector

resonance saturates unitarity of the scattering $W^\pm Z \rightarrow W^\pm Z$ for [181]

$$g_{W'WZ_{\max}} = g_{ZWW} \frac{M_Z^2}{\sqrt{3}M_{W'}M_W}. \quad (4.3)$$

In the analyses of this Chapter we use $g_{W'WZ_{\max}}$ and $g_{Z'WW_{\max}}$ simply as convenient normalizations for the couplings of the spin-1 resonances to SM gauge bosons.

As we have commented, for the present analyses only the couplings to light quarks have to be considered, in addition to the couplings to EW gauge bosons. Nevertheless, as we want to cover the larger possible range of models, we do not make any extra assumption on the rest of the couplings. This means that the widths of the new spin-1 resonances are assumed to receive contributions from its decay to light quarks and EW gauge boson pairs, as well as into other states, like t or b . To account for these decays, in this work we treat the Z' and W' total decay widths as free parameters. Thus for each final state, the relevant amplitude for $V' = Z', W'$ depends on three parameters: the mass of the resonance, $M_{V'}$; its width, $\Gamma_{V'}$; and the product of its couplings to light quarks (in the production vertex) and to SM gauge bosons (in the decay vertex), $g_{V'q\bar{q}} g_{V'WV}$. The only constraints that we have to impose are that the total decay widths need to account at least for the decays into EW gauge boson pairs and light quarks. Then, for a given value of the product of the couplings of the new resonance and of its mass, there is a lower bound on its width that reads [184]

$$\Gamma_{Z'} > 0.27 \text{ GeV} \left(\frac{g_{Z'q\bar{q}}}{g_{Zq\bar{q}}} \right) \left(\frac{g_{Z'WW}}{g_{Z'WW_{\max}}} \right) \left(\frac{M_{Z'}}{M_Z} \right)^2, \quad (4.4)$$

$$\Gamma_{W'} > 0.40 \text{ GeV} \left(\frac{g_{W'q\bar{q}}}{g_{Wq\bar{q}}} \right) \left(\frac{g_{W'WZ}}{g_{W'WZ_{\max}}} \right) \left(\frac{M_{W'}}{M_W} \right)^2, \quad (4.5)$$

where $g_{Zq\bar{q}} = g/c_\theta$ and $g_{Wq\bar{q}} = g/\sqrt{2}$.

After the three relevant parameters have been discussed, the cross sections for the processes in Eq. (4.1) can be expressed as

$$\begin{aligned} \sigma_{\text{tot}} = & \sigma_{SM} + \left(\frac{g_{V'q\bar{q}}}{g_{Vq\bar{q}}} \frac{g_{V'WV}}{g_{V'WV_{\max}}} \right) \sigma_{\text{int}}(M_{V'}, \Gamma_{V'}) \\ & + \left(\frac{g_{V'q\bar{q}}}{g_{Vq\bar{q}}} \frac{g_{V'WV}}{g_{V'WV_{\max}}} \right)^2 \sigma_{V'}(M_{V'}, \Gamma_{V'}) . \end{aligned} \quad (4.6)$$

There, the SM, interference and new resonance contributions are labeled as SM , int and V' respectively, much as in the same way we express the cross sections for anomalous TGV's in Eq. (3.37). For concreteness, if $V' = Z'$ then $g_{V'WV} \equiv g_{Z'WW}$ and $g_{V'q\bar{q}} \equiv g_{Z'q\bar{q}}$, while for $V' = W'$, $g_{V'WV} \equiv g_{W'WZ}$ and $g_{V'q\bar{q}} \equiv g_{W'q\bar{q}}$. In addition, in Section 4.3 we use the definition

$$G = \left(\frac{g_{Z'q\bar{q}}}{g_{Zq\bar{q}}} \right) \left(\frac{g_{Z'WW}}{g_{Z'WW_{\max}}} \right). \quad (4.7)$$

4.2. DETERMINATION OF THE SPIN

The technical details regarding the simulation tools that we have used, as well as the statistical discriminants that we have built, depend on the concrete analysis that we perform and present next.

4.2 Determination of the spin of new resonances

In this first analysis we focus on the capabilities of the LHC to determine the spin of new resonances. From the original work on relevant angular variables [188] to the more recent studies [189–203], much work has been devoted in the literature over the last years to this issue. As we have already commented VBF processes can be used to determine the spin of W' resonances at the LHC, but only on a limited range of masses and accumulated luminosities [182]. Alternative, here we study the potential of the LHC to decipher the spin of both Z' and W' through their direct production in pp collisions, as in Eq. (4.1).

In this Section we perform our analyses at the parton level, keeping the full helicity structure of the amplitudes. This is achieved using the package MadGraph4 [152] properly modified to include the new vector states and the desired couplings. We use the CTEQ6L parton distribution functions [153], in the present Section with renormalization and factorization scales given by $\mu_F^0 = \mu_R^0 = \sqrt{(p_T^{\ell+2} + p_T^{\ell-2})}/2$, where $p_T^{\ell\pm}$ is the transverse momentum of the two charged leptons in the Z' decay or of the two different flavor opposite sign leptons in the W' decay. For the case of W' decaying into three equal flavor leptons we choose the two opposite sign leptons whose invariant mass is not compatible with being the decay products of a Z . Nevertheless, the effects of these choices in the results that we present here are marginal. Finally, we simulate experimental resolutions by smearing the energies, but not directions, of all final state leptons with a Gaussian error given by a resolution $\Delta E/E = 0.1/\sqrt{E} \oplus 0.01$ (E in GeV). We also consider a lepton detection efficiency of $\epsilon^\ell = 0.9$.

The analyses follow the same structure for both the Z' and W' cases. We start describing the cuts imposed on the corresponding process, and we present afterwards the relevant cross sections and 5σ discovery regions. In these processes, the spin assignment of the new resonances is obtained from the spin correlation between the final state leptons, contrasting the expected results for spin-1 and spin-0 new states. We work then in the framework commonly used to analyze the spin of supersymmetric particles [189–193].

4.2.1 W' spin determination

For W' we study the channel

$$pp \rightarrow W' \rightarrow ZW^\pm \rightarrow \ell^+\ell^-\ell'^{\pm}\cancel{E}_T, \quad (4.8)$$

where as in the case of the previous Chapter only $\ell = e$ or μ are considered for a more realistic study. As we have described in the two exhaustive analyses that we have performed on this channel in Section 3.2, the main SM backgrounds for any BSM signal are the production of EW gauge boson pairs, WZ and ZZ , with its subsequent leptonic decay. In the ZZ production case one of the final state leptons must evade detection. Finally the SM production of top quarks can also lead to trilepton final states, however, this process is rather suppressed since one of the isolated leptons must originate from the semi-leptonic decay of a b -quark. In the present Section we neglect the contributions of $Z + \gamma$ production and both W and Z minor productions in association with extra jets, as these are marginal backgrounds in comparison to the rest of sources and to the uncertainties in the present analysis.

Selection of events

As in the previous analyses, the study starts with a series of kinematic cuts aiming to ensure the detection and the isolation of the final state leptons, plus a minimum transverse momentum requirement

$$|\eta_\ell| < 2.5, \quad \Delta R_{\ell\ell} > 0.2, \quad p_T^\ell > 10 \text{ GeV} \text{ and } \cancel{E}_T > 10 \text{ GeV}, \quad (4.9)$$

similar to the cuts in Eq. (3.38). Following the same structure than in Sec. 3.2, in the next step we look for at least a same flavor opposite charge lepton pair that is compatible with a Z , *i.e.*

$$|M_{\ell^+\ell^-} - M_Z| < 20 \text{ GeV}. \quad (4.10)$$

Furthermore we demand, in the search for the resonance, that the hardest observed lepton has a transverse momentum in excess of 120 GeV in order to tame the SM backgrounds.

Again, the neutrino momentum is reconstructed up to the two-fold ambiguity in Eq. (3.43). We demand that the events posses a solution to Eq. (3.43), and with the two values of the reconstructed neutrino momentum we obtain two possible solutions for the invariant mass of the $\ell\ell\nu$ system. In order to enhance the signal and to reduce the SM backgrounds we require that the final state is compatible with a W' production of a given mass,

$$|M_{\text{rec}}^{\text{min}} - M_{W'}| < \delta, \quad (4.11)$$

where in this case $M_{\text{rec}}^{\text{min}}$ is the smaller of the two possible solutions. In the analyses of the present Section we consider three reference V' masses 0.5, 1, and 1.5 TeV; and we take $\delta = 50, 100, \text{ and } 200$ GeV for each of the three cases, respectively.

We present in Fig. 4.1 (left panel) the values of the relevant cross sections at $\sqrt{s} = 14$ TeV, see Eq. (4.6), after the cuts are imposed. These are

4.2. DETERMINATION OF THE SPIN

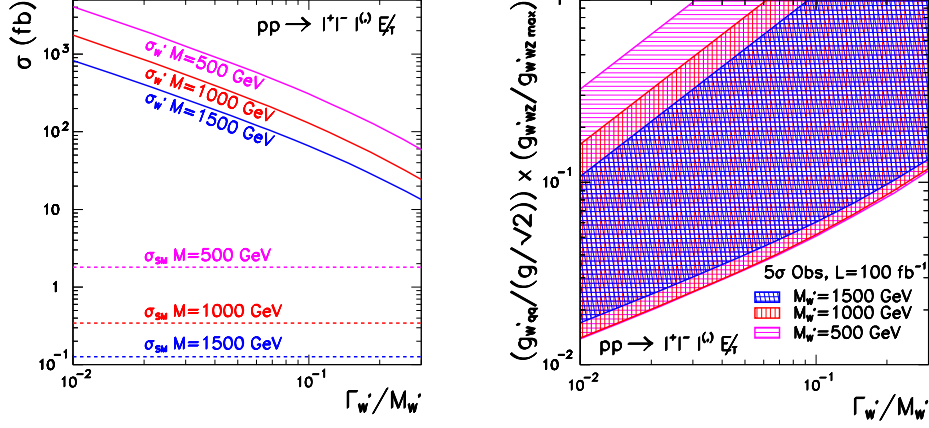


Figure 4.1: **Left panel:** signal and background cross sections at 14 TeV for the $\ell^+\ell^-\ell'^{\pm}\cancel{E}_T$ final state for all possible lepton flavor combinations without including lepton detection efficiencies. **Right panel:** the filled regions are the ranges of the parameters that allow for an observation of a W' with mass $M_{W'} = 0.5, 1,$ and 1.5 TeV with at least 5σ significance in the reaction $pp \rightarrow W' \rightarrow ZW^{\pm} \rightarrow \ell^+\ell^-\ell'^{\pm}\cancel{E}_T$ and an integrated luminosity of 100 fb^{-1} collected at 14 TeV.

$\sigma_{W'}(M_{W'}, \Gamma_{W'})$ and σ_{SM} , which after the cut in Eq. (4.11) is also a function of $M_{W'}$. The interference terms are negligible for all values of the W' mass and width considered after applying the described cuts. As it can be seen in Fig. 4.1, the SM backgrounds diminish as the new states become heavier. This is due to the fact that for a heavy state, the effect of the cut in Eq. (4.11) is more stringent on the SM backgrounds, as they present falling event distributions as a function of $M_{\text{rec}}^{\text{min}}$. Furthermore, as it was also expected, the signal cross section deteriorates as the width of the resonance grows. Altogether this channel presents at the end a small SM background due to the reduced leptonic branching ratio of the EW gauge bosons.

Discovery reach

Before we move to study the LHC capabilities to discriminate the spin of these W' new resonances, we briefly illustrate the LHC potential for a 5σ significance level discovery. This is depicted for the sake of completeness in the right panel of Fig. 4.1. There, the region of the parameter space where the LHC would be able to observe a W' with at least a 5σ significance level for an integrated luminosity of 100 fb^{-1} at 14 TeV is shown. This parameter space is obtained by counting the number of events after all the cuts are applied, assuming that the number of observed events is that expected in

the SM. For this hypothetical luminosity, the number of background events is large enough for Gaussian statistics to hold for $M_{W'} = 500$ and 1000 GeV and we impose $N_{W'} \geq 5\sqrt{N_{\text{SM}}}$ where $N_{W',\text{SM}} = \mathcal{L} \times \sigma_{W',\text{SM}} \times (\epsilon^\ell)^3$. For $M_{W'} = 1500$ GeV the number of expected background events is $N_{\text{SM}} = 9.8$ and we adopt the corresponding 5σ observability bound for Poisson statistics in the presence of this background, *i.e.* $N_{W'} > 18$. As expected, larger couplings are required for the observation as the resonances broaden, due to the fact that in this case the signal cross sections deteriorate as we have observed in Fig. 4.1. With this analysis we are able to determine the lower values of the parameter space allowing for a 5σ discovery. However, we still have to impose the constraint in Eq. (4.5). From this imposition we obtain the upper bounds on the discovery regions of the right panel of Fig. 4.1. We finally estimate the potential for a smaller collected data set. We note that with a reduced integrated luminosity of 10 fb^{-1} the lower line of the minimum coupling constant product needed for discovery is increased by a factor $\simeq 3$. However, a sizable fraction of the parameter space can still be probed.

Present bounds on W'

We can briefly compare the results depicted in the right panel of Fig. 4.1 with the direct searches for a W' that were performed either at Tevatron and in the 7 and 8 TeV LHC runs. Unfortunately, the comparison is not trivial since in most searches the experimental analyses relied on a specific model in which a concrete relation between the couplings, masses and total decay widths of the spin-1 resonances is assumed [204, 205], and sometimes the $W'WZ$ coupling is not unambiguously specified in the text. One exception is the CDF Collaboration search for new WW and WZ resonances in $p\bar{p} \rightarrow e^\pm jj\cancel{E}_T$ [206]. This analysis was performed in the Extended gauge model context [204, 205] (in which the couplings of the new resonance are a rescale of the SM ones), but with the strength of the $W'WZ$ coupling clearly specified, and indeed with the results expressed as a function of this coupling. We can infer from this work that a narrow 500 GeV W' is already excluded at 95% CL provided $\left(\frac{g_{W'q\bar{q}}}{g/\sqrt{2}} \times \frac{g_{W'WZ}}{g_{W'WZ_{max}}}\right) \gtrsim 0.21$. This exclusion limit is similar to the one derived by the DØ collaboration after they combine the leptonic and semileptonic $p\bar{p} \rightarrow W' \rightarrow WZ$ channels in [207]. There, the precise assumption for the $W'WZ$ coupling is not explicitly given. Nevertheless, we can estimate that, as in the CDF search, narrow light resonances are excluded at 95% CL for $\left(\frac{g_{W'q\bar{q}}}{g/\sqrt{2}} \times \frac{g_{W'WZ}}{g_{W'WZ_{max}}}\right) \gtrsim 0.2$. This implies that a small left corner of Fig. 4.1 was already excluded by these two Tevatron searches.

After the 7 and 8 TeV runs have finished, the LHC collaborations have already performed different analyses on the search for W' resonances. The

4.2. DETERMINATION OF THE SPIN

most recent searches for $W' \rightarrow WZ$ are performed using already the 8 TeV data sets [208–210]. In the case of the ATLAS searches, the 13 fb^{-1} –8 TeV data analysis in [208] was recently updated in [209]. There, the full 20.3 fb^{-1} of 8 TeV data is used to analyze the fully leptonic $pp \rightarrow \ell^+ \ell^- \ell'^{\pm} \cancel{E}_T$ channel. This analysis is performed using the Extended gauge model as one of the benchmark scenarios, and the $W'WZ$ coupling value is unambiguously specified. Therefore, the model dependent bounds can be reinterpreted in terms of the parameter space in Fig. 4.1. The 95% CL exclusion limits derived apply to narrow resonances (with $\Gamma_{W'}/M_{W'}$ below the W boson one in the SM), and can be translated into

$$\left(\frac{g_{W'q\bar{q}}}{g/\sqrt{2}} \times \frac{g_{W'WZ}}{g_{W'WZmax}} \right) \gtrsim 0.05 \text{ (0.05) [0.08] for } 500 \text{ (1000) [1500] GeV .} \quad (4.12)$$

This is, a sizable region on the left side of the right panel of Fig. 4.1 has been already excluded. In the CMS search [210], all the 8 TeV data set, accounting for 19.6 fb^{-1} of integrated luminosity, is analyzed in the same leptonic channel. Unfortunately CMS did not quote the precise value assumed for the $W'WZ$ coupling and consequently we cannot translate their bounds in precise constraints in our parameter space. The estimated bounds are expected to apply for narrow resonances and after considering the possible $O(M_W/M_Z)$ ambiguity they would cover a region of the space similar to that bounded by ATLAS [209].

Summarizing, after the LHC 7 and 8 TeV runs have concluded, the exclusion limits have already covered a large region of the parameter space for the narrowest resonances, while for the broader ones the exclusion regions are much milder. So there is still space for W' resonances after the present LHC exclusion limits are considered. Moreover the analyses of the spin and the techniques described in the present Section are valid for a large range of masses, widths and couplings.

Spin determination

In some of the previously cited studies of spin determination [189,190] it was shown that a convenient variable for contrasting the production of particles with different spin is

$$\cos \theta_{\ell\ell}^* \equiv \tanh \left(\frac{\Delta\eta_{\ell\ell}}{2} \right), \quad (4.13)$$

where $\Delta\eta_{\ell\ell}$ is defined as the rapidity difference between the same charge leptons. This quantity has the advantage of being invariant under longitudinal boosts. For illustration, we present in the left (center) [right] upper panel of Fig. 4.2 the $\cos \theta_{\ell\ell}^*$ spectrum for the production of spin-0 and spin-1 resonances and the reference mass considered, 500 (1000) [1500] GeV. The Figure illustrates the different relevant distributions after 100 fb^{-1} of data of

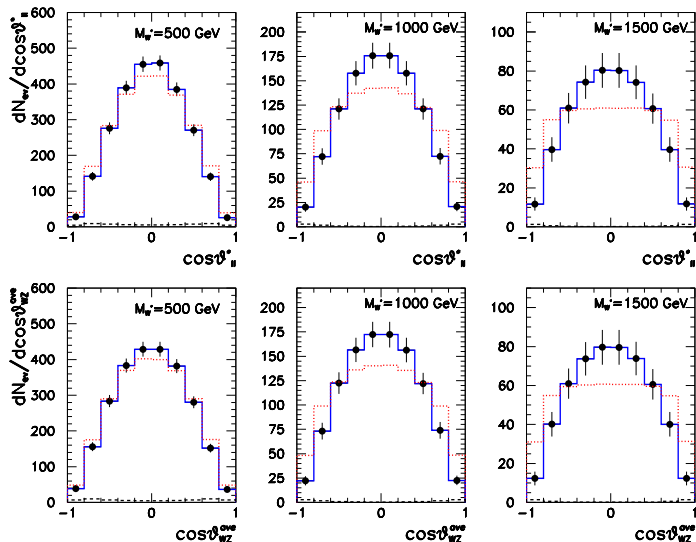


Figure 4.2: $\cos \theta_{\ell\ell}^*$ (upper panels) and $\cos \theta_{WZ}^{ave}$ (lower panels) distributions for the production of the charged vector resonance W' (solid blue line with error bars), and the production of a charged scalar resonance (dotted red line). The results are shown for $\Gamma_{W'} = 0.05M_{W'}$ and $\left(\frac{g_{W'q\bar{q}'}}{g_{Wq\bar{q}'}} - \frac{g_{W'WZ}}{g_{W'WZ_{max}}}\right) = 0.3$. The SM contribution (barely visible) is the dashed black line at the bottom, and we have assumed an integrated luminosity of 100 fb^{-1} for the 14 TeV run.

the 14 TeV run have been collected and the cuts in the selection procedure have been applied. For an easier comparison, we show the case of a vector angular distribution (solid blue line with error bars) and the case of a scalar contribution (dotted red line), where we normalize the production cross section of the scalar case to the one of the vector resonance. We assume the same mass and width for both spin assignments. The details on the values used for illustration can be seen in the caption of Fig. 4.2. The first thing we observe in the Figure is that in the present channel the SM background contributions (dashed black lines) are strongly suppressed and barely visible. This was already expected after looking at the left panel of Fig. 4.1. We can also observe that, as expected, the $\cos \theta_{\ell\ell}^*$ distribution for W' vector production exhibits a maximum at $\cos \theta_{\ell\ell}^* = 0$. On the other hand, the case of the scalar resonance deserves a discussion. In principle this spectrum should be completely flat for the production of scalars, however, the acceptance cuts, especially $|\eta_\ell| < 2.5$, distort this angular distribution. This reduces the discriminating power, especially for the lightest resonances. For the heaviest ones, we can foresee that the smaller cross section, see Fig. 4.1, will be par-

4.2. DETERMINATION OF THE SPIN

tially compensated by higher distinctive signals between the scalar case and the vector one with respect to the light mass case.

Alternatively, we can exploit the fact that once we have inferred the momentum of the neutrino, Eq. (3.43), we can build different angular correlations in the estimated WZ COM frame, as all the momenta are now determined. We study here the spin correlations using the reconstructed Z polar angle (θ_{WZ}) distribution evaluated in the WZ COM frame. The twofold ambiguity in Eq. (3.43) is logically translated into two possible angular distributions for θ_{WZ} . Here we consider the average of the two resulting distributions in our analysis. In [182] it was shown that the angular distribution of the reconstructed $\cos\theta_{WZ}$ variable for the solution yielding the minimum (maximum) WZ invariant mass, is peaked (has a valley) around zero when compared to the true θ_{WZ} one. Nevertheless, as it was also shown in there, the average of the two possible reconstructions has a very similar distribution to the true one. Thus, we plot in the lower panels of Fig. 4.2 the average spectrum, $\cos\theta_{WZ}^{\text{ave}}$. As in the case for $\cos\theta_{\ell\ell}^*$, we also show there the distributions for the production of spin-0 and spin-1 resonances and the three reference masses considered. We follow the same procedure regarding the normalization of the scalar distribution to the vector one, and, in addition, the curves are labeled with the same notation.

As we can observe, the behavior of the distributions in the two angular variables, $\cos\theta_{\ell\ell}^*$ and $\cos\theta_{WZ}^{\text{ave}}$, is very similar. The spin-1 resonances are peaked near $\cos\theta_{WZ}^{\text{ave}} = 0$, and the spin-0 are also peaked there for the lightest masses, while the behavior is flatter as we move to heavier masses, where the effects of the cuts are smaller. Indeed, $\cos\theta_{\ell\ell}^*$ and $\cos\theta_{WZ}^{\text{ave}}$ happen to be strongly correlated as shown in the upper panels of Fig. 4.3. There we plot the $\cos\theta_{\ell\ell}^* \otimes \cos\theta_{WZ}^{\text{ave}}$ spectrum for $M_{W'} = 0.5$ TeV (upper left panel) and 1.5 TeV (upper right panel). We show the distributions for $\Gamma_{W'} = 0.05M_{W'}$, but we have checked that the results are very insensitive to the precise value of the width. As it is clear from the Figure, there is a strong correlation between $\cos\theta_{\ell\ell}^*$ and $\cos\theta_{WZ}^{\text{ave}}$. This strong correlation could be somehow unforeseen, given the definitions of both variables and the different behaviors of the $\cos\theta_{WZ}^{\text{max}}$ and $\cos\theta_{WZ}^{\text{min}}$ distributions. As expected the correlation gets stronger as the W' mass increases. This is so because heavier resonances decay into more energetic EW gauge bosons and consequently the final state leptons have the tendency to follow the direction of the parent W or Z , correlating consequently even more strongly both angular distributions.

Due to the correlation between the two variables, it is expected that both have a comparable spin discriminating power. And this is actually the case, except for $M_{W'} = 500$ GeV, where $\cos\theta_{WZ}^{\text{ave}}$ performs slightly worse. Moreover larger systematic uncertainties are expected in the reconstruction of θ_{WZ} , as it requires better understanding and calibration of the detectors for the precise measurement of the missing transverse momentum needed to build $\cos\theta_{WZ}^{\text{ave}}$. This is similar to one of the argumentations we have used in

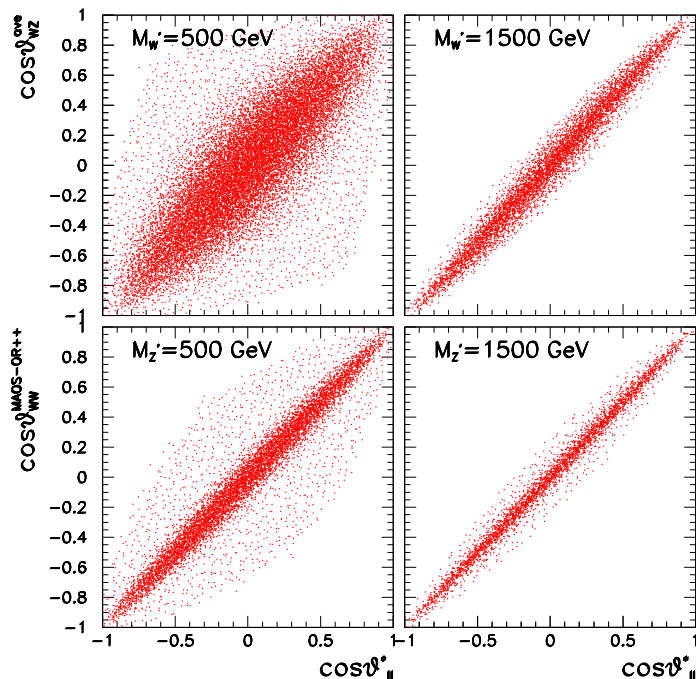


Figure 4.3: We show in the upper panels the $\cos \theta_{\ell\ell}^* \otimes \cos \theta_{WZ}^{\text{ave}}$ spectrum for W' and two masses: $M_{W'} = 0.5$ TeV in the upper left panel and 1.5 TeV in the upper right one. There, $\cos \theta_{WZ}^{\text{ave}}$ is the average of the two possible reconstructions as explained in the text. The lower panels depict the $\cos \theta_{\ell\ell}^* \otimes \cos \theta_{WW}^{\text{MAOS-OR}++}$ spectrum for Z' and $M_{Z'} = 0.5$ TeV in the lower left panel, and 1.5 TeV in the lower right one.

Sec. 3.2 to choose p_T^Z as the variable to estimate the updated LHC potential to measure $g_5^Z, g_4^Z, \tilde{\kappa}_Z$ and $\tilde{\lambda}_Z$.

Following the discussion, we proceed to estimate the potential to determine the spin of a vector resonance using the angular distribution $\cos \theta_{\ell\ell}^*$. In order to quantify the parameter space region for which a positive discrimination between spin-0 and spin-1 resonances is possible we construct the asymmetry

$$A_{\ell\ell} = \frac{\sigma(|\cos \theta_{\ell\ell}^*| < 0.5) - \sigma(|\cos \theta_{\ell\ell}^*| > 0.5)}{\sigma(|\cos \theta_{\ell\ell}^*| < 0.5) + \sigma(|\cos \theta_{\ell\ell}^*| > 0.5)}. \quad (4.14)$$

Notice that with this observable we can eliminate possible normalization systematics in the angular distributions. Using this angular asymmetry we build now the statistical test to estimate the parameter space where the spin can be established with a certain degree of confidence. In particular, the

4.2. DETERMINATION OF THE SPIN

99% CL spin discrimination condition reads

$$|A_{\ell\ell}^V - A_{\ell\ell}^S| \geq 2.58 \sigma_{A_{\ell\ell}^V} = 2.58 \frac{\sqrt{1 - A_{\ell\ell}^{V2}}}{\sqrt{N_{\text{tot}}}}, \quad (4.15)$$

where $\sigma_{A_{\ell\ell}^V}$ is the expected statistical error of the variable $A_{\ell\ell}^V$ and $N_{\text{tot}} = \mathcal{L} \times \sigma_{\text{tot}} \times (\epsilon^\ell)^3$ with σ_{tot} as in Eq. (4.6). In writing Eq. (4.15) we implicitly assume that for the 99% CL spin determination the number of events N_{tot} is always large enough for Gaussian statistics to hold. Indeed we verify that this is the case even for the smallest couplings for which 99% CL spin determination is possible.

The results of this exercise are shown in Fig. 4.4. There we display the region of the parameter space where the W' spin can be established with 99% CL using $A_{\ell\ell}$ for an integrated luminosity of $\mathcal{L}=100 \text{ fb}^{-1}$ collected at 14 TeV at the LHC, and for the three masses selected as benchmark points for this analysis. All the points inside the colored regions allow for the 99% CL spin discrimination for the corresponding mass. In obtaining the results we take into account only the statistical errors and we assume that the observed distributions follow that of a vector resonance, as could be inferred from Eq. (4.15). Notice that the lower limits are obtained from Eq. (4.15), but the upper bounds are obtained from the constraint on the total decay width as shown in Eq. (4.5).

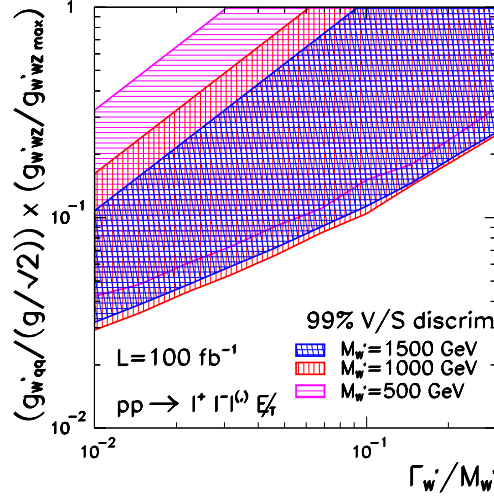


Figure 4.4: Parameter space region where the W' spin can be determined at 99% CL using the asymmetry $A_{\ell\ell}$ for an integrated luminosity of 100 fb^{-1} collected at the LHC 14 TeV run.

We can compare Fig. 4.4 to Fig. 4.1, *i.e.* the region where a 99% CL

spin discrimination is feasible to the region where a 5σ discovery is possible, in both cases for $\mathcal{L}=100 \text{ fb}^{-1}$ collected at 14 TeV. From this comparison we conclude that the minimum couplings necessary to determine the W' spin at 99% CL for this integrated luminosity are ~ 2 times larger than the minimum couplings needed for the W' discovery. Moreover, as seen in Fig. 4.2, the acceptance cuts modify more drastically the distributions for lighter W' masses, and consequently, the discrimination between spin-0 and spin-1 requires larger statistics, reflected in larger couplings and production cross sections required. In the same way, the decrease of the production cross section between a W' of 1 TeV and one of 1.5 TeV is partially compensated by the fact that for the heavier masses the spin-0 distribution is flatter because the effects of the cuts are less dramatical. This leads at the end to similar couplings required for the spin discrimination for both masses. In summary, we find that the LHC will be able to successfully unravel the spin of a possible new W' state with 99% CL in a large fraction of the parameter space of discovery.

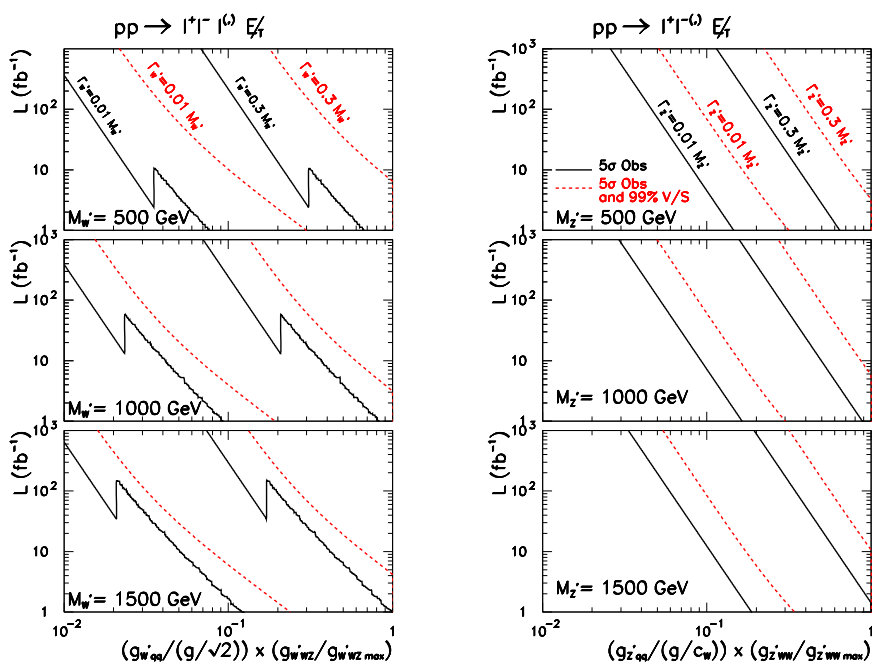


Figure 4.5: The solid (dashed) lines stand for the integrated luminosity at 14 TeV required for the 5σ discovery (99% CL spin determination) of W' in the left panels and Z' in the right ones, as a function of the vector resonance couplings. We present the results for three masses and two widths: $\Gamma_{V'} = 0.01M_{V'}$ and $\Gamma_{V'} = 0.3M_{V'}$. See the text for detailed information on the statistics used.

4.2. DETERMINATION OF THE SPIN

Finally, in order to address the potential of the LHC for earlier runs or with upgraded luminosity, but still at 14 TeV, we quantify the luminosity requirement for the discovery and the spin determination of the resonance as a function of its parameters. We use the same statistical procedures that we have described in the text, but here adding the luminosity as a free parameter. In the left panel of Fig. 4.5 we plot the integrated luminosity needed for a 5σ discovery of a W' (solid lines) and for a 99% CL spin determination based on Eq. (4.15) (dashed lines).

The results are presented as a function of the W' couplings for our three reference masses and for two widths ($\Gamma_{W'} = 0.01M_{W'}$ and $\Gamma_{W'} = 0.3M_{W'}$). We only show these two widths for an easier illustration, but intermediate values interpolate between the two plotted lines. As we have explained, the discovery requirements are obtained using Poisson or Gaussian statistics depending on whether the expected number of SM events is smaller or larger than 15, and the change from one statistics to the other determines the discontinuities in the corresponding lines. For the case of the 99% CL spin determination the number of expected events is always large enough for Gaussian statistics to hold. We can see from Fig. 4.5 that an earlier discovery, *e.g.* with 10 fb^{-1} , would still be possible even for rather weakly coupled W' . The W' spin determination requires in contrast larger couplings, but it can also be carried out in a sizable region of the parameter space in earlier runs. We remind the reader that, as we have explained, the LHC 8 TeV experimental measurements have already excluded some of the points that allow for an early spin discrimination, especially for the narrowest and lightest resonances.

4.2.2 Z' spin determination

In the case of a neutral vector resonance, we analyze the Z' spin through the channel

$$pp \rightarrow Z' \rightarrow W^+W^- \rightarrow \ell^+\ell^{(\prime)-}\cancel{E}_T . \quad (4.16)$$

As we already noted in the first part of Sec. 3.2, the main SM background for this process is the EW production of WW pairs with the subsequent leptonic decay. A smaller source of SM backgrounds is the EW ZZ production with one Z decaying into charged leptons and the other decaying invisibly into neutrinos or also with both Z decaying into charged leptons when two of which escape undetected, which is however a rare process. As we have commented, in this channel a dangerous additional source of background events is provided by the SM production of $t\bar{t}$ pairs with both top quarks decaying semileptonically. We will see that, as in the analysis of Sec. 3.2, a jet veto is required to suppress this background. Finally, we complete here the simulation of background sources including $\tau^+\tau^-$ production with both τ 's decaying leptonically.

Selection of events

As usual, the selection of events begins with a series of cuts aiming to ensure the detection and the isolation of the final state leptons. In the present case we require two final state leptons (e or μ) with opposite charge and

$$|\eta_\ell| < 2.5 \quad , \quad \Delta R_{\ell\ell} > 0.2 \quad \text{and} \quad p_T^\ell > 50 \text{ GeV} \quad . \quad (4.17)$$

One can notice that in this case the requirement on the lepton momentum is more stringent than previously. The reason behind a more aggressive cut is to tame the dangerous backgrounds in a channel where the full reconstruction of the final state particles presents a challenge. Actually, the presence of two neutrinos in the final state renders impossible the complete reconstruction of the event. In order to characterize the signal we can make use of the transverse invariant mass as a first alternative, just as we have done in Sec. 3.2. We thus recover the definition of M_T^{WW} in Eq. (3.44). Alternatively we can attempt to reconstruct the WW invariant mass by estimating the momenta of the two escaping neutrinos produced using the M_{T2} assisted on-shell (MAOS) reconstruction [211]. This reconstruction was built in [211] in the context of weakly interacting massive particle (WIMP) searches. There, the authors studied a pair production process where the mother particles decay to a visible SM particle and a WIMP. The reconstruction, whose main details we describe here, leads at the end to final state reconstructed momenta of the invisible particles correlated to the true momenta. This allowed for the possibility of reconstructing several distributions to study the properties of the mother particles, for instance their masses and spin. The reconstruction was later extended and applied to the case of the Higgs search in [212]. There, the channel $pp \rightarrow h \rightarrow W^+W^- \rightarrow \ell^+\nu_\ell\ell'^-\nu_{\ell'}$ was studied. This is indeed the same channel that we study here, although for a different range of masses. For $W^+(p_1 + p_2)W^-(k_1 + k_2) \rightarrow \ell^+(p_1)\nu(p_2)\ell^-(k_1)\nu(k_2)$ the variable M_{T2} is defined as [213]

$$M_{T2} \equiv \min_{\vec{p}_{2T} + \vec{k}_{2T} = \vec{p}_T} \left[\max \left\{ M_T(\vec{p}_{1T}, \vec{p}_{2T}), M_T(\vec{k}_{1T}, \vec{k}_{2T}) \right\} \right] \quad , \quad (4.18)$$

where M_T is the transverse mass defined as

$$M_T^2(\vec{p}_{1T}, \vec{p}_{2T}) = 2(p_{1T}p_{2T} - \vec{p}_{1T} \cdot \vec{p}_{2T}) \quad . \quad (4.19)$$

Assuming that the initial state radiation is negligible, the solution for the transverse MAOS momenta is simply given by

$$\vec{p}_{2T}^{\text{maos}} = -\vec{k}_{1T} \quad \text{and} \quad \vec{k}_{2T}^{\text{maos}} = -\vec{p}_{1T} \quad . \quad (4.20)$$

To estimate the longitudinal momentum components there are two possible approaches in this context. The first one is best suited for the cases where the mother particles of the invisible state are on-shell, while the second one

4.2. DETERMINATION OF THE SPIN

performs better for cases where they are off-shell (like in $h \rightarrow W^+W^- \rightarrow \ell^+\nu_\ell\ell^{(\prime)-}\nu_{\ell'}$). In the present analysis we are in the context of the former case, but we study for completeness the two possible reconstructions. In the first scheme one requires the on-shell conditions for both the invisible particles in the final state and the mother particles in the intermediate state (W) [211] (here called MAOS-original). This results into a four-fold degeneracy

$$\begin{aligned} p_{2L}^{\text{maos}}(\pm) &= \frac{1}{p_{1T}^2} \left[p_{1L} A \pm \sqrt{p_{1T}^2 + p_{1L}^2} \sqrt{A^2 - p_{1T}^2 p_{2T}^{\text{maos} 2}} \right], \\ k_{2L}^{\text{maos}}(\pm) &= \frac{1}{k_{1T}^2} \left[k_{1L} B \pm \sqrt{k_{1T}^2 + k_{1L}^2} \sqrt{B^2 - k_{1T}^2 k_{2T}^{\text{maos} 2}} \right], \end{aligned} \quad (4.21)$$

where $A \equiv M_W^2/2 + \vec{p}_{1T} \cdot \vec{p}_{2T}^{\text{maos}}$ and $B \equiv M_W^2/2 + \vec{k}_{1T} \cdot \vec{k}_{2T}^{\text{maos}}$. In the second possible scheme [212], one requires also on-shell conditions for the invisible particles in the final state, but for the mother particles one imposes instead

$$(\vec{p}_1 + \vec{p}_2^{\text{maos}})^2 = (\vec{k}_1 + \vec{k}_2^{\text{maos}})^2 = M_{T2}^2, \quad (4.22)$$

which gives unique longitudinal MAOS momenta (here called MAOS-modified)

$$p_{2L}^{\text{maos}} = \frac{p_{2T}^{\text{maos}}}{p_{1T}} p_{1L} \quad \text{and} \quad k_{2L}^{\text{maos}} = \frac{k_{2T}^{\text{maos}}}{k_{1T}} k_{1L}. \quad (4.23)$$

In order to illustrate the accuracy of the neutrino momenta determination in the MAOS reconstruction scheme we compare in Fig. 4.6 the reconstructed $Z' \rightarrow W^+W^-$ invariant mass using the MAOS-original (with sign $++$ in Eq. (4.21) for illustration), MAOS-modified as in Eq. (4.23), and the WW transverse invariant mass as in Eq. (3.44). In addition, for the sake of comparison the shaded green area represents the real spectrum. As we can see, the three methods lead to very similar results. This is expected as the signal is dominated by Z' decaying into on-shell W 's. In contrast to the W' analysis of the previous Subsection, here the reconstruction of the signal and the reduction of the background is more challenging as in all the reconstruction methods the characteristic peak associated with the production of the resonance is substantially broadened with respect to the true invariant mass. However, it is still possible to suppress the backgrounds and enhance the Z' signal demanding any of the reconstructed WW masses to be around $M_{Z'}$ within a broad width. Consequently in our study we demand the WW transverse invariant mass to comply with

$$M_T^{WW} > \frac{M_{Z'}}{2}, \quad (4.24)$$

where only a lower cut is required because the background distribution is a very steeply falling function of M_T^{WW} , decreasing much faster than the one for the Z' signal.

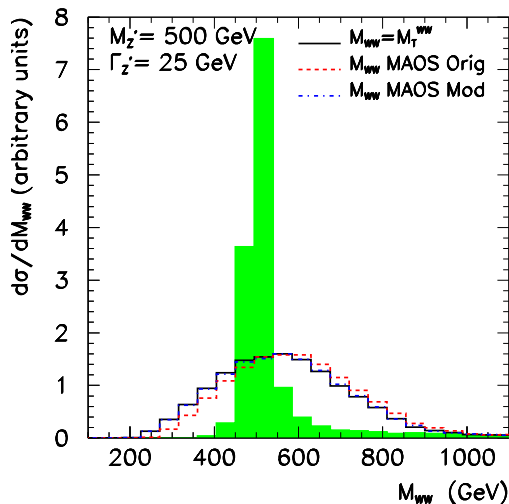


Figure 4.6: Reconstructed WW invariant mass distributions for $pp \rightarrow Z' \rightarrow W^+W^- \rightarrow \ell^-\ell^+\cancel{E}_T$ assuming $M_{Z'} = 500$ GeV and $\Gamma_{Z'} = 25$ GeV. The solid (black) line corresponds to $M_{WW} = M_T^{WW}$, as in Eq. (3.44). The dashed (red) line stands for the invariant mass reconstructed using the MAOS–original momentum prescription with sign $++$ in Eq. (4.21) and the dash–dot (blue) line represents MAOS–modified prescription, see Eq. (4.23). The shadow (green) area represents the true spectrum.

As in the analysis of Section 3.2, after the cuts in Eqs. (4.17) and (4.24), the $t\bar{t}$ SM background is still quite large. In order to suppress it, we veto the presence of the events with additional jets accomplishing

$$|\eta_j| < 3 \quad \text{and} \quad p_T^j > 20 \text{ GeV}. \quad (4.25)$$

As the QCD radiation and pile–up can lead to the appearance of an additional jet even in signal events, we can account for this in a simplified way introducing the probability of a QCD (EW) event to survive such a central jet veto [214]. The survival probability due to pile–up has been estimated to be 0.75 for a threshold cut of $p_T = 20$ GeV [215]. Thus, taking into account these two effects we include in our analysis veto survival probabilities with values

$$P_{\text{surv}}^{\text{EW}} = 0.56 \quad \text{and} \quad P_{\text{surv}}^{\text{QCD}} = 0.22. \quad (4.26)$$

Finally, for events presenting same flavor lepton pairs, *i.e.* ee or $\mu\mu$, there is an additional SM contribution stemming from ZZ production with one of the Z bosons decaying invisibly and the other into a charged lepton pair, or from Z production followed by its decay to leptons. For these final states,

4.2. DETERMINATION OF THE SPIN

we supplement the cuts in Eqs. (4.17), (4.24) and (4.25) further imposing that

$$\cancel{E}_T > 50 \text{ GeV and } M_{\ell\ell} > 100 \text{ GeV}, \quad (4.27)$$

in order to require a large missing transverse momentum, and to avoid the pair of leptons to be coming from a Z boson. The second cut resembles the one in Eq. (3.39) of the previous Chapter.

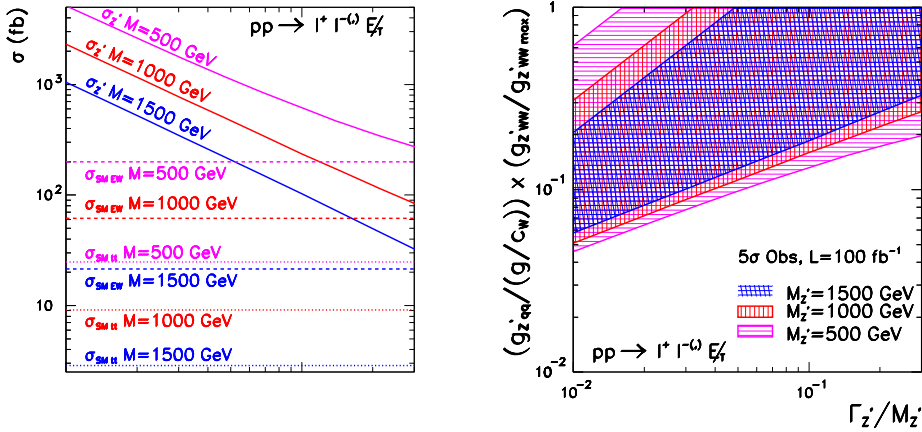


Figure 4.7: **Left panel:** signal and background cross sections for the $\ell^+ \ell'^- \cancel{E}_T$ final state for all possible lepton flavor combinations without including lepton detection efficiencies nor survival probabilities. The distributions are shown after applying all the cuts described in the text assuming 14 TeV of COM energy at the LHC. **Right panel:** the filled regions delimit the ranges of the parameters for an observation of a Z' with masses $M_{Z'} = 0.5, 1, \text{ and } 1.5$ TeV, with at least 5σ significance, in the reaction $pp \rightarrow Z' \rightarrow W^+ W^- \rightarrow \ell^+ \ell'^- \cancel{E}_T$. The regions correspond to an integrated luminosity of 100 fb^{-1} at 14 TeV.

We show in the left panel of Fig. 4.7 the values of $\sigma_{Z'}$ and σ_{SM} for the EW and $t\bar{t}$ backgrounds at $\sqrt{s} = 14$ TeV. We denote the sum of the SM backgrounds not originating from $t\bar{t}$ production as EW background. Once the cuts described above are imposed the interference terms are negligible for all the values of the Z' masses and widths considered, as it happened in the previous Subsection with W' . However, the backgrounds for Z' in the leptonic final states are considerably larger than the ones for W' . This is a consequence of the very broad reconstruction of the Z' invariant mass, as seen in Fig. 4.6. As we have done for the W' case we depict in the right panel of Fig. 4.7 the parameter space region where the LHC will be able to observe a Z' with at least 5σ significance for an integrated luminosity of 100 fb^{-1} at 14 TeV. The statistical analysis performed is the same we have described

for the W' case. However now, given the considered luminosity, the number of background events is always large enough for Gaussian statistics to hold and we simply impose $N_{Z'} \geq 5\sqrt{N_{SM}}$, where $N_{Z'} = \mathcal{L} \times \sigma_{Z'} \times P_{\text{surv}}^{\text{EW}} \times (\epsilon^\ell)^2$ and $N_{SM} = \mathcal{L} \times \left(\sigma_{SM}^{\text{EW}} \times P_{\text{surv}}^{\text{EW}} + \sigma_{SM}^{t\bar{t}} \times P_{\text{surv}}^{\text{QCD}} \right) \times (\epsilon^\ell)^2$. The worse signal reconstruction for a Z' affects also the results shown in the right panel of Fig. 4.7. Comparing it with the one for W' — see the right panel of Fig. 4.1— we find that establishing the existence of a Z' into the WW channel requires larger couplings to light quarks and vector boson pairs than for W' in WZ . This is a consequence of the larger SM backgrounds remaining after a more challenging signal reconstruction.

Present bounds on Z'

At present there are much less results from searches for Z' decaying into gauge bosons than for the case of a W' . This is probably related to the more challenging reconstruction required to measure or exclude a Z' in comparison to the easier $W' \rightarrow WZ$ reconstruction.

Still, a small corner of the right panel of Fig. 4.7 has been directly probed by Tevatron searches. The CDF analysis in [206], whose main features we have already discussed in the analogous Subsection for the W' case, indicates that for narrow and light masses, ~ 500 GeV, a Z' with $\left(\frac{g_{Z'q\bar{q}}}{g_{Zq\bar{q}}} \times \frac{g_{Z'WW}}{g_{Z'WW\text{max}}} \right) \gtrsim 0.19$ is excluded at 95% CL. Moving to the LHC, we note that there are currently no experimental searches from the LHC collaborations to exclude $Z' \rightarrow WW$ resonances. The $pp \rightarrow WW$ searches for BSM physics have usually been performed in the context of graviton models and cannot be directly translated in bounds for Z' .

In order to partially fill this gap, we present in the next Section our own re-analysis of LHC experimental results on the production of WW , that serves us to derive the strongest available exclusion bounds on Z' decaying into gauge boson pairs. We leave the details for the forthcoming Section, while here it suffices to note that those results still leave room for the discovery of Z' signals and its posterior spin determination at 14 TeV, which we now focus on.

Spin determination

In order to discriminate the spin of a neutral resonance we first employ the variable $\cos\theta_{\ell\ell}^*$ in Eq. (4.13), as we have already probed its utility in the W' analysis. As in there, the fact that this angular distribution does not require the reconstruction of the neutrino momentum avoids the presence of any reconstruction ambiguities. We plot in Fig. 4.8 (upper panels) the $\cos\theta_{\ell\ell}^*$ spectrum for the production of spin-0 and spin-1 resonances, for our three reference masses, and assuming a width of $\Gamma_{Z'} = 0.01M_{Z'}$

4.2. DETERMINATION OF THE SPIN

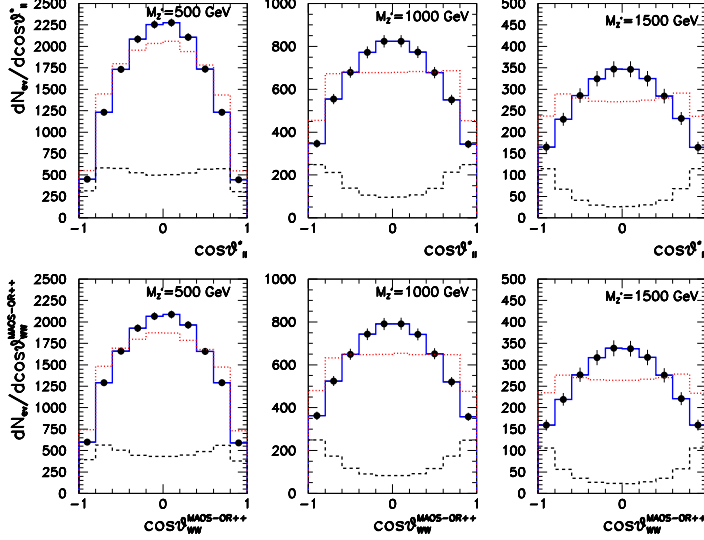


Figure 4.8: $\cos\theta_{ll}^*$ (upper panels) and $\cos\theta_{WW}^{\text{MAOS-OR++}}$ (lower panels) distributions for the production of the neutral vector resonance (solid blue line with error bars), and the production of a neutral scalar resonance (dotted red line). The results are shown for $\Gamma_{Z'} = 0.01M_{Z'}$ and $\left(\frac{g_{Z'q\bar{q}}}{g_{Zq\bar{q}}} \frac{g_{Z'WW}}{g_{Z'WW_{max}}}\right) = 0.3$. The contribution of the SM background is depicted by the dashed black line, and we have assumed an integrated luminosity of 100 fb^{-1} from the 14 TeV run.

and $\left(\frac{g_{Z'q\bar{q}}}{g_{Zq\bar{q}}} \frac{g_{Z'WW}}{g_{Z'WW_{max}}}\right) = 0.3$. The curves follow the same labeling than in Fig. 4.2: the Z' signals correspond to the solid blue lines with error bars, while the dotted red lines correspond to scalar resonances normalized to give the same production cross section than the vector ones for an easier comparison, exactly as we have done for the W' case. Finally the dashed black lines show the SM backgrounds, that in this case are not negligible anymore. Analogously to the W' case, we can see that the acceptance cuts distort considerably the spin-0 spectrum at lower masses, making the discrimination more difficult. For heavier states the production cross sections diminish, but as the final state leptons have a larger tendency to follow the direction of the parent W , since it is more energetic, the effects of the cuts ameliorate. Altogether the LHC potential to determine the spin of the vector resonance remains almost constant when we increase the mass considered, as we will see in the following. However, we study first the power of using the MAOS reconstruction scheme to perform the spin distinction.

We explore the expected distribution of the W polar angle in the WW COM frame, as reconstructed using the different MAOS prescriptions. As

an illustration we depict in the lower panels of Fig. 4.8 the reconstructed $\cos\theta_{WW}$ spectrum for the production of spin-0 and spin-1 resonances and our three reference masses. We assume the same values for the width and the relevant product of couplings than for the upper panels. The $\cos\theta_{WW}$ distributions are obtained from the MAOS-original momentum prescription with sign $++$ in Eq. (4.21). The two angular distributions in Fig. 4.8 present a very similar discrimination power. As it happened with the W' case, both distributions are strongly correlated as can be seen in the lower panels of Fig. 4.3. Consequently, we can foresee a similar spin discrimination power for both variables. Similar conclusions are reached when using either the MAOS-original momentum prescription with sign $--$ in Eq. (4.21), the average of the distributions with $+-$ and $-+$ signs, or the MAOS-modified prescription in Eq. (4.23). Although the different angular distributions present a similar power to discriminate between a spin-0 and a spin-1 new resonance, we choose again to estimate the LHC potential using the $\cos\theta_{\ell\ell}^*$ variable. As in the previous case, this variable avoids the need of reconstructing the neutrino momentum, minimizing the uncertainties related to the calibration of the detectors.

We proceed to estimate the LHC potential to determine the spin of the vector resonance running at 14 TeV and after 100 fb^{-1} of data are collected. From the statistical point of view, we apply exactly the same procedure than for the W' case. This means that we evaluate the asymmetry of Eq. (4.14) and we impose the 99% CL spin discrimination as in Eq. (4.15). The number of events required for a spin discrimination at the 99% CL is always enough for Gaussian statistics to hold. We present in Fig. 4.9 the Z' parameter space region for the 99% CL spin determination. As in the W' case, the minimum couplings needed for the spin discrimination are approximately twice the ones required for the Z' discovery. Moreover, the minimum couplings required for the spin determination exhibit a very mild dependence on the resonance mass. As we have anticipated, the reason is that the acceptance cut effects are smaller for heavier states, compensating partially the decrease in the production cross sections.

In order to close the present Section, we show the regions allowing for a discovery and a 99% CL spin discrimination using the collected luminosity as one of the free parameters of the study. This serves us to estimate the LHC potential with earlier and extended 14 TeV data sets. In the right panels of Fig. 4.5 we show the required integrated luminosity for a 5σ discovery (solid lines), and for a 99% CL spin determination based on Eq. (4.15) (dashed lines), for our three reference masses and two widths ($\Gamma_{Z'} = 0.01M_{Z'}$ and $\Gamma_{Z'} = 0.3M_{Z'}$), as a function of the Z' couplings. We find that for a given value of the Z' couplings the required luminosity for 99% CL spin determination based on the study of $A_{\ell\ell}$ is a factor ~ 20 (10) {9} larger than the one required for the 5σ discovery for $M_{Z'} = 500$ (1000) {1500} GeV, and that these factors are almost independent of $\Gamma_{Z'}/M_{Z'}$. Clearly,

4.3. BOUNDS ON Z' DECAYING TO W^+W^-

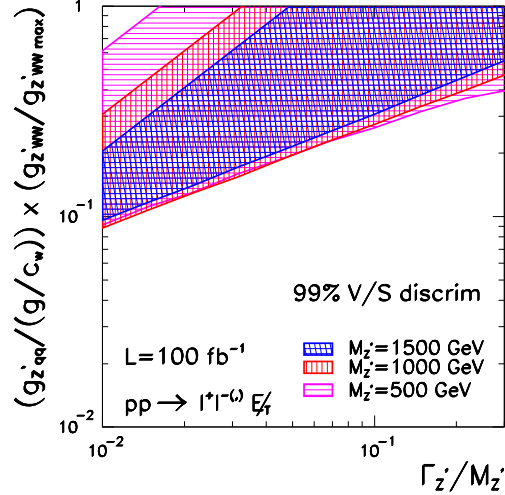


Figure 4.9: Parameter space region where the Z' spin determination can be performed at 99% CL for an integrated luminosity of 100 fb^{-1} at 14 TeV, using the asymmetry $A_{\ell\ell}$.

the discrimination of the spin of a new Z' resonance is more challenging than the one for W' .

4.3 Bounds on Z' decaying to W^+W^-

In this section we show how it is possible to derive bounds on new neutral spin-1 resonances associated to the EWSB from the available 7 TeV ATLAS and CMS data sets on WW pair production decaying in the channel in Eq. (4.16), where as usual ℓ and ℓ' stand for electrons and muons. We perform a model independent analysis using the same characterization framework described in Section 4.1. Consequently we present the results as constraints on the relevant spin-1 boson effective couplings, mass and width.

For the analysis we make use of the ATLAS experimental measurement of the $pp \rightarrow WW$ cross section, that was performed using 4.7 fb^{-1} of 7 TeV data [216], and the CMS experimental search in the same channel using 4.6 fb^{-1} of 7 TeV data [217]. In this analysis our strategy is to use as much as possible the information on the SM expectations carefully evaluated by the experimental collaborations, while we simulate the Z' signals expected after imposing the same cuts than the experimental collaborations have imposed in the evaluation of the SM expectations. In order to tune our Monte Carlo for the Z' signals we simulate the SM production of WW pairs and we scale

it to the results of the expectations presented by ATLAS and CMS.

We use two different methods for implementing this procedure. In the first one, we use the package MadGraph4 [152] to evaluate the $\mathcal{O}(\alpha_{\text{em}}^4)$ signal matrix elements for the subprocesses $q\bar{q} \rightarrow \ell^+ \nu \ell'^- \nu'$, with $\ell/\ell' = e, \mu$. In this case, we also estimate the contribution with $\ell/\ell' = \tau$, when the τ -leptons then decay to either e or μ and a neutrino. In the first analysis procedure this output is fed into PYTHIA [165] for parton shower and hadronization, and afterwards the events go through PGS 4 [166] for the detector simulation. This first procedure is labeled as “ME+Pythia+PGS–MC”. In a second evaluation we use a *homemade* Monte Carlo that evaluates the process in Eq. (4.16) at the parton level using the $\mathcal{O}(\alpha_{\text{em}}^4)$ signal matrix elements for the subprocesses $q\bar{q} \rightarrow \ell^+ \nu \ell'^- \nu'$, with $\ell/\ell' = e, \mu$. The scattering amplitudes for the relevant subprocesses are obtained using the package MadGraph4 [152]. This second procedure is labeled instead as “OUR ME–MC”. Both processes make again use of the CTEQ6L parton distribution functions [153] and the MadGraph4 default renormalization and factorization scales.

4.3.1 Selection of events and statistical analysis

Analysis of ATLAS results

The ATLAS measurement of WW production [216] was carried out using signal and background expectations evaluated at NLO and with accurate detector simulations. Here we perform an analysis based on exactly the same selection procedure. In order to take into account some of the realistic features included in the ATLAS evaluation, we normalize our total cross section predictions of the SM WW production for the ee , $e\mu$ and $\mu\mu$ channels by an overall factor such that our simulations yield the results presented in Table 5 of the ATLAS analysis [216], after the same cuts have been implemented. These overall factors are afterwards applied to our predictions for the Z' production. This procedure is similar to the one we have presented for the realistic update of the LHC potential to measure anomalous TGV deviations in the second part of the previous Chapter, Sec. 3.2.3.

The selection of events starts with the usual cuts to ensure the acceptance and detection of the two final state leptons in Eq. (4.16), similar to those in Eq. (3.49),

$$|\eta_e| < 1.37 \text{ or } 1.52 < |\eta_e| < 2.47 \text{ and } |\eta_\mu| < 2.4 \quad . \quad (4.28)$$

The lepton isolation requirement in the ME+Pythia+PGS–MC simulation imposes that the sum of the energy in the calorimeter cells within a cone $\Delta R < 0.3$ around the electron must be less than 4 GeV, while in a cone $\Delta R < 0.2$ around the muon the sum of p_T of all the other tracks is less than 10% of the p_T of the muon. To implement this requirement in OUR

4.3. BOUNDS ON Z' DECAYING TO W^+W^-

ME–MC we simply impose

$$\Delta R_{ee} > 0.3 \quad \text{and} \quad \Delta R_{e\mu, \mu\mu} > 0.2 \quad . \quad (4.29)$$

Next, the events are accepted only if the leading lepton in each channel and the electron in the $e\mu$ channel accomplish

$$p_T > 25 \text{ GeV} \quad , \quad (4.30)$$

while for the rest of leptons

$$p_T > 20 \text{ GeV} \quad . \quad (4.31)$$

Furthermore, we impose that

$$\begin{aligned} M_{ee, \mu\mu} &> 15 \text{ GeV} \quad , \quad M_{e\mu} > 10 \text{ GeV}, \\ |M_{ee, \mu\mu} - M_Z| &> 15 \text{ GeV}, \\ E_{T, rel}^{\text{miss}}(ee) &> 50 \text{ GeV} \quad , \quad E_{T, rel}^{\text{miss}}(\mu\mu) > 55 \text{ GeV} \\ \text{and } E_{T, rel}^{\text{miss}}(e\mu) &> 25 \text{ GeV} \quad , \end{aligned} \quad (4.32)$$

where $M_{\ell\ell}$ is the invariant mass of the lepton pair and the relative missing energy is defined as

$$E_{T, rel}^{\text{miss}} = \begin{cases} \cancel{E}_T \times \sin \Delta\phi_{\ell, j} & \text{if } \Delta\phi_{\ell, j} < \pi/2 \\ \cancel{E}_T & \text{if } \Delta\phi_{\ell, j} > \pi/2 \end{cases} \quad , \quad (4.33)$$

where $\Delta\phi_{\ell, j}$ is the difference in the azimuthal angle ϕ between the transverse missing energy and the nearest lepton or jet. The invariant mass cuts in Eq. (4.32) are imposed to avoid background events coming from processes containing a Z boson decaying to a pair of leptons, and also from processes containing low mass resonances and from the contribution of multi-jet hadronic processes. As it can be also observed, the transverse momentum cut is imposed to the variable $E_{T, rel}^{\text{miss}}$ instead of directly to \cancel{E}_T . This is done to reduce the rate of background events that arise from mis-measurements of leptons and jets, particularly the Drell–Yan background contributions we comment in the following. For instance, this requirement reduces the background contributions from $Z \rightarrow \tau\tau$, where the real \cancel{E}_T from the τ semileptonic decays is parallel to the momenta of the leptons.

Finally, in the ME+Pythia+PGS–MC simulation, jets are reconstructed with the anti- k_T algorithm [218] with a jet resolution parameter $\Delta R = 0.4$. At this point, the top-pair background still presents a dangerous contribution to the channel. As we have done in Sec. 4.2 for the spin determination analysis, and in Sec. 3.2.2 to study anomalous TGV interactions in the same channel, we have to veto events containing jets with

$$p_T > 30 \text{ GeV} \quad \text{and} \quad |\eta_j| < 4.5 \quad . \quad (4.34)$$

After this set of cuts is applied, we compare our simulations for the SM WW event rates to the ones quoted by ATLAS in Table 5 of [216]. We present then in Table 4.1 the overall normalization factors needed to tune our simulations to the ATLAS expectations. We have also verified that the relative event reduction in our simulations due to each of the cuts in Eqs. (4.30)–(4.32) is in agreement to the cut flow reported in Table 2 of [216].

| Experiment | Monte Carlo | ee | $e\mu$ | $\mu\mu$ |
|------------|------------------|------|--------|----------|
| ATLAS | OUR ME–MC | 0.51 | 0.70 | 0.92 |
| ATLAS | ME+Pythia+PGS–MC | 0.62 | 0.85 | 1.06 |
| CMS | OUR ME–MC | 0.56 | 0.83 | 0.95 |
| CMS | ME+Pythia+PGS–MC | 0.67 | 1.03 | 1.22 |

Table 4.1: Overall multiplicative factors used to tune our simulator to the total number of events in the different flavor channels predicted by the ATLAS and CMS simulations.

In order to validate our Monte Carlo simulations for the SM WW production, we compare our predictions with the ATLAS ones for the transverse mass spectrum after all the cuts are applied in the top–left panel of Fig. 4.10. The transverse mass is defined here as

$$M_T = \sqrt{(E_T^\ell + E_T^{\ell'} + \cancel{E}_T)^2 - (\vec{p}_T^\ell + \vec{p}_T^{\ell'} + \vec{\cancel{p}}_T)^2} . \quad (4.35)$$

The results shown correspond to an integrated luminosity of $\mathcal{L} = 4.7 \text{ fb}^{-1}$. In this Figure we evaluate only the SM WW production and we add the ATLAS results for all the rest of background sources. The background events mainly come from the same sources we considered in the previous Section, *i.e.* WW (labeled WW) and ZZ EW production followed by the decays we have described in Section 4.2 (included in the Diboson contribution), as well as top–pair related backgrounds (Top). However in the more realistic ATLAS estimation of the backgrounds, minor sources coming from W plus jets production (W+jets/Dijets), from other diboson minor processes like WZ (Diboson) or from $Z/\gamma^* \rightarrow \ell^+\ell^-$ (Drell–Yann) are also considered. Details for the different sources of backgrounds can be found in [216].

Next we check that both ME+Pythia+PGS–MC and OUR ME–MC simulations approximate very well the ATLAS expectations. In Fig. 4.10 we only show the distribution for OUR ME–MC simulation for a more clear illustration, however, the distribution for ME+Pythia+PGS–MC can be found in Fig. 1 of [186] and shows also good agreement with the ATLAS expectation. So since our two simulations present a very similar performance we adopt OUR ME–MC for the signal calculations for the rest of the analysis. The reason is that it is more efficient from the computational point of view, while it leads at the end to very similar bounds. Nevertheless, we verify that

4.3. BOUNDS ON Z' DECAYING TO W^+W^-

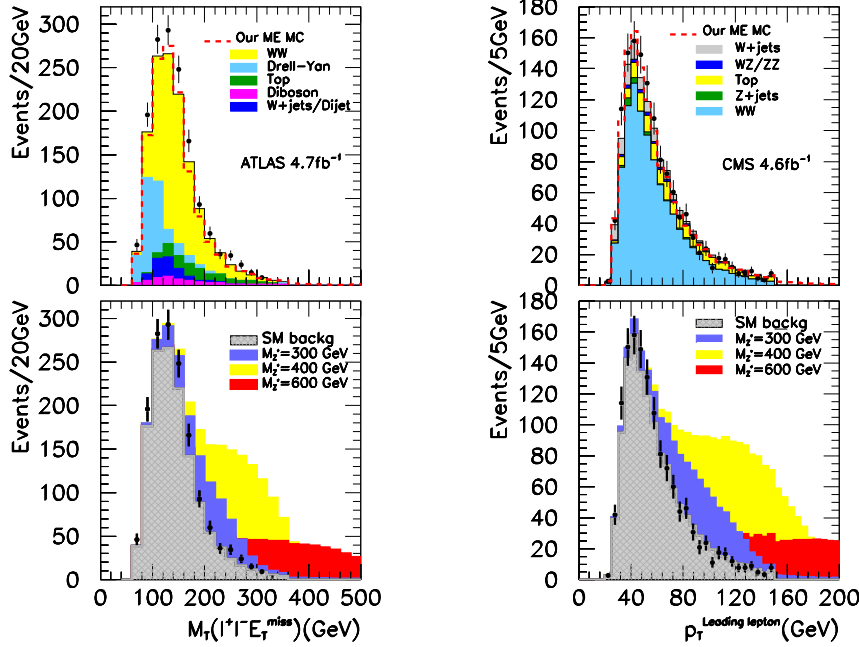


Figure 4.10: **Left panels:** Transverse mass distribution of the contributions to the process $pp \rightarrow \ell^+ \ell'^- \cancel{E}_T$, in the upper panel the SM processes calculated by ATLAS [216] (colored histograms) together with the number of observed events by ATLAS (points with error bars) and the performance of OUR ME-MC (red dashed). The results shown correspond to an integrated luminosity of $\mathcal{L} = 4.7 \text{ fb}^{-1}$ collected at 7 TeV. **Right panels:** Leading lepton transverse momentum of the contributions to the process $pp \rightarrow \ell^+ \ell'^- \cancel{E}_T$, in the upper panel the SM processes calculated by CMS [217] (colored histograms) together with the number of observed events by CMS (points with error bars) and the performance of OUR ME-MC (red dashed). The results correspond to an integrated luminosity of $\mathcal{L} = 4.6 \text{ fb}^{-1}$ collected at 7 TeV. For both distributions in the lower panels we show the total SM contribution (gray hashed) together with the total expected number of events including a Z' of 300 GeV with $G = 0.5$ (blue), a Z' of 400 GeV with $G = 1$ (yellow) and a Z' of 600 GeV with $G = 1$ (red). For the three masses we set $\Gamma_{Z'} = 0.06 M_{Z'}$.

the results obtained are in agreement with those from ME+Pythia+PGS-MC for a few points of the parameter space.

The characteristic signatures of a Z' signal we obtain are illustrated in the left lower panel of Fig. 4.10 where we plot the expected M_T distribution

for three different Z' masses for an integrated luminosity of 4.7 fb^{-1} collected at 7 TeV, as reported by ATLAS, and after all the cuts in Eqs. (4.28)–(4.34) have been applied. As expected the effect of new spin-1 neutral resonances is characterized by an excess of events with respect to the SM expectations at the higher values of M_T . Consequently, we can use the observed transverse mass spectrum to place bounds on the Z' properties. Regarding the statistical discriminants, we build a binned log-likelihood function based on the contents of the different bins in the transverse mass distribution. These are the observed number of events N_d^i , the expected events in the SM, N_B^i , plus the expected number of events in the presence of the Z' , N_S^i , in all cases after applying the cuts in Eqs. (4.28)–(4.34). Assuming independent Poisson distributed N_d^i the binned log-likelihood (or the related χ^2) reads

$$\begin{aligned}
 -2 \ln L_{\text{ATLAS}}(M_{Z'}, G, \Gamma_{Z'}) &= \text{Min}_{\xi_j} \left\{ 2 \sum_{i=1}^{N_{AT}^{\text{max}}} \left[N_B^i + N_S^i - N_d^i + N_d^i \log \frac{N_d^i}{N_B^i + N_S^i} \right] \right. \\
 &\quad \left. + \left(\frac{\xi_b^{st}}{\sigma_b^{st}} \right)^2 + \left(\frac{\xi_b^{sy}}{\sigma_b^{sy}} \right)^2 + \left(\frac{\xi_s^{st}}{\sigma_s^{st}} \right)^2 + \left(\frac{\xi_s^{sy}}{\sigma_s^{sy}} \right)^2 \right\} \\
 &\equiv \chi_{\text{ATLAS}}^2(M_{Z'}, G, \Gamma_{Z'}),
 \end{aligned} \tag{4.36}$$

where

$$N_B^i = N_b^i (1 + \xi_b^{st} + \xi_b^{sy}) + N_{\text{WW}}^i (1 + \xi_s^{st} + \xi_s^{sy}) \quad \text{and} \tag{4.37}$$

$$N_S^i = (G^2 N_{Z'}^i + G N_{\text{int}}^i) (1 + \xi_s^{st} + \xi_s^{sy}) \quad . \tag{4.38}$$

In Eq. (4.37) we have separated the number of background events expected in the i -th bin for the SM processes except for the WW contribution, N_b^i , from N_{WW}^i that stands for the number of events expected on the i -th bin for the SM WW contribution. Finally $G^2 N_{Z'}^i$ and $G N_{\text{int}}^i$ are the number of events expected on the i -th bin for the pure signal contribution and the interference respectively. We note that for the rest of the Chapter we use the simplified notation given on Eq. (4.7) for the Z' relevant product of couplings.

In the log-likelihood function in Eq. (4.36), we estimate the effect of the systematic uncertainties by means of a simplified treatment in terms of four pulls ξ [81, 82], in the same way we have included also the main theoretical uncertainties for the Higgs analysis, see Eq. (2.45). In the present case, ξ_b^{st} stands for the pull to account for the statistical uncertainty on the evaluations for all the SM processes, except for the WW contribution, ξ_b^{sy} is the one to account for the systematic uncertainty in the same processes, ξ_s^{st} is the pull to account for the statistical uncertainty on the expectations for WW and the Z' new contributions, and finally ξ_s^{sy} accounts for the systematic uncertainty on the same processes. In Eq. (4.37) we have separated the SM WW background from the rest of background sources to be able to use

4.3. BOUNDS ON Z' DECAYING TO W^+W^-

the same pull for both the SM WW process and the Z' signals, the reason is that we have used the former process to tune the Monte Carlo to simulate the later one. This way the uncertainties for both processes are expected to be correlated. The standard deviations for the pulls in Eq. (4.36) are obtained from Table 5 of [216]

$$\sigma_b^{st} = 0.026, \quad \sigma_b^{sy} = 0.09, \quad (4.39)$$

$$\sigma_s^{st} = 0.005, \quad \sigma_s^{sy} = 0.10. \quad (4.40)$$

Using the binned log-likelihood function in Eq. (4.36) we perform two analyses. We first compute the $\ln L_{\text{ATLAS}}$ with the 16 transverse mass bins in [216], these correspond to the bins from $M_T = 40$ GeV to $M_T = 360$ GeV in Figure 4.10, *i.e.* in the first analysis $N_{AT}^{\text{max}} = 16$. Afterwards, in the second analysis we add an extra 17th bin, *i.e.* here $N_{AT}^{\text{max}} = 17$. In this final case we sum the Z' expected contributions with $M_T > 360$ GeV and we assume that the number of observed events and SM expected predictions for the 17th bin are negligible. Nevertheless, we check that the exclusion bounds we derive are robust against alternative hypothesis for the background content of this last 17th bin.

Analysis of CMS results

We proceed now to present the details of our re-analysis of the CMS data. The structure is completely analogous to the one we have just described for ATLAS, although some of the details change. In relation to the simulation procedure, the process of validating our Monte Carlos is exactly the same. We tune our Monte Carlo to account for the different details of the simulation by comparing the SM WW pair production in the ee , $e\mu$, and $\mu\mu$ channels with respect to the expectations presented in [217]. There, the process in Eq. (4.16) was studied using $\mathcal{L} = 4.6 \text{ fb}^{-1}$ collected at 7 TeV, in the context of the Higgs searches. The analysis presented here exactly matches the initial part of the CMS search (Section 3 in [217]).

As usual, we start requiring that the electrons and muons accomplish the different acceptance cuts, first we impose

$$|\eta_e| < 2.5 \quad \text{and} \quad |\eta_\mu| < 2.4. \quad (4.41)$$

The lepton isolation requirement in the ME+Pythia+PGS-MC simulation imposes that the sum of p_T of all other tracks is less than 10% of the p_T of the lepton within a cone $\Delta R < 0.4$ (0.3) around the electron (muon). In OUR ME-MC we simply impose

$$\Delta R_{ee} > 0.4 \quad \text{and} \quad \Delta R_{e\mu, \mu\mu} > 0.3. \quad (4.42)$$

The minimum transverse momentum requirements and the invariant mass cuts are

$$\begin{aligned}
 p_T^{\text{leading}} &> 20 \text{ GeV} , \\
 p_{T\ e\mu}^{\text{subleading}} &> 10 \text{ GeV}, \quad p_{T\ ee,\mu\mu}^{\text{subleading}} > 15 \text{ GeV} , \\
 M_{ee,\mu\mu} &> 20 \text{ GeV} \quad \text{and} \quad M_{e\mu} > 12 \text{ GeV} , \\
 |M_{ee,\mu\mu} - M_Z| &> 15 \text{ GeV} , \\
 E_{T, \text{rel}}^{\text{miss}}(ee, \mu\mu) &> 40 \text{ GeV} \quad \text{and} \quad E_{T, \text{rel}}^{\text{miss}}(e\mu) > 20 \text{ GeV} .
 \end{aligned}
 \tag{4.43}$$

These cuts are very similar to the ones in the ATLAS search, Eqs. (4.30)–(4.32). They are also meant to increase the signal to background ratio (see [217] for the details). In the CMS analysis a new cut in the transverse momentum of the system formed by the pair of leptons is also imposed for all three channels, ee , $e\mu$ and $\mu\mu$,

$$p_T^{\ell\ell} > 45 \text{ GeV} . \tag{4.44}$$

The aim of this new cut is to further reduce the contribution of Drell–Yan processes and fake background contaminations. Finally, as it could be already expected, in the ME+Pythia+PGS–MC simulation jets are reconstructed with the anti- k_T algorithm with a jet resolution parameter $\Delta R = 0.5$ and we veto events containing jets with

$$p_T > 30 \text{ GeV} \quad \text{and} \quad |\eta_j| < 5.0 . \tag{4.45}$$

In addition, for events with same flavor leptons, the angle in the transverse plane between the dilepton system and the most energetic jet with $p_T > 15 \text{ GeV}$ is required to be smaller than 165 degrees.

At this point, we compare our simulation of the SM WW process with the one shown by the CMS collaboration in [217] (some details can be found in [219], that completes the missing flavor information needed). From this comparison we extract the normalization factors required to tune our simulation tools to a more realistic performance after all the cuts have been applied. We exhibit in Table 4.1 these overall normalization factors. As in the ATLAS case, in order to verify the quality of our simulations we compare our results with the kinematic distributions in [217]. We show in the top right panel of Figure 4.10 the leading lepton transverse momentum distribution for the different SM contributions and for the observed number of events. We follow the same procedure than for the ATLAS case, our SM WW prediction is added to the rest of background sources as estimated by CMS and then it is compared to the total sum of SM backgrounds by CMS. As we can see, our simulation tools are in good agreement with the CMS expectations. The background sources are, as expected, the same than for the ATLAS analysis, although in the right panel we keep the original labels

4.3. BOUNDS ON Z' DECAYING TO W^+W^-

used in the CMS search. This means that the Z +jets label corresponds to Drell–Yan label in the left (ATLAS) panel, whereas the WZ/ZZ label is equivalent to the Diboson one. We finally note here that, as in the ATLAS case, both simulation procedures, ME+Pythia+PGS–MC and OUR ME–MC, exhibit a very similar behavior, although we only show in the figure the case of OUR ME–MC for simplicity, while the ME+Pythia+PGS–MC distribution can be found in [186]. With both simulation procedures having a similar performance, and as we have done for the ATLAS case, for the rest of the analysis we use OUR ME–MC given that it is more efficient from the computational point of view.

With the derived normalization factors, we can tune now the simulation of the Z' signals for the channels ee , $e\mu$, and $\mu\mu$ to account for the proper detection efficiencies and corrections. In this case the presence of a new spin–1 resonance is illustrated by an enhancement at large p_T , as displayed in the lower right panel of Fig. 4.10 for the same sample of masses, widths and relevant product of couplings that we have shown in the ATLAS analogous panel. Thus, this variable can be used to set interesting exclusion limits on the existence of a new vector Z' in the same way we have used M_T for the ATLAS case. Indeed, the bounds on the production of a Z' are extracted using also a binned log–likelihood function, but this time it is based on the contents of the bins of the transverse momentum distribution of the leading lepton¹

$$-2 \ln L_{\text{CMS}}(M_{Z'}, G, \Gamma_{Z'}) = \text{Min}_{\xi_j} \left\{ 2 \sum_{i=1}^{N_{\text{CMS}}^{\text{max}}} \left[N_B^i + N_S^i - N_d^i + N_d^i \log \frac{N_d^i}{N_B^i + N_S^i} \right] + \left(\frac{\xi_b^{sy}}{\sigma_b^{sy}} \right)^2 + \left(\frac{\xi_s^{sy}}{\sigma_s^{sy}} \right)^2 \right\} \equiv \chi_{\text{CMS}}^2(M_{Z'}, G, \Gamma_{Z'}) \quad , \quad (4.46)$$

where

$$N_B^i = N_b^i (1 + \xi_b^{sy}) + N_{\text{WW}}^i (1 + \xi_s^{sy}) \quad \text{and} \quad (4.47)$$

$$N_S^i = (G^2 N_{Z'}^i + G N_{\text{int}}^i) (1 + \xi_s^{sy}) \quad . \quad (4.48)$$

As in the previous Subsection, N_b^i stands for the number of events expected on the i –th bin for the SM processes except for the WW contribution, N_{WW}^i is the number of events expected on the i –th bin for the WW contribution, $G^2 N_{Z'}^i$ and $G N_{\text{int}}^i$ are the number of events expected on the i –th bin for the pure signal contribution and the interference respectively and finally N_d^i is the observed number of events on the bin i .

In relation to the treatment of systematic uncertainties, in the CMS case we also make the treatment in terms of pulls. Here we introduce two pulls: ξ_b^{sy} is the pull to account for the systematic uncertainty on the expectations

¹Within the range of the kinematic variables presented in the different CMS plots [217], the leading lepton transverse momentum distribution is the most sensitive to the presence of a Z' .

for all the SM processes, except for the WW contribution, while ξ_s^{sy} is the one to account for the systematic uncertainty on WW and the Z' new contributions. The standard deviations for these pulls are obtained from [219]:

$$\sigma_b^{sy} = 0.20 , \quad (4.49)$$

$$\sigma_s^{sy} = 0.08 . \quad (4.50)$$

Similar to the ATLAS case, here we also perform two analyses. In the first one we calculate $\ln L_{\text{CMS}}$ with the event rates in the 26 leading transverse momentum bins between 20 GeV and 150 GeV (*i.e.* $N_{\text{CMS}}^{\text{max}} = 26$), see the right panels of Fig. 4.10. In the second analysis we add an extra bin where we include the number of observed events and background expectations that are left with values higher than 150 GeV. These values can be obtained from comparing the quantities read from the images with the values quoted in Table 2 of [217]. In this extra bin we also add the expected contributions from the Z' with $p_T^{\text{leading}} > 150$ GeV (*i.e.* $N_{\text{CMS}}^{\text{max}} = 27$).

Combined analysis

In order to get more stringent bounds on the production of a Z' that decays into EW gauge boson pairs we combine the ATLAS and CMS results by constructing a combined log-likelihood function assuming conservatively that the ATLAS and CMS systematic uncertainties are uncorrelated. The combined log-likelihood function reads

$$\chi_{\text{comb}}^2(M_{Z'}, G, \Gamma_{Z'}) = \chi_{\text{ATLAS}}^2(M_{Z'}, G, \Gamma_{Z'}) + \chi_{\text{CMS}}^2(M_{Z'}, G, \Gamma_{Z'}) . \quad (4.51)$$

In all cases we set the exclusion limits (2σ , 1 d. o. f.) on G by maximizing the corresponding likelihood function (or equivalently minimizing the χ^2), in Eqs. (4.36), (4.46) and (4.51), with respect to G for each value of $M_{Z'}$ and $\Gamma_{Z'}$ and imposing

$$|\chi^2(M_{Z'}, G, \Gamma_{Z'}) - \chi_{\text{min}}^2(M_{Z'}, \Gamma_{Z'})| > 4 . \quad (4.52)$$

4.3.2 Present bounds on Z'

The bounds we have derived from our analysis of the ATLAS results are shown in Fig. 4.11. In the Figure we can distinguish three different regions: the gray shadowed regions in the upper right (lower right) regions of the upper (lower) panels correspond to the points that are excluded by requiring the consistency of the total decay width of a Z' with its decay to light quarks and SM WW pairs, as expressed in Eq. (4.4). The other two regions correspond to the exclusion bounds that can be derived performing the two binned log-likelihood analyses that we have described in the previous Subsection. The red solid regions are derived making the analysis with $N_{\text{AT}}^{\text{max}} = 16$ bins, *i.e.* on the range between $M_T = 40$ GeV and

4.3. BOUNDS ON Z' DECAYING TO W^+W^-

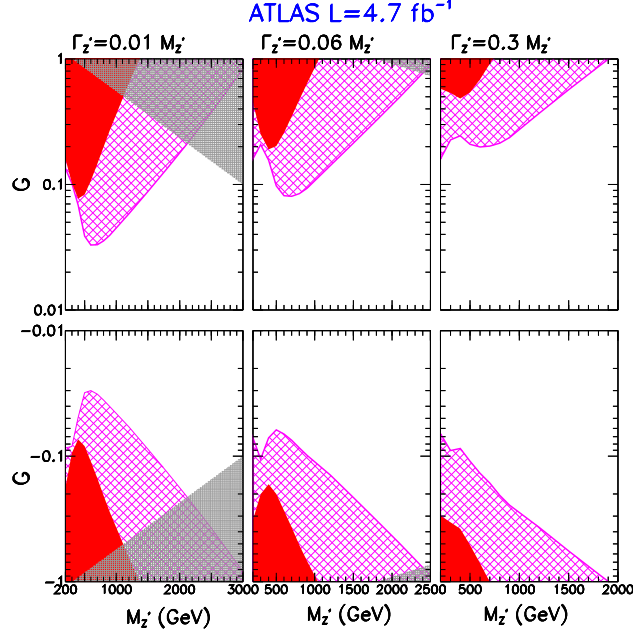


Figure 4.11: 2σ exclusion limits on the production of a Z' from our analysis of the M_T distribution measured by ATLAS with $\mathcal{L} = 4.7 \text{ fb}^{-1}$ collected at 7 TeV. The left, center and right panels correspond to three values of $\Gamma_{Z'}/M_{Z'} = 0.01, 0.06$ and 0.3 respectively. The red solid regions are derived using the log-likelihood function with $N_{AT}^{\text{max}} = 16$, while the purple hatched regions are derived using the log-likelihood function with $N_{AT}^{\text{max}} = 17$, see the text for the details. The shadowed regions in the upper (lower) right corner of the upper (lower) panels represent the excluded values by the condition in Eq. (4.4).

$M_T = 360 \text{ GeV}$, which is exactly the range specified in the ATLAS experimental search [216]. The purple hatched regions on the other hand contain the points excluded when the extra bin accounting for the events with transverse masses above $M_T > 360 \text{ GeV}$ is included, $N_{AT}^{\text{max}} = 17$. One can observe that the bounds are clearly stronger for narrow resonances, while including the extra bin has a bigger impact the wider and the heavier Z' is. This is due to the fact that a heavier and/or a wider Z' resonance gives a larger contribution to events with $M_T > 360 \text{ GeV}$. Finally the effect of the interference, that can be observed by comparing the upper and the lower panels, is noticeable only for wider and lighter new resonances, as expected from the interference term being roughly proportional to $\Gamma_{Z'}/M_{Z'}$.

The 2σ exclusion limits on the production of a Z' derived from the analysis of the p_T^{leading} distribution, measured with an integrated luminosity of $\mathcal{L} = 4.6 \text{ fb}^{-1}$ collected at 7 TeV by CMS, can be seen in Fig. 4.12. These

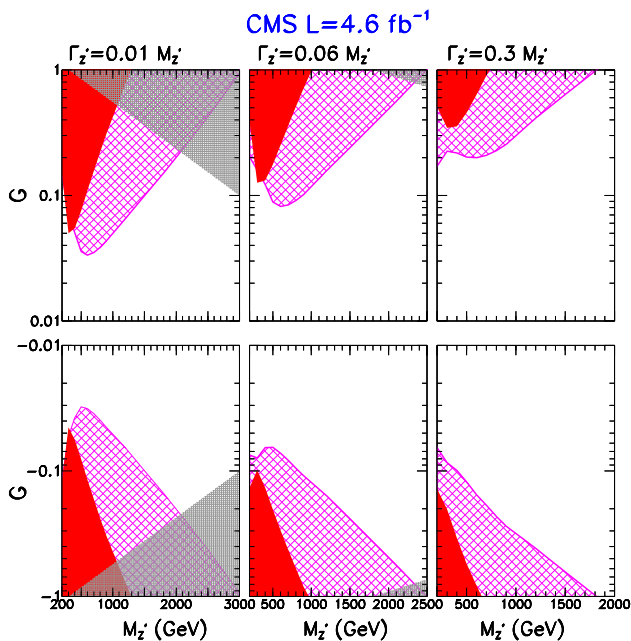


Figure 4.12: 2σ exclusion limits on the production of a Z' from our analysis of the p_T^{leading} distribution measured by CMS with $\mathcal{L} = 4.6 \text{ fb}^{-1}$ collected at 7 TeV. The left, center and right panels correspond to three values of $\Gamma_{Z'}/M_{Z'} = 0.01, 0.06$ and 0.3 respectively. The red solid regions are derived using the log-likelihood function with $N_{CMS}^{\text{max}} = 26$, while the purple hatched regions are derived using the log-likelihood function with $N_{CMS}^{\text{max}} = 27$. The shadowed regions in the upper (lower) right corner of the upper (lower) panels represent the excluded values by the condition Eq. (4.4).

bounds are very similar to the ones we have derived from the analysis of M_T distribution of ATLAS in Fig. 4.11, and the coloring of the regions has a similar meaning. The gray hatched regions cover the space forbidden by the constraint in Eq. (4.4), while the red solid regions contain the 2σ exclusion limits when using the leading lepton p_T distribution in the right panels of Fig. 4.10, with $N_{CMS}^{\text{max}} = 26$, *i.e.* up to 150 GeV. Finally the purple hatched regions add the extra bin as we have described. The only difference with respect to the bounds from the ATLAS analysis is in the shape of the exclusion limits without the extra bin. This is due to the fact that within the range of the kinematic values and the kinematic variables used, CMS is more sensitive than ATLAS to the lightest masses when no extra bins are included. When we add the extra bin both analyses lead to a similar power, which means that both kinematic variables have a similar sensitivity to a Z' .

Finally the 2σ exclusion limits on the production of a new Z' from the

4.3. BOUNDS ON Z' DECAYING TO W^+W^-

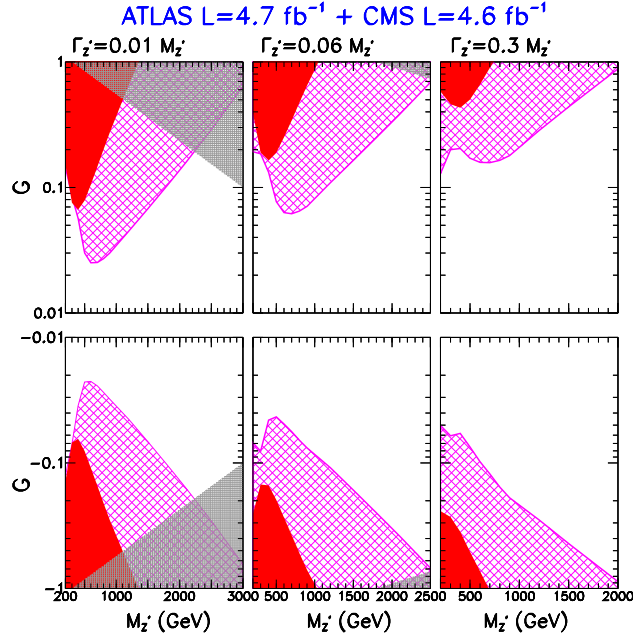


Figure 4.13: 2σ exclusion limits on the production of a Z' from our combined analysis of the measured M_T distribution in ATLAS with $\mathcal{L} = 4.7 \text{ fb}^{-1}$ and the p_T^{leading} distribution measured by CMS with $\mathcal{L} = 4.6 \text{ fb}^{-1}$, both sets were collected at 7 TeV. The red solid (purple hatched) regions are derived using the combined log-likelihood function with 16 and 26 (17 and 27) bins of the ATLAS and CMS distributions respectively. The shadowed regions in the upper (lower) right corner of the upper (lower) panels represent the excluded values by the condition in Eq. (4.4).

combination of the analysis of the transverse mass spectrum in ATLAS with an integrated luminosity of $\mathcal{L} = 4.7 \text{ fb}^{-1}$ and the p_T^{leading} distribution in CMS with $\mathcal{L} = 4.6 \text{ fb}^{-1}$ are shown in Fig. 4.13. In the Figure the labeling of the different regions is analogous to the Figures for ATLAS and CMS separately. We can observe that the combination of ATLAS and CMS data has already excluded a sizable region of the parameter space for the production of a Z' associated with the EWSB sector.

These results represent the strongest existing direct bounds on the production of new neutral vector resonances that decay to EW gauge boson pairs. For instance, we note that from our combined analysis with 17 and 27 bins, from the ATLAS and CMS distributions respectively, a narrow resonance of any mass with $\Gamma_{Z'}/M_{Z'} = 0.01$ and that saturates the partial wave amplitude for the process $W^+W^- \rightarrow W^+W^-$ is excluded at 2σ level if its coupling to the light quarks is larger than 19% of the SM $Z\bar{q}q$ coupling. From this combined analysis we can also see that a new neutral

vector resonance that saturates the partial wave amplitude for the process $W^+W^- \rightarrow W^+W^-$ and couples to light quarks with SM strength is completely excluded for $\Gamma_{Z'}/M_{Z'} = 0.01$ and $\Gamma_{Z'}/M_{Z'} = 0.06$, while for a wider resonance, $\Gamma_{Z'}/M_{Z'} = 0.3$, it is excluded for masses up to 2 TeV.

There is an important note to make before we end this Section. In all the three Figures, 4.11– 4.13, we have observed that the addition of the extra bin to the analyses enlarges the parameter space covered by the exclusion limits. This is so because a Z' has an enhanced contribution to the higher values of the M_T or the p_T^{leading} distributions with respect to the SM backgrounds. But the experimental measurements we have used were not made with the aim at searching for neutral vector resonances, thus they are not focused on this high M_T or p_T^{leading} regions of the kinematic space. As a consequence a considerable constraining power is lost if one only uses the presented data points. We partially compensate for this by including a data point for the “empty” extra bins. Experimental analyses with cuts and kinematic distributions focused on this type of high M_T or p_T^{leading} signals would clearly extend the reach attainable most notably for the heavier and wider resonances.

It is also interesting to compare our Z' bounds with the strongest ones that were available before LHC started its operation. These are the ones obtained by the CDF collaboration analyzing WW production at the Tevatron [206]. We have already partially introduced in Sec. 4.2 the bounds from this analysis, that was performed in the framework of the Extended gauge model and whose results were shown using the $Z'WW$ coupling as a free parameter. This feature makes the comparison with the bounds derived here easier. The CDF analysis generically leads to bounds on a narrow Z' with $\Gamma_{Z'}/M_{Z'} \lesssim 0.1$. For Z' masses of 250, 600 and 950 GeV the CDF constraints in the context of the Extended Gauge model read $|G| < 0.47, 0.27$ and 1.36 respectively. On the other hand, our analyses without (with) extra bins lead to bounds $|G| \lesssim 0.2, 0.1$ and 0.6 ($0.2, 0.05, 0.07$) for the same masses and model. In conclusion, translating our bounds into the model used by CDF we get that generically the constraints from our most conservative analysis of the ATLAS and CMS distributions, *i.e.* without the extra bins, already extend the CDF exclusion to couplings more than a factor of 2 smaller for the accessible mass range at Tevatron $M_{Z'} \lesssim 950$. In addition, the results of this Section widen the accessible $M_{Z'}$ mass range up to the multi-TeV region.

4.4 Conclusions

Models of EWSB beyond the minimal Higgs mechanism often predict the existence of new resonances in the EWSB sector, in many cases with spin-1, and interacting to the SM EW bosons. Generically these vector resonances

4.4. CONCLUSIONS

are responsible to tame the dangerous energy growth of longitudinal gauge boson scatterings that at the end leads to unitarity violation. We have focused this Chapter in the study of different properties of such vector resonances. In order to cover the largest possible range of theories, we have made a minimal number of assumptions, while leaving different properties of the new spin-1 particles as free parameters of the analysis. In particular, we have assumed that the new vector resonances couple to gauge boson pairs in order to establish their relation with EWSB. Moreover, to complement the existing studies on VBF processes, we have studied here the direct production of the vector particles at the LHC through a coupling to light quarks. Nevertheless, we have kept the relevant product of couplings to light quarks and to gauge bosons, the mass, and the width of the new vector resonances as free parameters of the analysis. This way the results are presented in the most model independent possible form, allowing for an easier translation to a broader class of specific models.

In the first part of the Chapter we have performed an analysis of the 14 TeV LHC potential to determine the spin of new charged and neutral resonances. In both cases we have first presented the studied channels, and then we have described the realistic selection of events that we have imposed to disentangle the signal from the background. Afterwards we have built several angular variables, and we have compared their sensitivity to discriminate between the assumed spin-1 state versus an alternative spin-0 hypothesis. Finally we have exploited the most sensitive angular distributions in order to build a proper asymmetry and we have estimated the potential reach at the LHC for a spin discrimination. We have presented the results as a function of the relevant parameters, *i.e.* the couplings, the mass and the width of the new resonance, as well as of the collected luminosity at the LHC.

In the case of a charged spin-1 resonance, W' , we have concluded that the study of the channel $pp \rightarrow W'^{\pm} \rightarrow W^{\pm} Z \rightarrow \ell^+ \ell^- \ell'^{\pm} \cancel{E}_T$ allows for the observation of W' signals in a large range of masses, widths and couplings at the LHC, as shown in Figure 4.1. The fact that there is only one missing neutrino in the final state makes the reconstruction of the final state possible under certain assumptions. This helps us to increase the signal to background ratio, while it allows as well for the construction of additional angular distributions. We have shown that the study of the $\cos \theta_{\ell\ell}^*$ and the reconstructed $\cos \theta_{WZ}$ distributions lead to a similar power to determine the spin of the new state. Another interesting conclusion we have derived is the fact that the selection cuts, especially the rapidity cuts, modify the angular distributions, making the distinction between scalar and vector resonances more challenging than what could be *a priori* expected. Finally we conclude that the analysis of the trilepton channel can discriminate at 99% CL the new charged state spin in a large fraction of the parameter space where this state can be observed at the LHC, for an integrated luminosity of 100 fb^{-1}

collected at 14 TeV, see Fig. 4.4. The strength of the coupling required to have a spin discrimination is found to be usually twice the size of the one required for a discovery. We have also presented the reachable sensitivity for earlier or extended 14 TeV data sets.

The study of a neutral vector resonance, Z' , has been performed in the channel $pp \rightarrow Z' \rightarrow W^+W^- \rightarrow \ell^+\ell^{(\prime)-}\cancel{E}_T$. The analysis of this channel is more challenging in comparison to the W' case. The presence of two neutrinos in the final state makes the reconstruction of the final state impossible, leading at the end to a lesser signal to background ratio. This is translated into a reduced LHC potential to determine the spin of a Z' . Nevertheless, a sufficient background reduction can still be accomplished by using proper invariant mass variables, either a transverse mass variable or one of the MAOS reconstructions we have presented. We have seen that the use of $\cos\theta_{\ell\ell}^*$, or any of the $\cos\theta_{WW}$ angular distributions that are built using the MAOS reconstruction scheme, all lead to a similar precision to determine the spin of a Z' . We have concluded that both the discovery and the 99% CL spin discrimination of a Z' is still possible in a sizable region of the parameter space at the LHC, see Figs. 4.7 and 4.9.

Interestingly, in the case of Z' we have concluded in the initial Sec. 4.2 that the strongest bounds on the existence of such resonances decaying to WW pairs are still coming from Tevatron. So far the LHC collaborations have not focused their efforts on the Z' searches in the WW final state, and the existing data on WW is only used to test the SM predicted cross section for gauge boson pair production and to search for the Higgs boson. We have studied in the second part of the chapter how this same data can be used to derive bounds on a Z' via its contribution to the same final state $pp \rightarrow Z' \rightarrow W^+W^- \rightarrow \ell^+\ell^{(\prime)-}\cancel{E}_T$. We have performed a realistic analysis making use of the background estimations and observed events from the 7 TeV LHC ATLAS 4.7 fb^{-1} data set [216], and the CMS 4.6 fb^{-1} data set [217]. After tuning our simulation tools comparing the outputs of the kinematic variables of the SM WW production, we have simulated the Z' signals. We have built binned log-likelihood functions based on M_T and p_T^{leading} in order to constrain the same parameter space of couplings, masses and widths of the previous spin analysis. From the combination of both ATLAS and CMS data sets we have obtained the strongest exclusion limits on a Z' decaying to WW pairs, see Fig 4.13. They cover a large range of masses, up to the multi-TeV region ($\sim 2.5 \text{ TeV}$), from narrow to broad resonances, and for a vast selection of possible couplings to light quarks and gauge boson pairs.

Chapter 5

New states in neutrino mass models

In the SM neutrinos are massless fermions for which no gauge invariant renormalizable mass terms can be built. Consequently, there is neither mixing nor CP violation in the lepton sector of the SM. The experimental observation of neutrino masses and mixing is therefore an unambiguous evidence of physics BSM [220]. As we have seen in the previous Chapters, the LHC operation is greatly improving our understanding in particle physics. Thus an interesting question is whether the NP associated to the neutrino masses and mixing could be within the LHC reach. In this Chapter we address this question and we study whether the LHC can shed light on the origin of neutrino masses. As we will discuss, the first point we have to consider is related to the scale of the NP responsible for generating the neutrino mass. From the point of view of the effective Lagrangian expansion the only dimension–five operator that can be built with the SM particle content, and respecting the SM gauge symmetry, is related to the mass of the neutrinos. As we have briefly commented in Chapter 2, this dimension–five operator is the commonly known as Weinberg operator [34]

$$\mathcal{L}_{\text{eff}}^5 = \frac{f_5^{ij}}{\Lambda_{\text{LN}}} (\bar{L}_i^c \tilde{\Phi}^*) (\tilde{\Phi}^\dagger L_j) , \quad (5.1)$$

where as in Eq. (2.23), $\tilde{\Phi} = i\sigma_2\Phi^*$ and L is the lepton $SU(2)_L$ doublet. The superscript c stands for the charge conjugate, and i, j are lepton flavor indices. After EWSB this operator generates a Majorana mass term for the neutrinos $m_\nu \sim f_5 v^2 / \Lambda_{\text{LN}}$. In principle, if one considers a neutrino mass of $O(1)$ eV, and a coupling f_5 also of $O(1)$, the relation implies that $\Lambda_{\text{LN}} \sim 10^{14}$ GeV. This scale is clearly out of the LHC reach. Hence, the first question we have to face in order to study the neutrino mass generation at the LHC is whether models explaining the tiny neutrino masses can still lead to observable effects at the TeV–LHC scale. As we will see, the answer

is positive. The key point lies on the fact that Λ_{LN} is associated to a total lepton number violating operator, and as we describe in the following, in certain consistent models the high energy scale of this tiny total lepton number violation may be separated from the rest of NP effects, that can instead be related to notably lower scales, for instance the TeV one. There, new states associated to the neutrino mass generation can live, and they can then lead to observable effects at the LHC that we analyze here.

Interestingly, while the setup that we describe in this Chapter leads to a consistent model with the total lepton number violation scale well separated from the scale where the new neutrino partners live, the phenomenology of these new states is strongly linked to the neutrino mass and mixing parameters. The model that we present in the following is based on the minimal lepton flavor violation (MLFV) see-saw constructions in Ref. [221]. In particular, in order to allow for a LHC observation, we implement here the MLFV realization in a type-III see-saw model.

The present Chapter is based on the published work in [222], and it is structured as follows. We start introducing in Section 5.1 the basics behind neutrino see-saw models and how TeV scale states can be present in this type of theories. In particular, we focus on summarizing the basics of the MLFV model considered here, where the flavor scale is given by the new fermion triplet mass and it can be naturally light to be within the LHC reach. We introduce the new states and operators that are added to the SM Lagrangian, and afterwards, we rotate the Lagrangian to the mass basis, that is the one relevant for the LHC physics. Along this procedure we describe how, in this model, the flavor structure of the total lepton number conserving couplings of the fermion triplets, and consequently their observable decay branching ratios to the SM leptons, can be reconstructed from the neutrino mass matrix. On the contrary the total lepton number violating decay modes of the fermion triplets are suppressed by the lightness of the neutrino mass and they can not be observed at the LHC. After the main details and the diagonalization of the model is presented, in Section 5.2 we describe the most promising signatures at the LHC that the model leads to. We study the processes $pp \rightarrow 3\ell + 2j + \cancel{E}_T$ and $pp \rightarrow 2\ell + 4j$, with $\ell = e$ or μ taking into account the present low energy data on neutrino physics and the corresponding SM backgrounds. The realistic collider analyses of these two processes are presented in Section 5.3. Our results allow for a promising test of the predicted flavor structure of the new particle decays. We estimate at the end of this Section how to probe at the LHC the neutrino ordering and how to measure the unknown Majorana phase. For that we combine the analyses of the two channels considered. In the original publication [222] we presented the prospective LHC reach for the initial 7 TeV run after applying the analysis we have described which is not included in here. Instead we close this Chapter with a brief summary of the published experimental limits on type-III see-saw partners after the 7 and 8 TeV runs have finished. We

summarize our conclusions in Section 5.4.

5.1 MLFV type-III see-saw model

As we have described, in the effective Lagrangian expansion, the only dimension-5 operator that can be built, shown in Eq. (5.1), breaks the total lepton number and after EWSB it generates Majorana masses for the neutrinos. Consequently, neutrinos are much lighter than the rest of SM fermions because of the large scale associated to the total lepton number violation, Λ_{LN} . Generically, in simple renormalizable NP theories this dimension-five operator is generated through the tree level exchange of heavy intermediate particles. These type of BSM realizations are known as see-saw models, and usually three type of setups are defined depending on the exchanged intermediate state. The three types of models are:

- Type-I see-saw [223–226]: it is arguably the simplest see-saw realization. There, one adds to the SM at least two fermions of mass M , singlets of the SM gauge group. These couple to the leptons through Yukawa-like interactions mediated by a Higgs doublet. The neutrino masses are $m_\nu \sim \lambda^2 v^2/M$, where λ is the Yukawa coupling between the SM leptons and the new states, for which extra Majorana mass terms are also added.
- Type-II see-saw [227–231]: in this case one adds to the SM an $SU(2)_L$ scalar triplet with hypercharge 2, $\Delta = (\delta^{++}, \delta^+, \delta^0)$, and mass M . It has a neutral component which in the presence of a scalar doublet-triplet mixing term in the scalar potential, μ_Δ , acquires a vev $v_\Delta = \mu_\Delta v^2/M^2$. The neutrino masses are then $m_\nu \sim \lambda \mu_\Delta v^2/M^2$, where here λ is the Yukawa coupling between the leptons and the scalar.
- Type-III see-saw [232]: this is the case of interest in the present Chapter. In type-III see-saw models one adds to the SM at least two $SU(2)_L$ fermion triplets with zero hypercharge, and with a mass M . Analogously to the type-I see-saw case, the new states couple to the leptons through Yukawa-like interactions mediated by a Higgs doublet. After adding also Majorana mass terms, they generate neutrino masses of size $m_\nu \sim \lambda^2 v^2/M$, where again λ corresponds to the Yukawa coupling.

In addition to these three simple realizations, hybrid scenarios combining more than one realization have also been constructed, see for instance [233–235]. A common feature of the three scenarios we have just enumerated is related to the size of the neutrino masses. In any of these mechanisms the smallness of the neutrino mass can be naturally explained with Yukawa couplings $\lambda \sim \mathcal{O}(1)$ if the masses of the heavy states are $M \sim \Lambda_{LN} \sim 10^{14}$

GeV (with $\mu_\Delta \sim M$ also for the type-II realization). This high scale is clearly out of the LHC reach, and thus, it may seem that one could not obtain information on neutrino mass generation at the LHC in these simplest cases. Nevertheless, it is also true that nothing prevents the new states to live at the TeV scale, in exchange of tuning for instance the size of the Yukawa couplings to account for the tiny neutrino masses. Actually, it is of no surprise that previous to the LHC operation there was an increasing literature studying the interesting signatures of the neutrino mass-inducing states with TeV scale masses at the LHC (see *e.g.* [236–242]). These interesting analyses studied several of the different possible golden channels and signatures characteristic of see-saw new neutrino states at the LHC. While being very interesting from the phenomenological point of view, a drawback in some cases was that such a low scale M was technically unnatural or, in some others, the low scale limit was simply not very well motivated theoretically.

Consistent TeV scale see-saw models exist in the literature for some time (see *e.g.* [243, 244]). From the point of view of the effective Lagrangian approach, we have already seen that generically one has at the leading expansion orders

$$\mathcal{L} = \mathcal{L}_{SM} + \frac{f_5}{\Lambda_{LN}} \mathcal{O}_5 + \sum_i \frac{f_{6,i}}{\Lambda_{FL}^2} \mathcal{O}_{6,i} + \dots \quad , \quad (5.2)$$

where \mathcal{O}_5 is the Weinberg’s operator in Eq. (5.1), *i.e.* the one responsible for the neutrino masses, and where we have denoted with $\mathcal{O}_{6,i}$ the dimension-six flavor-changing, but total lepton number conserving, operators. In this context attractive TeV scale see-saw models are those where it is possible to relate the mass of the new states $M \sim \Lambda_{FL} \sim \mathcal{O}(\text{TeV})$, but still keep $\Lambda_{LN} \gg \Lambda_{FL}$ to explain the smallness of the neutrino mass. This is different than the simplest implementations described above for which the relation is simply $M \sim \Lambda_{LN} \sim \Lambda_{FL}$.

In this effective Lagrangian expansion, the possibility of TeV scale see-saw models has been recently revised in the context of MLFV [221, 245–247]. Minimal flavor violation was first introduced for the quark sector [248–250]. Its origin was based on the assumption that the source of flavor mixing in the SM completely determines the flavor symmetry breaking in the complete BSM theory. This was thought as a way to explain the absence of NP effects in flavor changing processes in meson decays. In the quark sector the only relevant breaking terms of the $SU(3)^3$ quark flavor symmetry in the SM are the quark Yukawa terms, and they have to be then the only breaking source in the complete minimal flavor violating theory. The idea was later extended for the leptons [245, 246], however in the lepton sector the precise hypothesis corresponding to MLFV is less well defined. The SM by itself cannot account for lepton flavor violation, as the SM only contains Yukawa couplings for the

charged leptons, and they can always be set to a diagonal form by rotating the left handed $SU(2)_L$ lepton doublets, L , and the corresponding charged lepton right-handed $SU(2)_L$ singlets. Nevertheless, lepton flavor violation is observed in neutrino oscillations and thus the charged lepton SM Yukawas are not enough to explain the neutrino data. Thus, the MLFV hypothesis can be implemented in the theory, but it requires the SM to be first extended to account for the neutrino data, and this is of course model dependent. In summary, the couplings and the generation structure of the new states must also be considered when defining the conditions for MLFV, making them model dependent by default.

Interestingly, in [221] simple see-saw models were constructed which realize the conditions associated with MLFV as set up in [245]. There, while there is a large hierarchy between the total lepton number and the lepton flavor breaking scales, $\Lambda_{LN} \gg \Lambda_{FL}$, which is exactly the case we are interested in, the coefficients of the flavor violating (but total lepton number conserving) dimension-six operators, $f_{6,i}$, are completely determined by the dimension-five operator coefficient, f_5 . In other words, the flavor structure of the dimension-six operators is fixed by that of the Weinberg one, a relation that brings very interesting consequences as we will see in the next Sections. As discussed in [221], these two conditions are automatically fulfilled by the simplest type-II see-saw model if a light double-triplet mixing μ_Δ is assumed. Regarding the LHC phenomenology, this type-II see-saw leads to interesting signatures which have been studied in detail in [238, 251]. However, from the theoretical side, one drawback of this TeV scale type-II see-saw model is that it is difficult to keep such a low μ_Δ stable if generated by spontaneous breaking of lepton number.

Reference [221] also presented a simple model for type-I (the type-III case is analogous) see-saw with naturally light states and MLFV. From the point of view of the LHC phenomenology these models are very attractive for two reasons. First, the new states can be light enough to be produced at LHC after both scales have been well separated. Second, their observable (total lepton number conserving) signatures are fully determined by the neutrino parameters. In the case exposed in detail in [221], the type-I see-saw realization, the new states are SM singlets, which means that they can only be produced via their mixing with the SM neutrinos. Unfortunately, this leads to small production rates which make the model only marginally testable at the LHC. In contrast, for type-III see-saw new states, the production can be sizable, allowing for a potential test of the hypothesis of MLFV. This is the scenario which we explore here.

The simplest MLFV type-III see-saw model

We describe now the simplest MLFV model presented in [221], adapted to a type-III see-saw realization. The reason is that, as explained above, type-I

see-saw heavy fermions can only be marginally testable at LHC, even after we assume TeV scale new states. In the case of type-III see-saw, the triplet partners can be copiously pair-produced through their EW interactions with the gauge bosons that are introduced inside the new kinetic terms.

We start the presentation of the MLFV type-III see-saw model extending the SM Lagrangian with two fermion triplets, that are defined as $\vec{\Sigma} = (\Sigma_1, \Sigma_2, \Sigma_3)$ and $\vec{\Sigma}' = (\Sigma'_1, \Sigma'_2, \Sigma'_3)$. Each of the two fermion triplets is formed by three right-handed Weyl spinors of zero hypercharge. Together with the addition of these triplets we include Yukawa terms that couple the Higgs doublet with the SM leptons and the new fermion triplets. We also introduce new Majorana mass terms for the triplets, as well as the required kinetic terms for them. With these additions, the extended Lagrangian is written as

$$\mathcal{L} = \mathcal{L}_{\text{SM}} + \mathcal{L}_K + \mathcal{L}_Y + \mathcal{L}_\Lambda \quad , \quad (5.3)$$

with

$$\mathcal{L}_K = i \left(\vec{\Sigma} \not{D} \vec{\Sigma} + \vec{\Sigma}' \not{D} \vec{\Sigma}' \right) \quad , \quad (5.4)$$

$$\mathcal{L}_Y = -Y_i^\dagger L_i^w \left(\vec{\Sigma} \cdot \vec{\sigma} \right) \tilde{\Phi} - \epsilon Y_i'^\dagger L_i^w \left(\vec{\Sigma}' \cdot \vec{\sigma} \right) \tilde{\Phi} + \text{h.c.} \quad , \quad (5.5)$$

$$\mathcal{L}_\Lambda = -\frac{\Lambda}{2} \left(\vec{\Sigma}^c \vec{\Sigma}' + \vec{\Sigma}'^c \vec{\Sigma} \right) - \frac{\mu}{2} \vec{\Sigma}'^c \vec{\Sigma}' - \frac{\mu'}{2} \vec{\Sigma}^c \vec{\Sigma} + \text{h.c.} \quad . \quad (5.6)$$

In these expressions, $\vec{\sigma}$ stand as usual for the Pauli matrices. Furthermore, the gauge covariant derivative acting on the fermion triplets is given by $D_\mu = \partial_\mu + ig \vec{T} \cdot \vec{W}_\mu$, where \vec{T} stand for the three-dimensional representation of the $SU(2)_L$ generators, *i.e.*

$$T_1 = \begin{pmatrix} 0 & 0 & 0 \\ 0 & 0 & -i \\ 0 & i & 0 \end{pmatrix}, \quad T_2 = \begin{pmatrix} 0 & 0 & i \\ 0 & 0 & 0 \\ -i & 0 & 0 \end{pmatrix}, \quad T_3 = \begin{pmatrix} 0 & -i & 0 \\ i & 0 & 0 \\ 0 & 0 & 0 \end{pmatrix} . \quad (5.7)$$

Regarding the particle content, besides the presented fermion triplets ($\vec{\Sigma}^{(\prime)}$) and the Higgs doublet, in this case we have explicitly written the three SM lepton doublets as $L_i^w = (\nu_i^w, \ell_i^w)^T$. This way the index w makes reference to the fact that these are weak eigenstates, to be distinguished from those without the index, which correspond in the forthcoming expressions to the mass eigenstates.

In the MLFV type-III see-saw construction that we present in this Chapter, the flavor-blind parameters ϵ , μ and μ' are *small*, *i.e.*, the scales μ and μ' are much smaller than Λ and v , and $\epsilon \ll 1$. This is a fundamental characteristic of the model, it is needed to accomplish $M \sim \Lambda_{\text{FL}} \ll \Lambda_{\text{LN}}$, as we will further discuss by the end of the present Section. Here it suffices to state that the Lagrangian in Eq. (5.3) breaks total lepton number due to

5.1. MLFV TYPE-III SEE-SAW MODEL

the simultaneous presence of the Yukawa terms Y_i and $\epsilon Y'_i$, as well as to the presence of the μ and μ' terms. In the limit $\mu, \mu', \epsilon \rightarrow 0$ it is possible to define a conserved total lepton number by assigning $L(L^w) = L(\Sigma) = -L(\Sigma') = 1$.

After EWSB, and working in the unitary gauge, we can define six Weyl fermions of well defined electric charge. They are $\Sigma_{\pm}^{(\prime)} = \frac{1}{\sqrt{2}} \left(\Sigma_1^{(\prime)} \mp i \Sigma_2^{(\prime)} \right)$ and $\Sigma_0^{(\prime)} = \Sigma_3^{(\prime)}$. In addition, from those we define negatively charged Dirac fermions E and E' and the neutral Majorana fermions \tilde{N} and \tilde{N}'

$$E^{(\prime)} = \Sigma_-^{(\prime)} + \Sigma_+^{(\prime)c} \quad \text{and} \quad \tilde{N}^{(\prime)} = \Sigma_0^{(\prime)} + \Sigma_0^{(\prime)c}. \quad (5.8)$$

In this intermediate basis the leptonic mass terms read

$$\mathcal{L}_m = -\frac{1}{2} \left(\overline{\nu_L^w} \quad \overline{\tilde{N}_R} \quad \overline{\tilde{N}'_R} \right) M_0 \begin{pmatrix} \nu_L^w \\ \tilde{N}_R^c \\ \tilde{N}'_R^c \end{pmatrix} - \left(\overline{\ell_L^w} \quad \overline{E_L} \quad \overline{E'_L} \right) M_{\pm} \begin{pmatrix} \ell_R^w \\ E_R \\ E'_R \end{pmatrix} + \text{h.c.}, \quad (5.9)$$

with

$$M_0 = \begin{pmatrix} 0 & \frac{v}{\sqrt{2}} Y^T & \epsilon \frac{v}{\sqrt{2}} Y'^T \\ \frac{v}{\sqrt{2}} Y & \mu' & \Lambda \\ \epsilon \frac{v}{\sqrt{2}} Y' & \Lambda & \mu \end{pmatrix} \quad \text{and} \quad M_{\pm} = \begin{pmatrix} \frac{v}{\sqrt{2}} Y^{\ell} & v Y^{\dagger} & \epsilon v Y'^{\dagger} \\ 0 & \mu' & \Lambda \\ 0 & \Lambda & \mu \end{pmatrix}. \quad (5.10)$$

In these expressions Y^{ℓ} are the charged lepton Yukawa couplings of the SM, and $Y^{(\prime)} = (Y_1^{(\prime)}, Y_2^{(\prime)}, Y_3^{(\prime)})$, where the subscript refers to the lepton flavor family. As in the previous expressions, in writing Eq. (5.9) we denote by $\vec{\nu}^w$ and $\vec{\ell}^w$ the two column vectors containing the three neutrinos and charged leptons of the SM in the weak basis. Moreover, without loss of generality, we have chosen to work in a basis in which Λ is real, while both Y and Y' are complex. In general the parameters μ and μ' could be complex, but for the sake of simplicity we have taken them to be real in what follows, though it is straight forward to generalize the following expressions to include the relevant phases [252].

We proceed now to diagonalize the Lagrangian and rotate it to the final mass basis. The lepton mass matrix, M_{\pm} , can be diagonalized by a bi-unitary matrix transformation (one unitary matrix is required for the left handed components and one for the right handed ones), while the neutral part, M_0 , can be diagonalized by a single unitary matrix. After the diagonalization of \mathcal{L}_m one finds three light Majorana neutrinos ν_i , where the lightest is massless, and three light charged massive leptons ℓ_i that satisfy

$$m_{\nu}^{\text{diag}} = V^{\nu T} \left[-\frac{v^2}{2\Lambda} \epsilon \left(\widehat{Y'}^T Y + Y^T \widehat{Y'} \right) \right] V^{\nu}, \quad (5.11)$$

$$m_{\ell}^{\text{diag}} = \frac{v}{\sqrt{2}} V^{\ell \dagger} Y^{\ell} V^{\ell} \left[1 - \frac{v^2}{2\Lambda^2} Y^{\dagger} Y \right] V_L^{\ell}. \quad (5.12)$$

V^ν and $V_{L,R}^\ell$ are 3×3 unitary matrices that will be explicitly described in the following. For convenience we have defined also the combination

$$\widehat{Y}' = Y' - \frac{1}{\epsilon} \frac{\mu}{2\Lambda} Y. \quad (5.13)$$

As we have commented, in this simple setup one of the light neutrinos remains massless. However, the model could be easily extended to account for three massive light neutrinos by adding an extra fermion triplet field if necessary. After the diagonalization we find also two heavy Majorana neutral leptons and two charged heavy leptons with masses $M \simeq \Lambda(1 \mp \frac{\mu + \mu'}{2\Lambda})$. In the limit we are interested in, with *small* flavor-blind parameters ϵ , μ and μ' , the two heavy Majorana neutral states have almost the same mass, but opposite CP parities, and furthermore their Yukawa interactions are equal up to a complex phase. Thus we can construct a quasi-Dirac state N with the two Majorana neutral leptons. Analogously, in the charged sector we construct two combinations of the heavy charged leptons that give us the final mass eigenstates E_1^- and E_2^+ . These states have diagonal couplings with the quasi-Dirac state N . The final mass eigenstates are related then to the weak eigenstates by

$$\begin{aligned} \nu_L^w &= V^\nu \nu_L + \frac{v}{\sqrt{2}\Lambda} Y^\dagger N_L + \frac{v}{\sqrt{2}\Lambda} \left(\epsilon Y'^\dagger - \left(\frac{3\mu + \mu'}{4\Lambda} \right) Y^\dagger \right) N_R^c, \\ \ell_L^w &= \ell_L + \frac{v}{\Lambda} Y^\dagger E_{1L}^- + \frac{v}{\Lambda} \left(\epsilon Y'^\dagger - \left(\frac{3\mu + \mu'}{4\Lambda} \right) Y^\dagger \right) E_{2R}^{+c}, \\ \ell_R^w &= \ell_R, \\ N_L &= N_R^c - \left(\frac{\mu - \mu'}{4\Lambda} \right) N_L - \frac{v}{\sqrt{2}\Lambda} \left(\epsilon Y' - \frac{\mu}{\Lambda} Y \right) V^\nu \nu_L, \\ N_L' &= N_L + \left(\frac{\mu - \mu'}{4\Lambda} \right) N_R^c - \frac{v}{\sqrt{2}\Lambda} Y V^\nu \nu_L, \\ E_L &= E_{2R}^{+c} - \left(\frac{\mu - \mu'}{4\Lambda} \right) E_{1L}^- - \frac{v}{\Lambda} \left(\epsilon Y' - \frac{\mu}{\Lambda} Y \right) \ell_L, \\ E_R &= E_{1R}^- - \left(\frac{\mu - \mu'}{4\Lambda} \right) E_{2L}^{+c}, \\ E_L' &= E_{1L}^- + \left(\frac{\mu - \mu'}{4\Lambda} \right) E_{2R}^{+c} - \frac{v}{\Lambda} Y \ell_L, \\ E_R' &= E_{2L}^{+c} + \left(\frac{\mu - \mu'}{4\Lambda} \right) E_{1R}^-, \end{aligned} \quad (5.14)$$

where we have used that, in general, one can choose the flavor basis such that $V_L^\ell = V_R^\ell = I$.

Before writing the interaction Lagrangian in the mass basis, we describe how the Yukawa couplings, and thus the final interactions between the heavy

5.1. MLFV TYPE-III SEE-SAW MODEL

states and the light SM leptons, can be completely specified from the neutrino mass matrix, which is one of the most interesting features of this scenario. To first order in the small parameters, the neutral weak interactions of the light states take the same form as that in the SM, while the charged current interactions read¹

$$\mathcal{L}_W^{\text{light}} = -\frac{g}{\sqrt{2}} (\bar{\ell}_L \gamma^\mu U_{\text{LEP}} \nu_L W_\mu^-) + \text{h.c.} \quad , \quad (5.15)$$

where, as usual, g is the $SU(2)_L$ coupling constant. After absorbing three unphysical phases in the definition of the light charged leptons, the leptonic mixing matrix can be chosen

$$U_{\text{LEP}} = V^\nu \quad (5.16)$$

$$= \begin{pmatrix} 1 & 0 & 0 \\ 0 & c_{23} & s_{23} \\ 0 & -s_{23} & c_{23} \end{pmatrix} \begin{pmatrix} c_{13} & 0 & s_{13} e^{-i\delta_{\text{CP}}} \\ 0 & 1 & 0 \\ -s_{13} e^{i\delta_{\text{CP}}} & 0 & c_{13} \end{pmatrix} \begin{pmatrix} c_{21} & s_{12} & 0 \\ -s_{12} & c_{12} & 0 \\ 0 & 0 & 1 \end{pmatrix} \begin{pmatrix} e^{-i\alpha} & 0 & 0 \\ 0 & e^{i\alpha} & 0 \\ 0 & 0 & 1 \end{pmatrix} ,$$

where $c_{ij} \equiv \cos \theta_{ij}$ and $s_{ij} \equiv \sin \theta_{ij}$, and the angles θ_{ij} can be taken without loss of generality to lie in the first quadrant; $\theta_{ij} \in [0, \pi/2]$, and the phases δ_{CP} , $\alpha \in [0, 2\pi]$. The leptonic mixing matrix contains only two phases because there are only two heavy triplets and consequently only two light neutrinos are massive while the lightest one remains massless, as we have already commented.

In [221] it was shown that for this simple model one can fully reconstruct the neutrino Yukawa coupling Y and the combination \widehat{Y}' from the neutrino mass matrix up to a global normalization. In the process one first finds the matrix V^μ that diagonalizes the neutrino mass terms, see Eq. (5.11), in terms of Y and \widehat{Y}' . After one identifies V^μ with the neutrino mass matrix as in Eq. (5.16), the relation can be inverted to find Y and \widehat{Y}' as a function of U_{LEP} . This way, up to the global normalization and the unknown neutrino mixing phases, Y and \widehat{Y}' can be determined in each of the neutrino orderings². As we have commented, the reconstruction is different for normal and inverted orderings, as the determination of Y and \widehat{Y}' from the neutrino mass matrix depends on a parameter (ρ in the following) that is determined from the measured mass differences between the SM neutrinos, whose values depend on the chosen neutrino ordering. Thus we have:

- Normal ordering (NO): in this case $0 = m_1 < m_2 < m_3$ and the

¹Violation of unitarity (and flavor mixing) appears in the charged current (and neutral current) interactions of the light leptons to higher order [252–254].

²Notice that it is not possible to fully reconstruct the Yukawa couplings Y' from Eq. (5.13) without the knowledge of the parameters ϵ and μ , although this has no effect on the phenomenology analysis of the present Chapter.

Yukawa couplings are given by

$$\begin{aligned} Y_a &= \frac{y}{\sqrt{2}} \left(\sqrt{1+\rho} U_{\text{LEPa}3}^* + \sqrt{1-\rho} U_{\text{LEPa}2}^* \right), \quad (5.17) \\ \widehat{Y}'_a &= \frac{\widehat{y}'}{\sqrt{2}} \left(\sqrt{1+\rho} U_{\text{LEPa}3}^* - \sqrt{1-\rho} U_{\text{LEPa}2}^* \right), \end{aligned}$$

where y and \widehat{y}' are two real numbers and

$$\rho = \frac{\sqrt{1+r} - \sqrt{r}}{\sqrt{1+r} + \sqrt{r}}, \quad r = \frac{m_2^2 - m_1^2}{m_3^2 - m_2^2}, \quad (5.18)$$

$$m_1 = 0, \quad m_2 = \frac{\epsilon y \widehat{y}' v^2}{\Lambda} (1 - \rho), \quad m_3 = \frac{\epsilon y \widehat{y}' v^2}{\Lambda} (1 + \rho). \quad (5.19)$$

- Inverted ordering (IO): if we consider instead $0 = m_3 < m_1 < m_2$ the Yukawas can be written as

$$\begin{aligned} Y_a &= \frac{y}{\sqrt{2}} \left(\sqrt{1+\rho} U_{\text{LEPa}2}^* + \sqrt{1-\rho} U_{\text{LEPa}1}^* \right), \quad (5.20) \\ \widehat{Y}'_a &= \frac{\widehat{y}'}{\sqrt{2}} \left(\sqrt{1+\rho} U_{\text{LEPa}2}^* - \sqrt{1-\rho} U_{\text{LEPa}1}^* \right), \end{aligned}$$

with

$$\rho = \frac{\sqrt{1+r} - 1}{\sqrt{1+r} + 1}, \quad r = \frac{m_2^2 - m_1^2}{m_1^2 - m_3^2}, \quad (5.21)$$

$$m_3 = 0, \quad m_1 = \frac{\epsilon y \widehat{y}' v^2}{\Lambda} (1 - \rho), \quad m_2 = \frac{\epsilon y \widehat{y}' v^2}{\Lambda} (1 + \rho). \quad (5.22)$$

Interestingly, the behavior of the Yukawas as a function of the neutrino mixing parameters is different depending on the neutrino ordering, and thus the phenomenology of the new heavy states changes in the two cases as we see in the following. We first plot in Fig. 5.1 the ranges of the Yukawa couplings $|\widetilde{Y}_e|^2 \equiv |Y_1|^2/y^2$ and $|\widetilde{Y}_\mu|^2 \equiv |Y_2|^2/y^2$ obtained by projecting the allowed ranges of oscillation parameters from the global analysis of neutrino data [255] using Eqs. (5.17), (5.18), (5.20), and (5.21). The ranges are shown at 1σ , 2σ , and 99% CL (1 d. o. f.), while the dotted lines correspond to the best fit values. We show the ranges of these Yukawa couplings as a function of the unknown Majorana phase α for the two orderings in the four upper panels. We focus on the Yukawa couplings corresponding to the electron and the muon since these are the two leptons that are considered in the coming LHC analyses. Moreover, we present the correlation between the Yukawa couplings in these two flavors (e and μ), in the two bottom panels. As we can see from this Figure, the electron and muon Yukawa couplings exhibit a quite different behavior with respect to α for the NO and IO cases. It is

5.1. MLFV TYPE-III SEE-SAW MODEL

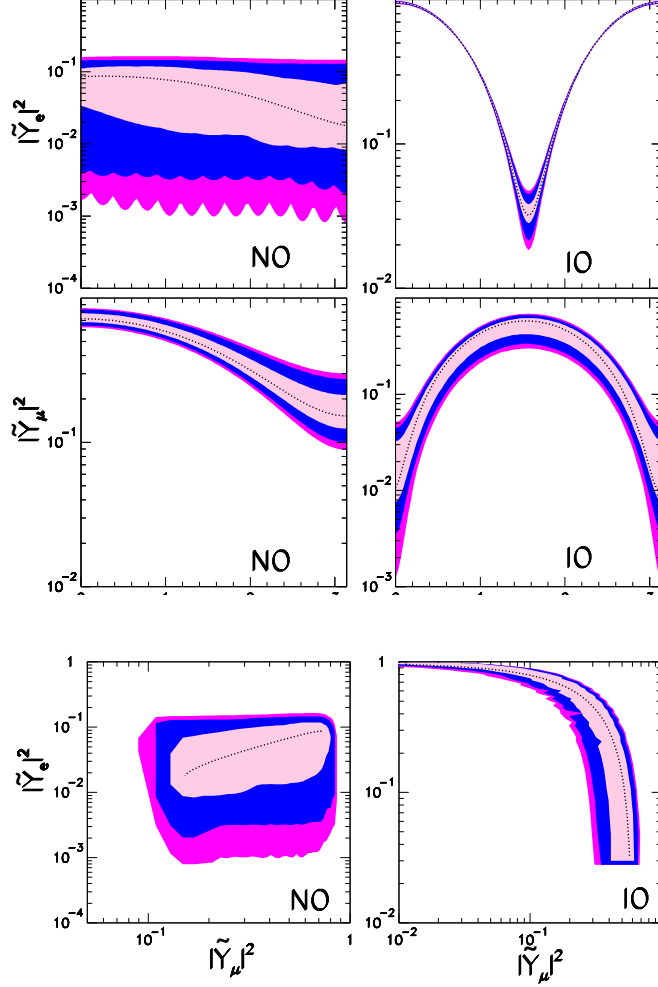


Figure 5.1: Allowed ranges of the Yukawa couplings $|\tilde{Y}_e|^2 \equiv |Y_1|^2/y^2$ and $|\tilde{Y}_\mu|^2 \equiv |Y_2|^2/y^2$ obtained from the global analysis of neutrino data [255]. The upper four panels show the values of the couplings as a function of the unknown Majorana phase α . The correlation between the two couplings is shown in the two lower panels. The left (right) panels correspond to normal (inverted) ordering. The dotted line corresponds to the best fit values. The ranges in the filled areas are shown at 1σ , 2σ , and 99% CL.

also interesting to notice that the two Yukawas are invariant under α going into $\pi - \alpha$ in the limit that s_{13}^3 or δ go to zero for the IO mass ordering.

Once we have determined the Yukawa couplings from the neutrino mass matrix, we can rotate the Lagrangian in Eq. (5.3) using the relations in Eq. (5.14) to obtain the final interactions that are of relevance in the present Chapter. The Lagrangian for the interactions of the heavy triplet states in

³This limit is now ruled out, see [256].

the mass basis then reads:

$$\mathcal{L}_W = -g \left(\overline{E_1^-} \gamma^\mu N W_\mu^- - \overline{N} \gamma^\mu E_2^+ W_\mu^- \right) + \text{h.c.} \quad (5.23)$$

$$\begin{aligned} & -\frac{g}{\sqrt{2}} \left(K_a \overline{\ell_{aL}} \gamma^\mu N_L W_\mu^- + K'_a \overline{\ell_{aL}} \gamma^\mu N_R^c W_\mu^- \right) + \text{h.c.} \\ & + g \left(\tilde{K}_a \overline{\nu_{aL}} \gamma^\mu E_{2L}^+ W_\mu^- + \tilde{K}'_a \overline{\nu_{aL}} \gamma^\mu E_{1R}^c W_\mu^- \right) + \text{h.c.} \end{aligned} \quad (5.24)$$

$$\begin{aligned} \mathcal{L}_Z = & g c_\theta \left(\overline{E_1^-} \gamma^\mu E_1^- Z_\mu - \overline{E_2^+} \gamma^\mu E_2^+ Z_\mu \right) \\ & + \frac{g}{2c_\theta} \left(\tilde{K}_a \overline{\nu_{aL}} \gamma^\mu N_L Z_\mu + \tilde{K}'_a \overline{\nu_{aL}} \gamma^\mu N_R^c Z_\mu \right) + \text{h.c.} \\ & + \frac{g}{\sqrt{2}c_\theta} \left(K_a \overline{\ell_{aL}} \gamma^\mu E_{1L}^- Z_\mu + K'_a \overline{\ell_{aL}} \gamma^\mu E_{2R}^c Z_\mu \right) + \text{h.c.} , \end{aligned} \quad (5.25)$$

$$\mathcal{L}_\gamma = e \left(\overline{E_1^-} \gamma^\mu E_1^- A_\mu - \overline{E_2^+} \gamma^\mu E_2^+ A_\mu \right) , \quad (5.26)$$

$$\begin{aligned} \mathcal{L}_h = & \frac{g\Lambda}{2M_W} \left(\tilde{K}_a \overline{\nu_{aL}} N_R + \tilde{K}''_a \overline{\nu_{aL}} N_L^c \right) h + \text{h.c.} \\ & + \frac{g\Lambda}{\sqrt{2}M_W} \left(K_a \overline{\ell_{aL}} E_{1R}^- + K''_i \overline{\ell_{aL}} E_{2L}^c \right) h + \text{h.c.} , \end{aligned} \quad (5.27)$$

where the matrices $K^{(\prime\prime)}$ and $\tilde{K}^{(\prime\prime)}$ are defined as

$$\begin{aligned} K_a &= -\frac{v}{\sqrt{2}\Lambda} Y_a^* , & \tilde{K}_a &= U_{\text{LEP}ba}^* K_b , \\ K'_a &= -\frac{v}{\sqrt{2}\Lambda} \left[\epsilon Y_a'^* - \left(\frac{3\mu + \mu'}{4\Lambda} \right) Y_a^* \right] , & \tilde{K}'_a &= U_{\text{LEP}ba}^* K'_b , \\ K''_a &= -\frac{v}{\sqrt{2}\Lambda} \left[\epsilon Y_a''^* - \left(\frac{\mu - \mu'}{4\Lambda} \right) Y_a^* \right] , & \tilde{K}''_a &= U_{\text{LEP}ba}^* K''_b . \end{aligned} \quad (5.28)$$

Recovering Eqs. (5.17)–(5.22) we observe that the flavor structure of the total lepton number conserving couplings of the heavy fermion triplets, K and \tilde{K} , is fully determined by the low energy neutrino parameters. Moreover, the strength of these total lepton number conserving couplings is controlled by the real number yv/Λ , while the combination $\epsilon y y'/\Lambda$ is fixed by the neutrino masses. On the other hand, the Yukawa combinations that appear on the L -violating couplings, $K^{(\prime\prime)}$ and $\tilde{K}^{(\prime\prime)}$, are different from the combination determined by the low energy neutrino parameters, \widehat{Y}' , see Eq. (5.13). This means that the L -violating couplings of the fermion triplets are not fixed by the low energy neutrino parameters. Nevertheless, as we discuss next, these L -violating couplings are very suppressed in the model under consideration, and they are of no relevance in the current analysis.

Let's remember that in the present MLFV framework the small neutrino masses naturally stem from the tiny total lepton number violation, which is associated with the smallness of the ϵ , μ and μ' parameters (see Eq. (5.11)). The low energy effective Lagrangian after integrating out the triplet states

5.2. SIGNATURES

takes the form in Eq. (5.2) with $\Lambda_{FL} = \Lambda$ and $\Lambda_{LN} \sim \Lambda/\sqrt{\epsilon}, \Lambda^2/\mu, \Lambda^2/\mu'$. Therefore, while the lepton flavor violating (but total lepton number conserving) scale is associated with the mass of the fermion triplets, that can be light enough to leave an imprint on the LHC phenomenology, there is instead no state with mass Λ_{LN} associated to the total lepton number violating scale. Furthermore, the hierarchy of scales dictated by the structure of this MLFV type-III see-saw model, $\Lambda_{LN} \gg \Lambda_{FL}$, is technically natural in the t'Hooft's sense, since this hierarchy is associated with the smallness of ϵ , μ and μ' parameters. As we have commented, if one takes the limit $\mu, \mu', \epsilon \rightarrow 0$, the total lepton number symmetry is restored after the proper lepton number assignments.

Moving to the phenomenology of the model, in the language of the interaction terms in Eq. (5.28), total lepton number violation appears in the heavy fermion triplet decays only as a consequence of the presence of both “primed” and “not primed” terms, as well as of the $\mathcal{O}(\mu/\Lambda, \mu'/\Lambda)$ mass splitting and mixing in the heavy states. Thus small total lepton number violation implies a strong hierarchy between the total lepton number conserving and the total lepton number violating effects in the heavy fermion collider phenomenology. This renders the observation of L -violating signals impossible at the LHC. This is one of the main differences of the expected LHC signatures with respect to the non-MLFV scenarios for type-III see-saw models, such as the ones studied for instance in [239, 241, 242]. There, $\Delta L = 2$ final states constitute a smoking gun signature which is very suppressed in the MLFV model here considered. The main signatures that the MLFV model leads to, that we proceed now to describe, are consequently associated to the lepton number conserving signals.

5.2 Signatures

The main signatures of the phenomenology of the considered model can be summarized in two main points. First the total lepton number violating signals are negligible, and also stemming from the same hierarchy of contributions there are not observable displaced vertices. Both features are instead typical of other type-III see-saw realizations, see for instance [238–242]. Second, the total lepton number conserving signals, which could be observed at the LHC, are predicted from the lepton mixing matrix, making the observation and verification of the model, as well as of the unknown mixing parameters, possible. We focus in this Section on which characteristics a collider process has to fulfill for the MLFV hypothesis to be testable at the LHC.

In contrast with the type-I see-saw realization, on type-III models the dominant production processes for the heavy fermion triplets are originated from the EW pair production included in the kinetic terms of the

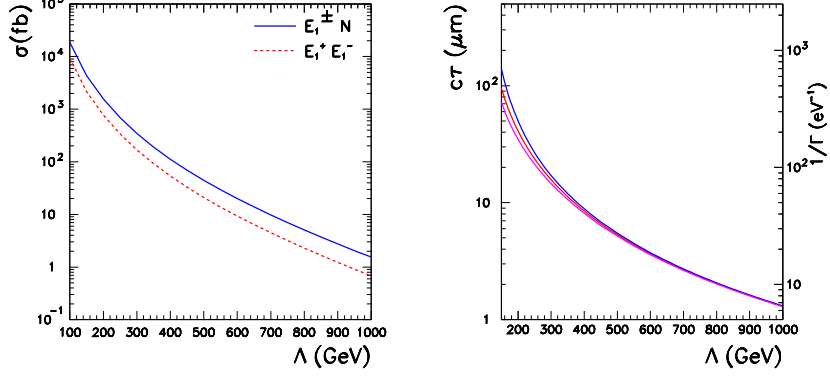


Figure 5.2: **Left panel:** cross sections for the triplet fermion pair productions NE_1^\pm and $E_1^+E_1^-$, that have the same values than the cross sections for NE_2^\pm and $E_2^+E_2^-$ respectively. **Right panel:** maximum decay length of the fermion triplets E_1^\pm (blue upper curve), N (red middle curve), and E_2^\pm (magenta lower curve). In all cases we have taken $M_H = 120$ GeV and we have assumed $k = 1/10$, see text for details.

Lagrangian, \mathcal{L}_K in Eq. (5.3). In the present model the fermion triplet gauge interactions lead to the processes

$$pp \rightarrow E_i^+ E_i^-, \quad \text{and} \quad pp \rightarrow E_i^\pm N \quad \text{for } i = 1, 2, \quad (5.29)$$

where for simplicity in the second reaction, and in the following, we generically denote by “ N ” either the N or the \bar{N} state. The cross section rates for these processes are well known functions of the mass of the new states, see for example [237]. For completeness we plot the cross sections in the left panel of Fig. 5.2.

The decay widths for the different decay modes read [237]:

$$\begin{aligned} \Gamma(N \rightarrow \ell_a^- W^+) &= \frac{g^2}{64\pi} |K_a|^2 \frac{\Lambda^3}{M_W^2} \left(1 - \frac{M_W^2}{\Lambda^2}\right) \left(1 + \frac{M_W^2}{\Lambda^2} - 2\frac{M_W^4}{\Lambda^4}\right), \\ \Gamma(N \rightarrow \nu_a Z) &= \frac{g^2}{128\pi c_\theta^2} |\tilde{K}_a|^2 \frac{\Lambda^3}{M_Z^2} \left(1 - \frac{M_Z^2}{\Lambda^2}\right) \left(1 + \frac{M_Z^2}{\Lambda^2} - 2\frac{M_Z^4}{\Lambda^4}\right), \\ \Gamma(N \rightarrow \nu_a h) &= \frac{g^2}{128\pi} |\tilde{K}_a|^2 \frac{\Lambda^3}{M_W^2} \left(1 - \frac{M_h^2}{\Lambda^2}\right)^2, \end{aligned} \quad (5.30)$$

5.2. SIGNATURES

$$\begin{aligned}
\Gamma(E_2^+ \rightarrow \nu_a W^+) &= \frac{g^2}{32\pi} |\tilde{K}_a|^2 \frac{\Lambda^3}{M_W^2} \left(1 - \frac{M_W^2}{\Lambda^2}\right) \left(1 + \frac{M_W^2}{\Lambda^2} - 2\frac{M_W^4}{\Lambda^4}\right), \\
\Gamma(E_1^- \rightarrow \ell_a^- Z) &= \frac{g^2}{64\pi c_\theta^2} |K_a|^2 \frac{\Lambda^3}{M_Z^2} \left(1 - \frac{M_Z^2}{\Lambda^2}\right) \left(1 + \frac{M_Z^2}{\Lambda^2} - 2\frac{M_Z^4}{\Lambda^4}\right), \\
\Gamma(E_1^- \rightarrow \ell_a^- h) &= \frac{g^2}{64\pi} |K_a|^2 \frac{\Lambda^3}{M_W^2} \left(1 - \frac{M_h^2}{\Lambda^2}\right)^2.
\end{aligned} \tag{5.31}$$

Using Eq. (5.28) and the fact that U_{LEP} is an unitary matrix, it can be shown that

$$\sum_{a=1}^3 |K_a|^2 = \sum_{a=1}^3 |\tilde{K}_a|^2 = \frac{y^2 v^2}{2\Lambda^2}. \tag{5.32}$$

This way the total decay widths for the three triplet fermions, $F = N, E_1^-,$ and $E_2^+,$ are

$$\Gamma_F^{\text{TOT}} = \frac{g^2 \Lambda^3}{64\pi M_W^2} \frac{y^2 v^2}{\Lambda^2} (1 + \mathcal{F}_F(\Lambda)), \tag{5.33}$$

where $\mathcal{F}_F(\Lambda) \rightarrow 0$ for $\Lambda \gg M_H, M_Z, M_W$. In a general type-III see-saw model it is possible that the branching ratio of N or E_i^\pm into a light lepton of a given flavor is vanishingly small. This is not the case for the type-III see-saw MLFV model studied here, where, as we have seen, the Yukawa couplings are fixed by the neutrino physics and they are non-vanishing; see Fig. 5.1. The same relation between the Yukawa couplings and the lepton mixing parameters leads to another important characteristic of this simple MLFV model. The values of the neutrino masses imply a lower bound on the total decay width of the triplet fermions as a consequence of the hierarchy between the L -conserving and L -violating y and $\epsilon\hat{y}'$ constants that is required in the MLFV framework we have described in the previous Section. Let us write simply $\epsilon\hat{y}' < ky$, where $k < 1$ is a constant we just introduced to generically characterize the smallness of the total lepton number violation. From Eq. (5.19) or (5.22) it follows that

$$\frac{y^2 v^2}{\Lambda^2} > \frac{m_{3(2)}}{k\Lambda(1+\rho)} = \frac{\sqrt{m_{3(2)}^2 - m_{1(3)}^2}}{k\Lambda(1+\rho)} > \frac{0.046 \text{ eV}}{k\Lambda}, \tag{5.34}$$

where the last number is obtained at 99% CL from the global analysis of neutrino data [255]. We depict in the right panel of Fig. 5.2 the resulting minimum decay width for the fermion triplets, as well as the corresponding maximum decay length for any value of $k < 0.1$. We note from this Figure that in this minimal model, even for heavy states as light as $\Lambda = 150$ GeV, the corresponding decay length is always

$$c\tau \lesssim 100 \mu\text{m}, \tag{5.35}$$

and in addition it decreases rapidly with Λ . Thus, such a small decay length is too short to produce a detectable displaced decay vertex [257, 258]. As we have commented, the use of detached vertices as signatures of the new neutrino heavy state decays has been discussed in the context of more general see–saw implementations, see for instance the models in [238–242]. In the present MLFV model the lack of this signature makes the background reduction more challenging. On the other hand, if a triplet fermion signal is found without a displaced vertex, it will point towards a very hierarchical neutrino spectrum, such as the one predicted in this simple model. Summarizing this first part of the Section, in the considered MLFV type–III see–saw realization there are not sizable total lepton number violating signals nor observable displaced vertices. The observation of the model relies in contrast on the highly predictive flavor composition of the total lepton number conserving signals. In order to optimize the search for these signatures we review in the following the main features that the most promising channels have to fulfill in order to test the MLFV hypothesis.

As we have explained, the most characteristic signature of the MLFV type–III see–saw model is the dependence of the decays of the triplet fermions on the low energy neutrino parameters through the Yukawa couplings as seen in Eqs. (5.17), (5.20), (5.23)–(5.28), (5.30), and (5.31). Thus, a key point for the observation of the MLFV nature of the model is the determination of the flavor of the leptons decaying from the fermion triplets. Consequently, in order to be able to tag the lepton flavors, we are led to consider processes where the new fermions have two–body decays exhibiting charged leptons, *i.e.*

$$pp \rightarrow F(\rightarrow \ell_a X)F'(\rightarrow \ell_b X') \quad , \quad (5.36)$$

for $F, F' = N, E_i$ and with $X, X' = Z, W, h$. In fact, it turns out that the production cross sections of these processes satisfy

$$\sigma [pp \rightarrow F(\rightarrow \ell_a X)F'(\rightarrow \ell_b X')] \propto |\tilde{Y}_a|^2 |\tilde{Y}_b|^2 \quad , \quad (5.37)$$

where $\tilde{Y}_a \equiv \frac{Y_a}{y}$. Therefore, the number of events expected for final states with different combinations of charged lepton flavors (a, b) can be fully determined in terms of the low–energy neutrino parameters. In order to test this prediction we take into account that the SM bosons, X and X' , decay and, in consequence, the final state contains at least six particles. This makes the reconstruction of the decay chain non trivial, a challenge that has to be added to the presence of the irreducible SM backgrounds, where the flavor composition of the final states is independent of the relation given in Eq. (5.37). Taking into account these considerations, we can qualitatively summarize in a few points the collider channel features that may allow for the observation of such particular signals. The most promising channels to both detect the triplet fermions, as well as to test the flavor predictions in this model are those in which:

5.2. SIGNATURES

- (i) The branching ratios into the final state after considering the decays of X and X' are not strongly suppressed.
- (ii) After reconstruction, the process should allow us to identify the charged leptons $\ell_{a,b}$ originating from the two body decays of the triplet fermions.
- (iii) The topology should permit the identification of the bosons X or X' to have further information to reconstruct the signal.
- (iv) We should be able to reconstruct the invariant mass of the systems $X\ell_{a,b}$ in order to identify the presence of the fermion triplet pair.

Altogether, we find that the most promising final states that can be fully reconstructed are the following. First the final state containing three leptons plus two jets and missing energy proceeding via

$$pp \rightarrow W^\pm \rightarrow N(\rightarrow l_a^\mp W^\pm \rightarrow l_a^\mp l_c^\pm \nu) E_1^\pm(\rightarrow \ell_b^\pm Z/h \rightarrow \ell_b^\pm jj) . \quad (5.38)$$

And, in addition, the channel leading to two leptons and four jets resulting from the processes

$$\begin{aligned} pp \rightarrow W^\pm \rightarrow N(\rightarrow \ell_a^\mp W^\pm \rightarrow \ell_a^\mp jj) E_1^\pm(\rightarrow \ell_b^\pm Z/h \rightarrow \ell_b^\pm jj) , \\ pp \rightarrow Z/\gamma \rightarrow E_1^\mp(\rightarrow \ell_a^\mp Z/h \rightarrow \ell_a^\mp jj) E_1^\pm(\rightarrow \ell_b^\pm Z/h \rightarrow \ell_b^\pm jj) . \end{aligned} \quad (5.39)$$

As we will describe in detail in the following Section, in order to establish the observability of these signals it is important to note that the final states present not only SM backgrounds, but they also receive contributions from other decays of the fermion triplets, modifying the simple flavor composition determined by Eq. (5.37). Notice also that we do not consider the production of the charged heavy fermion states E_2^\pm , since they decay exclusively into νW pairs, so flavor tagging of the final leptons is not possible, a key point to test the MLFV hypothesis if a signal was observed. Such processes can, however, contribute to extend the LHC potential to unravel the existence of the fermion triplets.

Thus, in the following Section we study the processes in Eqs. (5.38) and (5.39) in detail. The first one, is characterized by a good signal to background ratio [236], and the main challenges, as we will see, are the reconstruction conditions (*ii*) and (*iv*). In the case of the second process both bosons decay hadronically, what gives a high signal rate and, since there are only two leptons in the final state and no neutrinos, the reconstruction conditions are more easily fulfilled. Conversely, the main challenge in this case is the presence of larger QCD backgrounds.

In the following we perform our analysis at the parton level, keeping the full helicity structure of the amplitude for both signal and background processes. This is achieved using MadGraph4 [152], modified to include the

new fermions and their couplings. We also use MadGraph5 [86] for some particular background sources, as we will properly detail in the corresponding text description. As in the rest of the collider analyses of this thesis, we use CTEQ6L parton distribution functions [153], the MadGraph default renormalization and factorization scales and a pp COM energy $\sqrt{s} = 14$ TeV. Furthermore, we simulate experimental resolutions by smearing the energies, but not directions, of all final state leptons and jets, with a Gaussian error given by a resolution $\Delta E/E = 0.14/\sqrt{E}$ for leptons, while for jets we assume a resolution $\Delta E/E = 0.5/\sqrt{E} \oplus 0.03$, if $|\eta_j| \leq 3$ and $\Delta E/E = 1/\sqrt{E} \oplus 0.07$, if $|\eta_j| > 3$ (E in GeV). We also consider a lepton detection efficiency of $\epsilon^\ell = 0.9$ and a jet one of $\epsilon^j = 0.75$. For simplicity, we assume the Higgs mass to be 120 GeV in all the analyses of this Chapter. This mass is close to the one finally observed at the LHC, and the small difference has no observable effect on the results and the phenomenology that we present in the next Section.

5.3 Analysis and results

In this Section we describe the collider analysis for the processes in Eqs. (5.38) and (5.39). In both cases we present and simulate all the relevant background sources and we describe the kinematic cuts that we impose to increase the signal to background ratio. Furthermore we discuss the possibility to test the MLFV hypothesis through the lepton flavor composition of the final states. We finally estimate the potential for the observation of the fermion triplets depending on the lepton mixing parameters. We separate this description in two Subsections, one per collider channel, as their main characteristics and challenges are different. In a final Subsection we combine the results from both processes in order to study the possibility to measure the Majorana phase and the neutrino ordering within the MLFV type–III see–saw realization.

5.3.1 Process $pp \rightarrow \ell\ell jj\cancel{E}_T$

We start the analysis studying the process

$$pp \rightarrow \ell_1^\mp \ell_2^\pm \ell_3^\pm j j \cancel{E}_T \quad , \quad (5.40)$$

where we focus on final state leptons being either electrons or muons for an easier flavor tagging. This final state allows us to look for the events originating from the production of fermion triplets in type–III see–saw models, as shown in Eq. (5.38). The dominant irreducible SM backgrounds for this channel are:

- $t\bar{t}W$ production where the two b 's from the $t, \bar{t} \rightarrow Wb$ decays are identified as the jets, and the three W 's decay leptonically.

5.3. ANALYSIS AND RESULTS

- $t\bar{t}Z$ where the Z decays leptonically, while one top decays semi-leptonically and the other decays fully hadronically. Another possibility is that the two top quarks decay semi-leptonically, however, one of the four final state leptons is lost or misidentified in this case. This background source can contain up to 4 jets, in addition to the three leptons. Thus we require that at least two of the jets comply with the acceptance cuts described below; see Eqs. (5.41) and (5.42).
- $WZjj$ and $ZZjj$ with both W and Z decaying leptonically. In the $ZZjj$ case one lepton has to escape detection.

In principle the background events coming from channels containing leptonic Z decays could be reduced by vetoing events where the opposite-sign equal-flavor leptons have an invariant mass close to the Z mass, see for instance [236, 259], or the cuts in the previous collider analyses, *i.e.* Eqs. (3.39), (4.27), (4.32) or (4.43). However, as we will see, in the present MLFV model the signals are large only for relatively light fermion triplets, $\Lambda \leq 500$ GeV, and for them the characteristic invariant masses of the opposite-sign equal-flavor lepton pairs are not far from the Z mass. Thus if the Z -veto was applied it would be translated into a reduced background, but also into a reduced signal, and in consequence no gain in the observability would be obtained; for an illustration see Fig. 5.3. Consequently we do not impose such Z -veto, these background sources are only reduced thanks to the rest of reconstruction cuts. Additional backgrounds, like $t\bar{t}$ and $Zb\bar{b}$, that contain leptons produced from the semi-leptonic decays of the b 's are negligible in relation to the rest of background sources when no Z -veto is applied. To close the description of the background processes, we note that we do not take into account reducible backgrounds stemming from the misidentification of a jet as a lepton.

We start the collider analysis applying the typical acceptance and isolation cuts. As in the previous collider analyses we have presented in this thesis, this initial set of cuts is meant to ensure the detection and isolation of the final state leptons and jets,

$$|\eta_\ell| < 2.5, \quad |\eta_j| < 3, \quad \Delta R_{\ell\ell}, \Delta R_{\ell j}, \Delta R_{jj} > 0.4. \quad (5.41)$$

We impose as well a minimum transverse momentum

$$p_T^\ell, p_T^j > 20 \text{ GeV}, \quad (5.42)$$

and a minimum missing transverse energy requirement

$$\cancel{E}_T > 10 \text{ GeV}. \quad (5.43)$$

Next, we look for at least two jets compatible with a Z or a H , *i.e.*

$$M_Z - 10 \text{ GeV} < M_{jj} < M_H + 10 \text{ GeV}. \quad (5.44)$$

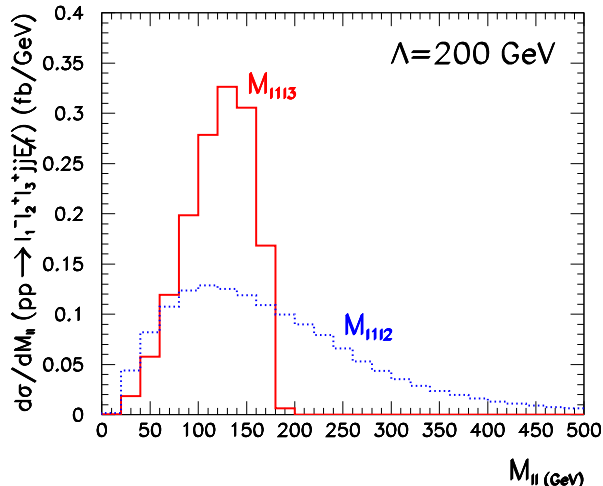


Figure 5.3: Invariant mass distribution of the two possible opposite-sign equal-flavor lepton pairs for the signal $pp \rightarrow \ell_1^- \ell_2^+ \ell_3^+ jj \cancel{E}_T$. We consider a heavy fermion mass $\Lambda = 200$ GeV.

As we have already stated, we use a reconstruction procedure that aims to single out events that originate from the reaction in Eq. (5.38), as our focus is to test the MLFV hypothesis. This means that the reconstruction is not optimized to get the full LHC potential for the heavy fermion triplets discovery, as it will be shown in the following. In order to reconstruct the E_1^\pm and N states a crucial point is that we need to identify which of the equal sign leptons $\ell_{2,3}$, is produced in the E_1^\pm two-body decay, as well as, which lepton comes from the W in the N decay chain. With this purpose in mind, we first reconstruct the two possible values of the invariant mass for each of the equal sign lepton plus two jet combinations, $M_{\ell_2 jj}$ and $M_{\ell_3 jj}$. If both $M_{\ell_2 jj}$ and $M_{\ell_3 jj}$ are incompatible with the heavy fermion mass, *i.e.*

$$M_{\ell_2 jj}, M_{\ell_3 jj} \notin (\Lambda - 40, \Lambda + 40) \text{ GeV} \quad , \quad (5.45)$$

the event is directly discarded in order to increase the signal to background ratio. If only one of the two reconstructions is inside this range we consider the corresponding lepton as the one coming from E_1^\pm , see Eq. (5.38). If both $M_{\ell_2 jj}$ and $M_{\ell_3 jj}$ are inside the range given in Eq. (5.45) we proceed to reconstruct the momentum of the neutrino. As usual, we use that in this final state the neutrino momentum can be reconstructed up to a two-fold ambiguity. After obtaining the transverse momentum from momentum conservation, the longitudinal component is inferred by requiring that $(\vec{p}_\nu + \vec{p}_{\ell_k})^2 = M_W^2$, that leads to Eq. (3.43). Here we write again the expression

5.3. ANALYSIS AND RESULTS

for a clearer presentation of the possible reconstructions

$$p_L^{\nu_{k,n}} = \frac{1}{2p_T^{\ell_k}} \left\{ [M_W^2 + 2(p_T^{\ell_k} \cdot \vec{p}_T)] p_L^{\ell_k} \pm \sqrt{[M_W^2 + 2(p_T^{\ell_k} \cdot \vec{p}_T)]^2 |\vec{p}^\ell|^2 - 4(p_T^{\ell_k} E^{\ell_k} \cancel{E}_T)^2} \right\}, \quad (5.46)$$

for $k = 2, 3$. We have labeled $n = 1, 2$ the solutions with $+, -$ respectively. If neither ℓ_2 nor ℓ_3 lead to a real value of Eq. (5.46), the event is rejected. If only one of them has an acceptable solution we classify this lepton as the one coming from W . Finally if both leptons lead to satisfactory solutions of Eq. (5.46), the ambiguity on the reconstruction still persists, so we proceed to reconstruct the neutral heavy fermion N . For each lepton $\ell_{2,3}$, and using the two possible solutions for the momentum of the neutrino $p^{\nu_{k,n}}$ ($k = 2, 3$ $n = 1, 2$) we evaluate the four invariant masses $M_{\ell_1 \ell_k \nu_{k,n}}$. If for both $k = 2$ and $k = 3$ the two $M_{\ell_1 \ell_k \nu_{k,1}}$ and $M_{\ell_1 \ell_k \nu_{k,2}}$ are outside the interval $(\Lambda - 40, \Lambda + 40)$ GeV we do not consider the event in order to reduce the background contributions. If only $k = 2$ or $k = 3$ has at least one of the corresponding $M_{\ell_1 \ell_k \nu_{k,n}}$ inside this range we select ℓ_k as the lepton coming from W . Finally, if the ambiguity is still there, and both leptons have at least one solution inside this range, we cut out the event. With this final cut in case of ambiguity, we reduce the amount of observable signal, but as we have commented, our focus is not the discovery of the fermion triplets, but the test of the MLFV hypothesis. Furthermore, the removed signal makes no big difference regarding the results that we show in the following. We also note here that, in the cases where we identify the leptons before using the reconstruction of the invariant mass of N , we also require at the end that at least one of the two possible reconstructions is inside the range $(\Lambda - 40, \Lambda + 40)$ GeV. This helps us to increase the signal to background ratio.

In order to illustrate the efficiency of this reconstruction procedure, we show in the left panel of Fig. 5.4 the invariant mass $M_{\ell_j j}$ distribution for the signal (empty back histogram) and the background (filled blue histogram), where we have averaged over the two possible combinations with $\ell = \ell_2$ and $\ell = \ell_3$. For this plot we impose the cuts in Eqs. (5.41)–(5.44), before the reconstruction of the E_1^\pm and N states. In the right panel we present the reconstructed invariant mass of the selected combination after the procedure described above. The procedure selects most of the right combination for the E_1^\pm signal peak while efficiently reducing the background, as can be observed in the Figure. In [259] the ambiguity in the assignment of the equal-sign leptons to the heavy lepton or the W decay was resolved associating to the W decay the lepton that leads to the smallest transverse mass

$$M_T^W = \sqrt{2p_T^{\ell_k} \cancel{E}_T (1 - \cos \Phi_{\ell_k \cancel{E}_T})}, \quad (5.47)$$

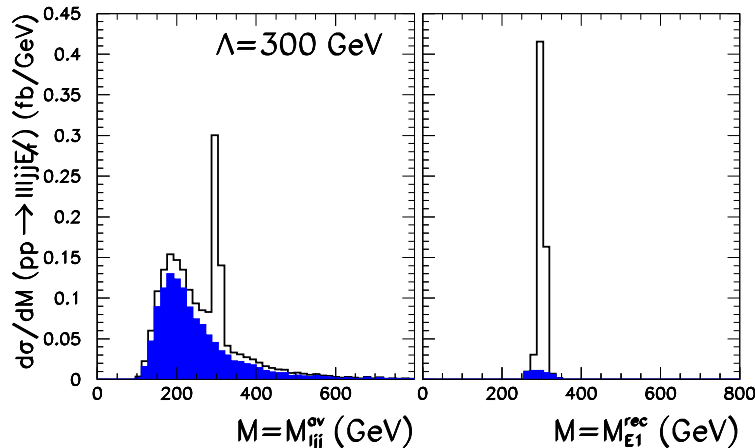


Figure 5.4: Invariant mass distribution $M_{\ell jj}$ for signal (empty back histogram) and background (filled blue histogram). In the left panel we show the distribution averaged over the two possible combinations with $\ell = \ell_2$ or $\ell = \ell_3$ after imposing the initial cuts in Eqs. (5.41)–(5.44) and before the reconstruction of the E_1^\pm and N states. In the right panel we show the E_1^\pm reconstructed invariant mass after the selection procedure described in the text. The Figure is shown for $\Lambda = 300$ GeV and for characteristic values of the neutrino parameters: $\Delta m_{31}^2 = 2.4 \times 10^{-3}$ eV² (NO), $\Delta m_{21}^2 = 7.65 \times 10^{-5}$ eV², $\sin^2 \theta_{23} = 0.5$, $\sin^2 \theta_{12} = 0.304$ and $\sin^2 \theta_{13} = 0.03$ and vanishing values of the phases $\alpha = \delta_{\text{CP}} = 0$ (for these parameters, $\tilde{Y}_e = 0.37$ and $\tilde{Y}_\mu = 0.84$).

where $\Phi_{\ell_k \cancel{E}_T}$ is the angle between the lepton and the missing energy. We verified that this procedure is almost equivalent to ours for high fermion triplet masses Λ . Notwithstanding, for lighter Λ our reconstruction procedure selects more often the correct lepton configuration and after applying the cuts on the invariant masses of N and E_1^\pm it renders a better signal to background ratio. For example, for $\Lambda = 200$ GeV our reconstruction procedure leads to a misidentification probability of 2% while using only the transverse invariant mass ordering this is increased to 12%.

After we apply all the cuts and the reconstruction procedure, the total cross section for the process in Eq. (5.38) can be written as

$$\sigma_0(2 - \delta_{ab})|\tilde{Y}_a|^2|\tilde{Y}_b|^2, \quad (5.48)$$

when we generate events with the flavor combination ab . Most of these events are classified as having the correct flavor combination ab by our selection procedure, nevertheless, a fraction of them are misidentified and labeled ac for $b \neq c$ with a cross section σ_1 . The reason is that in some

5.3. ANALYSIS AND RESULTS

cases we assign wrongly to the fermion triplets a same-sign lepton with a different flavor, which is indeed coming from the W boson decaying from the other heavy fermion. Notice that both classes of events are exclusive, since we reject through the reconstruction procedure events that are compatible simultaneously with the ab and ac flavor combinations. Furthermore, we also need to consider that Eq. (5.38) is not the only signal process leading to the same final state of Eq. (5.40) in the case we have two opposite sign leptons of the same flavor. In this case there are also contributions from:

$$\begin{aligned}
 pp \rightarrow W^\pm \rightarrow N(\rightarrow \nu_m/\bar{\nu}_m Z \rightarrow \nu_m/\bar{\nu}_m \ell_a^+ \ell_a^-) E_1^\pm(\rightarrow \ell_b^\pm Z/h^0 \rightarrow \ell_b^\pm jj), \\
 pp \rightarrow W^\pm \rightarrow N(\rightarrow \nu_m/\bar{\nu}_m Z/h^0 \rightarrow \nu_m/\bar{\nu}_m jj) E_1^\pm(\rightarrow \ell_b^\pm Z \rightarrow \ell_b^\pm \ell_a^+ \ell_a^-).
 \end{aligned}
 \tag{5.49}$$

After summing over the undetectable neutrino type m , and due to the fact that U_{LEP} is an unitary matrix, the cross section for these processes is proportional to $|\tilde{Y}_b|^2$. We thus denote the sum of these cross sections by $\sigma_2|\tilde{Y}_b|^2$. From the corresponding processes, events are classified as aa flavor combination with a cross section $\sigma_3|\tilde{Y}_b|^2$, or as ab with a cross section $(\sigma_2 - \sigma_3)|\tilde{Y}_b|^2$. Therefore, after combining all the possible contributions, the expected signal (S) cross section in each flavor channel is

$$\begin{aligned}
 \sigma_{ee}^S &= (\sigma_0 - \sigma_1) |\tilde{Y}_e|^4 + \sigma_1 |\tilde{Y}_e|^2 |\tilde{Y}_\mu|^2 + \sigma_2 |\tilde{Y}_e|^2 + \sigma_3 |\tilde{Y}_\mu|^2, \\
 \sigma_{\mu\mu}^S &= (\sigma_0 - \sigma_1) |\tilde{Y}_\mu|^4 + \sigma_1 |\tilde{Y}_e|^2 |\tilde{Y}_\mu|^2 + \sigma_2 |\tilde{Y}_\mu|^2 + \sigma_3 |\tilde{Y}_e|^2, \\
 \sigma_{e\mu}^S &= \sigma_1 \left(|\tilde{Y}_e|^4 + |\tilde{Y}_\mu|^4 \right) + 2(\sigma_0 - \sigma_1) |\tilde{Y}_e|^2 |\tilde{Y}_\mu|^2 + (\sigma_2 - \sigma_3) \left(|\tilde{Y}_e|^2 + |\tilde{Y}_\mu|^2 \right), \\
 \sigma_{\text{TOT}}^S &= \sigma_0 \left(|\tilde{Y}_e|^4 + |\tilde{Y}_\mu|^4 + 2|\tilde{Y}_e|^2 |\tilde{Y}_\mu|^2 \right) + 2\sigma_2 \left(|\tilde{Y}_e|^2 + |\tilde{Y}_\mu|^2 \right).
 \end{aligned}
 \tag{5.50}$$

We present in Table 5.1 the different contributions to the signal cross section σ_{ab}^S (in fb), after all the cuts in Eqs. (5.41)–(5.44) and the fermion triplet reconstruction are applied for several values of Λ . As we can see, the bulk of the events passing our cuts originate from correctly reconstructing the desired process in Eq. (5.38), although for the lightest masses considered the events coming from the signal processes in Eq. (5.49) have a sizable contribution. The SM background cross sections σ_{ab}^B are given in Table 5.2. There we can see that the dominant SM background is originating from $WZjj$ production.

Once we have presented all the relevant cross sections after applying the described selection procedure, we are now in a position to evaluate the expected number of signal (S) and background (B) events for the $\ell\ell jj \cancel{E}_T$ topology, with a given flavor combination ab and as a function of the neutrino mass and mixing parameters. This can be directly obtained from Eq. (5.50), Table 5.1, and using the values of the Yukawa couplings in Eqs. (5.17)–(5.22)

$$N_{ab}^{S,B} = \sigma_{ab}^{S,B} \times \mathcal{L} \times \epsilon, \tag{5.51}$$

| Λ (GeV) | σ_0 | σ_1 | σ_2 | σ_3 |
|-----------------|------------|-------------|-------------|-------------|
| 150 | 80.2 | 2.05 | 7.53 | 1.78 |
| 200 | 44.2 | 0.417 | 2.20 | 0.625 |
| 300 | 12.9 | 0.027 | 0.125 | 0.043 |
| 500 | 1.90 | $< 10^{-2}$ | $< 10^{-2}$ | $< 10^{-2}$ |

Table 5.1: Contributions to the signal cross sections (σ_{ab}^S) in fb for the processes $pp \rightarrow \ell^\mp \ell^\pm \ell^\pm j j \cancel{E}_T$ for $\ell = e, \mu$, according to Eq. (5.50) and at 14 TeV. The results are presented for different values of the fermion triplet mass Λ and they do not include the detection efficiencies for the leptons and jets.

| Process | $\Lambda = 150$ GeV | | $\Lambda = 200$ GeV | | $\Lambda = 300$ GeV | |
|-----------------------|-------------------------------------|-------------------|-------------------------------------|-------------------|-------------------------------------|-------------------|
| | $\sigma_{ee}^B = \sigma_{\mu\mu}^B$ | $\sigma_{e\mu}^B$ | $\sigma_{ee}^B = \sigma_{\mu\mu}^B$ | $\sigma_{e\mu}^B$ | $\sigma_{ee}^B = \sigma_{\mu\mu}^B$ | $\sigma_{e\mu}^B$ |
| $pp \rightarrow ttW$ | 0.016 | 0.037 | 0.021 | 0.045 | 0.003 | 0.005 |
| $pp \rightarrow ttZ$ | 0.082 | 0.068 | 0.115 | 0.074 | 0.036 | 0.011 |
| $pp \rightarrow WZjj$ | 1.66 | 1.15 | 1.58 | 0.950 | 0.27 | 0.118 |
| $pp \rightarrow ZZjj$ | 0.04 | 0.022 | 0.046 | 0.028 | 0.006 | 0.002 |
| Total | 1.80 | 1.28 | 1.76 | 1.10 | 0.31 | 0.14 |

Table 5.2: SM background cross sections (σ_{ab}^B) in fb for the processes $pp \rightarrow \ell^\mp \ell^\pm \ell^\pm j j \cancel{E}_T$ with $\ell = e, \mu$ at 14 TeV. The results are presented for different values of the fermion triplet mass Λ and they do not include the detection efficiencies for the leptons and jets.

where \mathcal{L} is the integrated luminosity and $\epsilon = \epsilon^{\ell^3} \times \epsilon^{j^2} = 0.41$ is the detection efficiency for leptons and jets. The number of signal events depends on the value of the fermion triplet mass Λ , as well as on the neutrino parameters, which we denote here by $\vec{\theta} = (\theta_{12}, \theta_{13}, \theta_{23}, \Delta m_{21}^2, \Delta m_{31}^2, \delta)$, and the Majorana phase α . As illustration, we present in Fig. 5.5 the range of predicted number of events in the different flavor combinations for a fermion triplet of mass $\Lambda = 200$ GeV and an integrated luminosity of $\mathcal{L} = 30 \text{ fb}^{-1}$ collected at 14 TeV. The results are shown as a function of the unknown Majorana phase α , while the other neutrino parameters $\vec{\theta}$ are obtained from the global analysis of neutrino data [255]. In the Figure, the left (right) panels correspond to the normal (inverted) neutrino ordering. The ranges are shown for values of $\vec{\theta}$ allowed at 1σ , 2σ , and 99% CL, while the dotted line corresponds to the best fit values. The horizontal dashed lines are the corresponding number of SM background events, as obtained from Eq. (5.51), with cross sections σ_{ab}^B in Table 5.2. It is important to notice from Fig. 5.5 that the two neutrino mass orderings lead to a quite distinct dependence of N_{ee}^S , $N_{\mu\mu}^S$, and $N_{e\mu}^S$ with the Majorana phase α . Given that the SM background is rather small compared to the expected signal, we might be able to determine the

5.3. ANALYSIS AND RESULTS

neutrino ordering by simply comparing the three different number of events for basically all values of α . Furthermore, we could even try to obtain information on the value of α itself. We will go back to this point at the end of the present Section, where we will combine the information from both the present channel and the one we describe in the forthcoming Subsection.

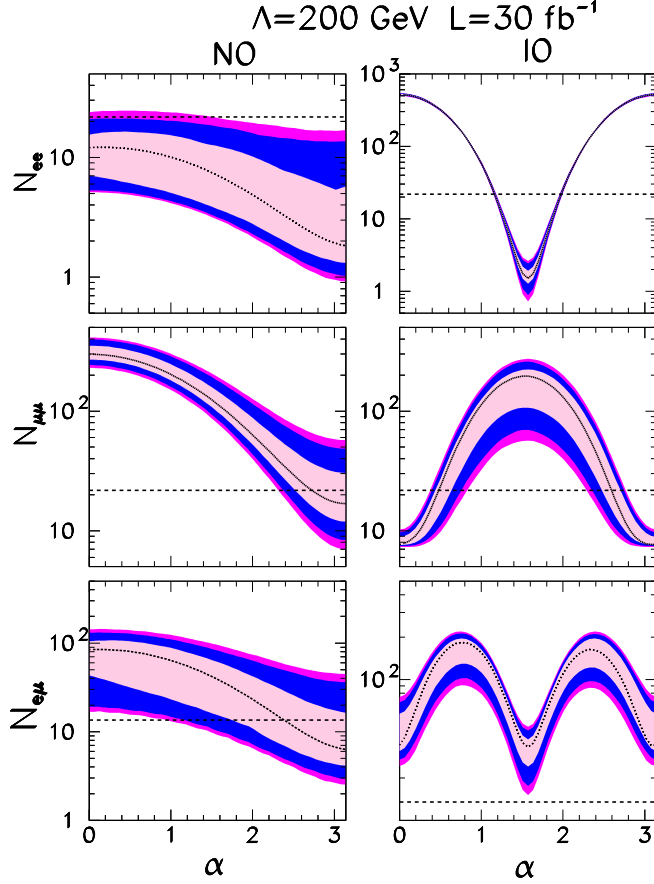


Figure 5.5: Predicted number of events N_{ab} for $pp \rightarrow \ell^\pm \ell^\mp \ell^\mp jj \cancel{E}_T$ with $\ell = e, \mu$, for a fermion triplet of mass $\Lambda = 200$ GeV and with an integrated luminosity of $\mathcal{L} = 30 \text{ fb}^{-1}$ collected at 14 TeV. The horizontal dashed lines are the corresponding number of background events; see Table 5.2. The conventions are the same as in Fig. 5.1.

Next we proceed to estimate the observability of this MLFV model as a function of the fermion triplet mass Λ , as well as the range of the neutrino parameters $\vec{\theta}$, the Majorana phase α and the neutrino ordering. To estimate the significance of the signal we construct a simple χ^2 function in terms of the three signal and background flavor rates for a given value of Λ . In other

words, we define χ^2 as

$$\begin{aligned}\chi^2(\vec{\theta}, \alpha) &= \sum_{ab=ee, e\mu, \mu\mu} \chi_{ab}^2(\vec{\theta}, \alpha), \\ \chi_{ab}^2(\vec{\theta}, \alpha) &= \frac{N_{ab}^S{}^2}{N_{ab}^B} \quad \text{for } N_{ab}^B \geq 10, \\ \chi_{ab}^2(\vec{\theta}, \alpha) &= 2(N_{ab}^S + N_{ab}^B \ln \frac{N_{ab}^B}{N_{ab}^B + N_{ab}^S}) \quad \text{for } N_{ab}^B < 10.\end{aligned}\tag{5.52}$$

These expressions assume a Poisson distribution of the events if the expected number (the one predicted by the SM backgrounds) is below 10, while we use a Gaussian distribution for higher expectations. This is similar to the different statistical analyses that we have performed through the thesis, such as the statistical analysis in Sec. 4.2. In Fig. 5.6 we show the estimated significance of the excess of signal events $pp \rightarrow \ell^\pm \ell^\mp \ell^\mp jj\cancel{E}_T$, for three values of the mass Λ and for $\mathcal{L} = 30 \text{ fb}^{-1}$ at 14 TeV. The significance is obtained as $\#\sigma = \sqrt{\chi^2}$, and it is shown as estimated for the best fit values of $\vec{\theta}$ (dotted lines), and 1σ , 2σ , and 99% CL ranges of $\vec{\theta}$ (filled areas) obtained from the global analysis of neutrino data in [255]. These results are shown as a function of the Majorana phase α and the neutrino ordering. The left (right) panels correspond to the normal (inverted) neutrino ordering. These results could be further extended to other luminosities as long as the number of background events is large enough. In this case, the results for alternative luminosities can be simply obtained by rescaling Fig. 5.6 by a factor $1/\sqrt{\mathcal{L}/30}$. From this rescaling we see that with $\mathcal{L} = 100 \text{ fb}^{-1}$ of 14 TeV LHC data, the LHC could discover/discard the MLFV model using this channel in most of the presently allowed neutrino parameter space for $\Lambda \leq 300 \text{ GeV}$. In some parts of the neutrino parameter space, and in particular if the neutrino masses have IO, where the signals are more promising, the reach could be extended to higher masses or to a pp COM energy $\sqrt{s} = 7 \text{ TeV}$, as we briefly discuss at the end of this Section.

5.3.2 Process $pp \rightarrow \ell\ell jjjj$

We present now the search for type–III see–saw heavy leptons via the processes in Eq. (5.39), *i.e.*

$$pp \rightarrow \ell_1^\mp \ell_2^\pm jjjj, \tag{5.53}$$

with $\ell_{1(2)} = e, \mu$. The most promising characteristic of this process, in relation to the four items we have described in the previous Section, is that it does not present ambiguities in the flavor tagging. This strongly favors the test of the MLFV hypothesis. However, there is a drawback: the process is plagued with a large SM background. The dominant sources of background for the process are:

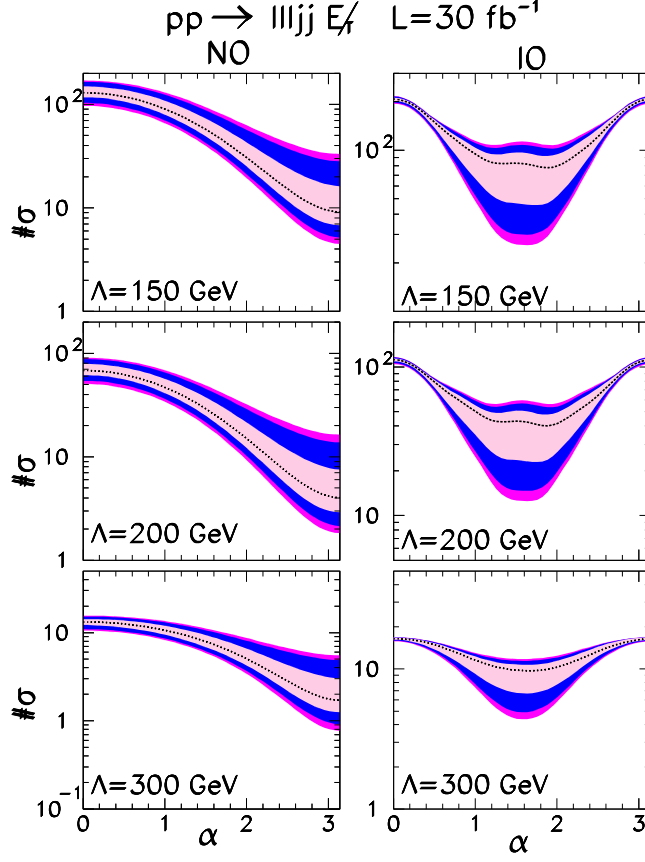


Figure 5.6: Signal significance ($\#\sigma$) in the channel $pp \rightarrow \ell^\pm \ell^\mp \ell^\mp jj \cancel{E}_T$ with $\ell = e, \mu$, for three fermion triplet masses and for an integrated luminosity of $\mathcal{L} = 30 \text{ fb}^{-1}$ collected at 14 TeV. The results are shown as a function of the Majorana phase α and the neutrino ordering, normal (left panel) and inverted (right panel). The rest of conventions are the same than in Fig. 5.1.

- $t\bar{t}jj$ production where the two b 's from the $t, \bar{t} \rightarrow Wb$ decays are identified as jets and both W 's decay leptonically.
- Z^*/γ^*jjjj with the Z^*/γ^* leading to a charged lepton pair. Notice that this process only contributes to the final state with equal flavor leptons.

There are additional background processes that include $t\bar{t}W$ and $t\bar{t}Z$ channels, but after the reconstruction requirements that we impose in the following, they are very much suppressed. Further details for the background sources in the present process can be found in [236, 239]. We use MadGraph5 [86] to simulate these backgrounds, as for the Z^*/γ^*jjjj process

MadGraph5 gives a 20-30% larger value of this background after all the cuts are imposed, as compared to previous versions of MadGraph.

The kinematic analysis starts applying the acceptance and isolation cuts for the final state leptons and jets, as well as the minimum transverse momentum requirements as described in Eqs. (5.41) and (5.42). In the present process, and in contrast to the previous analysis of Eq. (5.40), the signal does not contain any undetectable particle. Thus we require a maximum amount of missing energy in the event

$$\cancel{E}_T < 30 \text{ GeV} . \quad (5.54)$$

In what respects the reconstruction of the triplet fermions, there are six possible ways of grouping the leptons and jets in the final state in two sets of one lepton and two jets. However, since there are not ambiguities on the flavor assignment of the final state leptons, the reconstruction now is simpler than in the previous Subsection. Here we impose that at least one of the six combinations has the two invariant masses inside the fermion triplet mass region

$$\Lambda - 40 \text{ GeV} < M_{\ell jj} < \Lambda + 40 \text{ GeV} . \quad (5.55)$$

In addition, to increase the signal to background ratio, we further impose that the corresponding invariant masses of the two jet pairs verify

$$M_W - 10 \text{ GeV} < M_{jj} < M_H + 10 \text{ GeV} . \quad (5.56)$$

After the reconstruction of the invariant masses of the two fermion triplets, the SM backgrounds are still large, in particular the one arising from $Z^*/\gamma^* jjjj$. Consequently, to further reduce this background we make use of the fact that in the signal the characteristic invariant mass of the two leptons is larger than for the background, as illustrated in Fig. 5.7. In the present channel the background is reduced by a factor 20–8 for $\Lambda = 150\text{--}500 \text{ GeV}$ after we impose that the invariant mass of the two charged leptons verify

$$M_{\ell^+\ell^-} > 100 \text{ GeV} . \quad (5.57)$$

After all the reconstruction procedure is applied, and since there is no ambiguity in the assignment of the two charged leptons, the total cross section of the process in Eq. (5.39) is simply given by

$$\sigma_{ab}^S = \sigma_4(2 - \delta_{ab})|\tilde{Y}_a|^2|\tilde{Y}_b|^2 . \quad (5.58)$$

We present in Table 5.3 the cross sections for the signal and the SM backgrounds after the cuts in Eqs. (5.41), (5.42), (5.54)–(5.57) are applied. The predicted number of events for the fermion triplet signals in this channel, for the different flavor combinations, can be easily obtained from Eq. (5.51),

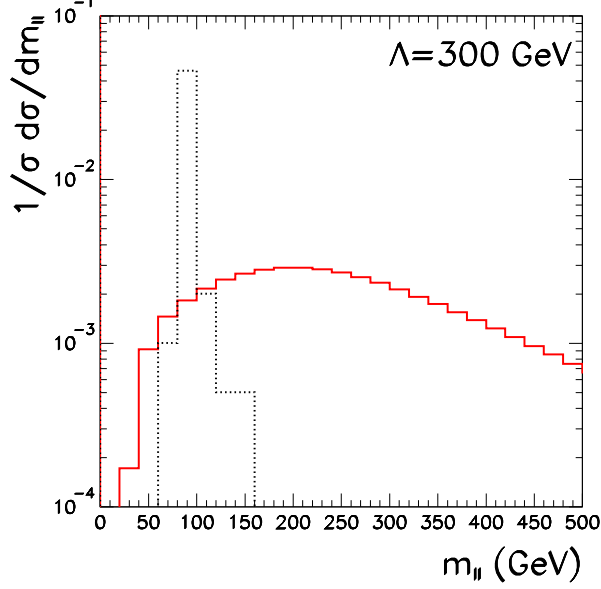


Figure 5.7: Distribution of the charged lepton pair invariant mass for the signal with $\Lambda = 300$ GeV (solid red histogram) and Z^*/γ^*jjjj background (dotted black histogram) of the process in Eq. (5.53). The distributions are shown after cuts in Eqs. (5.41), (5.42), (5.54)–(5.56) are imposed.

| $\Lambda(\text{GeV})$ | Signal (fb) | Background (fb) | |
|-----------------------|-------------|--|-------------------------------------|
| | σ_4 | $ttjj$ | Z^*/γ^*jjjj |
| | | $\sigma_{ee}^B = \sigma_{\mu\mu}^B = \sigma_{e\mu}^B/2.$ | $\sigma_{ee}^B = \sigma_{\mu\mu}^b$ |
| 150 | 276.0 | 6.0 | 29.3 |
| 200 | 216.0 | 9.7 | 33.2 |
| 300 | 74.9 | 0.89 | 4.6 |
| 500 | 11.3 | 0.018 | 0.057 |

Table 5.3: Signal and background cross sections at 14 TeV for $pp \rightarrow \ell_a^\mp \ell_b^\pm jjjj$, after the cuts in Eqs. (5.41), (5.42), (5.54)–(5.57) are applied, for different values of the fermion triplet mass Λ . These results do not include detection efficiencies for leptons and jets.

Table 5.3, and using the values of the Yukawa couplings in Eqs. (5.17)–(5.22) and a detection efficiency of $\epsilon = \epsilon^{j^4} \times \epsilon^{\ell^2} = 0.26$. We plot in Fig. 5.8 the range of the expected number of events in the different flavor combinations as a function of the unknown Majorana phase α , for a fermion triplet of mass $\Lambda = 500$ GeV, and an integrated luminosity of $\mathcal{L} = 30 \text{ fb}^{-1}$ collected at 14 TeV. The ranges are shown at 1σ , 2σ , and 99% CL from the global analy-

sis of neutrino data [255], while the dotted line corresponds to the best fit values. The left (right) panels correspond to the normal (inverted) neutrino ordering, while the horizontal dashed lines stand for the predicted number of SM background events. As it happened in Fig. 5.5, we can also see here that the dependence of N_{ee}^S , $N_{\mu\mu}^S$, and $N_{e\mu}^S$ on the CP violating Majorana phase α is quite distinct for the normal and the inverted neutrino orderings.

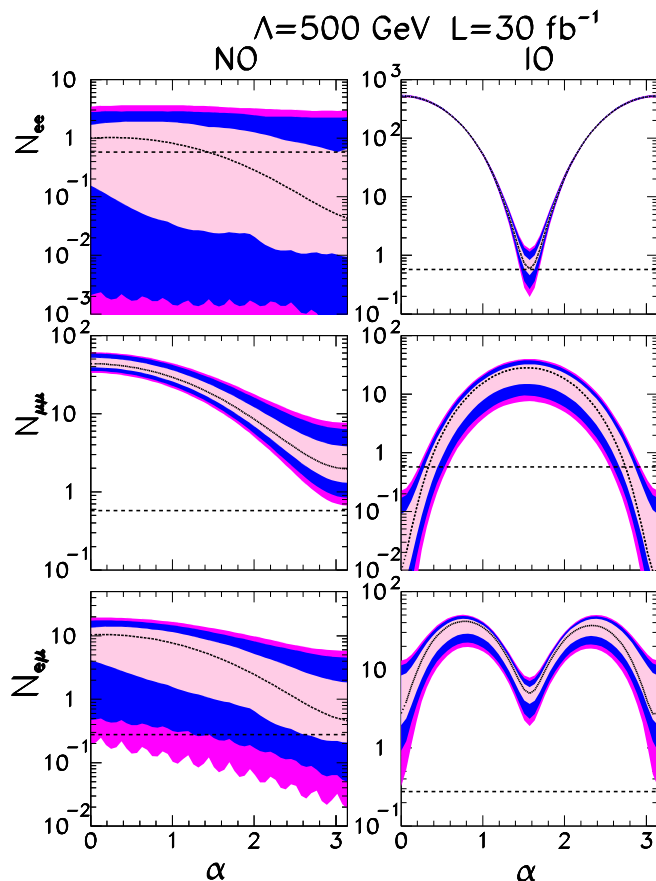


Figure 5.8: Predicted number of events N_{ab} for $pp \rightarrow \ell_a^\pm \ell_b^\mp jjjj$, for a fermion triplet of mass $\Lambda = 500$ GeV with an integrated luminosity of $\mathcal{L} = 30$ fb^{-1} collected at 14 TeV. The horizontal dashed lines are the corresponding number of background events, see Table 5.3. The conventions are the same as in Fig. 5.1.

Next we proceed to estimate the potential that the LHC has to observe the fermion triplets in this channel. Like in the previous analysis, we add the flavor combinations to define the signal significance and we follow the statistical analysis in Eq. (5.52). The observability of the MLFV type-III see-saw model in the $\ell l j j j j$ channel is depicted in Fig. 5.9. There we show

5.3. ANALYSIS AND RESULTS

the signal significance as a function of the Majorana phase α for different CL of the neutrino parameters. If we compare Figs. 5.6 and 5.9 we can see that, after the background reduction achieved by the mass reconstruction conditions, Eqs. (5.55) and (5.56), and the lepton pair invariant mass cut in Eq. (5.57), the channel $\ell\ell jjjj$ offers better potential statistical sensitivity for the discovery or exclusion of this MLFV model in particular for heavier masses Λ , despite its still larger SM backgrounds. One must keep in mind, however, that the final attainable precision depends on the systematic background uncertainties, which are expected to be larger for this channel [236].

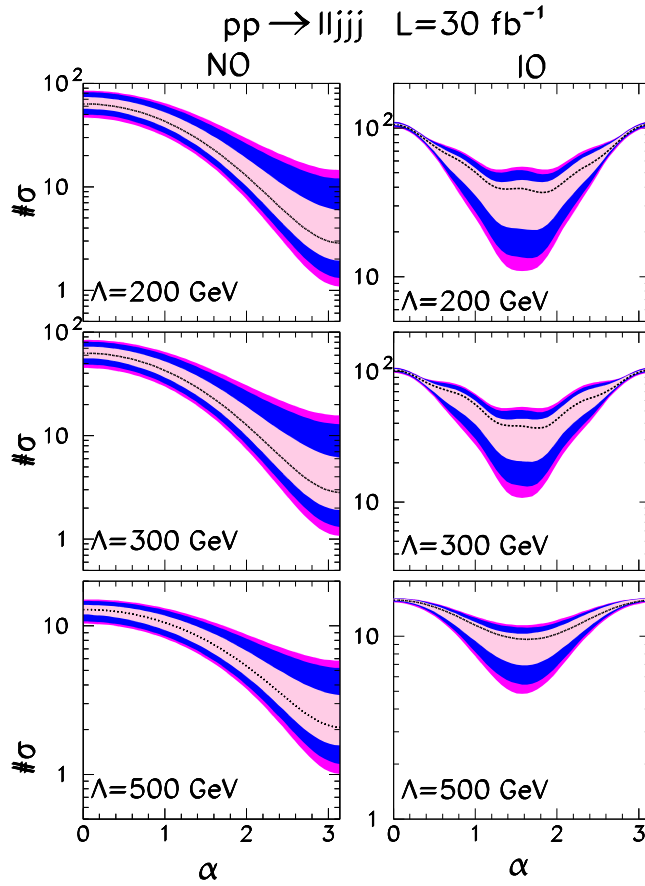


Figure 5.9: Expected significance $\#\sigma$ of signal versus background events for $pp \rightarrow \ell_a^\pm \ell_b^\mp jjjj$, for three fermion triplet masses, and for an integrated luminosity of $\mathcal{L} = 30 \text{ fb}^{-1}$ collected at 14 TeV. The conventions are the same as in Fig. 5.1.

We have observed that the prospects for the discovery of the fermion triplets are promising in both channels for a sizable range of light masses, below $\Lambda \lesssim 500 \text{ GeV}$. While the process in Eq. (5.40) is more suitable for

the lighter masses, the process in Eq. (5.53) covers better the heavier mass range. In both cases we have concluded that the observability of the partners strongly depends on the neutrino ordering and the Majorana phase. In the following we study how we can use this dependence to decipher this ordering and the unknown CP -violating phase.

5.3.3 Accessing the unknown lepton parameters

As we have commented, one can see from Figs. 5.5 and 5.8 that the two neutrino orderings lead to a very distinct dependence of N_{ee}^S , $N_{\mu\mu}^S$, and $N_{e\mu}^S$ as a function of α for both final states. It is particularly striking the upper right panels that present a very narrow range for the ee flavor combination for IO and a fixed value of α . Thus one could expect to be able to discriminate between the inverted and the normal ordering of the neutrino masses studying the correlations between the different flavor combinations, for a large fraction of the values of the unknown phase α . One could even try to determine the value of this phase.

In order to illustrate this point, we perform a statistical analysis combining the information from the two channels we have presented in detail in this Chapter, the processes in Eqs. (5.40) and (5.53). For this final analysis we assume that the observed number of events in the three flavor combinations, for both $pp \rightarrow \ell\ell jj\cancel{T}$ and $pp \rightarrow \ell\ell jjjj$, are those predicted for a given mass Λ (assumed to be independently determined) in the NO for the best fit values of oscillation parameters $\bar{\theta}_b$ and for some fixed value of the Majorana phase $\bar{\alpha}$, plus the expected background events, *i.e.*

$$N_i^{\text{obs}}(\bar{\theta}_b, \bar{\alpha}) = N_i^S(\bar{\theta}_b, \bar{\alpha}) + N_i^B, \quad (5.59)$$

where $i = 1, 6$ correspond to ee , $e\mu$, and $\mu\mu$ for the two processes. In order to reconstruct the ordering and value of $\bar{\alpha}$, we fit those six rates N_i^{obs} in either NO or IO with different values of $\vec{\theta}$ (within their 95% CL allowed region from oscillations) and α . In order to do so we define a new χ^2

$$\begin{aligned} \chi_{\min}^2(\alpha) &= \min_{\vec{\theta} \in 95\% \text{CL}} \sum_{i=1,6} \chi_i^2(\vec{\theta}, \alpha), \quad (5.60) \\ \chi_i^2(\vec{\theta}, \alpha) &= \frac{\left[N_i^S(\vec{\theta}, \alpha) + N_i^B - N_i^{\text{obs}}(\bar{\theta}_b, \bar{\alpha}) \right]^2}{N_i^{\text{obs}}(\bar{\theta}_b, \bar{\alpha})} \quad \text{for } N_i^{\text{obs}}(\bar{\theta}_b, \bar{\alpha}) \geq 10, \\ \chi_i^2(\vec{\theta}, \alpha) &= 2 \left[N_i^S(\vec{\theta}, \alpha) + N_i^B - N_i^{\text{obs}}(\bar{\theta}_b, \bar{\alpha}) \right. \\ &\quad \left. + N_i^{\text{obs}}(\bar{\theta}_b, \bar{\alpha}) \ln \frac{N_i^{\text{obs}}(\bar{\theta}_b, \bar{\alpha})}{N_i^S(\vec{\theta}, \alpha) + N_i^B} \right] \quad \text{for } N_i^{\text{obs}}(\bar{\theta}_b, \bar{\alpha}) < 10. \end{aligned}$$

Here we have assumed again a Poisson or a Gaussian distribution depending on whether the number of assumed observed events are large enough.

5.3. ANALYSIS AND RESULTS

We plot in Fig. 5.10 $\chi_{\min}^2(\alpha)$ for three values of $\bar{\alpha} = 0, \frac{\pi}{2}, \text{ and } \pi$ (full, dotted and dashed lines). The way to read the Figure is the following. A

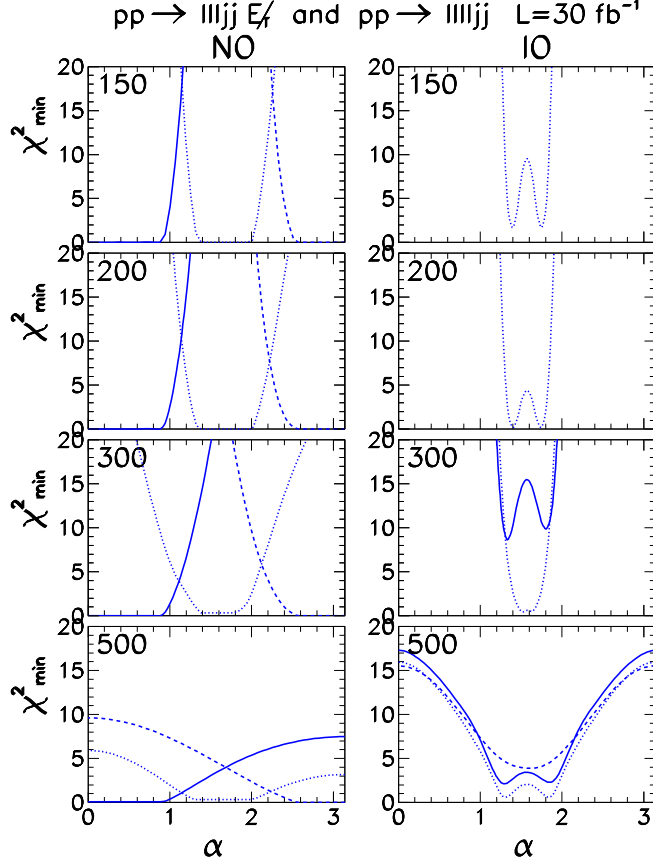


Figure 5.10: $\chi_{\min}^2(\alpha)$ defined in Eq. (5.60). The full, dotted and dashed lines correspond to a simulated value of the observed event rates in NO, for best fit values of oscillation parameters and $\bar{\alpha} = 0, \frac{\pi}{2}, \pi$ respectively. Whenever one of the curves do not appear in the right panels it is because the corresponding $\chi_{\min}^2(\alpha) > 20$ for all values of α , see the text for details.

given neutrino ordering and value of the Majorana phase are compatible with the assumed observed events at a $\sqrt{\chi_{\min}^2} \times \sigma$ CL. As an example, if one looks at the $\Lambda = 200$ GeV case, for the assumed values $\bar{\alpha} = 0$, and $\bar{\alpha} = \pi$ there is no value of the measured mixing neutrino parameters inside their 95% CL regions that give a $\chi_{\min}^2(\alpha)$ compatible at a CL below $\sqrt{20}\sigma$ for any Majorana phase for the IO case. For the assumed observed events corresponding to $\bar{\alpha} = \frac{\pi}{2}$, there is a small region around $\alpha = \frac{\pi}{2}$ that is compatible at better than 2σ CL for the IO case. On the other hand, for the panels in the left, which correspond to the NO, $\chi_{\min}^2(\alpha)$ clearly presents a minimum for $\alpha = \bar{\alpha}$.

This is true for any of the plotted Λ masses. Hence the panels on the right show for which cases the event rates simulated could also be predicted by IO with a somewhat different value of α . Whenever one of the curves do not appear in the right panels it is because the corresponding $\chi_{\min}^2(\alpha) > 20$ for all values of α . Figure 5.10 illustrates that for masses $\Lambda \lesssim 200$ GeV it is possible to discriminate between NO and IO except for $\bar{\alpha} \sim \frac{\pi}{2}$, where a narrow range of α 's in IO still gives a compatible χ^2 . Furthermore, in those cases for which the discrimination between NO and IO is possible, one also obtains information on the value of $\bar{\alpha}$, that could be constrained on a small range close to the real value. As the mass increases, it becomes harder to disentangle IO and NO. For the highest mass considered, 500 GeV, for any value of simulated $\bar{\alpha}$ there is always a value of α for which the expected rates in IO mimic the simulated ones in NO at better than $\sim 2\sigma$.

Present LHC limits on type–III see–saw models

In the original publication [222] we presented the prospective LHC reach for the initial 7 TeV run after applying the analysis we have described. The details can be found in [222] where it was concluded that the discovery of the new heavy fermions would be possible in a significant range of α for masses $\Lambda \lesssim 200$ GeV.

Indeed after the 7 and 8 TeV LHC runs have finished, parts of the collected data sets have been analyzed in the search for fermion triplet partners in type–III see–saw realizations [260, 261]. These analyses have been performed in general type–III see–saw models, but the obtainable exclusion limits can also be translated to cover a small part of the MLFV type–III see–saw parameter space.

The CMS search [260] was the first analysis of any LHC experimental collaboration looking for type–III see–saw signals. There, CMS analyzed the 4.9 fb^{-1} of 7 TeV collected data in the search for a fermion triplet resonance. They studied the final state that consists of three leptons ($\ell_1^+ \ell_2^+ \ell_3^-$) and missing energy. This analysis is then suitable for the production of $pp \rightarrow W^+ \rightarrow N(\rightarrow \ell_a^\mp W^\pm) E_2^+(\rightarrow \nu W^+)$ in the MLFV type–III see–saw realization. There, after the leptonic decays of the W bosons, the process leads to the three–leptonic final state with missing transverse energy that CMS studied. The analysis was performed for three different flavor mixing scenarios between the new triplets and the SM leptons. In the first case the fermion triplets were assumed to decay with the same rate to the three SM lepton families, e , μ and τ . This setup can be approximated in the MLFV realization assuming the best fit values for the leptonic mixing parameters, together with the inverted neutrino ordering and a Majorana phase close to $\frac{\pi}{4}$ or $\frac{3\pi}{4}$. After accounting for the differences in the branching ratios between the model considered in the experimental reference and the MLFV case, and neglecting the minor contributions from other new signal chan-

5.4. CONCLUSIONS

nels, we can conclude that for these points in the parameter space, partners around $\Lambda \simeq 180$ GeV have already been excluded at 95% CL by the CMS search. In the second case CMS assumes new fermion partners that only couple to muons. In our MLFV setup, this can be approximately accomplished, neglecting in the final state the contributions from heavy fermions decaying to τ 's or e 's, with best fit values for the measured mixing parameters, and an inverted neutrino ordering with $\alpha \simeq \frac{\pi}{2}$ or alternatively a normal neutrino ordering with Majorana phase $\alpha \simeq 0$. In these cases the exclusion bounds reach values around $\Lambda \simeq 200$ GeV. Finally, the third case considered in [260] assumes fermion partners that only couple to electrons. This scenario can be approximately obtained with best fit values for the measured neutrino mixing parameters, inverted neutrino ordering and $\alpha \simeq 0$ or π . In these cases the excluded 95% CL region goes up to values approximately above $\Lambda \simeq 200$.

A similar analysis was performed by the ATLAS collaboration in [261]. In this case 5.8 fb^{-1} of 8 TeV collected data were analyzed in the search for fermion partners in the context of type-III see-saw theories. In the ATLAS study, a final state with 4 leptons was analyzed. This channel can receive contributions from the MLFV process $pp \rightarrow W^\pm \rightarrow N(\rightarrow \ell_a^\mp W^\pm) E_1^\pm(\rightarrow \ell^\pm Z)$ when the Z boson decays also leptonically. The results in this case were presented for a heavy fermion triplet that decays roughly with the same rate to electrons and muons while it does not decay to τ 's. Neglecting the contributions of minor signal processes to the same channel, and neglecting also the contributions to the final state of possible decays of the heavy triplets to τ 's, as well as taking into consideration the differences between the assumed branching ratios, this setup could be approximately accomplished in the MLFV model with best fit values for the measured neutrino parameters and an inverted neutrino ordering with Majorana phase around $\frac{\pi}{4}$ or $\frac{3\pi}{4}$. For these points of the model parameter space, heavy partners are excluded at 95% CL up to masses around 250 GeV, a bound which is a bit more stringent than the CMS one.

As a conclusion, we note that the precise translation of the experimental bounds requires a more involved analysis of the concrete models and branching ratios assumed in the experimental searches. Nevertheless, here it suffices to state that for specific points of the parameter space, the MLFV type-III see-saw model has already been probed at the LHC up to masses around 200 – 250 GeV.

5.4 Conclusions

The LHC has been built with the aim of testing the physics of the TeV scale. The experimental observation of neutrino masses and mixing in oscillation experiments was an unambiguous first evidence of physics BSM [220]. Con-

sequently there is a natural question to ask: could the LHC say something about the origin of the neutrino masses? We have devoted this Chapter to seek for an answer to this question.

The first challenge we have faced is the fact that the tiny neutrino masses are related in the most common NP models to new extremely heavy partners, clearly out of the LHC reach. Nevertheless, based on the construction shown in [221], we have described a consistent TeV model for the generation of the neutrino masses that could lead, in addition, to measurable LHC signals. The MLFV type–III see–saw model contains fermion triplet partners that could live at the TeV scale, while the neutrino masses are related to the tiny total lepton number violation that has a very high energy scale associated. This separation of scales is accompanied in the model by a highly predictive flavor composition of the heavy partner couplings to the SM leptons due to the MLFV hypothesis, as shown in Figs. 5.1, 5.5 and 5.8. The final picture of the model is then a realization that contains TeV states, which can be produced at the LHC in the type–III case, and that lead to testable flavor signals.

Focusing on the phenomenology, we have first observed that, in contrast to regular type–III see–saw models, in the MLFV realization there are neither relevant total lepton number violating signals nor displaced vertices. Thus, the observation of triplet partners with or without any of these signals would help to test the MLFV realization, and the very hierarchical scale scenario that is associated to it. Second, the total lepton number conserving (but lepton flavor violating) signals can instead be measured in channels accomplishing a few points, necessary to test the MLFV hypothesis. This is one of the key purposes of the Chapter, besides the discovery of the partners, and it constrains us to look for final states where the flavor composition of the leptons decaying from the heavy partners can be tagged. After taking into consideration as well the signal to background ratios, we are led to make collider analyses of $pp \rightarrow \ell\ell jj\cancel{E}_T$ and $pp \rightarrow \ell\ell jjjj$ channels.

In both cases we have analyzed the signal of type–III see–saw models with MLFV taking into account the constraints emanating from low energy neutrino experiments. We have presented our results as a function of the Majorana phase α for the best fit and 1σ , 2σ , and 99% CL neutrino parameter ranges obtained from the global analysis of neutrino data [255]. After careful analyses of the signal and SM backgrounds we have established that mass scales of the order of 300 GeV can be probed in the $\ell\ell jj\cancel{E}_T$ channel, see Fig. 5.6. This channel presents a lesser SM background, but the reconstruction of the flavor composition of the final state is a challenge to test the MLFV hypothesis.

Conversely we have found that the $\ell\ell jjjj$ final state can be the best discovery channel at the LHC for fermion triplets with the heaviest masses of the range considered if its larger SM backgrounds are well understood, which is the biggest challenge of the channel. The easier flavor tagging of

5.4. CONCLUSIONS

the final state leptons allows mass scales of the order of 500 GeV to be accessed, see Fig. 5.9. Moreover, once a signal of a type-III see-saw model with MLFV is observed, its energy scale Λ can be precisely determined by measuring the mass of the new heavy fermions; as an illustration see Fig. 5.4.

Finally we have observed that the discovery at the LHC of the fermion triplets predicted by the MLFV type-III see-saw model is not only important for unraveling the mechanism responsible for the tiny observed neutrino masses, but it may also allow for the determination of the ordering of these neutrino masses, given the highly predictive signals the MLFV hypothesis leads to. In fact, the ratio of the flavor combinations ee , $\mu\mu$, and $e\mu$ can discriminate between inverted and normal ordering as we can see from Figs. 5.5, 5.8 and 5.10, especially for the lightest masses considered in the present Chapter.

Chapter 6

Summary: an amazing outlook

We are living a fascinating era in particle physics with the LHC pushing humanity to an energy frontier that we had not been able to directly explore before. In particular, one of the goals of the LHC is to guide us towards understanding the mechanism behind the generation of masses, as the collider is directly accessing for the first time ever the TeV scale, where the first EWSB signatures were expected to lay. Indeed, the discovery of the Higgs boson after the first two years of LHC operation has been a major scientific event, partially satisfying the high expectations in the community and giving us hope for progress on this program.

In this dissertation we have studied the potential that the LHC has to address some questions associated with the mechanism responsible for the generation of masses. We point the reader to Sections 2.5, 3.3, 4.4 and 5.4 for a detailed description of the main results that we have obtained. In this final chapter we present an overview of the main conclusions and outlook.

In Chapter 2 we have presented an effective Lagrangian approach to the Higgs couplings. In this first analysis we have assumed that the Higgs boson is part of an $SU(2)_L$ doublet and that EWSB is linearly realized. One of the most important conclusions we have obtained is related to the guiding principle in the analysis. We have shown that, currently, there is enough data arising from the LHC Higgs results, also from Tevatron searches, from TGV measurements at LEP, Tevatron and LHC, and in addition from EW precision low energy experiments, to make a robust data-driven analysis. We have presented a study based on a bottom-up approach in which the number of theoretical assumptions has been minimized. This analysis has led to relevant bounds on the dimension-six operators, as well as to very interesting correlations between different experimental sources of data. The philosophy of the approach has now been followed by different authors in posterior analyses.

From the global analysis of Higgs, TGV and EWPD, we have concluded that, currently, the measurements point to a SM-like observed particle, as after analyzing the 7 and 8 TeV LHC data sets there is no hint for deviations from the SM behavior in the EWSB sector.

The third main conclusion from Chapter 2 is the interesting complementarity that exists between the Higgs results and the TGV measurements when constraining the anomalous dimension-six operators. We have concluded that the current level of precision on the operators reachable from both types of experimental searches are at the same level. This allows for a further test of the nature of the discovered state, as in the linear realization any deviation in one of the sectors would directly relate to a deviation in the other. Indeed once the whole 8 TeV data sets are analyzed to measure TGV interactions, the combination of both Higgs and TGV measurements has the potential to furnish the strongest bounds on NP on the EWSB sector.

The effective Lagrangian approach based on the linear realization of the SM gauge symmetry has been compared to alternative Lagrangian expansions in Chapter 3. There, we have studied the non-linear or chiral effective Lagrangian expansion. This expansion is suitable, for instance, for models with strong dynamics, where the Higgs boson is a bound state of a global symmetry at a high energy scale. We have observed that both the linear and the non-linear expansions are structurally different, since in the non-linear case the lesser symmetry impositions are translated into more possible invariant operators, which furthermore follow a different ordering. This leads to testable phenomenological consequences that may allow to disentangle the Higgs nature.

First, we have seen that in the non-linear expansion there are important decorrelations between different couplings, that are instead correlated on the linear case. In particular, we have concluded that the interesting correlation between Higgs analyses and TGV measurements highlighted above, may disappear in the chiral Lagrangian. We have shown how a global analysis of the available experimental data can serve us to test this decorrelation, and in consequence, the ultimate Higgs nature. For that we have defined the proper discriminating variables and we have presented the first six-parameter global fit in the context of the non-linear expansion from the analysis of EWPO, TGV and Higgs data. The second type of disentangling signals are related to signatures which come from leading operators in one expansion, while they are originated from subleading operators in the alternative one. In particular, we have concluded that the observation of a TGV anomalous operator, historically parametrized with the coefficient g_5^Z (λ_Z), would point to a non-linear (linear) realization of the symmetry.

Thus we have found that, in both the linear and the non-linear expansions the study of TGV interactions can play a very important role in order to decipher the mechanism behind EWSB. With this motivation we have presented in the second part of Chapter 3 a realistic collider analysis of the

LHC capability to measure anomalous TGV interactions. Using the historical TGV parametrization we have shown that variables related to the event collision energy trace well the enhancement that the anomalous interactions would cause in the distributions, increasing as a consequence the reachable sensitivity. We have concluded that the optimization of the searches with respect to these transverse momentum and invariant mass variables improves the LHC reach on the anomalous TGV's. After estimating the LHC expectations at 7, 8 and 14 TeV, we have concluded that the LHC has the potential to increase the present existing bounds on all the different anomalous TGV's, in many cases simply after considering the— yet to be completely analyzed— initial data sets. As we have commented, particularly interesting are the cases of g_1^Z and κ_Z TGV's, as both (and the related κ_γ) are involved in the correlation between Higgs data and TGV measurements exploited in the linear effective Lagrangian analysis. In addition, the LHC can increase the g_5^Z and λ_Z current sensitivities, what could be translated into interesting conclusions regarding the nature of the Higgs boson.

In the second part of the thesis we have complemented this model independent approach with the direct search for new states related to several of the BSM extensions connected to the origin of masses. This complementary approach could be a faster track to NP depending on what is the real nature of the EWSB sector, something that hopefully we could understand in the near future.

Chapter 4 is devoted to study the LHC capabilities to observe and analyze spin-1 resonances that couple to EW gauge boson pairs. These are common new vector resonances in many BSM completions describing EWSB, as they are assumed to be responsible for the unitarization of the longitudinal gauge boson scattering in several theories. Instead of relying on a specific model, we have performed the analyses in a model independent way leaving as free parameters the main properties of the new state: *i.e.* its mass, its width and the relevant coupling strength to weak bosons and light fermions. In the first part of the Chapter we have studied the possibility of determining the spin of a charged (W') and of a neutral (Z') spin-1 resonance analyzing the EW pair production channels in fully leptonic final states at the 14 TeV LHC. There, the sensitivity for W' is higher than for Z' , as in the later case the presence of two neutrinos in the final state becomes a challenge for the reconstruction of the signal. Nevertheless, we have concluded that after defining the proper angular variables and the corresponding asymmetries, constructed from the final state lepton momenta, the determination of the spin of these hypothetical new vector resonances is possible for a sizable range of couplings, masses and widths of the new states.

Given the lack of experimental analyses for a Z' that couples to EW gauge boson pairs, we have devoted the second part of the Chapter to determine which are the current exclusion bounds on Z' 's after combining both the ATLAS and CMS 7 TeV available data sets on EW boson pair

production. We have presented a realistic collider analysis using as much information as possible from the experimental searches. After considering the proper invariant mass and transverse momentum variables we have combined the available information in a binned log-likelihood fit. From this combination we have concluded that new neutral vector resonances are excluded for a sizable region of the relevant parameter space up to the multi-TeV range, reaching values close to ~ 3 TeV. These results represent the strongest available bounds on neutral vector resonances within the model-independent approach considered.

On a different path, over the last two decades, neutrino oscillation experiments have shown beyond doubt the existence of neutrino masses and leptonic mixing. These results can not be explained in the SM, a clear experimental sign of NP BSM in the mass sector. We have devoted the final Chapter of this dissertation, Chapter 5, to study the potential of the LHC to address the physics of some extension of the SM built to account for the generation of the observed pattern of neutrino masses and mixing.

The first conclusion we have obtained is that consistent neutrino mass generation models can be built with observable signals at the TeV scale. In particular, we have considered a MLFV hypothesis applied to a type-III see-saw model in order to allow for sizable LHC signals. Besides the large hierarchy of scales that is necessary in order for the TeV model to be consistent, we have observed that the heavy partners that are introduced, two charged heavy leptons and one quasi-Dirac neutral heavy state, present a very interesting phenomenology. The signatures of the considered model are characterized, in the first place, by a lack of total lepton number violating signals, which are instead common in other TeV type-III see-saw models. Secondly, the decays of the new heavy leptons do not lead to measurable displaced vertices, in contrast again with alternative type-III see-saw realizations. The observation of heavy lepton partners with any of these signatures would point against MLFV see-saw models. Finally, the third signature is related to the observable total lepton number conserving (but lepton flavor violating) signals. In this case the couplings of the new heavy leptons to the SM charged leptons and neutrinos can be predicted, up to irrelevant normalization constants, from the known neutrino masses and mixing parameters. This allows for the study of the signals of the production of these heavy states in order to test and exploit the MLFV hypothesis, using the results of a global fit to the neutrino data, and, conversely, to analyze what could be inferred about some of the still unknown parameters of the neutrino sector in the event of an observation of such signals.

With this aim we have studied the 14 TeV LHC potential to observe signals coming from the heavy lepton partners in the $pp \rightarrow \ell\ell jj\cancel{E}_T$ and $pp \rightarrow \ell\ell jjjj$ channels. We have found that the distribution of the signal events in terms of the flavor of the final state leptons has a striking dependence on the unknown Majorana phase and neutrino ordering. Combining the

results from both channels we have concluded that the LHC running at 14 TeV could test the MLFV type-III see-saw heavy partners up to masses around 500 GeV depending on the unknown Majorana CP -violating phase and the neutrino ordering. As a consequence of this same dependence and after constructing the proper statistical tools, we have concluded that for the lightest masses considered, ~ 200 GeV, and for part of the neutrino mixing space, the observation of the neutrino partners would allow for the determination of the neutrino ordering and for an estimation of the unknown phase.

In summary the LHC 7 and 8 TeV runs have served to establish the existence of a new particle that seems related to the EWSB mechanism, opening the possibility of directly testing the EWSB sector. From the analyses of the Higgs, TGV and EWPD we have concluded that there are no hints so far for deviations with respect to the SM in the EWSB sector. This fact added to the many experimental exclusion bounds on a large variety of new resonances of several BSM extensions set the current picture: the SM is standing- with no sign of weakness- the LHC challenge. The message we extract is clearly positive. We have a better understanding of EWSB thanks to the LHC operation, and, as we have shown, the prospects for the future run are encouraging, given the potential that the LHC has to both measure the Higgs properties as well as to observe many of the new resonances predicted in the different EWSB extensions, and also in neutrino mass generation models.

So we would like to close this dissertation with this positive message. We are living an amazing era with a collider facility that is opening an unexplored range of energies, there its research can bring light to the open mysteries of matter.

Resumen

En marzo de 2010 se registraron las primeras colisiones a 7 TeV de energía en el centro de masas en el *Gran Acelerador de Hadrones* (LHC) del CERN. Esta fecha marcó el inicio del fascinante programa de investigación del LHC. Desde entonces su funcionamiento ha ido mejorando rápidamente y, después de solventar los difíciles retos ineludibles para un acelerador de tal magnitud, el período inicial de registro de colisiones tuvo su cénit en lo que es, sin lugar a dudas, el mayor éxito hasta la fecha en su operación: el descubrimiento del bosón de Higgs, anunciado el 4 de julio de 2012 [1, 2]. Tal hito culminó casi 50 años de investigación desde que se postuló la existencia del bosón de Higgs [3–8]. Su descubrimiento es, esperamos, el primero de los acontecimientos históricos asociados con la operación del LHC. La observación y el estudio de la primera partícula que parece directamente relacionada con la rotura de la simetría electrodébil, y, por lo tanto, con el origen del patrón observado de las masas de las partículas elementales, como explicaremos en breve, dibujan las primeras huellas de una nueva era en física de partículas. Indudablemente el futuro que se abre ante nosotros, con el LHC a punto de duplicar prácticamente su energía de operación, es prometedor.

El contenido de esta tesis se fue fraguando contemporáneamente al primer período de operaciones del LHC. De este modo, además de la disertación puramente científica, nos gustaría que esta tesis transmitiera al lector parte de la alegría e inspiración que los acontecimientos científicos que sucedieron durante su desarrollo causaron en su autor y en sus colaboradores científicos. Con este espíritu entusiasta, durante los diferentes Capítulos describimos el papel fundamental que pueden desempeñar los datos recogidos en el LHC para ayudarnos a entender varios de los misterios que yacen sin explicación en la física de altas energías. En este contexto único, el LHC puede sin duda guiarnos a través de un largo viaje, hacia el pasado más lejano, al origen de las masas.

El modelo estándar de física de partículas es la teoría que describe matemáticamente las diferentes interacciones de todas las partículas elementales conocidas. Durante años el modelo estándar fue capaz de explicar con éxito cada una de las nuevas medidas experimentales que se iban tomando, con una precisión única en muchos casos. De esta forma, el modelo

estándar es extensamente aceptado como una teoría extraordinaria, cuya formulación ha servido históricamente para predecir la existencia de varias de las partículas que posteriormente se han observado experimentalmente. ¿Es el descubrimiento del nuevo bosón el último de los logros del modelo estándar? Gran parte de la tesis versa en torno a esta pregunta, pero antes merece la pena describir de manera cualitativa el contexto histórico que precedía al inicio de las operaciones del LHC.

El modelo estándar fue construido basándose en el principio de invarianza ante simetrías locales (gauge) como uno de sus pilares básicos. Esta teoría cuántica de campos, cuya descripción matemática es invariante bajo el grupo $SU(3)_C \times SU(2)_L \times U(1)_Y$, es capaz así de describir las diferentes interacciones observadas de las fuerzas fundamentales: la fuerza nuclear fuerte, la fuerza nuclear débil y la fuerza electromagnética, dejando la fuerza gravitatoria al margen. Sin embargo, con las partículas conocidas antes del descubrimiento del bosón de Higgs¹, no era posible construir un término invariante bajo $SU(3)_C \times SU(2)_L \times U(1)_Y$ que sirviese para generar y describir en este contexto las masas de las partículas observadas (al menos en su realización lineal). En otras palabras, la simetría electrodébil debía estar rota. De esta forma, los diferentes bosones y fermiones descubiertos, que eran masivos según indicaban las medidas experimentales, no podían tener masa en nuestra descripción teórica simétrica. Sin el bosón de Higgs además, esta carencia estaba asociada con otros problemas de matiz teórico. Por ejemplo, introduciendo las masas observadas de una forma *ad hoc* en la teoría esta no era renormalizable. Además, el crecimiento con la energía de la amplitud de colisión de varios de los bosones existentes acababa dando lugar a la violación de unitariedad a una escala de energías relativamente cercana, el TeV. En otras palabras, nuestra descripción matemática parecía fallar cuando extendíamos su rango de validez a energías por encima del TeV.

El bosón de Higgs del modelo estándar fue propuesto como la solución más simple para explicar la rotura de la simetría electrodébil. La adición de una única nueva partícula escalar, que sea parte de un doblete de $SU(2)_L$ y cuyo potencial desarrolle un valor esperado del vacío, causa la rotura espontánea de la simetría gauge electrodébil. Esto es suficiente para generar las masas de los bosones de gauge observados. Si además introducimos en la teoría términos de Yukawa, que hacen interaccionar este nuevo doblete con los fermiones, conseguimos explicar también la generación de masas de estos últimos, con la posible excepción de los neutrinos, los fermiones más ligeros, cuya peculiar existencia trataremos más adelante. Por lo tanto, el bosón de Higgs del modelo estándar, que completaría lo que hoy en día conocemos

¹A lo largo de la tesis nos referimos como bosón de Higgs a la partícula recientemente descubierta, independientemente de su última naturaleza, ya sea el bosón del modelo estándar o no.

como modelo estándar, es capaz de dar cuenta del patrón observado de las masas de las partículas, mientras que al mismo tiempo mantiene al modelo estándar invariante bajo su grupo de gauge, consiguiendo también que la teoría sea renormalizable. El bosón de Higgs consigue solventar además el peligroso crecimiento energético de los diferentes procesos de colisión de los bosones de gauge longitudinales, manteniendo la descripción matemática, ahora sí, válida hasta energías arbitrariamente elevadas. Recapitulando entonces, antes del inicio de la operación del LHC el bosón de Higgs era la única pieza que faltaba por descubrir en el modelo estándar, con la cual, esta fascinante teoría estaría estructuralmente completa.

Por otro lado, y pese a ser la más simple de ellas, el bosón de Higgs del modelo estándar no es la única explicación posible para la generación de masas y la relacionada rotura de la simetría electrodébil. De hecho, la adición del bosón de Higgs no es la más satisfactoria desde el punto de vista teórico, ya que da lugar al bien conocido “problema de jerarquías” que describiremos en breve. Estas limitaciones sirvieron de motivación para la construcción de descripciones alternativas con el objetivo de explicar la rotura de la simetría electrodébil. Estas descripciones, generalmente llamadas teorías más allá del modelo estándar (o extensiones del modelo estándar) contienen normalmente estados adicionales, algunos de ellos parecidos al bosón de Higgs del modelo estándar. En algunas de estas teorías las nuevas partículas son las encargadas de solventar el papel que una sola resonancia, el bosón de Higgs, juega en el modelo estándar. En cualquier caso, independientemente del mecanismo considerado, y ya sea con o sin una partícula parecida al bosón de Higgs, dado que varios de los procesos de colisión rompen la unitariedad a una energía relativamente moderada, la expectativa general era que algún nuevo fenómeno tenía que observarse en el LHC.

Afortunadamente el descubrimiento de un nuevo fenómeno no se hizo esperar. En julio de 2012 la observación de una nueva partícula fue anunciada, tan solo con dos años de análisis de colisiones en el LHC, un acelerador que además estaba funcionando aproximadamente a *solo* la mitad de la energía para la que fue inicialmente diseñado. Como hemos dicho, el descubrimiento del bosón de Higgs culmina lo que parecía una interminable espera, pero lo que es más importante, el descubrimiento del bosón marca, al mismo tiempo, el inicio de un nuevo programa de investigación. Después de su descubrimiento hay varias preguntas obvias que debemos responder para entender el origen de las masas de las partículas conocidas y la naturaleza del estado descubierto. ¿Es este el bosón de Higgs del modelo estándar? ¿O es en realidad uno de los estados similares en alguna de las extensiones propuestas del modelo estándar? ¿Está siquiera el nuevo estado relacionado con la rotura de la simetría electrodébil y el origen de las masas observadas? La búsqueda de una respuesta a estas preguntas ha servido como una de las motivaciones principales para la tesis que aquí presentamos.

Análisis con Lagrangianos efectivos

En el contexto descrito, el estudio y la medida de las propiedades de la partícula descubierta: su espín, su paridad, o la manera en la que interacciona con el resto de estados conocidos, son un primer paso imprescindible para intentar descifrar si el nuevo estado es en realidad el bosón de Higgs predicho en el modelo estándar. Los estudios experimentales iniciales [9, 10] indican que la nueva partícula parece ser un bosón escalar y con paridad CP -par, básicamente como se esperaría si fuese el bosón de Higgs del modelo estándar. Además, considerando como interacciona con los bosones de gauge, WW y ZZ , y teniendo en cuenta los primeros análisis realizados justo después de su descubrimiento (como por ejemplo el análisis presentado en los primeros Capítulos de esta tesis), parece que la nueva partícula está directamente conectada a la rotura de la simetría electrodébil. Esto quiere decir que ahora, y por primera vez, podemos estudiar directamente el mecanismo responsable del origen de las masas de las partículas a través del análisis de las propiedades del estado recientemente descubierto. Con este objetivo dedicamos los Capítulos iniciales de esta tesis a intentar buscar respuesta a las preguntas anteriormente planteadas. El trabajo que aquí presentamos busca entender la naturaleza del nuevo estado, y en concreto se centra en el estudio de los acoplamientos del bosón de Higgs al resto de partículas, así como en las relacionadas auto-interacciones de los bosones de gauge.

Con el objetivo de estudiar los acoplamientos del estado recientemente descubierto, como una posible ruta de acceso directo al sector de la rotura de la simetría electrodébil, hay que considerar las diferentes maneras posibles de enfrentar los datos experimentales existentes con las diferentes descripciones teóricas propuestas. En lugar de centrarnos en una única de estas descripciones, preferimos realizar un acercamiento independiente del modelo, de forma que los resultados obtenidos sean aplicables al mayor número de teorías posibles. En esta tesis los datos disponibles son siempre uno de los pilares básicos que utilizamos como guía en los análisis, mientras que al mismo tiempo intentamos reducir al mínimo los prejuicios teóricos. Para ello la metodología más adecuada es el uso de Lagrangianos efectivos [11–13].

El uso de Lagrangianos efectivos permite parametrizar de forma genérica efectos de nueva física que se espera que se manifiesten directamente a una escala de energías Λ , que es más alta que la escala a la que los experimentos se realizan. Simplemente especificando las partículas incluidas en la teoría y las simetrías que esta respeta a bajas energías es posible extender el Lagrangiano del modelo estándar con operadores que están suprimidos por potencias de la escala de altas energías y que parametrizan los efectos de nueva física a la escala energética del experimento.

En la primera parte de esta tesis aplicamos el uso de Lagrangianos efec-

tivos al estudio de las propiedades del bosón de Higgs. Más concretamente, en los Capítulos 2 y 3 de la tesis estudiamos los acoplamientos de la partícula recientemente descubierta utilizando Lagrangianos efectivos.

La expansión lineal

En el Capítulo 2 de la tesis estudiamos la aplicación de Lagrangianos efectivos al sector del Higgs, asumiendo que la partícula observada forma parte de un doblete de $SU(2)_L$, y que por lo tanto, la simetría electrodébil se implementa linealmente en el Lagrangiano. Este Capítulo se basa en los trabajos publicados en [15–18]. Esta expansión es la adecuada para diferentes extensiones del modelo estándar donde el Higgs es un estado elemental, como, por ejemplo, en teorías supersimétricas.

En nuestro análisis utilizamos todos los datos disponibles y hacemos un especial énfasis en usarlos como principal guía del estudio. En particular, la elección de la base de operadores independientes que se utiliza está determinada por los datos existentes, evitando así el prejuicio teórico hacia ningún modelo específico. Concretamente, en el análisis utilizamos todos los datos disponibles de los diferentes estudios experimentales del Higgs recolectados por el LHC en sus operaciones a 7 y a 8 TeV, así como también los análisis del Higgs en Tevatron. Utilizamos también las medidas del vértice con tres bosones de gauge en el LHC, Tevatron, y LEP (las que son, todavía a día de hoy, más precisas). Finalmente, incluimos también la información de las medidas de alta precisión de procesos electrodébiles realizadas en LEP y a bajas energías. Todas estas fuentes de datos son estudiadas para analizar los acoplamientos del observado bosón de Higgs. Y para ello construimos las herramientas estadísticas adecuadas.

La primera conclusión que obtenemos del estudio está relacionada con el principio que utilizamos de guía en el análisis. En la tesis demostramos que actualmente ya hay una variedad de datos suficiente para realizar un análisis consistente y guiado por los datos. Los resultados dan lugar a límites interesantes en los coeficientes de los nuevos operadores, generando además importantes correlaciones comprobables experimentalmente. Utilizar como guía los datos experimentales sirve también para identificar más fácilmente qué señales en concreto tienen un mayor poder para constreñir qué coeficientes, y para cuál se espera una mejora más substancial en las siguientes fases de operación del LHC. Esta “filosofía” ha sido seguida con posterioridad por diferentes grupos.

Desde el punto de vista cuantitativo, el análisis nos sirve para concluir que la partícula descubierta se parece mucho al bosón de Higgs del modelo estándar, ya que después de analizar los sets de datos recogidos a 7 y a 8 TeV no hay ninguna indicación de una posible desviación respecto al comportamiento esperado en el modelo estándar.

Finalmente, la tercera gran conclusión del análisis del Capítulo 2 es

la complementariedad entre los datos de producción y desintegración del Higgs y las medidas del vértice con tres bosones de gauge a la hora de constreñir los nuevos operadores. Concluimos que en la actualidad ambos tipos de experimentos dan lugar a límites con una precisión similar, pero con distintas correlaciones. De este modo, testear la correlación entre los dos sectores es posible, y servirá en el futuro para caracterizar la naturaleza última del bosón de Higgs, ya que en la realización lineal la observación de una hipotética desviación en uno de los dos sectores tiene que ir acompañada de una desviación en el otro.

Descripciones alternativas

En el Capítulo 3 hacemos uso también de Lagrangianos efectivos, pero sin asumir que la partícula observada es un escalar fundamental y que forma parte de un doblete de $SU(2)_L$. Este Capítulo se basa en las publicaciones [94,97], y la principal diferencia con el Capítulo anterior es que ahora asumimos una expansión no lineal (*i.e.* quirral) de la simetría gauge en el Lagrangiano efectivo. Esta expansión es adecuada para la familia de extensiones del modelo estándar donde el Higgs no es un estado elemental, sino un estado compuesto de una teoría que contiene un sector de la rotura de la simetría electrodébil con interacciones fuertes. En consecuencia, la naturaleza de esta expansión es diferente al caso lineal, dando lugar a posibles desviaciones fenomenológicas relevantes. Nuestro análisis se centra en la comparación entre la fenomenología de la expansión lineal y la de la no lineal, y de cómo podrían distinguirse en el LHC.

La comparación de ambas expansiones, que son estructuralmente diferentes, da lugar a diferencias que dividimos en dos grupos. Por un lado, al no asumir que el bosón de Higgs es parte de un doblete, la expansión no lineal contiene un número mayor de posibles operadores, lo que al final se traduce en más parámetros libres que en la expansión lineal o, en otras palabras, en decorrelaciones entre acoplamientos que se encuentran correlacionados en la expansión lineal. En concreto, la correlación entre los acoplamientos del Higgs y los vértices con tres bosones de gauge que hemos estudiado en detalle en el Capítulo anterior, podría perderse en la expansión no lineal. De esta forma la medida de dicha (de)correlación nos podría ayudar a saber si el bosón de Higgs observado es un estado elemental o es un estado más complejo como en modelos con un Higgs compuesto. Para ello hemos propuesto algunas variables que permiten cuantificar esta (de)correlación y, además, hemos realizado el primer análisis general existente en la literatura utilizando la base de operadores no lineales. La segunda clase de diferencia se debe a que operadores que pueden ser de primer orden en una de las expansiones son de un orden superior y, por lo tanto, menos relevantes en la expansión alternativa. Este es el caso, por ejemplo, de alguno de los acoplamientos anómalos en el vértice con tres bosones de gauge.

Las conclusiones de ambos análisis, el lineal y el no lineal, nos indican la importancia que tiene estudiar en detalle el vértice con tres bosones de gauge. Con esta motivación estudiamos la parametrización histórica que las colaboraciones experimentales utilizan para estudiar el vértice WWZ . La primera conclusión que extraemos es que las variables cinemáticas relacionadas con la energía de la colisión elemental permiten caracterizar los diferentes acoplamientos anómalos que pueden aparecer en los vértices con tres bosones de gauge. Así que, después de optimizar los análisis con los cortes más adecuados, estimamos qué sensibilidad se puede alcanzar en la determinación de estos acoplamientos anómalos utilizando el LHC, a 7, a 8 y también a 14 TeV. De este análisis concluimos que el LHC tiene capacidad para incrementar la precisión sobre todos los acoplamientos anómalos del vértice triple con respecto a los límites pre LHC, en algunos casos simplemente cuando se usen los sets de datos ya existentes a 7 y a 8 TeV. Esta conclusión es especialmente importante para los acoplamientos anómalos que dan lugar a la correlación entre los análisis del Higgs y las medidas del vértice de tres bosones de gauge, tal y como hemos comentado, así como para el caso de los acoplamientos anómalos cuya observación nos ayudaría a entender la naturaleza del observado bosón de Higgs ya que aparecen a primer orden solo en una de las dos expansiones.

Buscando nuevas partículas

Alternativamente al uso de Lagrangianos efectivos, la observación o exclusión de nuevas partículas esperadas en muchas de las extensiones del modelo estándar es una manera complementaria de estudiar el mecanismo responsable de la rotura de la simetría electrodébil y de la generación de masas. Su observación es posible si estas nuevas partículas tienen masas dentro del alcance del LHC. En este caso el reto es diseñar y estudiar las técnicas de análisis que permitan cubrir de la forma más exhaustiva posible la gran variedad de nuevas partículas, y a este propósito dedicamos la segunda parte de la tesis.

Partículas asociadas a la rotura de la simetría electrodébil

En el Capítulo 4 (basado en las publicaciones [185, 186]) nos centramos en la posible observación y caracterización de partículas vectoriales que están relacionadas con la rotura de la simetría electrodébil en una variedad de extensiones del modelo estándar. En particular, analizamos y optimizamos el potencial que tiene el LHC para observar y estudiar resonancias que están relacionadas comúnmente con el restablecimiento de la unitariedad en los procesos de colisión de bosones de gauge. Para ello nos centramos en el estudio de partículas que interactúan con pares de bosones electrodébiles, WW y WZ . Unas pocas suposiciones genéricas son suficientes para realizar

un análisis de colisiones realista en el LHC, cuyas conclusiones son de este modo aplicables a un gran rango de teorías y resonancias, ya que mantenemos en todo momento el análisis lo más independiente del modelo posible, en coherencia con el mismo espíritu de los dos Capítulos anteriores de la tesis. De este modo, en un primer análisis estudiamos diferentes variables angulares y asimetrías que permitan determinar el espín de una hipotética nueva partícula W' o Z' . Esta determinación del espín se consigue comparando las distribuciones de estas hipotéticas partículas vectoriales con hipótesis escalares, como el bosón de Higgs. La conclusión a la que llegamos es que la determinación del espín es posible para un gran rango de acoplamientos, masas y anchuras de decaimiento de las nuevas partículas vectoriales.

Después de estimar el potencial del LHC para esta determinación del espín, que se extiende hasta la escala del multi-TeV, pasamos a derivar cuáles son los actuales límites que hay sobre algunas de estas resonancias vectoriales después de los datos recolectados a 7 TeV. La motivación de este estudio surge de que la búsqueda de resonancias neutras de espín 1 que decaen a pares de bosones de gauge electrodébiles no ha sido realizada todavía por las colaboraciones experimentales del LHC. Nuestro objetivo es, por lo tanto, limitar la existencia de nuevos Z' utilizando los resultados publicados pero no analizados en este contexto. Así pues, realizamos un análisis utilizando toda la información pública sobre estados finales relevantes acumulada por ATLAS y CMS. Combinando ambos sets de datos concluimos que estas hipotéticas resonancias neutras de espín 1 están excluidas en una región considerable del espacio de parámetros que estudiamos, alcanzando los límites masas de casi 3 TeV. Estos límites que derivamos son de hecho los más fuertes de entre todos los existentes, considerando resonancias con características similares a las estudiadas. Como detallamos, el LHC tiene un increíble potencial para descubrir y excluir este tipo de resonancias de espín 1, mejorando consecuentemente nuestra capacidad de entender la rotura de la simetría electrodébil.

Nuevas partículas y la masa de los neutrinos

Hasta este punto solo hemos estudiado la capacidad que tiene el LHC para buscar explicaciones al misterio que hay detrás de la rotura de la simetría electrodébil y, por lo tanto, al origen de las masas observadas en el modelo estándar. Sin embargo, el origen de la rotura de la simetría electrodébil no es el único misterio relacionado genéricamente con el origen de las masas que permanece abierto. Cuestiones como la naturaleza de la materia oscura, o la asimetría materia-antimateria observada en el universo, o la extrema ligereza de los neutrinos, están lejos de ser entendidas. Es en esta última cuestión, el origen de las masas de los neutrinos, en la que enfocamos la última parte de la tesis.

En el modelo estándar, incluso después de incluir el bosón de Higgs, los neutrinos siguen siendo partículas sin masa. Esto es así porque no se puede construir un término de masas renormalizable mientras solo incluyamos en el modelo los estados necesarios para explicar las interacciones. En consecuencia, la observación del patrón de masas y mezclas de los neutrinos en los experimentos de oscilación de estos mismos es una prueba irrefutable de que hay física más allá del modelo estándar. Si a esta necesidad le añadimos el impresionante potencial del LHC, nos abocamos directamente a una pregunta obvia, ¿podría ser el LHC útil también para entender el origen de las masas de los neutrinos? Esta pregunta motiva el estudio que presentamos en el Capítulo 5 de esta tesis, y que está basado en la publicación [222].

Para intentar dar respuesta a esta pregunta, el primer reto que se nos plantea es el de construir un modelo consistente y que además de generar las masas de los neutrinos, dé señales que puedan ser observadas en la escala del TeV, la escala hasta la que tiene acceso el LHC. Normalmente una masa tan pequeña para los neutrinos se origina en los modelos más simples debido a la introducción de nuevas partículas extremadamente pesadas y, por lo tanto, claramente fuera del alcance del LHC. Sin embargo, una de las primeras conclusiones que sacamos es que es posible construir modelos consistentes que permiten explicar la ligereza de los neutrinos y que podrían dar señales en el LHC. Estas señales presentan la forma de nuevas partículas, nuevos compañeros pesados de los neutrinos que podrían ser producidos en el LHC. El modelo que presentamos contiene varias características adicionales interesantes. Además de la carencia de estados finales observables que violen el número leptónico total, o de vértices desplazados en los detectores, las señales observables, que conservan el número leptónico total, presentan una característica prometedora desde un punto de vista fenomenológico. Y es que en el modelo que estudiamos la interacción de las nuevas partículas con los estados conocidos en el modelo estándar, leptones y bosones de gauge, se puede predecir directamente a partir del patrón de mezcla observado en el sector leptónico, es decir, en los experimentos de oscilación de neutrinos. Esto supone que las señales en el LHC son altamente predecibles y, por lo tanto, el modelo podría ser testado. Para ello realizamos el último de los análisis de colisiones en el LHC de esta tesis y, de hecho, concluimos que la observación de estos nuevos compañeros pesados de los neutrinos no es solo posible en el LHC para un rango de masas y valores de mezcla considerable, sino que su hipotética observación podría ayudar a extender nuestro conocimiento sobre la matriz de mezcla en el sector leptónico.

Cerrando ya el resumen de la tesis podemos concluir que los análisis a 7 y 8 TeV del LHC nos han servido para establecer la existencia de una nueva partícula que parece relacionada con el mecanismo responsable de la rotura de la simetría electrodébil, abriendo, por lo tanto, la posibilidad de testear directamente este mecanismo. De los análisis de datos del Higgs,

pero también de las medidas experimentales del vértice con tres bosones de gauge y de medidas de alta precisión a bajas energías de observables electrodébiles, hemos concluido que con la precisión existente actualmente no hay ninguna desviación significativa respecto al comportamiento esperado en el modelo estándar. Además, después de los dos primeros años de operación del LHC, los muchos análisis experimentales realizados han excluido una gran variedad de nuevas partículas correspondientes a diferentes extensiones del modelo estándar. Es decir, el modelo estándar está demostrando la misma impresionante concordancia con los datos que ha demostrado durante las últimas décadas y experimentos. La lectura que hacemos del momento actual es claramente positiva. Como esperamos haber demostrado a lo largo de la tesis, el futuro que nos aguarda es prometedor, dado el potencial que tiene el LHC tanto para medir las propiedades del bosón de Higgs como para observar muchas de las resonancias predichas en varias de las extensiones del modelo estándar, que pretenden explicar tanto la rotura de la simetría electrodébil como el origen de las masas de los neutrinos. Con este mensaje tan positivo nos encantaría concluir esta tesis. Estamos viviendo una era fascinante con un acelerador que está abriendo a nuestros ojos un rango de energías que nunca antes había sido explorado. Sin lugar a dudas el LHC puede alumbrarnos el largo camino en la búsqueda de respuestas a los misterios sobre el origen de las masas.

List of Figures

| | | |
|-----|---|-----|
| 2.1 | $\Delta\chi^2$ dependence on the fit parameters | 43 |
| 2.2 | $\Delta\chi^2$ dependence on the Higgs branching ratios and production cross sections | 46 |
| 2.3 | 95% and 99% CL allowed regions in the plane $f_{WW} \times f_{BB}$ when we fit the Higgs collider data | 47 |
| 2.4 | 68%, 90%, 95%, and 99% CL allowed regions in the plane $f_g \times f_{\Phi,2}$ when we fit the Higgs collider and TGV data | 48 |
| 2.5 | 68%, 90%, 95%, and 99% CL allowed regions in the plane $\sigma_{gg}^{\text{ano}}/\sigma_{gg}^{\text{SM}} \times \text{Br}(h \rightarrow \gamma\gamma)^{\text{ano}}/\text{Br}(h \rightarrow \gamma\gamma)^{\text{SM}}$ when we fit the Higgs collider and TGV data | 49 |
| 2.6 | 68%, 90%, 95%, and 99% CL allowed regions in the plane $f_{\text{bot}} \times f_g$ when we fit the Higgs collider and TGV data | 50 |
| 2.7 | 95% CL allowed regions on the plane $\Delta\kappa_\gamma \otimes \Delta g_1^Z$ | 55 |
| | | |
| 3.1 | $\Delta\chi^2$ dependence on the coefficients of the bosonic operators from the analysis of all Higgs collider data | 78 |
| 3.2 | A BSM sensor irrespective of the type of expansion and a non-linear versus linear discriminator | 81 |
| 3.3 | Normalized spectra for the SM and the anomalous TGV's for $pp \rightarrow \ell^+ \ell'^- \cancel{E}_T$ and $pp \rightarrow \ell'^\pm \ell^+ \ell^- \cancel{E}_T$ | 89 |
| 3.4 | Distribution of events with respect to p_T^Z for the 7 and 14 TeV runs | 96 |
| | | |
| 4.1 | Signal and background cross sections for the $\ell^+ \ell^- \ell'^\pm \cancel{E}_T$ final state, and ranges of the parameters allowing for a 5σ observation of a W' at 14 TeV | 109 |
| 4.2 | $\cos \theta_{\ell\ell}^*$ and $\cos \theta_{WZ}^{\text{ave}}$ distributions for the production of a charged vector resonance W' and a charged scalar one | 112 |
| 4.3 | $\cos \theta_{\ell\ell}^* \otimes \cos \theta_{WZ}^{\text{ave}}$ spectrum for W' , and $\cos \theta_{\ell\ell}^* \otimes \cos \theta_{WW}^{\text{MAOS-OR++}}$ spectrum for Z' | 114 |
| 4.4 | Parameter space region where the W' spin can be determined at 99% CL using the asymmetry $A_{\ell\ell}$ for an integrated luminosity of 100 fb^{-1} collected at 14 TeV | 115 |

| | | |
|------|---|-----|
| 4.5 | Integrated luminosity required for the 5σ discovery and 99% CL spin determination of W' and Z' as a function of the vector resonance couplings at 14 TeV | 116 |
| 4.6 | Reconstructed WW invariant mass distributions for $pp \rightarrow Z' \rightarrow W^+W^- \rightarrow \ell^- \ell^+ \cancel{E}_T$ | 120 |
| 4.7 | Signal and background cross sections for the $\ell^+ \ell'^- \cancel{E}_T$ final state, and regions of the ranges of the parameters for a 5σ observation of a Z' at 14 TeV | 121 |
| 4.8 | $\cos \theta_{ll}^*$ and $\cos \theta_{WW}^{\text{MAOS-OR++}}$ distributions for the production of a neutral vector resonance and a neutral scalar one | 123 |
| 4.9 | Parameter space region where the Z' spin determination can be performed at 99% CL using the asymmetry $A_{\ell\ell}$ for an integrated luminosity of 100 fb^{-1} at 14 TeV | 125 |
| 4.10 | Transverse mass distribution of the contributions to the process $pp \rightarrow \ell^+ \ell'^- \cancel{E}_T$ and leading lepton transverse momentum of the contributions to the same process | 129 |
| 4.11 | 2σ exclusion limits on the production of a Z' from our analysis of the M_T distribution measured by ATLAS | 135 |
| 4.12 | 2σ exclusion limits on the production of a Z' from our analysis of the p_T^{leading} distribution measured by CMS | 136 |
| 4.13 | 2σ exclusion limits on the production of a Z' from our combined analysis of the measured M_T distribution in ATLAS and the p_T^{leading} distribution measured by CMS | 137 |
| 5.1 | Allowed ranges of the Yukawa couplings $ \tilde{Y}_e ^2 \equiv Y_1 ^2/y^2$ and $ \tilde{Y}_\mu ^2 \equiv Y_2 ^2/y^2$ obtained from the global analysis of neutrino data | 151 |
| 5.2 | Cross sections for the fermion triplet pair production, and maximum decay length of the fermion triplets | 154 |
| 5.3 | Invariant mass distribution of the two possible opposite-sign equal-flavor lepton pairs for the signal $pp \rightarrow \ell_1^\mp \ell_2^\pm \ell_3^\pm jj \cancel{E}_T$ | 160 |
| 5.4 | Invariant mass distribution $M_{\ell jj}$ for signal and background | 162 |
| 5.5 | Predicted number of events for $pp \rightarrow \ell^\pm \ell^\mp \ell^\mp jj \cancel{E}_T$ with an integrated luminosity of $\mathcal{L} = 30 \text{ fb}^{-1}$ collected at 14 TeV | 165 |
| 5.6 | Signal significance ($\#\sigma$) in $pp \rightarrow \ell^\pm \ell^\mp \ell^\mp jj \cancel{E}_T$ for an integrated luminosity of $\mathcal{L} = 30 \text{ fb}^{-1}$ collected at 14 TeV | 167 |
| 5.7 | Distribution of the charged lepton pair invariant mass for the signal and $Z^*/\gamma^* jjjj$ background | 169 |
| 5.8 | Predicted number of events for $pp \rightarrow \ell_a^\pm \ell_b^\mp jjjj$ with an integrated luminosity of $\mathcal{L} = 30 \text{ fb}^{-1}$ collected at 14 TeV | 170 |
| 5.9 | Significance ($\#\sigma$) of the signal in $pp \rightarrow \ell_a^\pm \ell_b^\mp jjjj$ for an integrated luminosity of $\mathcal{L} = 30 \text{ fb}^{-1}$ collected at 14 TeV | 171 |
| 5.10 | $\chi_{\text{min}}^2(\alpha)$ distribution for simulated values of the observed event rates in NO | 173 |

List of Tables

| | | |
|-----|--|-----|
| 2.1 | Results included in the analysis for the Higgs decay modes, except for $\gamma\gamma$ results | 34 |
| 2.2 | $H \rightarrow \gamma\gamma$ results from ATLAS | 34 |
| 2.3 | $H \rightarrow \gamma\gamma$ results from CMS | 35 |
| 2.4 | Weight of each production mechanism for the different $\gamma\gamma$ categories in the 7 and 8 TeV ATLAS analyses | 36 |
| 2.5 | Weight of each production mechanism for the different $\gamma\gamma$ categories in the 7 and 8 TeV CMS analyses | 37 |
| 2.6 | Best fit values and 90% CL allowed ranges for the combination of Higgs and TGV data | 45 |
| 3.1 | Effective couplings parametrizing the VW^+W^- vertices | 71 |
| 3.2 | The trilinear Higgs–gauge boson couplings | 72 |
| 3.3 | 90% CL allowed ranges of the coefficients of the operators contributing to Higgs data and to TGV measurements | 76 |
| 3.4 | Compilation of available limits on the anomalous TGV interactions | 83 |
| 3.5 | Cross sections for the process $pp \rightarrow \ell^+ \ell'^- \cancel{E}_T$ and $pp \rightarrow \ell'^{\pm} \ell^+ \ell^- \cancel{E}_T$ after the corresponding cuts are applied | 87 |
| 3.6 | Attainable 2σ bounds on anomalous TGV's at the LHC at 7 TeV with 1 fb^{-1} | 90 |
| 3.7 | Values of the cross section predictions for the process $pp \rightarrow \ell'^{\pm} \ell^+ \ell^- \cancel{E}_T$ after applying all the selection cuts | 95 |
| 3.8 | Expected sensitivity on $g_5^Z, g_4^Z, \tilde{\kappa}_Z$ and $\tilde{\lambda}_Z$ at the LHC | 97 |
| 3.9 | Values of the sign–weighted cross section at 14 TeV for $g_4^Z, \tilde{\kappa}_Z$ and $\tilde{\lambda}_Z$ | 99 |
| 4.1 | Overall multiplicative factors used to tune the simulator | 128 |
| 5.1 | Contributions to the signal cross sections for the process $pp \rightarrow \ell^\mp \ell^\pm \ell^\pm j j \cancel{E}_T$ at 14 TeV | 164 |
| 5.2 | SM background cross sections for the process $pp \rightarrow \ell^\mp \ell^\pm \ell^\pm j j \cancel{E}_T$ at 14 TeV | 164 |

| | | |
|-----|---|-----|
| 5.3 | Signal and background cross sections at 14 TeV for $pp \rightarrow \ell_a^\mp \ell_b^\pm jjjj$, after the selection cuts are applied | 169 |
|-----|---|-----|

Bibliography

- [1] S. Chatrchyan *et al.* [CMS Collaboration], Phys. Lett. B **716** (2012) 30 [arXiv:1207.7235 [hep-ex]].
- [2] G. Aad *et al.* [ATLAS Collaboration], Phys. Lett. B **716** (2012) 1 [arXiv:1207.7214 [hep-ex]].
- [3] F. Englert and R. Brout, Phys.Rev.Lett. **13**, 321 (1964).
- [4] P. W. Higgs, Phys.Rev.Lett. **13**, 508 (1964).
- [5] P. W. Higgs, Phys.Lett. **12**, 132 (1964).
- [6] G. Guralnik, C. Hagen, and T. Kibble, Phys.Rev.Lett. **13**, 585 (1964).
- [7] P. W. Higgs, Phys.Rev. **145**, 1156 (1966).
- [8] T. Kibble, Phys.Rev. **155**, 1554 (1967).
- [9] G. Aad *et al.* [ATLAS Collaboration], Phys. Lett. B **726**, 120 (2013) [arXiv:1307.1432 [hep-ex]].
- [10] S. Chatrchyan *et al.* [CMS Collaboration], arXiv:1312.5353 [hep-ex].
- [11] S. Weinberg, *Physica* **96A**, 327 (1979);
- [12] H. Georgi, *Weak Interactions and Modern Particle Theory* (Benjamin/Cummings, Menlo Park, 1984)
- [13] J. F. Donoghue, E. Golowich and B. R. Holstein, *Dynamics of the Standard Model* (Cambridge University Press, 1992).
- [14] C. Delaunay, T. Flacke, J. Gonzalez-Fraile, S. J. Lee, G. Panico and G. Perez, JHEP **1402**, 055 (2014) [arXiv:1311.2072 [hep-ph]].
- [15] T. Corbett, O. J. P. Eboli, J. Gonzalez-Fraile and M. C. Gonzalez-Garcia, Phys. Rev. D **86**, 075013 (2012) [arXiv:1207.1344 [hep-ph]].
- [16] T. Corbett, O. J. P. Eboli, J. Gonzalez-Fraile and M. C. Gonzalez-Garcia, Phys. Rev. D **87**, 015022 (2013) [arXiv:1211.4580 [hep-ph]].

-
- [17] T. Corbett, O. J. P. Eboli, J. Gonzalez-Fraile and M. C. Gonzalez-Garcia, Phys. Rev. Lett. **111**, 011801 (2013) [arXiv:1304.1151 [hep-ph]].
- [18] T. Corbett, O. J. P. Eboli, J. Gonzalez-Fraile and M. C. Gonzalez-Garcia, arXiv:1306.0006 [hep-ph].
- [19] W. Buchmuller and D. Wyler, Nucl.Phys. **B268**, 621 (1986).
- [20] C. N. Leung, S. Love, and S. Rao, Z.Phys. **C31**, 433 (1986).
- [21] A. De Rujula, M. Gavela, P. Hernandez, and E. Masso, Nucl.Phys. **B384**, 3 (1992).
- [22] K. Hagiwara, S. Ishihara, R. Szalapski, and D. Zeppenfeld, Phys.Rev. **D48**, 2182 (1993).
- [23] K. Hagiwara, R. Szalapski, and D. Zeppenfeld, Phys.Lett. **B318**, 155 (1993), arXiv:hep-ph/9308347.
- [24] K. Hagiwara, S. Matsumoto, and R. Szalapski, Phys.Lett. **B357**, 411 (1995), arXiv:hep-ph/9505322.
- [25] K. Hagiwara, T. Hatsukano, S. Ishihara and R. Szalapski, Nucl. Phys. B **496**, 66 (1997) [hep-ph/9612268].
- [26] M. Gonzalez-Garcia, Int.J.Mod.Phys. **A14**, 3121 (1999), arXiv:hep-ph/9902321;
- [27] F. de Campos, M. C. Gonzalez-Garcia and S. F. Novaes, Phys. Rev. Lett. **79**, 5210 (1997) [hep-ph/9707511];
- [28] M. C. Gonzalez-Garcia, S. M. Lietti and S. F. Novaes, Phys. Rev. D **57**, 7045 (1998) [hep-ph/9711446];
- [29] O. J. P. Eboli, M. C. Gonzalez-Garcia, S. M. Lietti and S. F. Novaes, Phys. Lett. B **434**, 340 (1998) [hep-ph/9802408];
- [30] M. C. Gonzalez-Garcia, S. M. Lietti and S. F. Novaes, Phys. Rev. D **59**, 075008 (1999) [hep-ph/9811373];
- [31] O. J. P. Eboli, M. C. Gonzalez-Garcia, S. M. Lietti and S. F. Novaes, Phys. Lett. B **478**, 199 (2000) [hep-ph/0001030].
- [32] G. Passarino, Nucl. Phys. B **868**, 416 (2013) [arXiv:1209.5538 [hep-ph]].
- [33] T. Appelquist and J. Carazzone, Phys. Rev. D **11**, 2856 (1975).
- [34] S. Weinberg, Phys. Rev. Lett. **43** (1979) 1566.
- [35] B. Grzadkowski, M. Iskrzynski, M. Misiak and J. Rosiek, JHEP **1010**, 085 (2010) [arXiv:1008.4884 [hep-ph]].

BIBLIOGRAPHY

- [36] H. D. Politzer, Nucl. Phys. B **172**, 349 (1980);
- [37] H. Georgi, Nucl. Phys. B **361**, 339 (1991);
- [38] C. Arzt, Phys. Lett. B **342**, 189 (1995) [hep-ph/9304230];
- [39] H. Simma, Z. Phys. C **61**, 67 (1994) [hep-ph/9307274].
- [40] J. Beringer *et al.* [Particle Data Group Collaboration], Phys. Rev. D **86**, 010001 (2012).
- [41] F. Bonnet, M. B. Gavela, T. Ota and W. Winter, Phys. Rev. D **85**, 035016 (2012) [arXiv:1105.5140 [hep-ph]].
- [42] The LEP collaborations and The LEP TGC Working group LEPEWWG/TGC/2003-01
- [43] V. M. Abazov *et al.* [D0 Collaboration], Phys. Lett. B **718**, 451 (2012) [arXiv:1208.5458 [hep-ex]].
- [44] T. Aaltonen *et al.* [CDF Collaboration], Phys. Rev. D **86**, 031104 (2012) [arXiv:1202.6629 [hep-ex]].
- [45] T. Aaltonen *et al.* [CDF Collaboration], Phys. Rev. Lett. **104**, 201801 (2010) [arXiv:0912.4500 [hep-ex]].
- [46] G. Aad *et al.* [ATLAS Collaboration], arXiv:1210.2979 [hep-ex].
- [47] G. Aad *et al.* [ATLAS Collaboration], Eur. Phys. J. C **72**, 2173 (2012) [arXiv:1208.1390 [hep-ex]].
- [48] G. Aad *et al.* [The ATLAS Collaboration], arXiv:1302.1283 [hep-ex].
- [49] CMS Collaboration,
[http://twiki.cern.ch/twiki/bin/view/CMSPublic/
PhysicsResultsSMP12005](http://twiki.cern.ch/twiki/bin/view/CMSPublic/PhysicsResultsSMP12005)
- [50] CMS Collaboration,
[http://twiki.cern.ch/twiki/bin/view/CMSPublic/
PhysicsResultsEWK11009](http://twiki.cern.ch/twiki/bin/view/CMSPublic/PhysicsResultsEWK11009)
- [51] S. Chatrchyan *et al.* [CMS Collaboration], Eur. Phys. J. C **73**, 2283 (2013) [arXiv:1210.7544 [hep-ex]].
- [52] K. Hagiwara, R. Peccei, D. Zeppenfeld, and K. Hikasa, Nucl. Phys. **B282**, 253 (1987).
- [53] [ALEPH and CDF and D0 and DELPHI and L3 and OPAL and SLD and LEP Electroweak Working Group and Tevatron Electroweak Working Group and SLD Electroweak and Heavy Flavour Groups Collaborations], arXiv:1012.2367 [hep-ex].

-
- [54] S. Alam, S. Dawson, and R. Szalapski, *Phys.Rev.* **D57**, 1577 (1998), arXiv:hep-ph/9706542.
- [55] J. Elias-Miro, J. R. Espinosa, E. Masso and A. Pomarol, *JHEP* **1311**, 066 (2013) [arXiv:1308.1879 [hep-ph]].
- [56] F. del Aguila and J. de Blas, *Fortsch. Phys.* **59**, 1036 (2011) [arXiv:1105.6103 [hep-ph]];
- [57] J. Wudka, *Int. J. Mod. Phys. A* **9**, 2301 (1994) [hep-ph/9406205].
- [58] C. Arzt, M. B. Einhorn and J. Wudka, *Nucl. Phys. B* **433**, 41 (1995) [hep-ph/9405214].
- [59] S. Kanemura, T. Ota and K. Tsumura, *Phys. Rev. D* **73** (2006) 016006 [hep-ph/0505191].
- [60] P. Paradisi, *JHEP* **0602** (2006) 050 [hep-ph/0508054].
- [61] E. Gabrielli and B. Mele, *Phys. Rev. D* **83** (2011) 073009 [arXiv:1102.3361 [hep-ph]].
- [62] S. Davidson and G. J. Grenier, *Phys. Rev. D* **81** (2010) 095016 [arXiv:1001.0434];
- [63] S. Davidson and P. Verdier, *Phys. Rev. D* **86**, 111701 (2012) [arXiv:1211.1248 [hep-ph]].
- [64] A. Goudelis, O. Lebedev and J. -h. Park, *Phys. Lett. B* **707** (2012) 369 [arXiv:1111.1715].
- [65] G. Blankenburg, J. Ellis and G. Isidori, *Phys. Lett. B* **712**, 386 (2012) [arXiv:1202.5704 [hep-ph]].
- [66] B. Tuchming [D0 and CDF Collaborations], *EPJ Web Conf.* **60**, 02003 (2013) [arXiv:1307.4873 [hep-ex]].
- [67] ATLAS Collaboration, ATLAS-CONF-2012-160
- [68] ATLAS Collaboration, ATLAS-CONF-2013-079
- [69] ATLAS Collaboration, ATLAS-CONF-2013-013
- [70] ATLAS Collaboration, ATLAS-CONF-2013-030
- [71] ATLAS Collaboration, ATLAS-CONF-2013-009
- [72] CMS Collaboration, CMS PAS HIG-13-004
- [73] CMS Collaboration, CMS PAS HIG-13-012

BIBLIOGRAPHY

- [74] CMS Collaboration, CMS PAS HIG-13-011
- [75] CMS Collaboration, CMS PAS HIG-13-002
- [76] CMS Collaboration, CMS PAS HIG-13-003
- [77] S. Chatrchyan *et al.* [CMS Collaboration], Phys. Lett. B **726**, 587 (2013) [arXiv:1307.5515 [hep-ex]].
- [78] ATLAS Collaboration, ATLAS-CONF-2012-091.
- [79] ATLAS Collaboration, ATLAS-CONF-2013-012.
- [80] CMS Collaboration, CMS PAS HIG-13-001.
- [81] G. Fogli, E. Lisi, A. Marrone, D. Montanino, and A. Palazzo, Phys.Rev. **D66**, 053010 (2002), arXiv:hep-ph/0206162.
- [82] M. Gonzalez-Garcia and M. Maltoni, Phys.Rept. **460**, 1 (2008), arXiv:0704.1800.
- [83] LHC Higgs Cross Section Working Group, S. Dittmaier *et al.*, (2011), arXiv:1101.0593.
- [84] J. R. Espinosa, M. Muhlleitner, C. Grojean and M. Trott, JHEP **1209**, 126 (2012) [arXiv:1205.6790 [hep-ph]].
- [85] M. Raidal and A. Strumia, Phys.Rev. **D84**, 077701 (2011), arXiv:1108.4903.
- [86] J. Alwall, M. Herquet, F. Maltoni, O. Mattelaer, and T. Stelzer, JHEP **1106**, 128 (2011), arXiv:1106.0522.
- [87] N. D. Christensen and C. Duhr, Comput.Phys.Commun. **180**, 1614 (2009), arXiv:0806.4194.
- [88] A. Pukhov *et al.*, (1999), arXiv:hep-ph/9908288.
- [89] CompHEP Collaboration, E. Boos *et al.*, Nucl.Instrum.Meth. **A534**, 250 (2004), arXiv:hep-ph/0403113.
- [90] K. Arnold *et al.*, (2011), arXiv:1107.4038.
- [91] S. Banerjee, S. Mukhopadhyay and B. Mukhopadhyaya, Phys. Rev. D **89**, 053010 (2014) [arXiv:1308.4860 [hep-ph]].
- [92] E. Masso and V. Sanz, Phys. Rev. D **87**, no. 3, 033001 (2013) [arXiv:1211.1320 [hep-ph]].
- [93] J. Ellis, V. Sanz and T. You, arXiv:1404.3667 [hep-ph].

- [94] O. J. P. Eboli, J. Gonzalez-Fraile and M. C. Gonzalez-Garcia, Phys. Lett. B **692**, 20 (2010) [arXiv:1006.3562 [hep-ph]].
- [95] M. Baak, A. Blondel, A. Bodek, R. Caputo, T. Corbett, C. Degrande, O. Eboli and J. Erler *et al.*, arXiv:1310.6708 [hep-ph].
- [96] R. Alonso, M. B. Gavela, L. Merlo, S. Rigolin and J. Yepes, Phys. Lett. B **722**, 330 (2013) [Erratum-ibid. B **726**, 926 (2013)] [arXiv:1212.3305 [hep-ph]].
- [97] I. Brivio, T. Corbett, O. J. P. Eboli, M. B. Gavela, J. Gonzalez-Fraile, M. C. Gonzalez-Garcia, L. Merlo and S. Rigolin, JHEP **1403**, 024 (2014) [arXiv:1311.1823 [hep-ph]].
- [98] B. Gavela, M. C. Gonzalez-Garcia, J. Gonzalez-Fraile, L. Merlo, S. Rigolin and J. Yepes, work in progress.
- [99] D. B. Kaplan and H. Georgi, Phys. Lett. B **136**, 183 (1984).
- [100] D. B. Kaplan, H. Georgi and S. Dimopoulos, Phys. Lett. B **136**, 187 (1984).
- [101] T. Banks, Nucl. Phys. B **243**, 125 (1984).
- [102] H. Georgi, D. B. Kaplan and P. Galison, Phys. Lett. B **143**, 152 (1984).
- [103] H. Georgi and D. B. Kaplan, Phys. Lett. B **145**, 216 (1984).
- [104] M. J. Dugan, H. Georgi and D. B. Kaplan, Nucl. Phys. B **254**, 299 (1985).
- [105] K. Agashe, R. Contino and A. Pomarol, Nucl. Phys. B **719**, 165 (2005) [hep-ph/0412089].
- [106] R. Contino, L. Da Rold and A. Pomarol, Phys. Rev. D **75**, 055014 (2007) [hep-ph/0612048].
- [107] B. Gripaios, A. Pomarol, F. Riva and J. Serra, JHEP **0904**, 070 (2009) [arXiv:0902.1483 [hep-ph]].
- [108] D. Marzocca, M. Serone and J. Shu, JHEP **1208**, 013 (2012) [arXiv:1205.0770 [hep-ph]].
- [109] N. Arkani-Hamed, A. G. Cohen and H. Georgi, Phys. Lett. B **513**, 232 (2001) [hep-ph/0105239].
- [110] M. Schmaltz and D. Tucker-Smith, Ann. Rev. Nucl. Part. Sci. **55**, 229 (2005) [hep-ph/0502182].

BIBLIOGRAPHY

- [111] W. D. Goldberger, B. Grinstein and W. Skiba, *Phys. Rev. Lett.* **100**, 111802 (2008) [arXiv:0708.1463 [hep-ph]].
- [112] E. Halyo, *Mod. Phys. Lett. A* **8**, 275 (1993).
- [113] L. Vecchi, *Phys. Rev. D* **82**, 076009 (2010) [arXiv:1002.1721 [hep-ph]].
- [114] B. A. Campbell, J. Ellis and K. A. Olive, *JHEP* **1203**, 026 (2012) [arXiv:1111.4495 [hep-ph]].
- [115] S. Matsuzaki and K. Yamawaki, *Phys. Lett. B* **719**, 378 (2013) [arXiv:1207.5911 [hep-ph]].
- [116] Z. Chacko, R. Franceschini and R. K. Mishra, *JHEP* **1304**, 015 (2013) [arXiv:1209.3259 [hep-ph]].
- [117] B. Bellazzini, C. Csaki, J. Hubisz, J. Serra and J. Terning, *Eur. Phys. J. C* **73**, 2333 (2013) [arXiv:1209.3299 [hep-ph]].
- [118] C. G. Callan, Jr., S. R. Coleman, J. Wess and B. Zumino, *Phys. Rev.* **177**, 2247 (1969).
- [119] L. Susskind, *Phys. Rev. D* **20**, 2619 (1979).
- [120] S. Dimopoulos and L. Susskind, *Nucl. Phys. B* **155**, 237 (1979).
- [121] S. Dimopoulos and J. Preskill, *Nucl. Phys. B* **199**, 206 (1982).
- [122] J. Bagger, V. D. Barger, K. -m. Cheung, J. F. Gunion, T. Han, G. A. Ladinsky, R. Rosenfeld and C. P. Yuan, *Phys. Rev. D* **49**, 1246 (1994) [hep-ph/9306256].
- [123] V. Koulovassilopoulos and R. S. Chivukula, *Phys. Rev. D* **50**, 3218 (1994) [hep-ph/9312317].
- [124] C. P. Burgess, J. Matias and M. Pospelov, *Int. J. Mod. Phys. A* **17**, 1841 (2002) [hep-ph/9912459].
- [125] B. Grinstein and M. Trott, *Phys. Rev. D* **76**, 073002 (2007) [arXiv:0704.1505 [hep-ph]].
- [126] A. Azatov, R. Contino and J. Galloway, *JHEP* **1204**, 127 (2012) [Erratum-ibid. **1304**, 140 (2013)] [arXiv:1202.3415 [hep-ph]].
- [127] G. Buchalla, O. Cata and C. Krause, *Nucl. Phys. B* **880**, 552 (2014) [arXiv:1307.5017 [hep-ph]].
- [128] R. Contino, D. Marzocca, D. Pappadopulo and R. Rattazzi, *JHEP* **1110**, 081 (2011) [arXiv:1109.1570 [hep-ph]].

-
- [129] M. S. Chanowitz, M. Golden and H. Georgi, Phys. Rev. D **36**, 1490 (1987).
- [130] C. P. Burgess and D. London, Phys. Rev. Lett. **69**, 3428 (1992).
- [131] C. P. Burgess and D. London, Phys. Rev. D **48**, 4337 (1993) [hep-ph/9203216].
- [132] R. Alonso, M. B. Gavela, L. Merlo, S. Rigolin and J. Yepes, JHEP **1206**, 076 (2012) [arXiv:1201.1511 [hep-ph]].
- [133] R. Alonso, M. B. Gavela, L. Merlo, S. Rigolin and J. Yepes, Phys. Rev. D **87**, no. 5, 055019 (2013) [arXiv:1212.3307 [hep-ph]].
- [134] R. Contino, C. Grojean, M. Moretti, F. Piccinini and R. Rattazzi, JHEP **1005**, 089 (2010) [arXiv:1002.1011 [hep-ph]].
- [135] C. Grojean, O. Matsedonskyi and G. Panico, JHEP **1310**, 160 (2013) [arXiv:1306.4655 [hep-ph]].
- [136] D. Barducci, A. Belyaev, M. S. Brown, S. De Curtis, S. Moretti and G. M. Pruna, JHEP **1309**, 047 (2013) [arXiv:1302.2371 [hep-ph]].
- [137] J. Elias-Miro, J. R. Espinosa, E. Masso and A. Pomarol, JHEP **1308**, 033 (2013) [arXiv:1302.5661 [hep-ph]].
- [138] A. Falkowski, F. Riva and A. Urbano, JHEP **1311**, 111 (2013) [arXiv:1303.1812 [hep-ph]].
- [139] I. Brivio, O. J. P. Éboli, M. B. Gavela, M. C. Gonzalez-Garcia, L. Merlo and S. Rigolin, [arXiv:1405.5412 [hep-ph]].
- [140] [CMS Collaboration], [arXiv:1307.7135 [hep-ex]].
- [141] [ATLAS Collaboration], [arXiv:1307.7292 [hep-ex]].
- [142] O. J. P. Eboli, S. M. Lietti, M. C. Gonzalez-Garcia and S. F. Novaes, Phys. Lett. B **339**, 119 (1994) [hep-ph/9406316].
- [143] S. Dawson and G. Valencia, Phys. Lett. B **333**, 207 (1994) [hep-ph/9406324].
- [144] O. J. P. Eboli, M. C. Gonzalez-Garcia and S. F. Novaes, Mod. Phys. Lett. A **15**, 1 (2000) [hep-ph/9811388].
- [145] G. Abbiendi *et al.* [OPAL Collaboration], Eur. Phys. J. C **33**, 463 (2004) [hep-ex/0308067].
- [146] P. Achard *et al.* [L3 Collaboration], Phys. Lett. B **586**, 151 (2004) [hep-ex/0402036].

BIBLIOGRAPHY

- [147] S. Schael *et al.* [ALEPH Collaboration], Phys. Lett. B **614**, 7 (2005).
- [148] G. Abbiendi *et al.* [OPAL Collaboration], Eur. Phys. J. C **19**, 229 (2001) [hep-ex/0009021].
- [149] J. Abdallah *et al.* [DELPHI Collaboration], Eur. Phys. J. C **54**, 345 (2008) [arXiv:0801.1235 [hep-ex]].
- [150] U. Baur and D. Zeppenfeld, Phys. Lett. B **201**, 383 (1988).
- [151] M. Dobbs, AIP Conf. Proc. **753**, 181 (2005) [arXiv:hep-ph/0506174].
- [152] F. Maltoni and T. Stelzer, JHEP **0302**, 027 (2003) [arXiv:hep-ph/0208156].
- [153] J. Pumplin, D. R. Stump, J. Huston, H. L. Lai, P. M. Nadolsky and W. K. Tung, JHEP **0207**, 012 (2002) [arXiv:hep-ph/0201195].
- [154] S. Dawson, X. -G. He and G. Valencia, Phys. Lett. B **390**, 431 (1997) [hep-ph/9609523].
- [155] J. Kumar, A. Rajaraman and J. D. Wells, Phys. Rev. D **78**, 035014 (2008) [arXiv:0801.2891 [hep-ph]].
- [156] T. Han and Y. Li, Phys. Lett. B **683**, 278 (2010) [arXiv:0911.2933 [hep-ph]].
- [157] M. Suzuki, Phys. Lett. B **153**, 289 (1985);
- [158] C. Bilchak, M. Kuroda and D. Schildknecht, Nucl. Phys. B **299**, 7 (1988);
- [159] G. J. Gounaris, J. Layssac, J. E. Paschalis and F. M. Renard, Z. Phys. C **66**, 619 (1995) [arXiv:hep-ph/9409260];
- [160] G. J. Gounaris, F. M. Renard and G. Tsirigoti, Phys. Lett. B **350**, 212 (1995) [arXiv:hep-ph/9502376].
- [161] U. Baur, T. Han and J. Ohnemus, Phys. Rev. D **51**, 3381 (1995) [arXiv:hep-ph/9410266];
- [162] U. Baur, T. Han and J. Ohnemus, Phys. Rev. D **53**, 1098 (1996) [arXiv:hep-ph/9507336].
- [163] F. Campanario, C. Englert and M. Spannowsky, Phys. Rev. **D82** (2010) 054015. [arXiv:1006.3090 [hep-ph]].
- [164] E. Accomando and A. Kaiser, Phys. Rev. D **73**, 093006 (2006) [arXiv:hep-ph/0511088].

- [165] T. Sjostrand, S. Mrenna and P. Z. Skands, JHEP **0605**, 026 (2006) [hep-ph/0603175].
- [166] John Conway, PGS4
<http://www.physics.ucdavis.edu/~conway/research/software/pgs/pgs4-general.htm>
- [167] B. W. Lee, C. Quigg and H. B. Thacker, Phys. Rev. D **16**, 1519 (1977).
- [168] C. Csaki, C. Grojean, H. Murayama, L. Pilo, and J. Terning, Phys. Rev. D **69**, 055006 (2004) [arXiv:hep-ph/0305237].
- [169] C. Csaki, C. Grojean, L. Pilo and J. Terning, Phys. Rev. Lett. **92**, 101802 (2004) [hep-ph/0308038].
- [170] G. Cacciapaglia, C. Csaki, C. Grojean and J. Terning, Phys. Rev. D **70**, 075014 (2004) [hep-ph/0401160].
- [171] G. Cacciapaglia, C. Csaki, G. Marandella and J. Terning, Phys. Rev. D **75**, 015003 (2007) [hep-ph/0607146].
- [172] Y. Nomura, JHEP **0311**, 050 (2003) [hep-ph/0309189].
- [173] R. S. Chivukula, D. A. Dicus and H. -J. He, Phys. Lett. B **525**, 175 (2002) [hep-ph/0111016].
- [174] R. S. Chivukula and H. -J. He, Phys. Lett. B **532**, 121 (2002) [hep-ph/0201164].
- [175] N. Arkani-Hamed, M. Porrati and L. Randall, JHEP **0108**, 017 (2001) [hep-th/0012148].
- [176] R. Rattazzi and A. Zaffaroni, JHEP **0104**, 021 (2001) [arXiv:hep-th/0012248].
- [177] M. Perez-Victoria, JHEP **0105**, 064 (2001) [arXiv:hep-th/0105048].
- [178] S. Weinberg, Phys. Rev. D **19**, 1277 (1979).
- [179] C. T. Hill and E. H. Simmons, Phys. Rept. **381**, 235 (2003) [Erratum-ibid. **390**, 553 (2004)] [hep-ph/0203079].
- [180] B. Bellazzini, C. Csaki, J. Hubisz, J. Serra and J. Terning, JHEP **1211**, 003 (2012) [arXiv:1205.4032 [hep-ph]].
- [181] A. Birkedal, K. Matchev, and M. Perelstein, Phys. Rev. Lett. **94**, 191803 (2005) [arXiv:hep-ph/0412278].
- [182] A. Alves, O. J. P. Eboli, M. C. Gonzalez-Garcia *et al.*, Phys. Rev. **D79**, 035009 (2009). [arXiv:0810.1952 [hep-ph]].

BIBLIOGRAPHY

- [183] M. Asano, Y. Shimizu, JHEP **1101**, 124 (2011). [arXiv:1010.5230 [hep-ph]].
- [184] A. Alves, O. J. P. Eboli, D. Goncalves *et al.*, Phys. Rev. **D80**, 073011 (2009). [arXiv:0907.2915 [hep-ph]].
- [185] O. J. P. Eboli, C. S. Fong, J. Gonzalez-Fraile and M. C. Gonzalez-Garcia, Phys. Rev. D **83**, 095014 (2011) [arXiv:1102.3429 [hep-ph]].
- [186] O. J. P. Eboli, J. Gonzalez-Fraile and M. C. Gonzalez-Garcia, Phys. Rev. D **85**, 055019 (2012) [arXiv:1112.0316 [hep-ph]].
- [187] J. Gonzalez-Fraile, arXiv:1205.5802 [hep-ph].
- [188] N. Cabibbo and A. Maksymowicz, Phys. Rev. **137**, B438 (1965) [Erratum-ibid. **168**, 1926 (1968)].
- [189] A. J. Barr, Phys. Lett. B **596**, 205 (2004) [hep-ph/0405052].
- [190] A. J. Barr, JHEP **0602**, 042 (2006) [hep-ph/0511115].
- [191] J. M. Smillie and B. R. Webber, JHEP **0510**, 069 (2005) [hep-ph/0507170].
- [192] A. Alves, O. Eboli and T. Plehn, Phys. Rev. D **74**, 095010 (2006) [hep-ph/0605067].
- [193] A. Alves and O. Eboli, Phys. Rev. D **75**, 115013 (2007) [arXiv:0704.0254 [hep-ph]].
- [194] R. Cousins, J. Mumford, J. Tucker and V. Valuev, JHEP **0511**, 046 (2005).
- [195] Y. Gao, A. V. Gritsan, Z. Guo, K. Melnikov, M. Schulze and N. V. Tran, Phys. Rev. D **81**, 075022 (2010) [arXiv:1001.3396 [hep-ph]].
- [196] C. Englert, C. Hackstein and M. Spannowsky, Phys. Rev. D **82**, 114024 (2010) [arXiv:1010.0676 [hep-ph]].
- [197] M. R. Buckley, H. Murayama, W. Klemm and V. Rentala, Phys. Rev. D **78**, 014028 (2008) [arXiv:0711.0364 [hep-ph]].
- [198] L. -T. Wang and I. Yavin, JHEP **0704**, 032 (2007) [hep-ph/0605296].
- [199] L. Edelhauser, W. Porod and R. K. Singh, JHEP **1008**, 053 (2010) [arXiv:1005.3720 [hep-ph]].
- [200] W. Ehrenfeld, A. Freitas, A. Landwehr and D. Wyler, JHEP **0907**, 056 (2009) [arXiv:0904.1293 [hep-ph]].

-
- [201] F. Boudjema and R. K. Singh, JHEP **0907**, 028 (2009) [arXiv:0903.4705 [hep-ph]].
- [202] O. Gedalia, S. J. Lee and G. Perez, Phys. Rev. D **80**, 035012 (2009) [arXiv:0901.4438 [hep-ph]].
- [203] L. -T. Wang and I. Yavin, Int. J. Mod. Phys. A **23**, 4647 (2008) [arXiv:0802.2726 [hep-ph]].
- [204] J. C. Pati and A. Salam, Phys. Rev. D **10**, 275 (1974) [Erratum-ibid. D **11**, 703 (1975)].
- [205] G. Altarelli, B. Mele and M. Ruiz-Altaba, Z. Phys. C **45**, 109 (1989) [Erratum-ibid. C **47**, 676 (1990)].
- [206] T. Aaltonen *et al.* [CDF Collaboration], Phys. Rev. Lett. **104**, 241801 (2010) [arXiv:1004.4946 [hep-ex]].
- [207] V. M. Abazov *et al.* [D0 Collaboration], Phys. Rev. Lett. **107**, 011801 (2011) [arXiv:1011.6278 [hep-ex]].
- [208] [ATLAS Collaboration], ATLAS-CONF-2013-015.
- [209] The ATLAS collaboration, ATLAS-CONF-2014-015.
- [210] CMS Collaboration [CMS Collaboration], CMS-PAS-EXO-12-025.
- [211] W. S. Cho, K. Choi, Y. G. Kim *et al.*, Phys. Rev. **D79**, 031701 (2009). [arXiv:0810.4853 [hep-ph]].
- [212] K. Choi, S. Choi, J. S. Lee *et al.*, Phys. Rev. **D80**, 073010 (2009). [arXiv:0908.0079 [hep-ph]].
- [213] C. G. Lester, D. J. Summers, Phys. Lett. **B463**, 99-103 (1999). [hep-ph/9906349].
- [214] D. L. Rainwater, Ph.D. thesis, hep-ph/9908378.
- [215] S. Asai, G. Azuelos, C. Buttar, V. Cavasinni, D. Costanzo, K. Cranmer, R. Harper and K. Jakobs *et al.*, Eur. Phys. J. C **32S2**, 19 (2004) [hep-ph/0402254].
- [216] The ATLAS Collaboration, ATLAS-CONF-2012-025
<https://atlas.web.cern.ch/Atlas/GROUPS/PHYSICS/CONFNOTES/ATLAS-CONF-2012-025/>
- [217] S. Chatrchyan *et al.* [CMS Collaboration], Phys. Lett. B **710**, 91 (2012) [arXiv:1202.1489 [hep-ex]].
<https://twiki.cern.ch/twiki/bin/view/CMSPublic/Hig11024TWiki>

BIBLIOGRAPHY

- [218] M. Cacciari, G. P. Salam and G. Soyez, *JHEP* **0804**, 063 (2008) [arXiv:0802.1189 [hep-ph]].
- [219] The CMS Collaboration CMS-EWK-11-010
- [220] For a review on neutrino physics, see for example M. C. Gonzalez-Garcia, M. Maltoni, *Phys. Rept.* **460**, 1-129 (2008). [arXiv:0704.1800 [hep-ph]].
- [221] M. B. Gavela, T. Hambye, D. Hernandez and P. Hernandez, *JHEP* **0909** (2009) 038 [arXiv:0906.1461 [hep-ph]].
- [222] O. J. P. Eboli, J. Gonzalez-Fraile and M. C. Gonzalez-Garcia, *JHEP* **1112**, 009 (2011) [arXiv:1108.0661 [hep-ph]].
- [223] P. Minkowski, *Phys. Lett. B* **67**, 421 (1977).
- [224] T. Yanagida, *Conf. Proc. C* **7902131**, 95 (1979).
- [225] M. Gell-Mann, P. Ramond and R. Slansky, *Conf. Proc. C* **790927**, 315 (1979) [arXiv:1306.4669 [hep-th]].
- [226] R. N. Mohapatra and G. Senjanovic, *Phys. Rev. Lett.* **44**, 912 (1980).
- [227] W. Konetschny and W. Kummer, *Phys. Lett. B* **70**, 433 (1977).
- [228] T. P. Cheng and L. -F. Li, *Phys. Rev. D* **22**, 2860 (1980).
- [229] G. Lazarides, Q. Shafi and C. Wetterich, *Nucl. Phys. B* **181**, 287 (1981).
- [230] J. Schechter and J. W. F. Valle, *Phys. Rev. D* **22**, 2227 (1980).
- [231] R. N. Mohapatra and G. Senjanovic, *Phys. Rev. D* **23**, 165 (1981).
- [232] R. Foot, H. Lew, X. G. He and G. C. Joshi, *Z. Phys. C* **44**, 441 (1989).
- [233] E. Ma, *Phys. Rev. Lett.* **81**, 1171 (1998) [hep-ph/9805219].
- [234] B. Bajc and G. Senjanovic, *JHEP* **0708**, 014 (2007) [hep-ph/0612029].
- [235] P. Fileviez Perez, *Phys. Lett. B* **654**, 189 (2007) [hep-ph/0702287].
- [236] F. del Aguila and J. A. Aguilar-Saavedra, *Nucl. Phys. B* **813** (2009) 22 [arXiv:0808.2468 [hep-ph]].
- [237] F. del Aguila and J. A. Aguilar-Saavedra, *Phys. Lett. B* **672** (2009) 158 [arXiv:0809.2096 [hep-ph]].
- [238] P. Fileviez Perez, T. Han, G. -y. Huang, T. Li and K. Wang, *Phys. Rev. D* **78**, 015018 (2008) [arXiv:0805.3536 [hep-ph]].

-
- [239] R. Franceschini, T. Hambye and A. Strumia, Phys. Rev. D **78**, 033002 (2008) [arXiv:0805.1613 [hep-ph]].
- [240] T. Li and X. -G. He, Phys. Rev. D **80**, 093003 (2009) [arXiv:0907.4193 [hep-ph]].
- [241] A. Arhrib, B. Bajc, D. K. Ghosh, T. Han, G. -Y. Huang, I. Puljak and G. Senjanovic, Phys. Rev. D **82**, 053004 (2010) [arXiv:0904.2390 [hep-ph]].
- [242] B. Bajc, M. Nemevsek and G. Senjanovic, Phys. Rev. D **76**, 055011 (2007) [hep-ph/0703080].
- [243] R. N. Mohapatra and J. W. F. Valle, Phys. Rev. D **34**, 1642 (1986).
- [244] J. Kersten and A. Y. .Smirnov, Phys. Rev. D **76**, 073005 (2007) [arXiv:0705.3221 [hep-ph]].
- [245] V. Cirigliano, B. Grinstein, G. Isidori and M. B. Wise, Nucl. Phys. B **728**, 121 (2005) [hep-ph/0507001].
- [246] S. Davidson and F. Palorini, Phys. Lett. B **642**, 72 (2006) [hep-ph/0607329].
- [247] R. Alonso, G. Isidori, L. Merlo, L. A. Munoz and E. Nardi, JHEP **1106**, 037 (2011) [arXiv:1103.5461 [hep-ph]].
- [248] R. S. Chivukula and H. Georgi, Phys. Lett. B **188**, 99 (1987).
- [249] A. J. Buras, P. Gambino, M. Gorbahn, S. Jager and L. Silvestrini, Phys. Lett. B **500**, 161 (2001) [hep-ph/0007085].
- [250] G. D'Ambrosio, G. F. Giudice, G. Isidori and A. Strumia, Nucl. Phys. B **645**, 155 (2002) [hep-ph/0207036].
- [251] J. Garayoa and T. Schwetz, JHEP **0803**, 009 (2008) [arXiv:0712.1453 [hep-ph]].
- [252] A. Abada, C. Biggio, F. Bonnet, M. B. Gavela and T. Hambye, JHEP **0712** (2007) 061 [arXiv:0707.4058 [hep-ph]].
- [253] J. Schechter and J. W. F. Valle, Phys. Rev. D **21**, 309 (1980).
- [254] S. Antusch, C. Biggio, E. Fernandez-Martinez, M. B. Gavela and J. Lopez-Pavon, JHEP **0610**, 084 (2006) [hep-ph/0607020].
- [255] M. C. Gonzalez-Garcia, M. Maltoni and J. Salvado, JHEP **1004**, 056 (2010) [arXiv:1001.4524 [hep-ph]].

BIBLIOGRAPHY

- [256] F. P. An *et al.* [DAYA-BAY Collaboration], Phys. Rev. Lett. **108**, 171803 (2012) [arXiv:1203.1669 [hep-ex]].
- [257] G. Aad *et al.* [ATLAS Collaboration], JINST **3**, S08003 (2008).
- [258] S. Chatrchyan *et al.* [CMS Collaboration], JINST **3**, S08004 (2008).
- [259] E. Gross, D. Grossman, Y. Nir and O. Vitells, Phys. Rev. D **81**, 055013 (2010) [arXiv:1001.2883 [hep-ph]].
- [260] S. Chatrchyan *et al.* [CMS Collaboration], Phys. Lett. B **718** (2012) 348 [arXiv:1210.1797 [hep-ex]].
- [261] [ATLAS Collaboration], ATLAS-CONF-2013-019.